วัสดุท่อนาโนคาร์บอนไฮบริดด้วยพอลิเมอร์และอนุภาคนาโนโลหะสำหรับการตรวจวัดสารอินทรีย์ระเหยง่ายด้วยประสิทธิภาพการตอบสนองสูงและความสามารถในการเลือกตรวจวัด

POLYMER/METAL NANOPARTICLE/CARBON NANOTUBE HYBRID MATERIALS FOR HIGHLY SENSITIVE AND SELECTIVE VOLATILE ORGANIC COMPOUND DETECTION

วรวุฒิ เมืองรัตน์

WORAWUT MUANGRAT

วิทยานิพนธ์นี้เป็นส่วนหนึ่งของการศึกษาตามหลักสูตรปริญญาปรัชญาดุษฎีบัณฑิต

สาขาวิชานาโนวิทยาและนาโนเทคโนโลยี

วิทยาลัยนาโนเทคโนโลยีพระจอมเกล้าลาดกระบัง

สถาบันเทคโนโลยีพระจอมเกล้าเจ้าคุณทหารลาดกระบัง

พ.ศ. 2559

KMITL-2016-NT-D-001-008

POLYMER/METAL NANOPARTICLE/CARBON NANOTUBE HYBRID MATERIALS FOR HIGHLY SENSITIVE AND SELECTIVE VOLATILE ORGANIC COMPOUND DETECTION

WORAWUT MUANGRAT

A THESIS SUBMITTED IN PARTIAL FULFILLMENT

OF THE REQUIREMENT FOR THE DEGREE OF

DCOTOR OF PHILOSOPHY IN NANOSCIENCE AND NANOTECHNOLOGY

COLLEGE OF NANOTECHNOLOGY

KINGMONGKUT'S INSTITUTE OF TECHNOLOGY LADKRABANT

2016

KMITL-2016-NT-D-001-008

หัวข้อวิทยานิพนธ์	วัสดุท่อนาโนคาร์บอนไฮบริดด้วยพอลิเมอร์และอนุภาคนาโนโลหะสำหรับการตรวจวัดสารอินทรีย์ระเหยง่ายด้วยประสิทธิภาพการตอบสนองสูงและความสามารถในการเลือกตรวจวัด
นักศึกษา	นายวรวุฒิ เมืองรัตน์
รหัสประจำตัว	55670101
ปริญญา	ปรัชญาดุษฎีบัณฑิต
สาขาวิชา	นาโนวิทยาและนาโนเทคโนโลยี
พ.ศ.	2559
อาจารย์ที่ปรึกษาวิทยานิพนธ์	ผศ.ดร.วินัดดา วงศ์วิริยะพันธ์
อาจารย์ที่ปรึกษาวิทยานิพนธ์ร่วม	ดร.ศุภนิจ พรธีระภัทร

บทคัดย่อ

งานวิจัยนี้ได้ศึกษาเกี่ยวกับวัสดุไฮบริดของท่อนาโนคาร์บอนตกแต่งด้วยพอลิเมอร์และอนุภาคนาโนโลหะสำหรับการตรวจวัดสารอินทรีย์ระเหยง่ายด้วยประสิทธิภาพการตอบสนองสูงและความสามารถในการเลือกตรวจวัด มอนอเมอร์และพอลิเมอร์ที่เลือกใช้ คือ ไทโอฟีน เอทิลเซลลูโลส พอลิเมทิลเมทาคริเลต พอลิสไตรีน และพอลิไวนิลอะซีเตด อนุภาคนาโนโลหะที่เลือกใช้ คือ ทอง พาลาเดียม และแพลทินัม ขั้นตอนการเตรียมก๊าซเซนเซอร์ เริ่มต้นจากการเตรียมโครงข่ายท่อนาโนคาร์บอนแบบผนังชั้นเดี่ยวด้วยวิธีการหยดลงบนแผ่นรองรับที่ประกอบด้วยขั้วไฟฟ้าโครงสร้างอินเตอร์ดิจิเตท แล้วทำการเคลือบทับด้วยพอลิเมอร์ด้วยวิธีการเคลือบแบบหมุนเหวี่ยง หลังจากนั้นทำการเคลือบด้วยอนุภาคนาโนโลหะด้วยวิธีระเหยสารด้วยลำอิเล็กตรอน (อ้างอิงเป็นอนุภาคนาโนโลหะ/พอลิเมอร์/ท่อนาโนคาร์บอน) ในการศึกษาประสิทธิภาพการตรวจวัดก๊าซของวัสดุไฮบริดอนุภาคนาโนโลหะ/พอลิเมอร์/ท่อนาโนคาร์บอน จะศึกษาการตอบสนองต่อสารอินทรีย์ระเหยง่ายที่อุณหภูมิห้อง โดยศึกษาการเปลี่ยนแปลงสมบัติทางไฟฟ้าของวัสดุไฮบริด สารอินทรีย์ระเหยง่ายที่ใช้ได้การทดลองได้แก่ อะซีโตน เอทานอล เมทานอล เบนซีน คลอโรฟอร์ม และไดคลอโรมีเทน ผลการตรวจวัดสารอินทรีย์ระเหยง่ายของก๊าซเซนเซอร์ของพอลิเมอร์/ท่อนาโนคาร์บอนพบว่า เอทิลเซลลูโลส/ท่อนาโนคาร์บอนสามารถตอบสนองต่อไอระเหยของเบนซีน คลอโรฟอร์ม และไดคลอโรมีเทนได้สูงที่สุด ในส่วนของก๊าซเซนเซอร์ของอนุภาคนาโนโลหะ/ท่อนาโนคาร์บอนพบว่า อนุภาคนาโนพาลาเดียม/ท่อนาโนคาร์บอนสามารถตอบสนองต่อไอระเหยของเบนซีนได้สูงสุด ในขณะที่อนุภาคนาโนแพลทินัม/ท่อนาโนคาร์บอนสามารถตอบสนองต่อไอระเหยของไดคลอโรมีเทน และคลอโรฟอร์มได้สูงสุด โดยมีค่าความต้านทานเพิ่มมากขึ้น ในส่วนของก๊าซเซนเซอร์ของวัสดุไฮบริดอนุภาคนาโนโลหะ/พอลิเมอร์/ท่อนาโนคาร์บอนพบว่า วัสดุไฮบริดอนุภาคนาโนพาลาเดียม/เอทิลเซลลูโลส/ท่อนาโนคาร์บอน มีค่าการตอบสนองต่อเบนซีนเพิ่มขึ้นถึง 8 เท่า และอนุภาคนาโนแพลทินัม/เอทิลเซลลูโลส/ท่อนาโนคาร์บอนมีค่าการตอบสนองต่อคลอโรฟอร์มและไดคลอโรมีเทนเพิ่มขึ้นถึง 71 และ 194 เท่า ตามลำดับ กลไกการตอบสนองต่อไอระเหยของไฮบริดอนุภาคนาโนโลหะ/พอลิเมอร์/ท่อนาโนคาร์บอนเกิดจากการพองตัวของพอลิเมอร์ และตัวเร่งปฏิกิริยาออกซิเดชันบนอนุภาคนาโนโลหะ ผลการทดลองที่ได้แสดงให้เห็นว่าวัสดุไฮบริดอนุภาคนาโนโลหะ/พอลิเมอร์/ท่อนาโนคาร์บอนแสดงมีศักยภาพในการนำไปใช้

งานสำหรับตรวจวัดสารอินทรีย์ระเหยง่ายที่มีประสิทธิภาพการตอบสนองสูงที่อุณหภูมิห้องและมีความสามารถในการเลือกตรวจวัด

คำสำคัญ : ท่อนาโนคาร์บอน, พอลิเมอร์, อนุภาคนาโนโลหะ, สารอินทรีย์ระเหยง่าย, ก๊าซเซนเซอร์

Thesis Title	Polymer/Metal Nanoparticle/Carbon Nanotube Hybrid Materials for Highly Sensitive and Selective Volatile Organic Compound Detection
Student	Mr.Worawut Muangrat
Student ID	55670101
Degree	Doctor of Philosophy
Program	Nanoscience and Nanotechnology
Year	2016
Thesis advisor	Asst. Prof. Dr. Winadda Wongwiriyapan
Thesis Co-advisor	Dr. Supanit Porntheeraphat

ABSTRACT

This research studies on hybrid materials based on metal nanoparticle (NP) and polymer-functionalized carbon nanotube (CNT) for highly sensitive and selective volatile organic compound (VOC) detection. Thiophene, ethyl cellulose (EC), poly(methyl methacrylate) (PMMA), polystyrene (PS), and polyvinyl acetate (PVA) were used as monomer and polymer, while gold (Au), palladium (Pd), and platinum (Pt) were used as a metal NPs. A pristine single-walled CNT network was firstly formed by drop-casting onto printed circuit board (PCB) substrates consisting of an interdigitated electrode. Next, monomer or polymer was coated on the pre-dropped CNT network by spin coating, followed by the deposition of metal NPs by electron-beam evaporation (hereafter referred to as metal NP/polymer/CNT). The VOC sensing characterization of the hybrid metal NP/polymer/CNT was investigated at room temperature by the change of electrical property of hybrid material. The hybrid metal NP/polymer/CNT was exposed to acetone, ethanol, methanol, benzene, chloroform, and dichloromethane. For gas sensor based on polymer/CNT, EC/CNT showed the highest response to benzene, chloroform, and dichloromethane. For gas sensor based on metal NP/CNT, Pd/CNT showed the highest response to benzene, while Pt/CNT showed the highest response to chloroform and dichloromethane with an increase in resistance. For hybrid metal NP/polymer/CNT sensor, the hybrid Pd/EC/CNT enabled an approximately 8-fold improvement in benzene detection, while Pt/EC/CNT enabled an approximately 71- and 194-fold improvement in chloroform and dichloromethane detection, respectively compared to the pristine CNT. The mechanism of the hybrid metal NP/polymer/CNT could be contributed to the swelling of polymer and the catalytic oxidation on the metal NPs. These results suggest that the hybrid metal NP/polymer/CNT is a promising approach for improving VOC detection with a high response and selectivity at room temperature.

Keywords : Carbon nanotube, Polymer, Metal nanoparticle, Volatile organic compound, Gas sensor

ACKNOWLEDGEMENTS

First of all, I would like to express my deep and sincere gratitude to my advisor Asst. Prof. Dr. Winadda Wongwiriyapan (College of Nanotechnology, King Mongkut's Institute of Technology Ladkrabang (KMITL)) and co-advisor Dr. Supanit Porntheeraphat (National Electronics and Computer Technology Center (NECTEC)) for their encouragement, helpful suggestion, remarkable patience, and kind support during my PhD.

I am deeply grateful to Asst. Prof. Dr. Apiluck Eiad-ua, Asst. Prof. Dr. Darinee Promyothin, Dr. Nongluck Houngkamhang (College of Nanotechnology, KMITL), and Dr. Chanchana Thanachayanont (National Metal and Materials Technology Center (MTEC)), for their comments and suggestions on this dissertation.

I would like to acknowledge the financial support from the Thailand Graduate Institute of Science and Technology (TGIST) under contact number 01-55-13, the King Prajadhipok and Queen Rambhai Barni Memorial Foundation, and the Toray Science Foundation (TSF), Japan. This work has partially been supported by the National Nanotechnology Center (NANOTEC), NSTDA, Ministry of Science and Technology, Thailand, through its program of Center of Excellence Network.

I wish to thank the Thai Microelectronics Center (TMEC), NECTEC for their facility support such as electron-beam (EB) evaporator and field emission scanning electron microscope. I also thank to Dr. Win Bunjongpru (TMEC, NECTEC) and Dr. Apichart Sungthong (Department of Applied Physics, Faculty of Science and Technology, Rajabhat Rajanagarindra University) for their EB evaporation technique suggestion.

I would like to thank Mr. Visittapong Yordsri, senior technician at MTEC, for his useful advice and partly assistance in field emission scanning electron microscopy, transmission electron microscopy and X-ray diffraction analysis.

I wish like to thank all the colleagues and friends, especially those who are Nanocarbon Materials Research Laboratory, College of Nanotechnology, KMITL for their supports and kindnesses.

Finally, this dissertation is dedicated to my parent, my wife, my brother and sister, and all members of my family for all supports.

Worawut Muangrat

CONTENTS

Page

ABSTRACT (THAI) I

ABSTRACT III

Acknowledgements V

CONTENTS VI

LIST OF TABLES XI

LIST OF FIGURES XII

CHAPTER 1 INTRODUCTION 1

1.1 Background and Problem 1

1.2 Objectives of the Study 2

1.3 Scope of the Study 3

1.4 Expected Results 3

CHAPTER 2 THEORY AND LITERATURE REVIEW 4

2.1 Type of Carbon Nanotubes 4

2.2 Properties of Carbon Nanotube 6

2.2.1 Electrical Property 6

2.2.2 Thermal Property 6

2.2.3 Mechanical Property 6

2.3 Synthesis of Carbon Nanotube 7

2.3.1 Arc Discharge 7

2.3.2 Laser Ablation 8

2.3.3 Chemical Vapor Deposition 9

2.4 Growth Mechanism of Carbon Nanotube 10

2.5 Composition and Definition of Chemical Sensor 11

2.5.1 Recognition Methods 12

2.5.2 Transduction Methods 13

2.6 Adsorption Isotherm 13

CONTENTS (Cont.)

Page

2.7 Development of Carbon Nanotube for Volatile Organic Compound Detection 16
2.7.1 Volatile Organic Compound Detection 16
2.7.2 Gas Sensor Based on Carbon Nanotube 18
2.7.3 Gas Sensing Mechanism 37
2.8 Hansen Solubility Parameter 40
2.9 Principal Component Analysis 41
2.10 Thin Film Deposition 43
2.10.1 Spin Coating 43
2.10.2 Electron Beam Evaporation 44
2.11 Analytical Instrument 45
2.11.1 Scanning Electron Microscopy 45
2.11.2 Energy-Dispersive X-Ray Spectroscopy 45
2.11.3 Transmission Electron Microscopy 46
2.11.4 Raman Spectroscopy 47
2.11.5 Fourier Transform Infrared 47
2.11.6 X-Ray Diffraction 48
2.11.7 Fluorescence spectroscopy 49

CHAPTER 3 POLYMER-FUNCTIONALIZED SINGLE-WALLED CARBON NANOTUBE FOR VOLATILE ORGANIC COMPOUNDS DETECTION 50
3.1 Fabrication of Gas Sensor Device 50
3.1.1 Preparation of Sensor Platform 50
3.1.2 Fabrication of Sensor Based on Polymer-Functionalized Carbon Nanotubes 51
3.2 Morphology and Structural Characterization of Sensing Materials 52
3.2.1 Scanning Electron Microscopy Characterization 52
3.2.2 Raman Spectroscopy Characterization 53
3.3 Sensor Performance of Polymer-Functionalized Carbon Nanotubes. 55
3.3.1 Gas Sensor Measurement System 55

CONTENTS (Cont.)

Page

3.3.2 Sensor Response of Polymer-Functionalized Single-Walled Carbon Nanotube to Volatile Organic Compound System 57
3.3.3 Volatile Organic Compound Discrimination by Principal Component Analysis 62
3.4 Summary 63

CHAPTER 4 METAL NANOPARTICLE-FUNCTIONALIZED SINGLE-WALLED CARBON NANOTUBE FOR VOLATILE ORGANIC COMPOUNDS DETECTION 65
4.1 Fabrication of Gas Sensor Based on Polymer-Functionalized Carbon Nanotubes 65
4.2 Morphology and Structural Characterization of Sensing Materials 66
4.2.1 Transmission Electron Microscopy Characterization 66
4.2.2 Raman Spectroscopy Characterization 67
4.3 Sensor performance of metal nanoparticles-functionalized carbon nanotubes 68
4.3.1 Gas Sensor Measurement System 68
4.3.2 Sensor Response of Metal Nanoparticles-Functionalized Single-Walled Carbon Nanotube to Volatile Organic Compound 69
4.4 Summary 73

CHAPTER 5 POLYMER AND METAL NANOPARTICLE-FUNCTIONALIZED SINGLE-WALLED CARBON NANOTUBE FOR VOLATILE ORGANIC COMPOUNDS DETECTION 74
5.1 Fabrication of Gas Sensor Based on Metal Nanoparticles/Polymer-Functionalized Carbon Nanotubes 74

CONTENTS (Cont.)

Page

5.2 Morphology and Structural Characterization of Sensing Materials 76

5.2.1 Scanning Electron Microscopy Characterization 76

5.2.2 Transmission Electron Microscopy Characterization 78

5.2.3 Fourier Transform Infrared Spectroscopy Characterization 79

5.2.3 X-ray Diffraction Characterization 80

5.2.4 Raman Spectroscopy Characterization 81

5.3 Sensor Performance of Metal Nanoparticles/Polymer-Functionalized Single-Walled Carbon Nanotubes 82

5.3.1 Gas Sensor Measurement System 82

5.3.2 Sensor Response of Metal nanoparticles/Polymer Functionalized Single-Walled Carbon Nanotube to Volatile Organic Compound 85

5.4 Investigation of Sensing Mechanism 94

5.4.1 Fluorescence Spectroscopy Characterization 94

5.4.2 The Proposed Sensing Mechanism of Polymer-Functionalized Carbon Nanotubes 94

5.5 Dichloromethane Sensor Based on Platinum Nanoparticle/ Poly(methyl methacrylate)/Single-Walled Carbon Nanotube 95

5.5.1 Fabrication of Gas Sensor Based on Platinum Nanoparticles/Poly (methyl methacrylate)-Functionalized Carbon Nanotubes 96

5.5.2 Morphology and structural characterization of sensing materials 96

CONTENTS (Cont.)

Page

Page 5.5.3 Sensor Performance of Platinum Nanoparticles/Poly (methyl methacrylate)-Functionalized Single-Walled Carbon Nanotubes 101

5.6 Summary 105

CHAPTER 6 CONCLUSIONS 106

REFERENCES 108

APPENDIX 116

AUTHOR BIOGRAPHY 122

LIST OF TABLES

Table Page

2.1 Comparison of thermal properties 6
2.2 Comparison of mechanical properties 7
2.3 Summary and comparison of three CNT synthesis methods. 9
2.4 Standard average concentration of VOCs 16
2.5 Summary and comparison of various VOCs detection. 17
2.6 Comparison sensitivity (10^{-2} % ppm^{-1}) to the different vapors and gases 29
2.7 Summary of sensing performance of CNT and CNT-functionalized polymer 32
3.1 Specifications of PCB substrate 50
3.2 List of monomer and polymers used in this research 51
3.3 Conditions for gas sensing characterization 56
3.4 Initial resistance of SWNT, monomer/SWNT and polymer/SWNT. 57
3.5 Hansen solubility parameter and RED between polymer and VOCs. 61
4.1 List of metal elements and their purity 66
4.2 Conditions for gas sensing characterization 68
4.3 Initial resistance of SWNT and metal NP/SWNT. 69
5.1 Summary of sensors based on hybrid SWNTs. 75
5.2 Conditions for gas sensing characterization 83
5.3 Conditions for gas sensing characterization for ppm level detection. 84
5.4 Initial resistance of SWNT, EC/SWNT, Pd/SWNT, Pt/SWNT, Pd/EC/SWNT and Pt/EC/SWNT. 86
5.5 Summary of sensors based on hybrid SWNTs. 96
5.6 Conditions for gas sensing characterization 101

LIST OF FIGURES

Figure Page

2.1 Schematic diagrams of (a) SWNT and (b) MWNT 4
2.2 Schematic diagrams of (a) the chiral vector of the unit cell of a SWNT and (b) models of SWNT exhibiting different chirality; armchair (n,n), zigzag (n,0), and chiral n,m) configurations 5
2.3 Schematic diagram of arc discharge 8
2.4 Schematic diagrams of laser ablation 8
2.5 Schematic diagrams of CVD 9
2.6 Growth mechanisms for CNTs: (a) tip-growth model and (b) base-growth model 11
2.7 Schematic diagram of a chemical sensor. A sensor is an assembly of a receptor and transduction unit 11
2.8 Types of gas adsorption isotherms 14
2.9 (a) An image of SWNT (b) electrical conductance response of a semiconducting SWNT to (b) 200 ppm NO_2 and (c) 1% NH_3 vapor 19
2.10 (a) SEM image of SWNT (b) drain currents are shown as a function of time toward a saturated vapor of various kinds of alcohols 19
2.11 (a) Sensor response of f-MWNT-PMMA composite as a function of time toward a saturated vapor of VOCs and (b) DCM in a partial pressure range of 27-273 Torr. (c) Schematic diagram of junction resistance change between two CNTs due to polymer matrix swelling 20
2.12 Responses of the poly(3-methylthiophene)-MWNT nanocomposite for different VOCs 21
2.13 (a) A SEM image of the SWNT-EC composite film. (b) The gas sensing properties of the SWNT-EC composites for benzene vapor in range of 1000-5000 ppm. The inset shows the linear relationship 22

LIST OF FIGURES (Cont.)

Figure Page

2.14 (a) AFM image of a SWNT network. (b) Conductance change of the sensor upon exposure to varying concentrations of DMMP. (C) Calibration curve of the sensor at DMMP concentration of 0.05-25 ppm. (d) Conductance change of the SWNT sensors in response to organic solvents and DMMP diluted to 1% saturated vapor conditions at room temperature 22

2.15 A SEM image of aligned MWNTs (a) before and (b) after coated with polymer on top and turned upside down. Sensor response as a function of time: PVA/MWNT toward (c) various VOCs (d) THF (e) cyclohexane and (f) ethanol: PI/MWNT toward (g) cyclohexane and (h) ethanol: PVA-PI/MWNT toward (I) ethanol and cyclohexane 24

2.16 (a) AFM images of PMMA-CNT composite. (b) Response of PMMA-CNT sensors towards cyclic exposures to VOCs. (c) Compared average selectivity over 15 cycles of sensors exposure to the VOCs. (d) 3D PCA plots of nine VOCs 25

2.17 (a) Schematic diagram of pristine random network of MWNT and random network of MWNT coated by drop casting of different concentration of polymer. (b) PMMA thickness with different concentration in solution. (c) Response of vQRS to acetone vapor (d) Summary of relative amplitude for all vQRS. (e) 2D PCA map showing VOC discrimination ability of vQRS 26

2.18 (a) SEM image of Pd-decorated SWNT [52]. (b) Sensor response before gas exposure (R_0) and during the gas exposure (R_t). PCA plots of (c) discrimination of gases and organic vapors (d) discrimination of toxic gases 27

2.19 TEM images of MWNT (a) before and (b) after decorated with Pd NPs. (c) Gas sensing performance characterization: response to 50-500 ppb for benzene of the sensors based on Rh, Ni, Pd or Au-decorated MWNTs 28

2.20 TEM images of the (a) Pd- and (b) Pt-decorated MWNTs. (c) Comparison between the response of Pd-MWNTs and Pt-MWNTs to different gases and vapors tested 29

LIST OF FIGURES (Cont.)

Figure Page

2.21 TEM and electron diffraction patterns of (a) Pd NPs and (b) Pd-PANI nanocomposites. (c) Responses of PANI exposed to saturated vapor of methanol (2000 ppm) and Pd-PANI nanocomposites exposed to saturated vapor of methanol concentrations of (d) 1 ppm, (e) 5 ppm, (f) 10 ppm, (g) 100 ppm and (h) 2000 ppm 30
2.22 TEM images of nanocomposites prepared with Ag concentration of (a) 0.5 and (b) 2.5 mol%. Responses of the (c) pure PANI and (d) PANI-Ag nanocomposites sensors on exposure to ethanol vapor at different concentration at room temperature. (e) Variations in sensor response of pure PANI and PANI-Ag nanocomposite as a function of ethanol concentration 31
2.23 SEM images of (a) PANI NWs and (b) PANI NWs-Au NPs. (c) Response of PANI sensor toward 50 ppm of H_2S gas. (d) Response of PANI NWs-Au NPs sensor toward 0.1 ppb, 1 ppb, 10 ppb, 100 ppb, 500 ppb and 1000 ppb concentrations of H_2S gas. (d) Response of PANI NWs-Au NPs sensor as a function of H_2S concentration 32
2.24 The energy band diagram of Pt and p-type SWNT before (left) and after (right) merging. 39
2.25 Schematic diagrams of HSP sphere. 41
2.26 Schematic diagrams of spin coating process 44
2.27 Schematic diagrams of electron beam evaporation 44
2.28 Schematic diagrams of SEM 45
2.29 Principle of EDS 46
2.30 Schematic diagrams of TEM 46
2.31 (a) Schematic diagrams of Raman spectroscopy and (b) Energy-level diagram involves in Raman scattering 47
2.32 Schematic diagrams of FTIR 48
2.33 Schematic diagrams of XRD 49

LIST OF FIGURES (Cont.)

Figure Page

2.34 Absorption to an excited energy state followed fluorescence emission 49
3.1 Monomer and polymer structures of (a) thiophene, (b) EC, (c) PMMA, (d) PS and (e) PVA 52
3.2 Schematic view of (a) SWNTs and (b) polymer/SWNTs sensors 52
3.3 FESEM images of (a) pristine SWNT, (b) thiophene/SWNT, (c) EC/SWNT, (d) PMMA/SWNT, (e) PS/SWNT, and (f) PVA/SWNT. 53
3.4 Raman spectra of pristine SWNT, thiophene-, EC-, PMMA-, PS- and PVA-coated SWNT 54
3.5 Schematic view of a gas sensor measurement 55
3.6 Schematic view of flow profile of gas sensor measurement. 55
3.7 Sensor response as a function of time for pristine SWNT and polymer-coated SWNT toward (a) benzene (b) chloroform (c) dichloromethane (d) acetone (e) ethanol and (f) methanol. 58
3.8 Normalized sensor response of pristine SWNT and metal NP/SWNT toward (a) benzene (b) chloroform (c) dichloromethane (d) acetone (e) ethanol and (f) methanol. 59
3.9 Schematic diagram of gas sensing mechanism of pristine CNT for VOC detection 60
3.10 Schematic diagram of gas sensing mechanism of monomer- and polymer-coated CNT for VOC detection. 61
3.11 PCA plots of dichloromethane, acetone and methanol vapors 63
4.1 Schematic view of (a) SWNTs and (b) metal NPs/SWNTs sensors. 66
4.2 TEM images of (a) Au, (b) Pd and (c) Pt-decorated SWNT 67
4.3 Raman spectra of pristine SWNT, Au-, Pd- and Pt-decorated SWNT. 68
4.4 Sensor response as a function of time for pristine SWNT and metal NP-decorated SWNT toward (a) benzene (b) chloroform (c) dichloromethane (d) acetone (e) ethanol and (f) methanol 70

LIST OF FIGURES (Cont.)

Figure Page

4.5 Normalized sensor response of pristine SWNT and metal NP/SWNT toward (a) benzene (b) chloroform (c) dichloromethane (d) acetone (e) ethanol and (f) methanol 71
4.6 Sensing mechanism of metal NPs/polymer/SWNT upon VOC exposure 73
5.1 Schematic view of (a) SWNTs, (b) polymer/SWNTs, (c) metal NP/SWNTs and (d) metal NPs/polymer/SWNTs sensors 75
5.2 FESEM images of (a) EC(1 wt%)/SWNT and (b) EC(5 wt%)/SWNT 76
5.3 FESEM of (a) Pd(5 nm)/EC(5 wt%)/SWNT, EDS mapping of (c) palladium, (e) carbon, and (g) oxygen elements. FESEM of (b) Pt(5 nm)/EC(5 wt%)/SWNT, EDS mapping of (d) platinum, (f) carbon, and (h) oxygen elements. 77
5.4 TEM images of (a) Pd(5 nm)/SWNT, (b) Pt(2 nm)/SWNT and (c) Pt(5 nm/ SWNT). 78
5.5 FTIR spectra of SWNT, EC(5 wt%)/SWNT, Pd(5 nm)/EC(5 wt%)/SWNT and Pt(5 nm)/EC(5 wt%)/SWNT 79
5.6 XRD spectra of EC(5 wt%)/SWNT, Pd(5 nm/SWNT), Pt(5 nm)/SWNT, Pd(5 nm)/ EC(5 wt%)/SWNT and Pt(5 nm)/EC(5 wt%)/SWNT 80
5.7 Raman spectra of (a) pristine SWNT, EC/SWNT, Pd/SWNT and Pd/EC/SWNT and (b) pristine SWNT, EC/SWNT, Pt/SWNT and Pt/EC/SWNT. RBM spectra of (c) SWNT, Pd(2 nm)/SWNT, Pd(5 nm)/SWNT and Pd(5 nm)/EC(5 wt%)/SWNT, and (d) SWNT, Pt(2 nm)/SWNT, Pt(5 nm)/SWNT, Pt(5 nm)/EC(5 wt%)/SWNT 81
5.8 Schematic view of flow profile of gas sensor measurement. 83
5.9 Schematic view of a gas sensor measurement for ppm level detection. 85
5.10 Schematic view of flow profile of gas sensor measurement for ppm level detection. 85
5.11 Sensor response as a function of time of pristine SWNT, EC/SWNT, Pd/SWNT and Pd/EC/SWNT toward (a-b) benzene and pristine SWNT, EC/SWNT, Pt/ SWNT and Pt/EC/SWNT toward (c-d) chloroform and (e-f) dichloromethane 87

LIST OF FIGURES (Cont.)

Figure Page

5.12 Normalized sensor response of pristine SWNT, EC/SWNT, Pd/SWNT and Pd/EC/SWNT toward (a) benzene and pristine SWNT, EC/SWNT, Pt/SWNT and Pt/EC/SWNT toward (b) chloroform and (c) dichloromethane 88

5.13 Sensor response as a function time of sensor Pd(5 nm)/EC(5 wt%)/SWNT toward (a) benzene vapor and sensor Pt(5 nm)/EC(5 wt%)/SWNT toward (b) chloroform and (c) dichloromethane vapors at 250-3000 ppm. (d) Sensor response of sensor Pd(5 nm)/EC(5 wt%)/SWNT and Pt(5 nm)/EC(5 wt%)/ SWNT as a function of benzene, chloroform and dichloromethane concentration..... 90

5.14 Relationship between sensor response and concentration; C/SR vs. C of (a) benzene, (c) chloroform and (e) dichloromethane. Relationship between sensor response and VOC concentration of (b) benzene, (d) chloroform and (f) dichloromethane..... 93

5.15 Schematic view of (a) the swelling process of VOC adsorption and (b) emission spectra before and after VOC adsorption..... 94

5.16 Emission of EC/SWNT in air (black) and after 10 min exposure to saturated (a) benzene (b) chloroform and (c) dichloromethane vapors (red). 95

5.17 FESEM images of (a) PMMA(1 wt%)/SWNT and (b) PMMA(5 wt%)/SWNT 97

5.18 FESEM of (a) Pt(5 nm)/PMMA(5 wt%)/SWNT, EDS mapping of (b) platinum, (c) carbon, and (d) oxygen elements..... 97

5.19 FTIR spectra of SWNT, PMMA(5 wt%)/SWNT, Pt(5 nm)/PMMA(5 wt%)/ SWNT 99

5.20 XRD spectra of PMMA(5 wt%)/SWNT, Pt(5 nm)/SWNT and Pt(5 nm)/PMMA (5 wt%)/SWNT 99

5.21 (a) Raman spectra of pristine SWNT, PMMA/SWNT, Pt/SWNT and Pt/ PMMA/SWNT. (b) RBM spectra of pristine SWNT, Pt(2 nm)/SWNT, Pt(5 nm)/ SWNT and Pt(5 nm)/PMMA(5 wt%)/SWNT 100

LIST OF FIGURES (Cont.)

Figure Page

5.22 Sensor response as a function of time of (a) pristine SWNT, PMMA/SWNT, Pt/SWNT and (b) Pt/PMMA/SWNT toward dichloromethane. (c) Normalized sensor response of pristine SWNT, PMMA/SWNT, Pt/SWNT and Pt/PMMA/ SWNT toward dichloromethane. (d) Sensor response of Pt(5 nm)/PMMA (5 wt%)/SWNT as a function of dichloromethane concentration. . 103

A.1 SEM images of synthesized CNMs from different metal catalyst; (a) Ni, (b) Co and (c) Fe 117

A.2 TEM images of synthesized CNMs from different metal catalyst; (a) Ni, (b) Co and (c) Fe. TEM images at low magnification of CNMs synthesized from (g) Ni and (h) Co 118

A.3 Raman Spectroscopy of synthesized CNMs from different metal catalysts 119

CHAPTER 1

INTRODUCTION

1.1 Background and Problem

Nowadays, air pollution is an important problem to human health and environment. The main causes of this problem are the toxic chemicals and waste released from chemical industries, especially volatile organic compounds (VOCs) [1]. VOCs easily evaporate into the air at room temperature. VOCs are of extreme danger to human health, cause eye, nose and throat irritation, can also damage the liver and central nervous system, and present a risk of cancer [2–4]. According to the annual report on air quality in Bangkok and Map Ta Phut industrial estate in 2015 by the pollution control department (Thailand), there are many VOCs that their concentrations exceed the standard concentrations such as benzene, chloroform, 1,3-butadiene and 1,2-dichloroethane [5]. Although, concentrations of some VOCs (chloroform, dichloromethane, vinyl chloride and trichloroethane) are lower than that of the standard concentration but it is still necessary to monitor their concentrations. Hence, environmental monitoring and industrial safety are absolutely crucial for the protection of human health and environment. Thus, gas sensor technology is proposed for VOC monitoring and detection.

Carbon nanotubes (CNTs) are an allotrope of carbon with a cylindrical nanostructure. CNTs are divided in two types: single-walled carbon nanotubes (SWNTs) and multi-walled carbon nanotubes (MWNTs). CNTs have unique properties such as electrical, chemical, optical and mechanical properties. CNTs are applied in various fields such as electronic devices, optical devices, energy devices and sensors. CNTs have been focused as the most promising materials for next-generation innovative chemical sensor applications, owing to their nanostructure, large specific area, high electron mobility, superior electrical properties and room temperature operation. Gas sensors based on CNTs have been demonstrated to be ultrasensitive to oxidizing gases down to the parts per billion (ppb) level at room temperature [6–9]. However, CNT-based sensors are still insensitive to many kinds of gas molecules, such as VOCs, owing to the weak or nonspecific interactions between the CNTs and these molecules. Furthermore, another drawback of CNT-based sensors is their lack of selectivity for different kinds of gases. These issues limit the practical applications of CNT-based sensors to on-site monitoring. To overcome these drawbacks, combining polymer functionalization or metal nanoparticles (NPs) decoration with CNTs is the most

promising route [10–20]. Gas sensors based on polymer or metal NPs-functionalized CNTs are effective in improving VOC sensitivity and selectivity by different mechanisms. Thus, utilizing the functions of both polymer and the metal NPs is a promising route to improving its VOC sensitivity and selectivity. However, gas sensor based on metal NPs/polymer-functionalized CNTs for VOC detection has not been fully explored.

In this research, gas sensors based on hybrid materials of dual-functionalized SWNTs through polymer coating and metal NP deposition were studied for highly sensitive and selective VOC detection. This research consists of 3 parts; sensor fabrication based on (1) polymer-coated CNT, (2) metal NPs-decorated CNTs and (3 metal NPs/polymer-functionalized CNTs. The hybrid gas sensor based on polymer-coated CNTs by spin coating, metal NP-decorated CNTs by electron beam evaporation, and metal NPs/polymer-dual functionalized CNTs were fabricated. Materials were characterized by field emission scanning electron microscopy (FESEM), transmission electron microscopy (TEM), Raman spectroscopy, Fourier transform infrared spectroscopy (FTIR) and X-ray diffraction (XRD). For gas sensor measurement, sensor responses to VOCs such as benzene, chloroform and dichloromethane, acetone, ethanol and methanol were investigated. The sensing mechanism was proved by fluorescence spectroscopy. The pattern of sensor response to each VOC exposure was analyzed by principal component analysis (PCA) technique.

1.2 Objectives of the Study

1.2.1 To study the fabrication of hybrid gas sensor based on polymer and metal NP-functionalized and metal NP/polymer-functionalized CNTs by spin coating and electron beam evaporation methods

1.2.2 To study the sensitivity and selectivity of hybrid gas sensor based on polymer and metal NP-functionalized CNTs and metal NP/polymer-functionalized CNTs on VOCs detection

1.2.3 To study the sensing mechanisms of sensor based on polymer to VOC detection.

1.2.4 To study the pattern recognition of hybrid gas sensor on VOC detection by principal component analysis.

1.3 Scope of the Study

1.3.1 Preparation of polymer and metal NP-functionalized CNTs by spin coating and electron beam evaporation methods

1.3.2 Measurement of VOCs sensing performance of polymer and metal NP-functionalized CNTs

1.3.3 Preparation of metal NPs/polymer-functionalized CNTs

1.3.4 VOCs sensing performance measurement of dual-functionalization through polymer coating and metal nanoparticle deposition

1.3.5 Proof of sensing mechanism

1.3.6 Pattern recognition of hybrid gas sensor on VOC detection by principal component

1.4 Expected Results

1.4.1 Successfully fabricate the hybrid gas sensor based on polymer and metal NP- functionalized CNTs and metal NP/polymer-functionalized CNTs

1.4.2 Understand the sensing performance and sensing mechanism of polymer/ CNTs sensor to VOCs

1.4.3 Improve the sensitivity and selectivity to VOCs by hybrid gas sensor based on polymer and metal NP-functionalized CNTs and metal NP/polymer-functionalized CNTs

CHAPTER 2

THEORY AND LITERATURE REVIEW

In this chapter, the fundamentals of carbon nanotube (CNT) such as type, property, synthesis and growth mechanism of CNT, composition and definition of chemical sensor, gas sensor based on CNT, Hansen solubility parameter (HSP), thin film preparation, analytical instrument are described.

2.1 Type of Carbon Nanotubes

Since the discovery of carbon nanotubes (CNT) in 1991 by professor Sumio Iijima using arc discharge method [21], CNT has attracted intensive interest from many researchers due to their unique structure and superior properties. CNT is an allotrope in carbon family like diamond, graphene, and fullerene. CNT can be categorized as single-wall carbon nanotubes (SWNT) and multi-wall carbon nanotubes (MWNT). SWNT consists of only one carbon layer which seems like the roll up of graphene sheet as cylinder with a few nanometers in diameter and microns or millimeters length. MWNT consist of multiple rolled layers, the interlayer distance is close to the distance between graphene layers in graphite about 0.34-0.36 nm. The schematic diagrams of SWNT and MWNT are shown in Fig. 2.1.

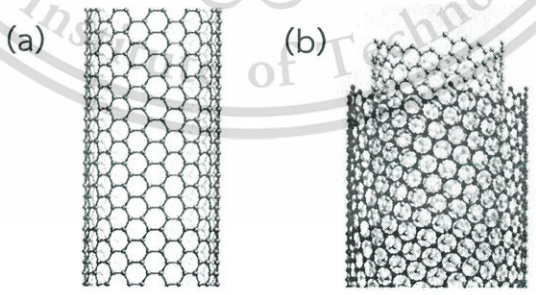

Figure 2.1 Schematic diagrams of (a) SWNT and (b) MWNT [22].

The structure of CNT is classified into three groups such as armchair (n,n), zigzag (n,0), and chiral (n,m) are shown in Figure 2.2. The chirality is used to calculate the

structure of CNT in terms of chiral vector ($\vec{C}$) in equation (2.1). This vector determines the direction of rolling a graphene sheet into a cylinder along an (n,m) lattice vector in graphene. The (n,m) indices determine the chirality of CNT: if m = 0, CNT is called zigzag type (θ = 30°), and if n = m, CNT is called armchair type (θ = 0°). Otherwise, if n ≠ m, CNT is called chiral CNT (0° < θ < 30°). The (n,m) indices also determines the electronic property. The angle (θ) and diameter (d) of CNT can be calculated from its (n,m) indices is shown in equation (2.2) and (2.3), respectively.

$$\vec{c} = n\vec{a}_1 + n\vec{a}_2 \tag{2.1}$$

$$\theta = \frac{\sqrt{3}m}{(m+2n)} \tag{2.2}$$

$$d = \frac{a\sqrt{n^2 + nm + m^2}}{\pi} \tag{2.3}$$

where a = 0.246 nm corresponds to the lattice constant in the graphite sheet.

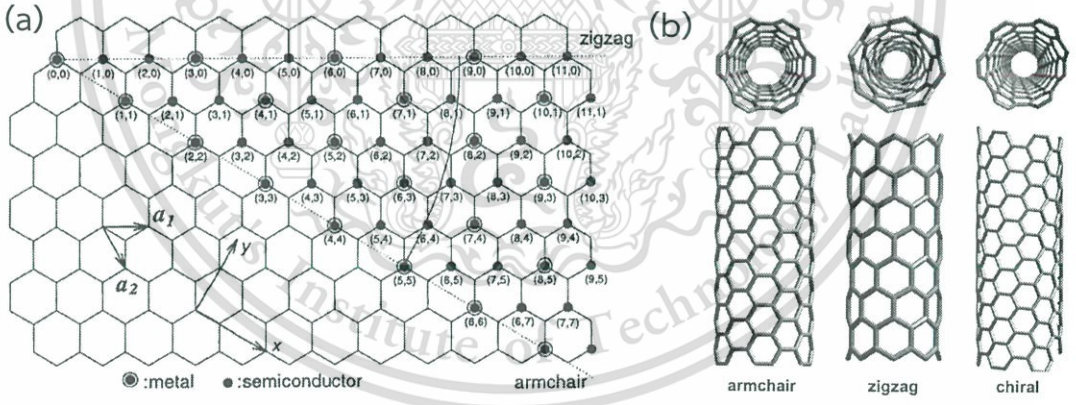

Figure 2.2 Schematic diagrams of (a) the chiral vector of the unit cell of a SWNT and (b) models of SWNT exhibiting different chirality; armchair (n,n), zigzag (n,0), and chiral n,m) configurations [23].

2.2 Properties of Carbon Nanotube

2.2.1 Electrical Property

CNT has unique electronic properties. CNT can be either metallic or semiconducting depending on their diameter and chirality. If n = m, the CNT is metallic; and if n – m is a multiple of 3, then the CNT is semiconducting. All armchair CNT and one-third of all zigzag CNT are metallic and the rest are semiconducting. From theoretical calculation, the electric density of metallic CNT is 4×10^9 A/cm^2 [24], which is higher than that of copper about 1,000 times.

2.2.2 Thermal Property

CNT has very high thermal conductivity comparable to other materials. The low-temperature thermal conductivity show direct evidence of 1-D quantization of the phonon band structure. The thermal conductivity of SWNT at room temperature is 3500 w/mK [25] and over 3000 w/mK for MWNT [26], which is higher than that of copper about 9 times. The thermal properties of CNT compare to the other materials are shown in table 2.1.

Table 2.1 Comparison of thermal properties [25–28].

Materials	Thermal conductivity (W/mK)
CNT	>3000
Copper	400
Diamond	2200

2.2.3 Mechanical Property

CNT is the strongest material in terms of young's modulus, tensile strength and elastic modulus due to the covalent sp^2 bond formed between the individual carbon atoms. Although, the strength of individual of CNT layer is extremely high but the interaction between adjacent layers and tubes of MWNT is only a few GPa. To increase the strength of individual of CNT layer, applying high-energy electron to inner layer

increase the strength of MWNT to ~60 GPa [29]. The mechanical properties of CNT compare to the other materials are shown in table 2.2.

Table 2.2 Comparison of mechanical properties [30–34].

Material	Young modulus (TPa)	Tensile strength (GPa)	Elongation at break (%)
SWNT	~1 (from 1 to 5)	13-53	16
Armchair SWNT	0.94	126.2	23.1
Zigzag SWNT	0.94	94.5	15.6-17.5
Chiral SWNT	0.92	-	-
MWNT	0.2-0.95	11-150	-
Stainless steel	0.186-0.214	0.38-1.55	15-50
Kevlar	0.06-0.18	3.6-3.8	~2

2.3 Synthesis of Carbon Nanotube

Several techniques have been developed for CNT synthesis, which mainly involve gas phase processes. Generally, the synthesis of CNT consists of three main techniques such as arc discharge, laser ablation, and chemical vapor deposition (CVD).

2.3.1 Arc Discharge

Arc discharge is the first technique for synthesis of CNT [21]. The arc discharge technique uses two high purity graphite electrodes as the anode and cathode, the distance between two electrodes are maintained in the range of 1-2 mm. The electrodes were applied the direct current and voltage under inert gas atmosphere such as helium or argon gases. The quality and quantity of CNT can be controlled by gas pressure, type of gas, plasma arc, and synthesis temperature. Arc discharge technique can mostly synthesize MWNT but can also synthesize SWNT with the addition of metal catalyst such as cobalt, iron, and nickel on either the anode or cathode. A schematic diagram of arc discharge is shown in Fig. 2.3.

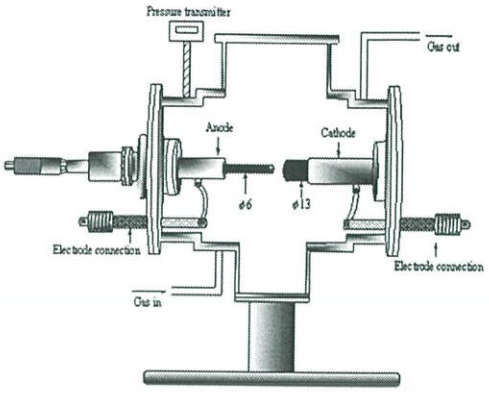

Figure 2.3 Schematic diagram of arc discharge [35].

2.3.2 Laser Ablation

The synthesis of CNT by laser ablation technique [36], a high power laser was used to vaporize graphite target at high temperature. The inert gas is passed through the chamber carrying the grown CNTs for collection. This technique can synthesize both SWNT and MWNT. To control the type of CNT, metal catalyst must be added to graphite target. In addition, the quantity and quality of CNT can be controlled by amount and type of catalyst, temperature and pressure. The purity of synthesized CNT from laser ablation technique is higher than that of arc discharge technique. However, the disadvantages of laser ablation technique require the high power laser which has a high cost. A schematic diagram of laser ablation is shown in Fig. 2.4.

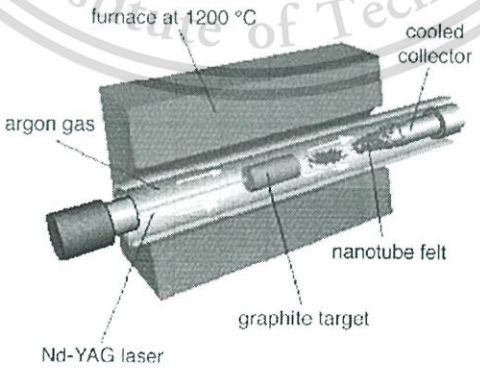

Figure 2.4 Schematic diagrams of laser ablation [35].

2.3.3 Chemical Vapor Deposition

The chemical vapor deposition (CVD) is a simple technique to synthesize the CNT. The CVD process uses hydrocarbon as the carbon sources such as acetylene [37,38], methane [39] and ethanol [40]. The hydrocarbon source was flowed through the quartz tube within a furnace at a high temperature (700-900 °C). CNT was grown on the metal catalyst (cobalt, iron, and nickel) by the decomposition of hydrocarbon gas at high temperature. The diameter of CNT can be controlled by the size of the metal catalyst. The advantages of CVD are simple technique, low cost, and low temperature-synthesis. Both SWNT and MWNT can be synthesized by CVD method. A schematic diagram of CVD is shown in Fig. 2.5.

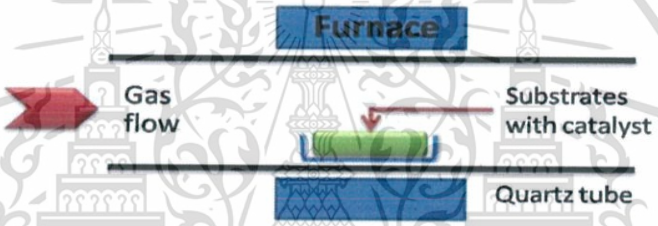

Figure 2.5 Schematic diagrams of CVD [35].

The summary and comparison of CNT synthesis method is shown in Table 2.3.

Table 2.3 Summary and comparison of three CNT synthesis methods.

Synthesis method	Advantage	Disadvantage
Arc discharge	- High quality CNT	- High temperature
	- Well crystallized CNT	- Purification require
Laser ablation	- High purity	- Low yield
	- Few defects	- Expensive
	- Good diameter control	- Purification required

Table 2.3 (Continued)

Synthesis method	Advantage	Disadvantage
		- Method limited to the lab
Chemical vapor deposition	- Simple method - Low cost - Low temperature - Control diameter, purity, quantity and orientation - Directly synthesize on substrate - Large scale	- Defective CNT

2.4 Growth Mechanism of Carbon Nanotube

The widely-accepted growth mechanisms of CNT have been generally divided into two methods; tip growth and base growth [41]. Firstly, a carbon source adsorbs and decomposes on the surface of the metal catalyst to form carbon atoms, then the carbon atoms dissolve into the metal catalyst to form metal carbides, leading to formation of CNT. In the case of tip growth, the metal catalyst-substrate interaction is weak. The decomposed carbon atoms diffuse and precipitate to the junction between metal catalyst and substrate, metal catalyst was lifted off from the substrate during CNT growth due to weak catalyst-substrate interaction. A schematic diagram of tip growth model is shown in Fig. 2.6(a). In the case of base growth, the metal catalyst-substrate interaction is strong. The decomposed carbon atom diffused and precipitated into the metal catalyst, the metal catalyst strongly adheres to the substrate while the CNT is grown up above metal catalyst. A schematic diagram of tip growth model is shown in Fig. 2.6(b).

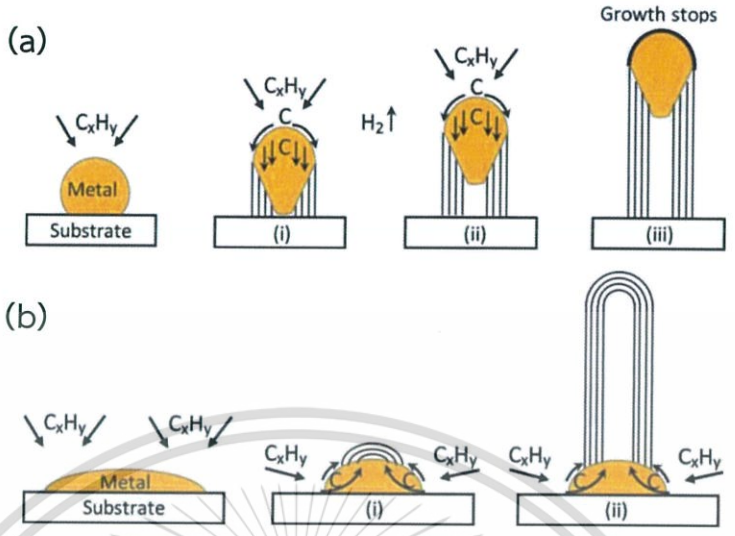

Figure 2.6 Growth mechanisms for CNTs: (a) tip-growth model and (b) base-growth model [41].

2.5 Composition and Definition of Chemical Sensor

Chemical sensor is a self-contained analytical device that can provide information about the chemical composition of its environment that is a liquid or a gas phase. Chemical sensor consists of two parts such as receptor and transducer. The chemical information derives from the interaction between chemical and sensor, the reaction is converted as electric signal such as electrical resistance, electrical conductance or electrical capacitance.

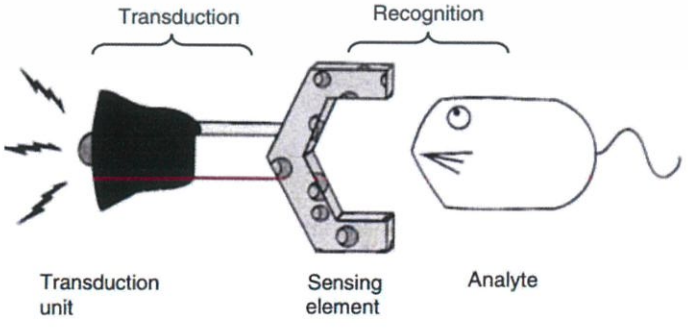

Figure 2.7 Schematic diagram of a chemical sensor. A sensor is an assembly of a receptor and transduction unit [42].

2.5.1 Recognition Methods

2.5.1.1 General Aspects

Recognition method is widely utilized in chemical sensor application. The recognition process can be described by the reaction in equation (2.4). *A* is the analyte, *R* is the recognition receptor and *P* is a product of the analyte-receptor interaction [42].

$$\underset{Sample}{A} + \underset{Sensing\ element}{R} \leftrightarrows P \tag{2.4}$$

The arrow shows the recognition process which is a reversible process at equilibrium. The product involves the noncovalent chemical bonds such as ionic bonds, hydrogen bonds and van der Waals interactions. The recognition process can be described by its equilibrium constant K_A in equation as shown in equation (2.5) [42].

$$K_A = \frac{c_P}{c_A c_R} \tag{2.5}$$

where *c* is concentrations of the species indicated subscripts. The equilibrium constant indicates the affinity of the recognition receptor for the analyte. Great affinity, high value of the equilibrium constant. In addition, the other important factor of recognition process is selectivity, which is the ability of the sensor to favorably respond to the analyte and not to another species B. The receptor-interferent interaction can be represented in equation (2.6) [42].

$$B + R \leftrightarrows Q \tag{2.6}$$

The affinity of the receptor for the species B is indicated by equilibrium constant as shown in equation (2.7) [42].

$$K_B = \frac{c_Q}{c_B c_R} \tag{2.7}$$

The selectivity of sensor for analyte can be calculated by the ratio between K_A and K_B. The good selectivity is obtained if $K_A/K_B>>1$.

2.5.1.2 Gas and Vapor Sorption

The gas and vapor detections are topics of great interest in various areas such as the monitoring of air quality and control of hazardous gases and vapors in industrial environmental. The general recognition method is based on either at the surface (adsorption) or within (absorption) of solid material. The sorption is both physisorption or chemisorption [42]. The physisorption is a kind of adsorption which involves the intermolecular force such as van der Waal's force, while the chemisorption involves the chemical bond force.

2.5.2 Transduction Methods

2.5.2.1 General Aspects

Transduction method consists of 2 compositions such as chemical transduction and physical transduction. The chemical transduction is performed by monitoring in the chemical composition of the sensing element in response to the recognition process. Physical transduction focuses on a specific physical property of sensing element that is affected by its interaction with the analyte. General physical transduction methods are mass, reflective index, dielectric constant properties or electrical resistivity [42].

2.5.2.2 Resistive and Capacitive Transduction

The interaction between analyte and selected recognition lead to change in the electrical property of material sensor. For example, the interaction of gases with semiconductor metal oxides changes the electrical resistivity, basis of resistive transducer. Furthermore, the other electrical property can be affected on the recognition process is the dielectric constant. The dielectric constant is applied to measure the capacitance of capacitor or capacitive transduction [42].

2.6 Adsorption Isotherm

Adsorption is the adhesion of atoms, ions or molecules from a gas or liquid to a surface. The adsorption isotherm is used to describe the relationship between the amount of the adsorbate on the adsorbent as a function of its pressure (in case gas)

or concentration (in case liquid) at constant temperature. Adsorption isotherms are classified according to international union of pure and applied chemistry (IUPAC)-recommendations in six different types as shown in Fig. 2.8.

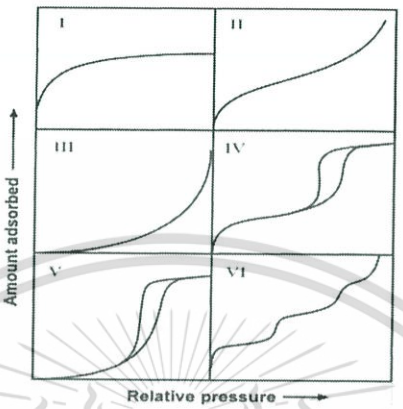

Figure 2.8 Types of gas adsorption isotherms [43].

Type I isotherm is a monolayer adsorption of adsorbate at the adsorbent surface. This isotherm can be explained using Langmuir adsorption isotherm. Langmuir adsorption isotherm is derived based on the surface is uniform and all the surface sites have the same activity for adsorption. Adsorbed molecules do not interaction with the other adsorbed molecules on the surface, adsorption of all molecules occurs by the same mechanism and results in the same adsorbed structure and the extent of adsorption is less than one complete monolayer coverage.

$$A_g + S \leftrightarrows A_{ad} \tag{2.8}$$

where A_g is unadsorbed gas molecule, S is unoccupied surface and A_{ad} is adsorbed gas molecule. This isotherm depicted a relationship between the number of active sites of the surface undergoing adsorption and pressure.

$$\theta = \frac{KP}{1+KP} \tag{2.9}$$

where θ is the number of sites of the surface which covered with gas molecule, P is pressure and K is the equilibrium constant for distribution of adsorbate between the surface and the gas phase. For example, the adsorption of oxygen on carbon black at -183 °C.

Type II isotherm is not saturation limit as type I isotherm. Type II isotherm exhibits an indefinitely multi-layer formation after completion of the monolayer. This isotherm can be explained using Brunauer, Emmett and Teller (BET) isotherm. BET adsorption isotherm is based on the multilayer formation. At the low pressure, molecules start to adsorb onto the surface according to Langmuir adsorption isotherm. As the pressure is increased, next molecules will adsorb to preadsorbed molecules, resulting in a multilayer formation.

$$\frac{P}{V(P_0-P)} = \frac{1}{V_m C} + \frac{(C-1)P}{V_m C P_0} \tag{2.10}$$

Where V is volume of adsorbed vapor at standard temperature and pressure (STP), V_m is monolayer capacity at STP, P is partial pressure of the adsorbate and P_0 is the saturation vapor pressure of the adsorbate, C is BET constant. For example, the adsorption of water on carbon black at 30 °C is type II isotherm.

Type III isotherm is obtained when the amount of gas adsorbed increases without limit as its relative saturation approaches unity. For example, bromine is adsorbed on silica gel at 20 °C. Type IV isotherm, at lower pressure region is quite similar to type II isotherm which involve the formation of monolayer followed by multilayer. The saturation reaches at a pressure below the saturation vapor pressure. This type of isotherm is obtained by the adsorption of benzene on silica gel at 500 °C. Type V isotherm is similar variation of type III and this can be attributed to relatively weak adsorbent-adsorbate interactions. For example, the water vapor is adsorbed on charcoal at 1000 °C. Type VI isotherm is representation of layer-by-layer adsorption on a highly uniform surface. For example, the adsorption of argon on graphitized carbon blacks at low temperature.

2.7 Development of Carbon Nanotube for Volatile Organic Compound Detection

2.7.1 Volatile Organic Compound Detection

Volatile organic compounds (VOCs) [1] are organic chemicals that have a high vapor pressure at ordinary temperature. Their high vapor pressure results from a low boiling point, which causes large numbers of molecules to evaporate and sublimate from the liquid or solid form of the compound and enter the surrounding air. VOCs have been widely used in various industrial processes and commercial products, such as transport, household chemicals, paints and adhesives. VOCs are directly harmful to environmental and human health, cause eye, nose and throat irritation, can also damage the liver and central nervous system, and present a risk of cancer [2–4]. The standard of average VOC concentration is shown in Table 2.4.

Table 2.4 Standard average concentration of VOCs [44,45].

Volatile Organic Compounds	Standard VOCs Concentration in 24 h by Pollution Control Department of Thailand ($\mu g/m^3$)*	Occupational Safety and Health Administration Permissible Exposure Limit (OSHA PEL) (mg/m^3)**	Immediately Dangerous to Life or Health Concentrations (IDLH) (ppm)***
1,3-Butadiene	< 5.3	2.21	2,000
Benzene	< 7.6	3.19	500
Carbon tetrachloride	< 150	62.9	200
Chloroform	< 57	240	500
Dichloromethane	< 210	86.8	2,300
1,2-Dichloroethane	< 48	202.5	50
Trichloroethylene	< 130	537	1,000

* microgram per cubic meter ($\mu g/m^3$)

** milligram per cubic meter (mg/m^3)

*** parts per million (ppm)

Hence, environmental monitoring and industrial safety are absolutely crucial for the protection of environmental and human health. Since the last decade, the most widely used analytical methods for VOC detection have been gas chromatography/mass spectrometry (GC/MS), high-performance liquid chromatography (HPLC) and photoionization detection (PID) because of their high sensitivity and reliability. Nevertheless, their practical application is highly limited as a result of their complexity, relatively high cost, unportability and calibration requirements to maintain accuracy. Recently, a gas sensor based on the simple change in its resistance in response to analytes has become a promising candidate for practical sensing devices. The advantages of a gas sensor include its compact size, real-time monitoring and low power consumption. Gas sensors based on metal oxide materials have been widely developed for VOC detection with a detection limit down to the ppm level [46,47]. Despite their high sensitivity, these sensors exhibit drawbacks, including nonselectivity and high power consumption (operating temperature > 200 °C).

Table 2.5 Summary and comparison of various VOCs detection.

Techniques	Advantage	Disadvantage
Semiconductor or metal oxide sensors	- Portable device - Real-time monitoring - Low cost	- Non-selectivity - Poor sensitivity (ppm level) - Slow response time - Interference from humid and temperature - High power consumption and temperature operation (> 200 °C)

Table 2.5 (Continued)

Techniques	Advantage	Disadvantage
Photoionization detection	- High sensitivity - High response time	- Disposable device - High cost
Gas chromatography/ mass spectrometry and high-performance liquid chromatography	- High selectivity - High sensitivity	- Complexity - Non-portable device - High cost - Calibration requirements to maintain accuracy

2.7.2 Gas Sensor Based on Carbon Nanotube

CNT has attracted considerable attentions as alternative sensing materials because of their distinctive characteristics in structural, electrical, mechanical and thermal properties. SWNT has shown outstanding potential for gas sensing applications because of their well-organized nanostructure, large specific area [48] and electrical properties [24,49]. SWNT-based sensors have demonstrated high response to oxidizing gases down to parts per billion (ppb) level under room-temperature operation [6–9]. However, CNT is weakly sensitive to VOCs. In recently years, to overcome these obstacles, many efforts have been made aiming to improve the VOC sensing performance of CNT by functionalized with polymer and metal nanoparticles (NPs).

The pioneer work of gas sensor using CNT was reported by Dai and coworkers. Pristine SWNT was synthesized by CVD on silicon dioxide/silicon (SiO_2/Si) substrate as shown in Fig. 2.9(a). Pristine SWNT-based sensor showed fast and sensitive to ammonia (NH_3) and nitrogen dioxide (NO_2) at room temperature. The conductance of the SWNT increase by three orders of magnitude within several seconds when exposed to 200 ppm NO_2, while the conductance decrease about two orders of magnitude within two minutes when exposed to 1% NH_3 as shown in Fig. 2.9(b-c). Pristine SWNT exhibited p-type semiconducting with several orders of magnitude change in conductance [50].

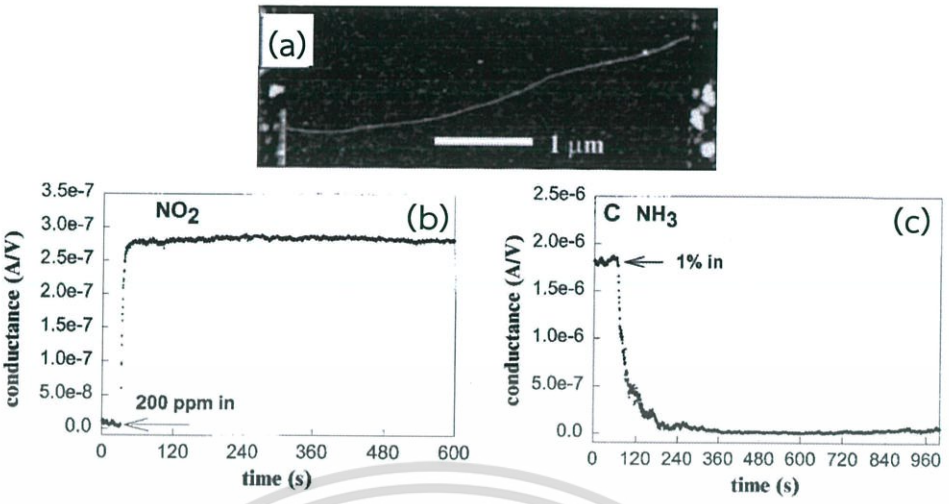

Figure 2.9 (a) An image of SWNT (b) electrical conductance response of a semiconducting SWNT to (b) 200 ppm NO_2 and (c) 1% NH_3 vapor [50].

Someya and coworkers fabricated SWNT-based sensor using CVD method as shown in Fig. 2.10(a). The SWNT-based sensor was detected several saturated vapors of ethanol, methanol, 1-propanol, 2-propanol, 1-butanol, tertiary-butanol, 1-pentanol and 1-octanol as shown in Fig. 2.10(b). The SWNT-based sensor showed high response to 1-propanol, tertiary-butanol, 2-propanol, 1-butanol and ethanol vapors. Furthermore, the SWNT-based sensor exhibited good reversibility and reproducibility over many cycles of vapor exposure. The response time was within 5-15 s. The SWNT-based sensor are sensitive to a wide range of alcoholic vapors [51].

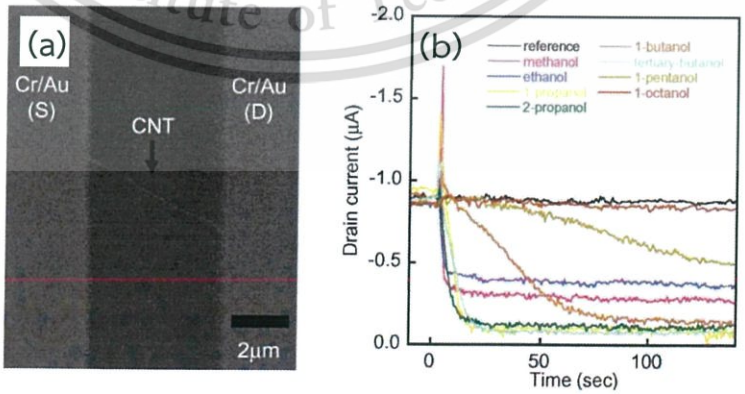

Figure 2.10 (a) SEM image of SWNT (b) drain currents are shown as a function of time toward a saturated vapor of various kinds of alcohols [51].

However, the CNT is weakly sensitive to some kind of VOCs, especially aromatic-VOCs. To improve the sensitivity of VOCs, polymer or metal nanoparticles (NPs)-functionalized CNT were proposed. A gas sensor based on functionalized-multi-walled carbon nanotubes and poly(methyl methacrylate) composite (f-MWNT-PMMA) by dip-coating technique has been demonstrated for VOC detection [10,11]. The f-MWNT-PMMA sensors can detect dichloromethane, acetone, and chloroform vapors with a fast response as shown in Fig. 2.11(a-b). The f-PMMA-MWNT sensor exhibited fast response time within 2-5 s and 100-1000-fold improvement in the resistance when exposed to saturated VOCs such as dichloromethane (DCM), chloroform and acetone vapors (Fig. 2.11(a)). The sensing mechanism of the polymer-functionalized CNTs is attributed to the swelling of the polymer matrix because of the organic vapor molecule, leading to volume expansion, and thereby an increase in the CNT–CNT distance, resulting in an increase in the resistance as shown in Fig. 2.11(c). However, the f-MWNT-PMMA-base sensor shows a high response to a saturated vapor of VOCs [10] but a low sensor response to VOCs in a partial pressure range of 27-273 Torr (Fig. 2.11(b)) [11]. In addition, MWNTs were functionalized using potassium permanganate with the help of a phase transfer catalyst. Although the major advantage of this process is a high yield of functionalized MWNTs, but it is time consuming and involves the use of hazardous chemicals.

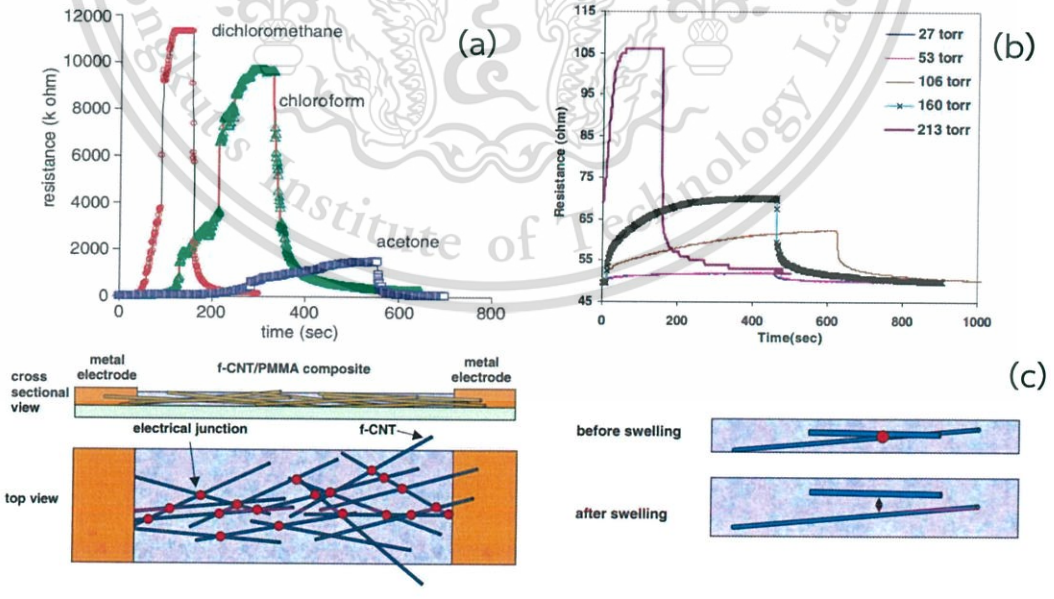

Figure 2.11 (a) Sensor response of f-MWNT-PMMA composite as a function of time toward a saturated vapor of VOCs [10] and (b) DCM in a partial pressure range of 27-273 Torr [11]. (c) Schematic diagram of junction resistance change between two CNTs due to polymer matrix swelling [11].

Santhanam *et al.* fabricated poly (3-methylthiophene)/MWNT nanocomposite sensor using *in situ* chemical polymerization of 3-methylthiophene. The sensor showed good response to chloromethane, chloroform, carbon tetrachloride, while no response to methane and many other VOCs (e.g. acetone, acetaldehyde, benzaldehyde, tetrahydrofuran, methanol and ethanol) as shown in Fig. 2.12. The electrical resistance increased exposure to chloromethane, chloroform and carbon tetrachloride as shown in Fig. 2.12. The response time of the sensor is generally about 60-120 s. Moreover, the sensor shows good selectivity between chloromethane and methane. The sensing mechanism was proposed to be based on the ionization potential of the VOCs [12].

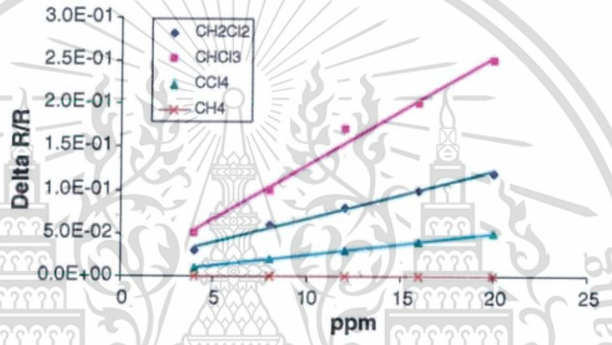

Figure 2.12 Responses of the poly(3-methylthiophene)-MWNT nanocomposite for different VOCs [12].

The ethyl cellulose (EC)-CNT composite using simple spraying technique was fabricated by Cho *et al.* as shown in Fig. 2.13(a). The EC-CNT composite showed typical percolation behaviors, the percolation threshold is around 1-2 wt.% of the CNT contents. The EC-CNT composite sensor was detected benzene (C_6H_6) in range of 1000-5000 ppm as shown in Fig. 2.13(b). The electrical resistance increased when exposure to C_6H_6 vapor. The sensing mechanism can be explained by polymer swelling due to adsorb with C_6H_6 vapor, increase the distance between CNT-CNT, resulting in an increase in electrical resistance. Moreover, the EC-CNT composite with 5 wt.% of SWNT showed the highest response to C_6H_6 vapor ~ 9% at 5000 ppm [13].

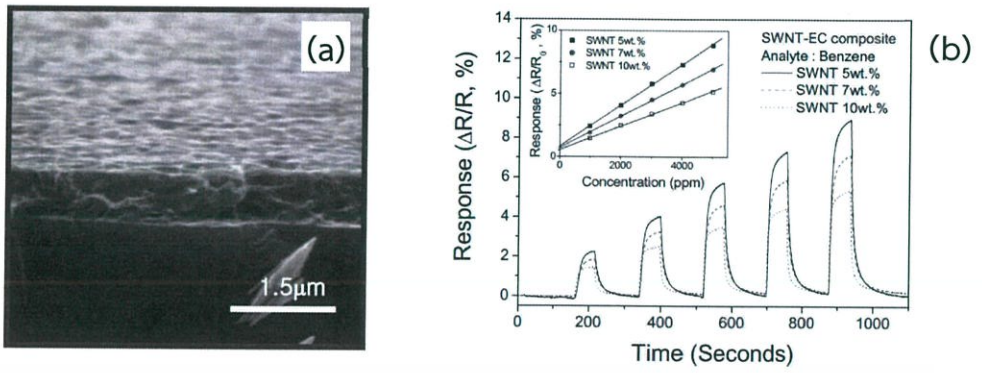

Figure 2.13 (a) A SEM image of the SWNT-EC composite film. (b) The gas sensing properties of the SWNT-EC composites for benzene vapor in range of 1000-5000 ppm. The inset shows the linear relationship [13].

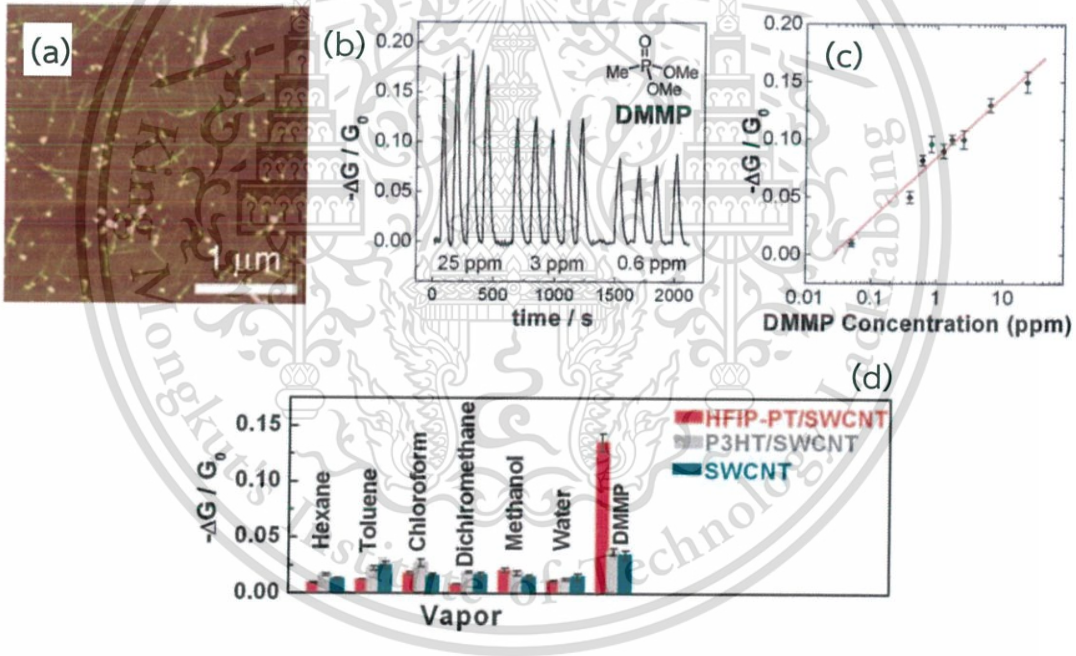

Figure 2.14 (a) AFM image of a SWNT network. (b) Conductance change of the sensor upon exposure to varying concentrations of DMMP. (C) Calibration curve of the sensor at DMMP concentration of 0.05-25 ppm. (d) Conductance change of the SWNT sensors in response to organic solvents and DMMP diluted to 1% saturated vapor conditions at room temperature [14].

Wang *et al.* proposed CNT/hexafluoroisopropanol substituted polythiophene (CNT/HFIP-PT) sensor using very simple spin-casting technique. The HFIP group was attached to PT due to adsorb the phosphate esters via H-binding. AFM image of a

simple sensor structure by spin-casting technique is shown in Fig. 2.14(a). The CNT/HFIP-PT sensor detected chloroform, dimethyl methylphosphonate (DMMP), DCM, hexane, toluene, methanol and water. The CNT/HFIP-PT sensor exhibited fast and reversible to DMMP vapor even at ppb-ppm level as shown in Fig. 2.13(b). A linear relationship was obtained between the sensor response and the concentration of DMMP as shown in Fig. 2.14(c). Furthermore, CNT/HFIP-PT showed good selectivity to DMMP as show in Fig. 2.14(d). The sensing mechanism can be attributed the charge transfer and polymer swelling by increased physical separation of the CNT caused by the interaction of the PT and VOC [14].

However, the CNT-polymer composites are prepared mostly in the form of CNTs dispersed in a polymer matrix on the basis of percolation theory by a complicated polymerization process [10–14]. A novel multifunctional gas sensor based on vertically aligned MWNTs and polymer composites were developed by Wei and coworkers. The sensors were fabricated by coating of selected polymer (e.g. poly(vinyl acetate) (PVA) or polyisoprene (PI)) on the vertically aligned MWNTs as shown in Fig. 2.15(a-b). Pristine aligned MWNT without polymer coating do not respond to VOCs as shown in Fig. 2.15(c). Coating with polymer, PVA-coated MWNT (PVA/MWNT) shows ~290% increase in the electrical resistance change at equilibrium sensor response upon exposure to tetrahydrofuran (THF) (Fig. 2.15(d)). The equilibrium sensor response reaches approximately 80% and 12% upon exposure to ethanol and cyclohexane, respectively as shown in Fig. 2.15(e-f). For PI-coated MWNT (PI/MWNT), the equilibrium sensor response exposure to cyclohexane enhanced approximately 12% to 55% as shown in Fig. 2.15(g). However, PI/MWNT shows low response to ethanol approximately 10% as shown in Fig. 2.15(h). Additionally, the binary polymer composite-coated MWNT (PVA-PI/MWNT) shows good responses to both cyclohexane and ethanol. The equilibrium sensor response of PVA-PI/MWNT reaches approximately 50% and 45% upon exposure to cyclohexane and ethanol, respectively as shown in Fig. 2.15(I). The sensing mechanism was attributed to the charge transfer interaction with gas molecules and/or the inter-tube distance change induced by polymer swelling during gas adsorption [15].

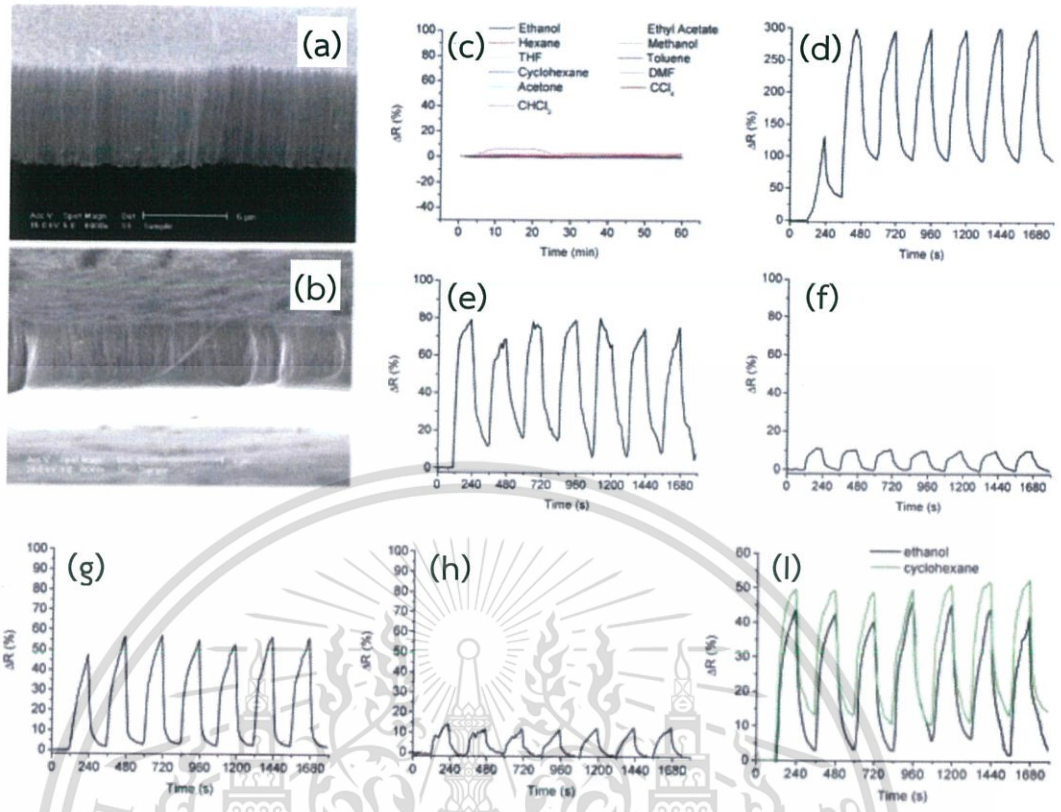

Figure 2.15 A SEM image of aligned MWNTs (a) before and (b) after coated with polymer on top and turned upside down. Sensor response as a function of time: PVA/MWNT toward (c) various VOCs (d) THF (e) cyclohexane and (f) ethanol: PI/MWNT toward (g) cyclohexane and (h) ethanol: PVA-PI/MWNT toward (I) ethanol and cyclohexane [15].

Another type of gas sensor was fabricated using conductive polymer-MWNT composites by spray layer by layer (sLbL) assembly technique for VOC detection at a saturated vapor such as isopropanol, THF, DCM, *n*-heptane, cyclohexane, methanol, ethanol, water and toluene. The five different conductive polymer are poly(caprolactone) (PCL), poly(lactic acid) (PLA), poly(carbonate) (PC), poly(methyl methacrylate) (PMMA) and biobased polyester (BPR). AFM image of a schematic of simple sensor structure by sLbL assembly technique is shown in Fig. 2.16(a). The conductive polymer-MWNT composites showed the excellent sensitivity and selectivity to VOCs as shown in Fig. 2.16(b-c). Three dimensional principal component analysis (PCA) exhibited excellence pattern recognition to discriminate VOCs as shown in Fig. 2.16(d) [16].

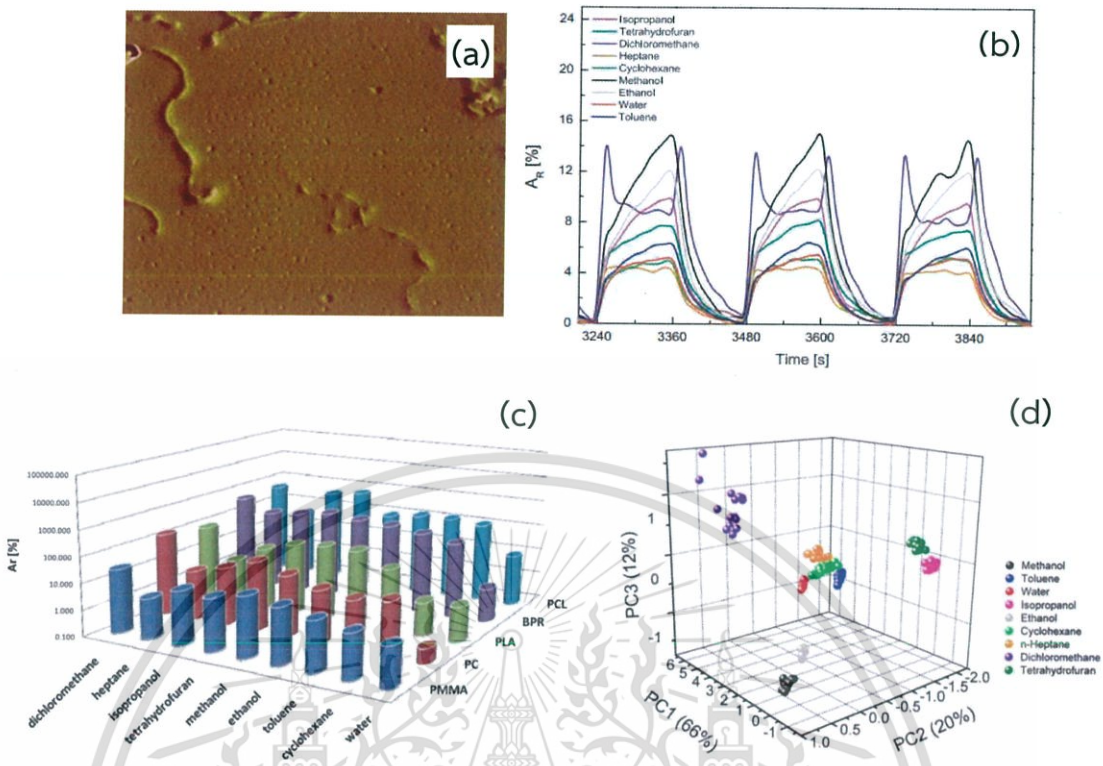

Figure 2.16 (a) AFM images of PMMA-CNT composite. (b) Response of PMMA-CNT sensors towards cyclic exposures to VOCs. (c) Compared average selectivity over 15 cycles of sensors exposure to the VOCs. (d) 3D PCA plots of nine VOCs [16].

In addition, the similar technique was proposed to simple fabricate the vapor quantum resistive sensors (vQRS) for VOC detection. The vQRS were fabricated in two steps, firstly a random network of MWNT was sLbL on substrate and secondly prepared random network of MWNT was coated by a nanometric layer of drop-casting of polymer as shown in Fig. 2.17(a). The thickness of polymer can be controlled by the amount of polymer deposited on CNT network as shown in Fig. 2.17(b). The five different conductive polymers are PC, PCL, PLA, PMMA and polyethylene oxide (PEO). The vQRS were exposure to VOCs such as acetone, isopropanol, THF, DCM, chloroform, butanol, toluene and ethanol which are biomarkers for lung cancer detection. Fig. 2.17(c) shows response of vQRS to acetone vapor at different concentration. Moreover, the sensitivity of vQRS change significant with the thickness of the polymer film (Fig. 2.17(c)). The vQRS showed fast response, high sensitivity and selectivity as shown in Fig. 2.17(d). The 2D PCA exhibit the good discrimination ability between clusters of vapors which are elementary components of cancer patient breath as shown in Fig.

2.17(e). This technique is very effective to develop arrays of gas sensor by the control the amount of polymer deposited on CNT network [17].

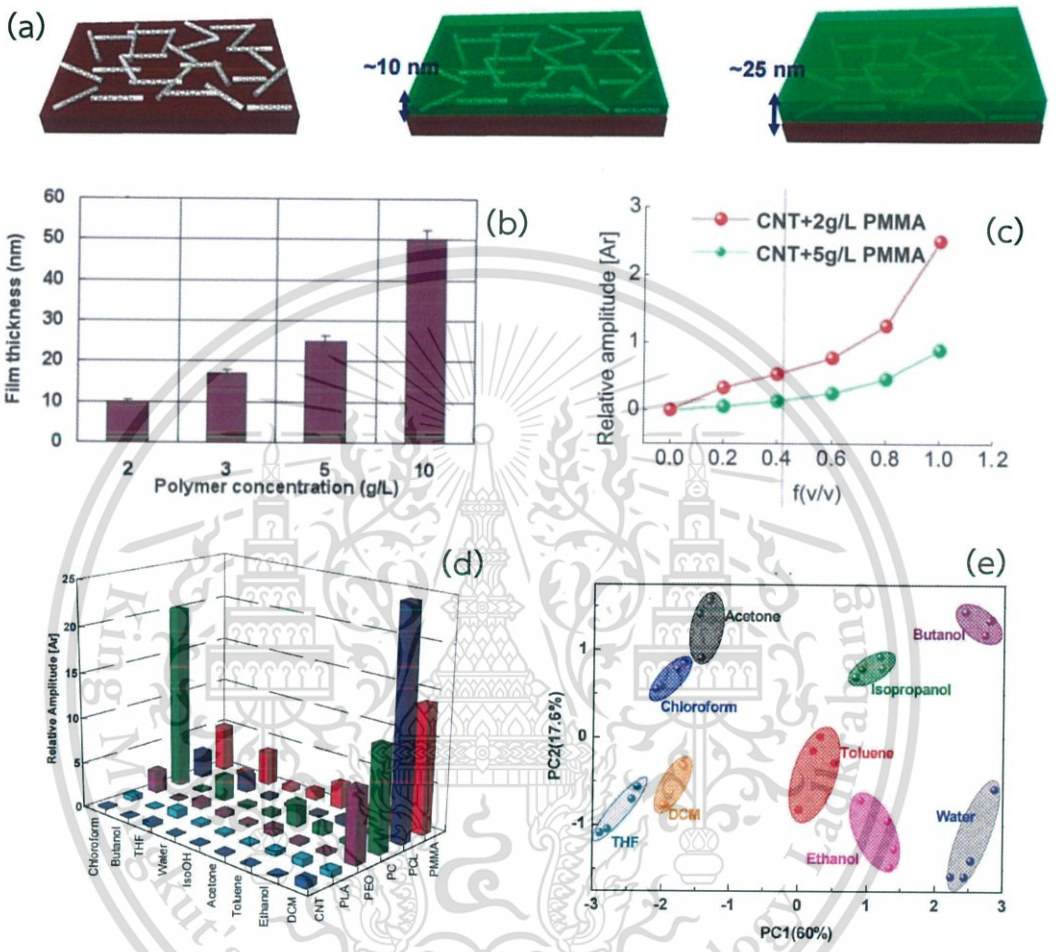

Figure 2.17 (a) Schematic diagram of pristine random network of MWNT and random network of MWNT coated by drop casting of different concentration of polymer. (b) PMMA thickness with different concentration in solution. (c) Response of vQRS to acetone vapor (d) Summary of relative amplitude for all vQRS. (e) 2D PCA map showing VOC discrimination ability of vQRS [17].

Additionally, the deposition of metal NPs on CNT enhances the sensor response toward VOCs was studied. Lu and co-workers proposed palladium (Pd)-coated SWNT (Pd/SWNT) for discriminating NO_2, hydrogen cyanide, hydrogen chloride, chlorine, acetone and C_6H_6 in ppm concentration levels [18]. Pd NPs were sputter coated onto

a pile of SWNT powder, then dispersed in distilled deionized water. The mixed solution was sonicated and drop-deposited onto the substrate. Fig. 2.18(a) showed Pd-decorated SWNT. The bright spots are Pd NPs with the average size of 10 nm [52]. The response of sensor before and after exposure to C_6H_6 is shown in Fig. 2.18(b). All tested gases and vapors can be discriminated by their chemical nature in the low concentration at ppm levels [18]. The gases and vapors were completely separated by PCA as shown in Fig. 2.18(c-d). However, the sensor showed low sensitivity [18,52] at low concentrations three orders of magnitude higher than those require for environmental protection applications [18].

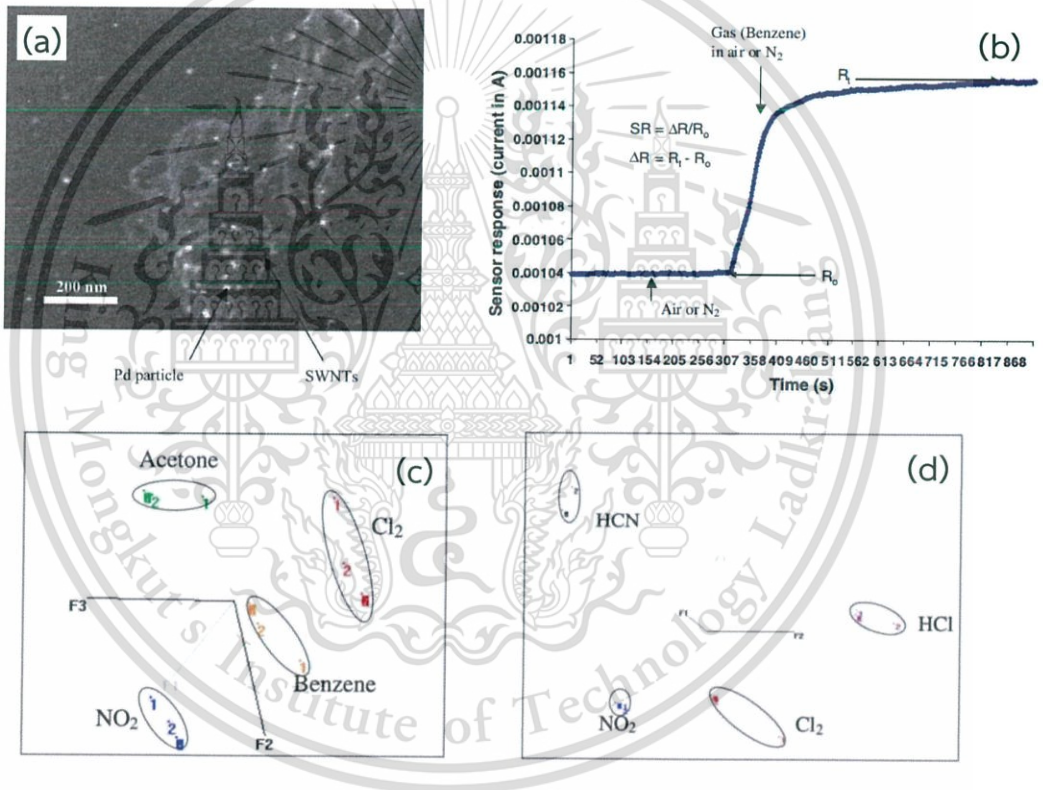

Figure 2.18 (a) SEM image of Pd-decorated SWNT [52]. (b) Sensor response before gas exposure (R_0) and during the gas exposure (R_t). PCA plots of (c) discrimination of gases and organic vapors (d) discrimination of toxic gases [18].

Leghrib *et al.* proposed oxygen plasma functionalized MWNTs (O_2 plasma-MWNT) decorated with rhodium (Rh), palladium (Pd), nickel (Ni) and gold (Au) using spray metal colloid solution and evaporation. O_2 plasma on the MWNT create functional oxygen species attached to the CNT sidewalls, resulting in an increase the adhesion of metal

NPs on sidewall of O_2 plasma-MWNT as shown in Fig. 2.19(a-b). The metal NPs-decorated O_2 plasma-MWNT was detected to benzene in range of 500-5000 ppm as shown in Fig. 2.19(c). The Rh- and Pd-decorated O_2 plasma-MWNT showed high response to benzene, while Au-decorated O_2 plasma-MWNT exhibited non-response to benzene. The sensing mechanism of metal NP-decorated CNTs can be explained by the electron transport from the metal NPs to the CNTs, resulting in an increase in the resistance. The gas detection could be performance at room temperature, but the recovering the sensor baseline require heating at 150 °C [19].

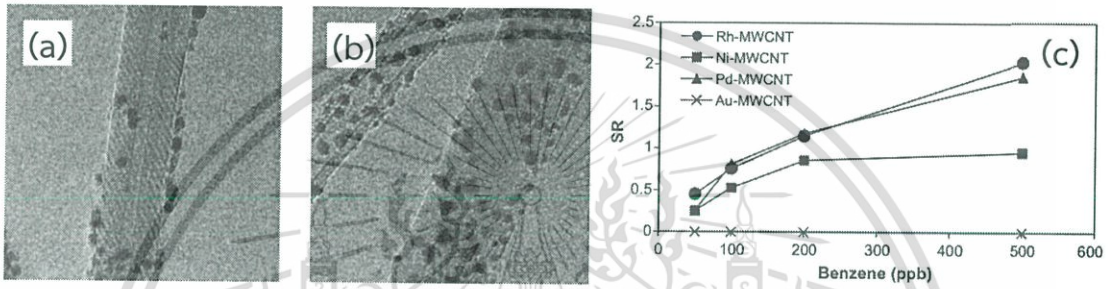

Figure 2.19 TEM images of MWNT (a) before and (b) after decorated with Pd NPs. (c) Gas sensing performance characterization: response to 50-500 ppb for benzene of the sensors based on Rh, Ni, Pd or Au-decorated MWNTs [19].

Baccar *et al.* reported on the gas sensing properties of O_2 plasma MWNT decorated with sputtered Pt or Pd NPs. The decoration with the 2 nm Pt or the 3 nm Pd NPs is very homogenous as shown in Fig. 2.20(a-b). The Pt- and Pd-decorated MWNT were responsive to non-aromatic VOCs (e.g. acetone, ethanol and methanol) and NO_2 at room temperature, while no response to aromatic VOCs (benzene and toluene vapors). The sensing mechanism can be described by work function, the work function of O_2 plasma MWNT is in range from 4.9 to 5.1 eV, which is very close to the work function of metal such as Pt (4.8 eV) and Pd (4.95 eV), enabling electrons to pass easily between metal NPs and CNTs. The sensor response of Pt-decorated MWNT to non-aromatic VOCs showed higher than that of Pd-decorated MWNT as shown in Fig. 2.20(c). First reason, the diameter of Pt NPs is slightly smaller than that of Pd NPs. A small diameter means a larger overall surface area which may result in higher sensitivity. Second reason, duration of the sputtering process decoration, the power used for decorating MWNT with Pd NPs is higher than that of Pt NPs. Thus, this may lead to a more defective surface of Pd-decorated MWNT, resulting in a degradation of the

electronic properties of CNT. Table 2.6 shows the comparison sensitivity of pristine MWNTs, Pt- and Pd-decorated MWNTs to different vapors and gases [20].

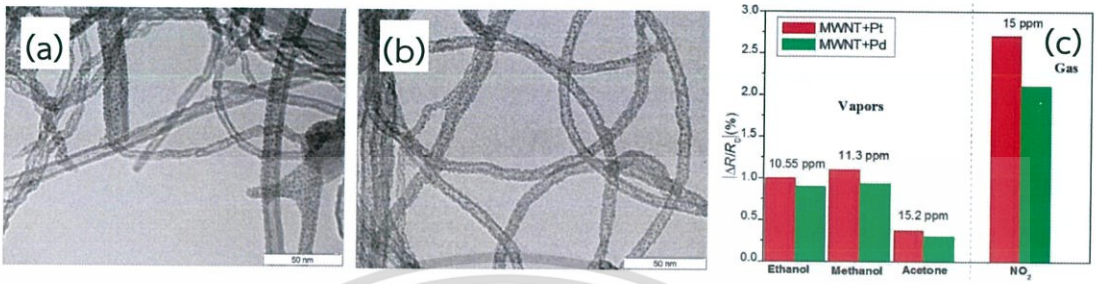

Figure 2.20 TEM images of the (a) Pd- and (b) Pt-decorated MWNTs. (c) Comparison between the response of Pd-MWNTs and Pt-MWNTs to different gases and vapors tested [20].

Table 2.6 Comparison sensitivity (10^{-2} % ppm^{-1}) to the different vapors and gases testes for Pt-MWNTs, Pd-MWNTs and pristine MWNTs sensors [20].

	Ethanol	Methanol	Acetone	NO_2
Pt-MWNTs	9.9	6.7	2.1	9.4
Pd-MWNTs	9.5	6.7	1.9	6.9
Pristine MWNTs	7.1	6.3	1.7	17.8

Furthermore, a new type gas sensor based on metal-polymer composite for VOCs detection was proposed. Athawale *et al* fabricated a Pd-polyaniline (Pd-PANI) composites by oxidative polymerization of an aniline solution which containing Pd NPs. Fig. 2.21(a-b) showed the TEM and electron diffraction patterns of Pd NPs and Pd-PANI nanocomposites. The Pd-PANI composite sensor was detected to alcohol vapor such as ethanol, methanol and isopropanol. The Pd-PANI composite sensor was found to be a highly selective and sensitive sensor for methanol vapor as shown in Fig. 2.21(c). Furthermore, the Pd-PANI nanocomposites showed a stable response for a long time [53].

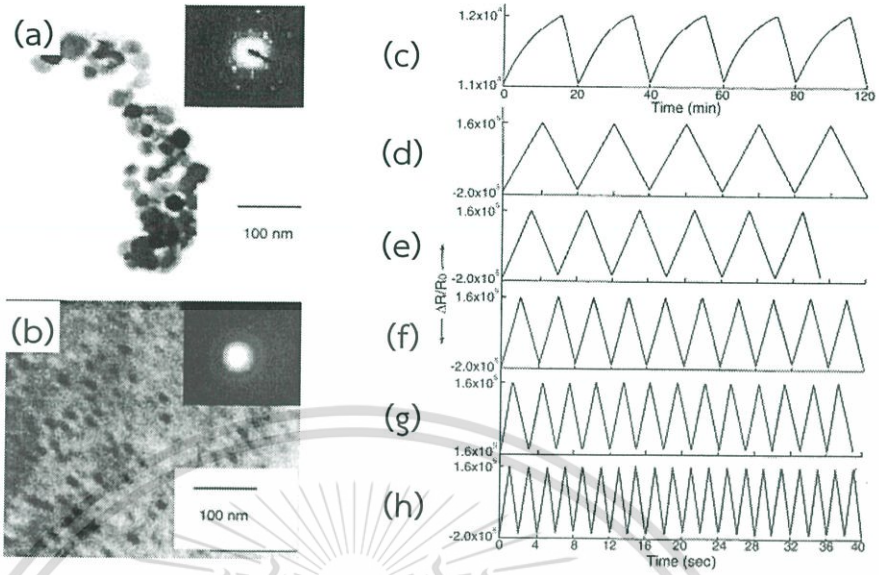

Figure 2.21 TEM and electron diffraction patterns of (a) Pd NPs and (b) Pd-PANI nanocomposites. (c) Responses of PANI exposed to saturated vapor of methanol (2000 ppm) and Pd-PANI nanocomposites exposed to saturated vapor of methanol concentrations of (d) 1 ppm, (e) 5 ppm, (f) 10 ppm, (g) 100 ppm and (h) 2000 ppm [53].

The PANI-silver (PANI-Ag) nanocomposites were prepared by in-situ oxidative polymerization of aniline monomer at different concentrations of Ag NPs (0-2.5 mol%). Fig. 2.22(a-b) showed TEM images of nanocomposites prepared with Ag concentration of 0.5 and 2.5 mol%. The PANI-Ag nanocomposites exhibited remarkable improvement of conductivity compare with pure PANI, increased by two orders of magnitude with respect to pure PANI. The PANI-Ag nanocomposites showed higher response to ethanol than that of pure PANI as shown in 2.22(c-d). The sensor response, response time and reproducibility depend on the Ag concentration. The sensor response showed a good linear relationship with ethanol concentration as shown in 2.22(e). The PANI-Ag nanocomposite demonstrates the potential application as a selective ethanol sensor. The sensing mechanism can be attributed the decrease in the conjugation length as a result of the formation of H-bonding between the –OH group of ethanol and both the amine and imine group of PANI [54].

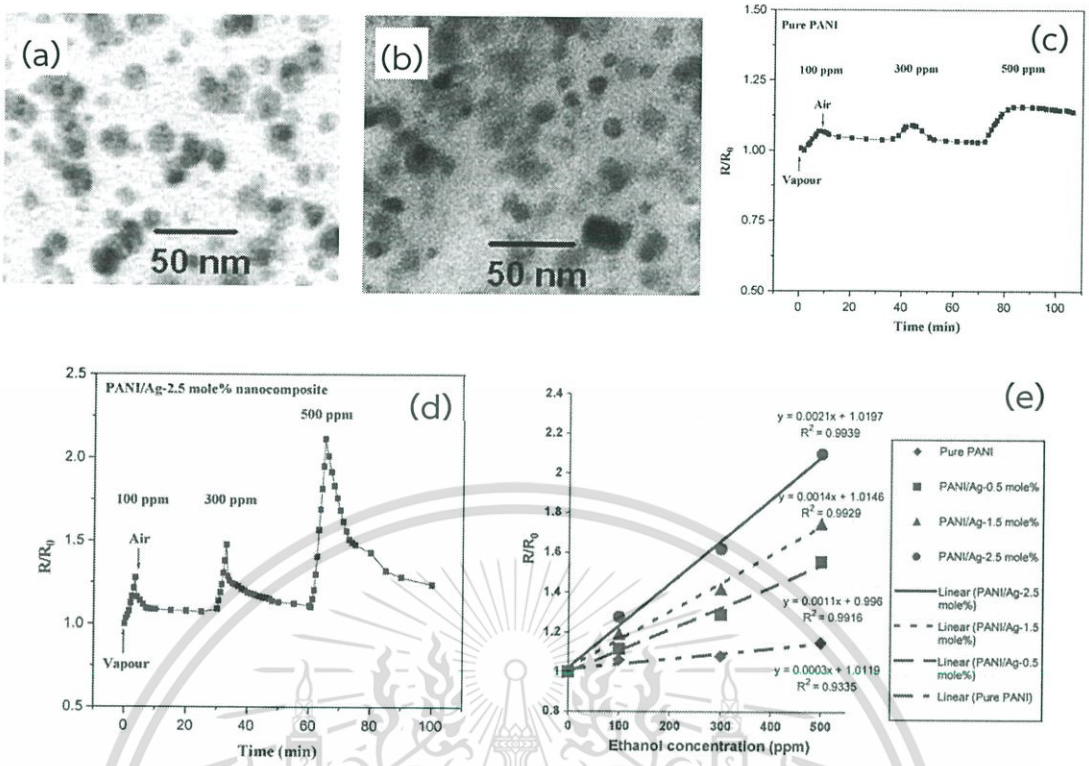

Figure 2.22 TEM images of nanocomposite prepared with Ag concentration of (a) 0.5 and (b) 2.5 mol%. Responses of the (c) pure PANI and (d) PANI-Ag nanocomposite sensors on exposure to ethanol vapor at different concentration at room temperature. (e) Variations in sensor response of pure PANI and PANI-Ag nanocomposite as a function of ethanol concentration [54].

Shirsat *et al.* reported a sensitive, selective and fast response at room temperature for hydrogen sulfide (H_2S) detection using PANI nanowires-Au NPs (PANI NWs-Au NPs) hybrid. The sensor was fabricated by facile electrochemical technique. Firstly, PANI NWs with a diameter of 250-320 nm were synthesized using templateless electrochemical polymerization, then electrochemically functionalized with Au NPs using cyclic voltammetry technique. SEM images of PANI NWs and PANI NWs-Au NPs are shown in Fig. 2.23(a-b). The PANI NWs-Au NPs sensor exhibit response to H_2S in range of 0.1-1000 ppb, while PANI NWs sensor non-respond to H_2S even at ppm level as shown in Fig. 2.23(c-d). The PANI NWs-Au NPs sensors exhibited sensing response to H_2S in terms of limit of detection, dynamic range, response and recovery time, reproducibility and selectivity [55].

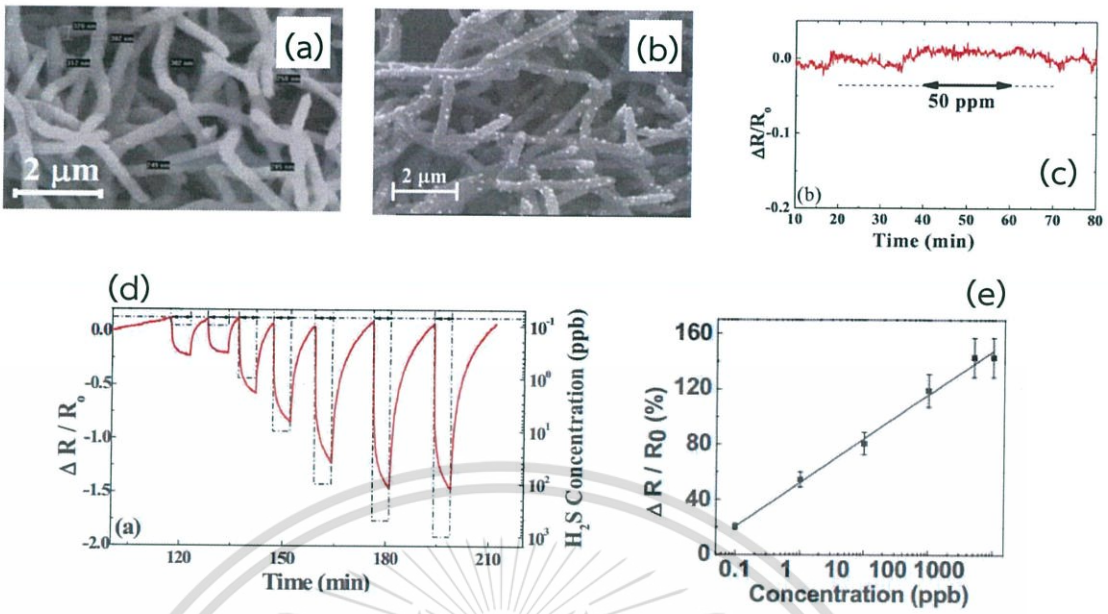

Figure 2.23 SEM images of (a) PANI NWs and (b) PANI NWs-Au NPs. (c) Response of PANI sensor toward 50 ppm of H_2S gas. (d) Response of PANI NWs-Au NPs sensor toward 0.1 ppb, 1 ppb, 10 ppb, 100 ppb, 500 ppb and 1000 ppb concentrations of H_2S gas. (d) Response of PANI NWs-Au NPs sensor as a function of H_2S concentration [55].

Table 2.7 Summary of sensing performance of CNT and CNT-functionalized polymer and metal NPs [10–20,50–55].

Sensor type	Targeted VOCs	Sensor Response	Reference
SWNT	NO_2 (2 ppm) NH_3 (1%)	- High response with several orders of magnitude change in conductance	[50]
SWNT	Methanol, DCM, chloroform, acetone at saturated vapors	- High response to 1-propanol, tertiary-butanol, 2-propanol, 1-butanol and ethanol vapors - Response time: 5-15 s	[51]

Table 2.7 (Continued.

Sensor type	Targeted VOCs	Sensor Response	Reference
f-MWNT-PMMA	DCM, chloroform, acetone, methanol, ethyl acetate, toluene and hexane	- Good reversibility and reproducibility - 100-1000-fold improvement in the resistance when exposed to saturated vapors of DCM, chloroform and acetone - response time: 2-5 s	[10,11]
poly(3-methylthiophene)-MWNT	Chloroform, Chloromethane, Carbon tetrachloride, acetone, acetaldehyde, benzaldehyde, THF, methanol and ethanol	- High response to chloroform, chloromethane and carbon tetrachloride - Good selectivity between chloromethane and methane - Response time: 60-120 s	[12]
EC-MWNT	benzene and ethanol (1000-5000 ppm)	- EC-CNT composite with 5wt.% of SWNT exhibited the highest response to C_6H_6 vapor ~ 9% at 5000 ppm	[13]

Table 2.7 (Continued)

Sensor type	Targeted VOCs	Sensor Response	Reference
CNT/HFIP-PT	Chloroform, DMMP, DCM, hexane, toluene, methanol and water	- Fast and reversible to DMMP vapor at ppb-ppm level - Good selectivity to DMMP	[14]
PVA/MWNT and PI/MWNT	Ethanol, Cyclohexane and THF	- PVA/MWNT high response to THF and ethanol, but low response to cyclohexane - MWNT high response to cyclohexane, but low response to ethanol - PVA-PI/MNWT can detect both ethanol and cyclohexane	[15]
Conductive polymer-MNWT (PCL, PLA, PC, PMMA and BPR)	Cyclohexane, DCM, *n*-heptane, isopropanol, toluene, ethanol, methanol, THF and water	- Excellent sensitivity and selectivity to VOCs - Good discrimination by PCA technique	[16]

Table 2.7 (Continued)

Sensor type	Targeted VOCs	Sensor Response	Reference
Quantum resistive sensors (vQRS) (PC, PCL, PLA, PMMA and PEO)	Butanol, chloroform, DCM,THF isopropanol, acetone and ethanol	- Fast response, high sensitivity and selectivity - Selectivity can be controlled by the thickness of the polymer film - Good discrimination by PCA	[17]
Pd/SWNT	Acetone, chlorine, C_6H_6, hydrogen chloride, hydrogen cyanide and NO_2	- Discriminated in the low concentration at ppm levels - Good discrimination by PCA	[18,52]
O_2 plasma-MWNT-decorated with Rh, Pd, Ni and Au	C_6H_6 and NO_2 (50-500 ppb)	- Sensor response to C_6H_6: Rh/MWNT > Pd/MWNT > Ni/MWNTs - Au-decorated O_2 plasma-MWNT non-respond to C_6H_6	[19]
O_2 plasma MWNT decorated with Pt and Pd NPs	Acetone, ethanol, methanol and NO_2	- Sensor response: Pt/MWNT > Pd/MWNT > pristine MWNT	[20]

Table 2.7 (Continued)

Sensor type	Targeted VOCs	Sensor Response	Reference
Pd-PANI	Ethanol, methanol and isopropanol	highly selective and sensitive to methanol - stable response for a long Time	[53]
PANI and PANI-Ag	Ethanol	- remarkable improvement of conductivity compare with pure PANI, increased by two orders of magnitude with respect to pure PANI - Sensor response: PANI-Ag > PANI - Sensor response, response time and reproducibility depend on the Ag concentration - good linear relationship with ethanol concentration	[54]
PANI NWs and PANI NWs-Au NPs	H_2S (0.1-1000 ppb) (50 ppm)	- PANI NWs-Au NPs respond to H_2S (0.1-1000 pp)	[55]

Table 2.7 (Continued)

Sensor type	Targeted VOCs	Sensor Response	Reference
		- PANI NWs-Au NPs: good response and recovery time, reproducibility and selectivity - PANI NWs sensor non-respond to H_2S even at ppm level - good linear relationship with H_2S concentration	

2.7.3 Gas Sensing Mechanism

Sensing mechanisms of pristine CNT and its functionalization with polymer or metal NP are different. In this section, the possible sensing mechanisms of the pristine CNT, polymer and metal NP-functionalized CNT-based gas sensors were summarized.

2.7.3.1 Charge Transfer

One possible sensing mechanism of pristine CNT is the charge transfer according to gas molecule or organic vapor adsorption on the CNT surface. The adsorption of gas molecule on the CNT surface induces an electron transfer between gas molecules and CNTs, thereby changing the sensor conductivity or resistivity [50]. The change in conductivity or resistivity depends on the gas species. In general, oxidizing gases (e.g., NO_2) withdraw electrons from CNTs, whereas reducing gases (e.g., carbon monoxide (CO)) donate electrons to CNTs, which could lead to opposite changes in the conductivity or resistivity of CNT. For example, upon oxidizing gas adsorption, electron transferred from p–type CNT to oxidizing gas molecule. Consequently, hole density of p-type CNT was increased, resulting in an decrease in resistance. In the other hand, upon reducing gas adsorption, electron transferred from reducing gas to p-type CNT, thereby hole density of p-type CNT was decreased, resulting in an increase in resistance.

2.7.3.2 Schottky barrier modulation

Another possible sensing mechanism of pristine CNT is the Schottky barrier modulation at the CNT-metal contact due to adsorption of polarized gas molecules at interface. For example, when reducing gas (NH_3) molecules are adsorbed on the CNT-Au interface, the work function of Au electrode is reduced. The holes could tunnel through the barrier, resulting in the change the conductivity and resistivity [56].

2.7.3.3 Polymer Swelling

Normally, the sensing mechanism of polymer/CNT composites is based on polymer swelling. The swelling of the polymer due to the adsorption of organic vapors into the polymer increases the volume and thus increases in distance between CNTs in polymer, thereby increasing the contact resistance, resulting in an increase of electrical resistance [10,11]. The extents of swelling and electrical response depend on the solubility between polymer and organic vapor. The schematic diagram of the contact resistance change between CNT-CNT due to polymer swelling is shown in Fig. 2.11.

2.7.3.4 Catalytic Oxidation

One possible sensing mechanism of metal NP/CNT is electron donation due to the oxidation of target gas on metal NP. For example, in the case of CO sensing by Pt-decorated SWNT, the sensing mechanism can be explained as follows; under atmospheric pressure, O_2 reacts at the surface of the Pt catalyst and dissociates into O^-. Upon CO adsorption, the CO molecule on the Pt catalyst surface interacts with the preadsorbed O^- by equation (2.8) proceeds via the Langmuir-Hinshelwood mechanism [57,58]. Finally, the residual electron captured by pre-adsorbed O^- is released and donated to the p-type semiconducting SWNT, resulting in an increase in electrical resistance.

$$CO(ad) + O^-(ad) \rightarrow CO_2(g) + e^- \quad (2.8)$$

2.7.3.5 Work Function Adjustment

In the solid phase, the work function (ø) of a material is defined as the minimum energy require by an electron to escape from the Fermi level of material to the vacuum level. Fermi level (E_F) is the highest occupied energy level in the band gap.

Vacuum level is threshold energy at which electron can leave atom. The work function can be calculated by equation (2.9).

$$hf = \emptyset + E_k \tag{2.9}$$

where, h is the Plank constant, f is the frequency of the incident light and E_k is maximum kinetic energy of the emitted electrons

The decoration of metal NP on CNT cause electrons to pass easily between metal NPs and CNTs [20]. It can be explained by work function adjustment which involve the metal-semiconductor CNT contact. For example, the Pt and p-type SWNT contact, the work function of SWNT ($\emptyset_{\text{p-type SWNT}}$) and Pt ($\emptyset_{\text{Pt}}$) are 5.05 eV [59] and 5.65 eV [60], respectively. The work function of p-type SWNT is higher than that of Pt. After the Pt and p-type are brought into contact, electron flow from the p-type SWNT down into Pt until the Fermi levels of both sides are equal. The band diagram of Pt and p-type SWNT contact is shown in Fig. 2.25. The contact between Pt and p-type SWNT is ohmic contact which is a low resistance contact, allows current to flow both ways. When the gas molecule adsorb on the metal surface, electron easily transfer between metal and CNT, resulting in an increase in sensor response.

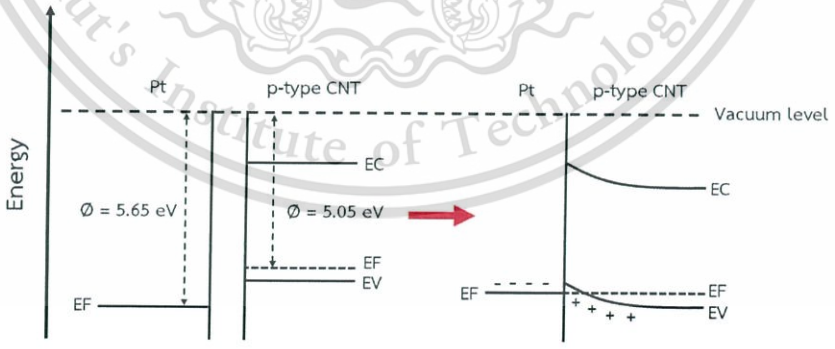

Figure 2.24 The energy band diagram of Pt and p-type SWNT before (left) and after (right) merging.

2.8 Hansen Solubility Parameter

Hansen solubility parameter (HSP) is the principle for prediction the solubility between solvent and solute. HSP is based on the idea of like dissolves like. HSP consists of three components such as dispersion force (δ_d), polar interaction (δ_p), and hydrogen bonding (δ_h) that describe the thermodynamics of dissolving. The solubility between solvent and solute can be calculated by equation (2.10)-(2.11) which involve the relative energy distance (*RED*). The *RED* value can be classified as 3 cases.

(1) *RED* < 1: solvent and solute are alike and will dissolve
(2) *RED* = 1: solvent and solute will partially dissolve
(3) *RED* > 1: solvent and solute will not dissolve

$$RED = R_a/R_0 \tag{2.10}$$

R_a is the distance between Hansen parameters of two substances

R_0 is the interaction radius

$$R_a = \sqrt{4(\delta_{d2} - \delta_{d1})^2 + (\delta_{p2} - \delta_{p1})^2 + (\delta_{h2} - \delta_{h1})^2} \tag{2.11}$$

δ_d is the energy from dispersion forces between molecules

δ_p is the energy from dipolar intermolecular force between molecules

δ_h is the energy from hydrogen bonds between molecules

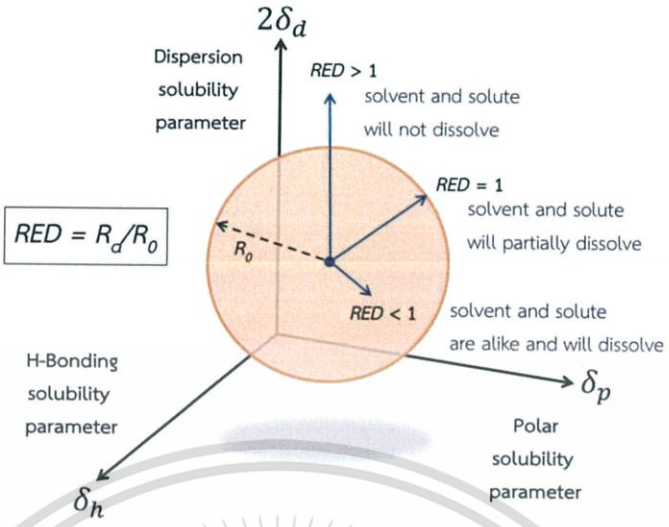

Figure 2.25 Schematic diagrams of HSP sphere.

2.9 Principal Component Analysis

Principal component analysis (PCA) is one of several statistical tools available for reducing the dimensionality of a data set. PCA is the most popular technique for pattern recognition, especially pattern recognition and/or gas discrimination [61–63]. PCA uses the data involving a substantial number of correlated variables. A dimension-reduction technique used to reduce a large set of variables to a small set which contain most of the information in the large set. This technique transforms a number of correlated variables into a smaller number of uncorrelated variables. The statistics is based on the big set of data analyses in terms of the relationships between the individual points in that data set. The dispersion of a set of data is measured by standard deviation (SD). In the case of data points are further from the mean, there is higher deviation within the data set. SD is calculated by the root of variance by determining the variation between each data point relative to mean. The equation (2.12) shows the information of set of numbers samples of set X.

$$x = [\,7\ 5\ 3\ 10\ 14\ 16\ 20\ 24\ 34\ 100\,] \qquad (2.12)$$

The mean of the sample X is calculation by equation (2.13), where n is the number of elements in the set X. The SD of a data set X is calculated by equation (2.14). The variance (S^2) measure of data in a data set X is calculated by equation (2.15).

$$\bar{x} = \frac{\sum_{i=1}^{n} x_i}{n} \tag{2.13}$$

$$SD = \sqrt{\frac{\sum_{i=1}^{n}(X_i - \bar{X})^2}{n-1}} \tag{2.14}$$

$$s^2 = \frac{\sum_{i=1}^{n}(X_i - \bar{X})^2}{n-1} \tag{2.15}$$

SD and S^2 perform on 1 dimension, thus the calculation of the SD for each dimension of the data set independently of the other dimensions. Nevertheless, this method is similar measure to find out the dimensions vary from mean. Next, covariance is measured between 2 dimensions, which calculate the covariance between one dimension and itself. The sample of a 3-dimensional data set (x, y, z) is measured the covariance between the x and y dimensions, the x and z dimensions, and the y and z dimensions. Measuring the covariance between x and x or y and y or z and z would give the variance of the x, y and z dimensions respectively. The variances and covariance of the elements of a random vector x are collected to a covariance matrix whose i, j-th element is simply the covariance of x_i and x_j. The variance and covariance formulas are calculated by equation (2.16) and (2.17), respectively. The sample of covariance matrix has 3 rows and 3 columns, and the values are shown in equation (2.18).

$$var(x) = \frac{\sum_{i=1}^{n}(X_i - \bar{X})(X_i - \bar{X})}{(n-1)} \tag{2.16}$$

$$cov(x,y) = \frac{\sum_{i=1}^{n}(X_i - \bar{X})(Y_i - \bar{Y})}{(n-1)} \tag{2.17}$$

$$C = \begin{pmatrix} cov(x,x) & cov(x,y) & cov(x,z) \\ cov(y,x) & cov(y,y) & cov(y,z) \\ cov(z,x) & cov(z,y) & cov(z,z) \end{pmatrix} \tag{2.18}$$

The determination of the eigenvectors and eigenvalues of a system is extremely important in PCA, where it is equivalent to matrix diagonalization and arises in such common applications as stability analysis. Each eigenvector is paired with a corresponding so-called eigenvalue. The eigenvalue for the covariance matrix C is calculated by equation (2.19), where v is an eigenvector of the linear transformation

A and the scale factor λ is the eigenvalue corresponding to that eigenvector and I is the n by n identity matrix. The determinant of the equation (2.19) is zero. Thus, the eigenvalues of matrix C are values of λ that satisfy the equation (2.20), where each λ_i may be real but in general is a complex number. The numbers λ_1, λ_2,... λ_n, which may not all have distinct values, are roots of the polynomial and are the eigenvalues of C.

$$(C - \lambda I)v = 0 \tag{2.19}$$

$$|C - \lambda I| = 0 \tag{2.20}$$

The equation (2.21) is the PCA matrix based on a decomposition of the data matrix PCA into two matrices C and P, which are orthogonal. The matrix C is called the scores matrix or matrix of observation (covariance matrix) while the matrix P is called the loadings matrix or eigenvector. The matrix C contains the original data in a rotated coordinate system. The loadings can be understood as the weights for each original variable when calculating the principal component.

$$[PCA] = [C][\,v^T] \tag{2.21}$$

where $PCA_{(nxm)}$ is matrix of principle components score, $C_{(nxm)}$ is matrix of observation (scaled original data matrix) and $v^T{}_{(mxm)}$ is (v transpose) square matrix of loading matrix or eigenvector.

2.10 Thin Film Deposition

2.10.1 Spin Coating

Spin coating is a general technique for depositing thin film in range of a few nanometers to a few of microns in thickness. A solution of the desired material is dropped on the substrate which is fixed on the spin-coater. The substrate is rotated at high speed in order to spread the coating material by centrifugal force, the solvent solution spins off the edges of the substrate until the desired the thin film is achieved. The thickness of thin film relates with the dispersion viscosity and spin time. A schematic diagram of spin coating process is shown in Fig. 2.26.

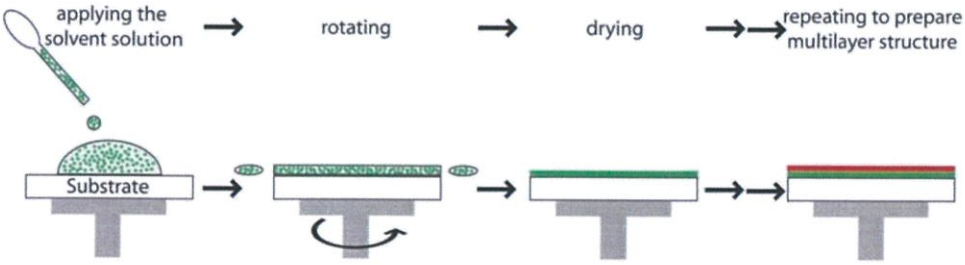

Figure 2.26 Schematic diagrams of spin coating process [64].

2.10.2 Electron Beam Evaporation

Electron beam (EB) evaporation is a physical vapor deposition technique to deposit thin films on substrate. The generated electrons by thermionic emission in a vacuum system can be precisely controlled using electric or magnetic fields as electrode beam to irradiate onto the target material in the form of pellet or powder are placed in the crucible (eg. alumina, graphite or boron nitride crucibles). Substance was heated and evaporated to the substrate that mount at the top of chamber and form as a thin film or metal nanoparticle on a desired substrate. A schematic diagram of EB evaporation is shown in Fig. 2.7.

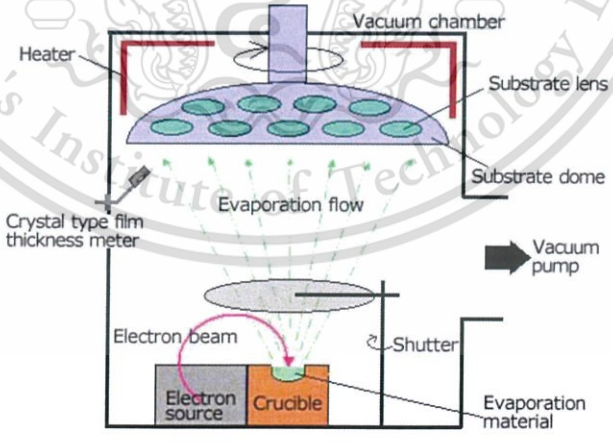

Figure 2.27 Schematic diagrams of electron beam evaporation [65].

2.11 Analytical Instrument

2.11.1 Scanning Electron Microscopy

Scanning electron microscopy (SEM) is a technique for imaging of the morphology and structural properties of CNT. The principle of SEM, primary electrons were generated via electron gun under vacuum and focused as electron beam, then accelerated toward the surface sample. The primary electrons knock the secondary electron within the atoms of sample. The emitted secondary electron is converted to 3 dimensions signal imaging. A schematic diagram of SEM is shown in Fig. 2.28.

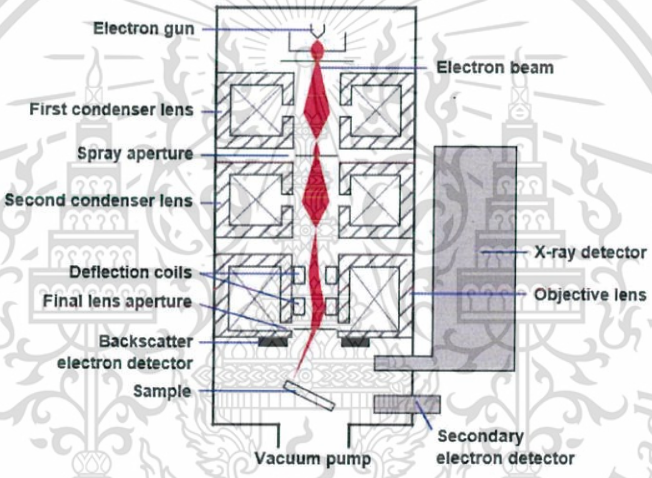

Figure 2.28 Schematic diagrams of SEM [66].

2.11.2 Energy-Dispersive X-Ray Spectroscopy

Energy-dispersive X-ray spectroscopy (EDS) is a technique used to analyze the element composition and distribution. The principle of EDS is based on the interaction between X-ray and atoms results in the emission of a characteristic X-ray. An electron beam bombards to sample and knocks an electron in an inner shell of sample. The electron vacancy is filled by outer electron from a higher energy state. An X-ray is emitted to balance the energy difference between two electron's states. The energy of emitted X-ray is characteristic of the atomic structure of the element. A principle of EDS is shown in Fig. 2.29.

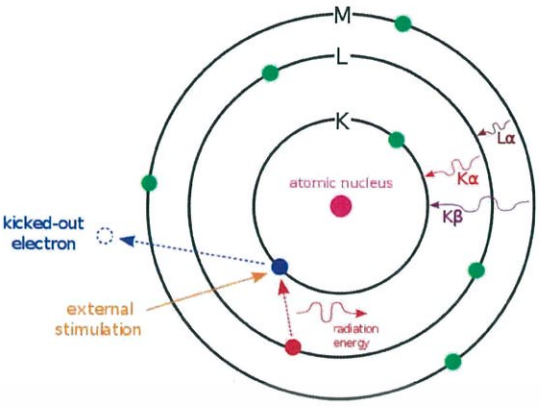

Figure 2.29 Principle of EDS [67].

2.11.3 Transmission Electron Microscopy

Transmission electron microscopy (TEM) is a technique for internal structure and crystallinity analysis of CNT. The principle of TEM, electron was generated via electron gun from high voltage under vacuum and focused as electron beam by condenser lens, then accelerated toward the sample. A beam electron is transmitted through a thin sample and converted to 2 dimensions signal imaging. A schematic diagram of TEM is shown in Fig. 2.30.

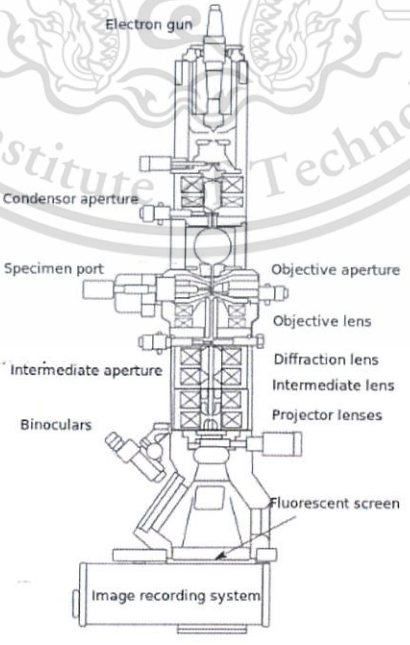

Figure 2.30 Schematic diagrams of TEM [68].

2.11.4 Raman Spectroscopy

Raman spectroscopy is a technique used to analyze the carbon structure, purity, and crystallinity of CNT. This technique can analyze the sample in solid, liquid and gaseous samples. The principal of Raman spectroscopy is a technique based on inelastic scattering of monochromatic light or Raman scattering. The laser light interacts with vibrating molecules, resulting in the energy is shifted up or down due to the adsorption and desorption energy in atom. This shift of energy gives information about the vibrational modes of sample. A schematic diagram of Raman spectrometer is shown in Fig. 2.31(a) [69]. Energy-level diagram of the states involves in Raman scattering is shown in Fig. 2.31(b) [70].

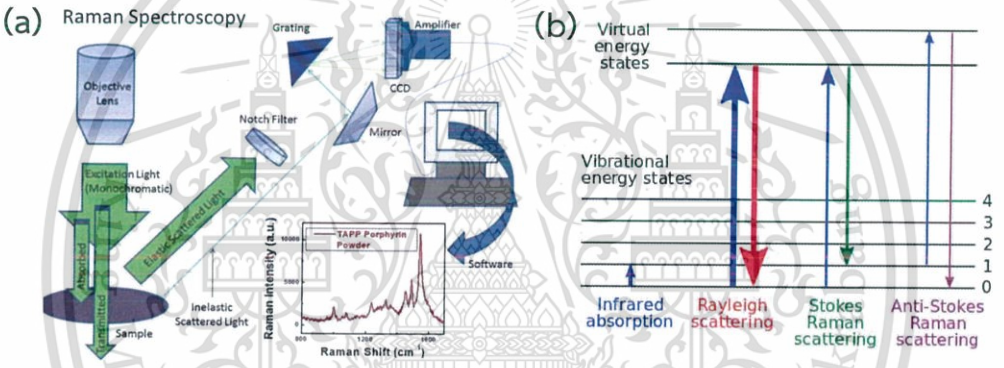

Figure 2.31 (a) Schematic diagrams of Raman spectroscopy [69] and (b) Energy-level diagram involves in Raman scattering [70].

2.11.5 Fourier Transform Infrared Spectroscopy

Fourier Transform Infrared (FTIR) is a technique used to identify the chemical bonding, chemical structure, and functional group of element or composited material. The principle of FTIR is based on adsorption and transmission of light in the infrared (IR) region. The molecule was excited into a higher vibrational and rotational state. The IR absorption and transmission are characteristic of its chemical bonding and functional group. A schematic diagram of FTIR is shown in Fig. 2.32.

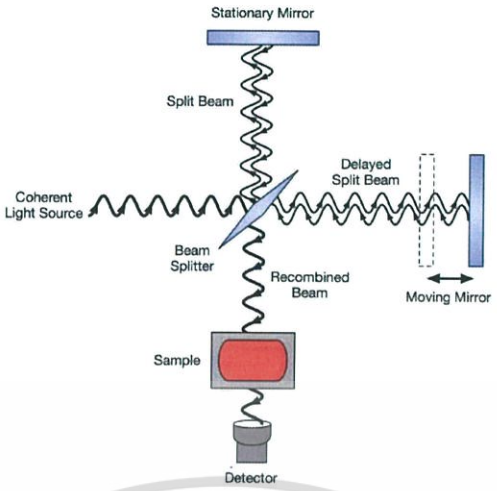

Figure 2.32 Schematic diagrams of FTIR [71].

2.11.6 X-Ray Diffraction

X-ray diffraction (XRD) is a technique used to analyze the crystal structure of materials. The XRD analysis is based on constructive interference of monochromatic X-ray and a crystalline sample. X-rays are generated by cathode ray tube and accelerated to the sample. XRD result is produced the constructive interference of a monochromatic beam of X-rays diffracted at specific angle by lattice planes separated by the interplanar distance (*d*) which correspond to Bragg's law in equation (2.4). A schematic diagram of XRD is shown in Fig. 2.33.

$$n\lambda = 2dsin\theta \tag{2.4}$$

where n is a positive integer

λ is the wavelength of incident X-ray

d is the interplanar distance of lattice

θ is the scattering angle

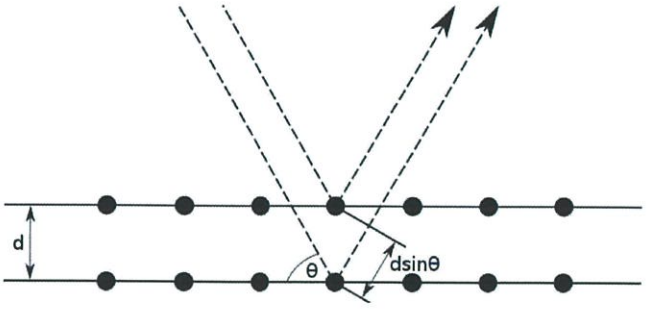

Figure 2.33 Schematic diagrams of XRD [72].

2.11.7 Fluorescence spectroscopy

Fluorescence spectroscopy is a technique used to analyze the fluorescence from sample. This technique is concerned with electronic and vibrational states. It involves using a beam of light, usually ultraviolet light, to excite the electrons in molecules of compounds and causes them to emit light. The emitted light is possible to record both excitation spectrum which the light that is absorbed by the sample or an emission spectra which the light emitted by the sample. The excitation and emission wavelengths specific to the compound. A schematic diagram of the adsorption to excited energy state followed fluorescence emission is shown in Fig. 2.34.

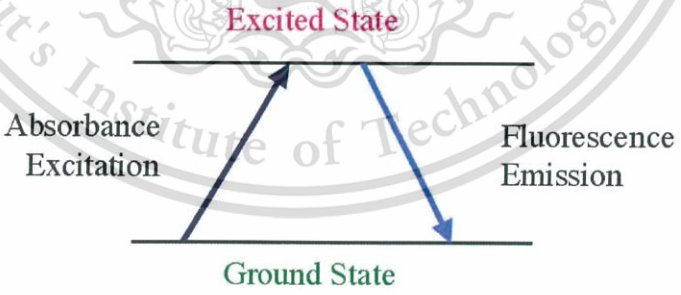

Figure 2.34 Absorption to an excited energy state followed fluorescence emission [73].

CHAPTER 3

POLYMER-FUNCTIONALIZED SINGLE-WALLED CARBON NANOTUBE FOR VOLATILE ORGANIC COMPOUNDS DETECTION

This chapter describes the fabrication of gas sensor from pristine single-walled carbon nanotube (SWNT) and hybrid materials based on polymer-functionalized SWNT. Polymer-coated SWNTs were prepared by spin coating. Morphology and structure of sensing materials were characterized by field emission scanning electron microscopy (FESEM) and Raman spectroscopy. The sensing performances to volatile organic compound (VOC) were investigated in terms of sensitivity and selectivity.

3.1 Fabrication of Gas Sensor Device

3.1.1 Preparation of Sensor Platform

A printed circuit board (PCB) consisting of an interdigitated Cu/Au electrode with a gap of 250 μm was used as the sensor platform. The specifications of PCB are shown in Table 3.1.

Table 3.1 Specifications of PCB substrate

Electrode gap:	250 μm
Electrode type:	Interdigitated Au/Cu
Sensing area:	22.65 mm^2
Substrate:	PCB

Prior to sensor preparation, the PCB was cleaned by sequential sonication in potassium hydroxide, acetone, methanol and deionized water for 10 min. with ultrasonication for 10 min. Finally, the cleaned PCB was dried by N_2 flow.

3.1.2 Fabrication of Sensor Based on Polymer-Functionalized Carbon Nanotubes

An SWNT suspension was prepared by dispersing SWNTs, (diameter and length in the ranges of 1.2-1.5 nm and 2-5 μm, respectively) in 1,2-dichloroethane by ultrasonication for 3 h and subsequently dropping onto the PCB prepared by the process explained in section 3.1.1. The electrical resistance of the SWNT on the PCB was adjusted to approximately 100 kΩ. Next, a solution of monomer or polymer was prepared in toluene and stirred for 24 h. Then, the monomer or polymer solution was spin-coated onto the predropped SWNT network. The spinning speed was 3000 rounds per minute and the spinning time was 5 min. After spinning, the sample was heated at 100 °C for 24 h to eliminate the solvent in the sensor samples. The monomer and polymer concentrations were fixed at 5 wt%. The monomer and polymers used in this research are shown in Table 3.2. The monomer and polymer structures used in this research are shown in Fig. 3.1. The schematic view of pristine SWNT and polymer/SWNT sensors are shown in Fig. 3.2.

Table 3.2 List of monomer and polymers used in this research.

Monomer and polymers	Molecular weight (M_w) (g/mol)
Thiophene	84
ethyl cellulose (EC)	-
poly(methyl methacrylate) (PMMA)	94,600
polystyrene (PS)	35,000
poly(vinyl acetate) (PVA)	140,000

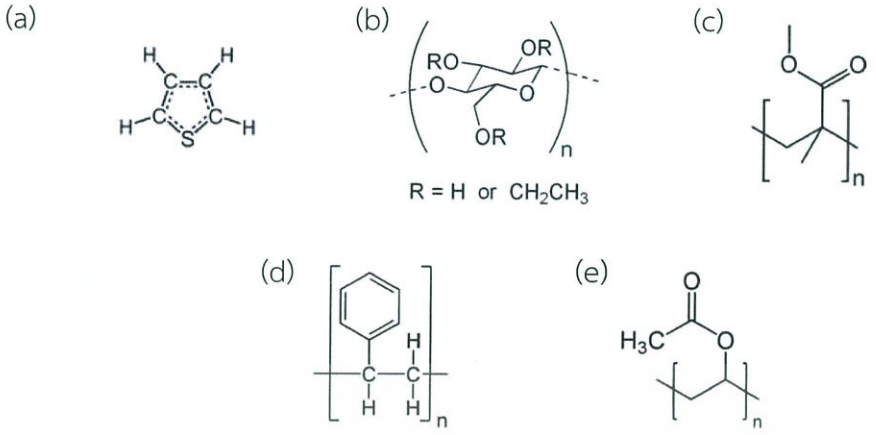

Figure 3.1 Monomer and polymer structures of (a) thiophene, (b) EC, (c) PMMA, (d) PS and (e) PVA [74–78].

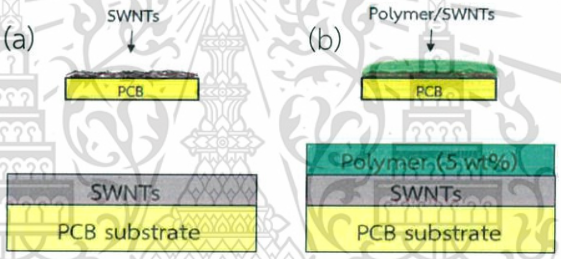

Figure 3.2 Schematic view of (a) SWNTs and (b) polymer/SWNTs sensors.

3.2 Morphology and Structural Characterization of Sensing Materials

3.2.1 Scanning Electron Microscopy Characterization

The morphologies of the pristine SWNT and polymer/SWNT were characterized by field emission scanning electron microscopy (FESEM; JEOL JSM-7800F). The FESEM observation was carried out in a high vacuum mode with a base pressure of approximately 1×10^{-4} Pa and an acceleration voltage of 1 kV without any surface treatment with metallic materials. The samples for FESEM was prepared by the process explained in sections 3.1 using silicon (Si) as a substrate instead of the PCB.

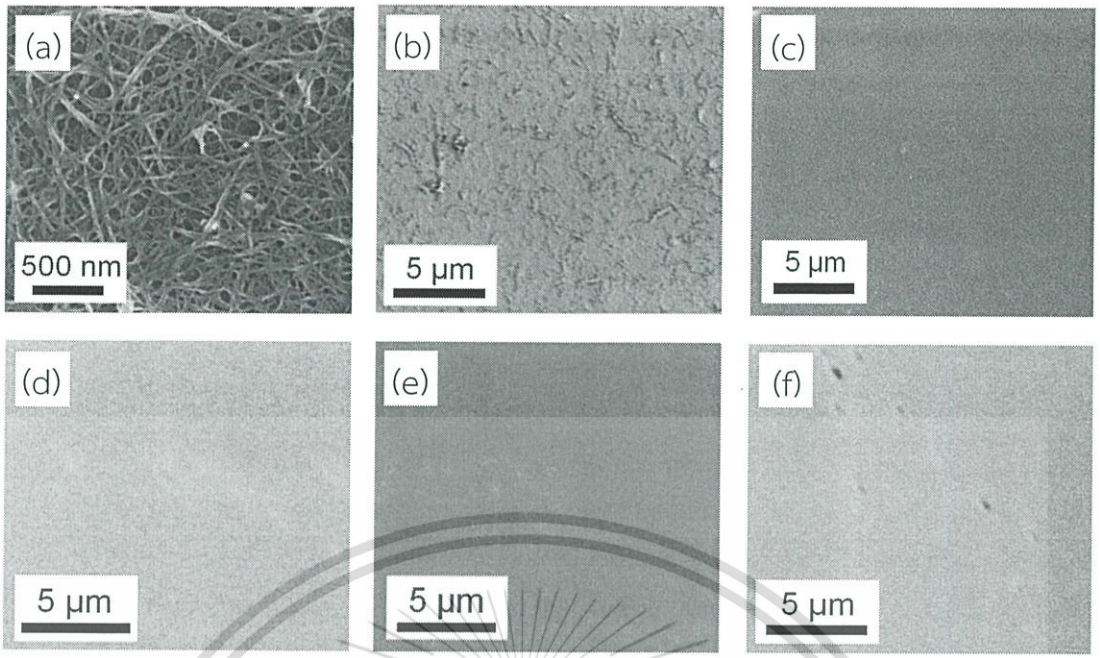

Figure 3.3 FESEM images of (a) pristine SWNT, (b) thiophene/SWNT, (c) EC/SWNT, (d) PMMA/SWNT, (e) PS/SWNT, and (f) PVA/SWNT.

Pristine SWNT and polymer/SWNT were morphologically characterized by FESEM as shown in Fig. 3.3. The pristine SWNT assembled into a network of overlying SWNTs, forming a conductive network structure on the substrate, as shown in Fig. 3.3(a). Fig. 3.3(b-f) shows FESEM images of thiophene/SWNT, EC/SWNT, PMMA/SWNT, PS/SWNT and PVA/SWNT, respectively. After EC, PMMA, PS or PVA solutions were spin-coated onto the pristine SWNT network, polymer completely covered the pristine SWNT network (Fig. 3.3(c-f)), whereas thiophene solution, which has a low viscosity, could penetrate into spaces between the entangled SWNTs, resulting in the appearance of the SWNT network on the surface of thiophene/SWNT (Fig. 3.3(b)).

3.2.2 Raman Spectroscopy Characterization

The carbon structure, purity and crystallinity of pristine SWNT and polymer/SWNT were analyzed by Raman spectroscopy (Thermo SCIENTIFIC DXR) with an Ar ion laser wavelength of 532 nm (2.33 eV).

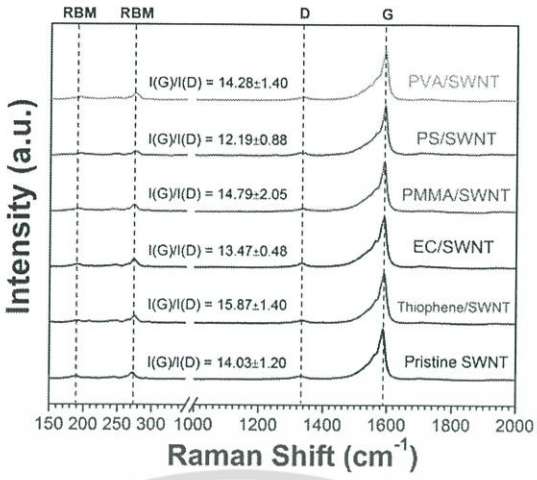

Figure 3.4 Raman spectra of pristine SWNT, thiophene-, EC-, PMMA-, PS- and PVA-coated SWNT.

Raman spectroscopy was utilized to characterize the structure, purity and crystallinity of pristine SWNT and polymer-coated SWNT. Fig. 3.4 shows the four significant Raman peaks: SWNT-derived Radial breathing mode (RBM) at 190 and 273 cm^{-1}, disorder carbon-derived D-band at 1332 cm^{-1} and graphitic-structure-derived G-band at 1588 cm^{-1}. The intensity ratio between the G- and D-bands (I_G/I_D) of pristine SWNT was approximately 14.03±1.20. After polymer-deposition, the I_G/I_D ratio of thiophene/SWNT, EC/SWNT, PMMA/SWNT, PS/SWNT and PVA/SWNT were 15.87±1.40, 13.47±0.48, 14.79±2.05, 12.19±0.88 and 14.28±1.40 respectively, implying that the structure of SWNTs was maintained even when coated with monomer or polymer. In addition, the diameter of the pristine SWNTs (d) can be estimated from the RBM peak using the formula as shown in equation (3.1) [79].

$$d = \frac{248}{\Omega_{RBM}} \tag{3.1}$$

where Ω_{RBM} is the Raman shift of RBM peak.

Although SWNTs with d ≥ 2 nm are generally difficult to detect by Raman spectroscopy, this laser excitation shows the existence of SWNT with diameter of 0.91 and 1.31 nm.

3.3 Sensor Performance of Polymer-Functionalized Carbon Nanotubes

3.3.1 Gas Sensor Measurement System

The sensor response to VOC vapor was investigated at room temperature by recording the electrical resistance using a FLUKE NetDAQ during cycles of alternating supply of dry N_2 gas and VOC vapor. Benzene (C_6H_6), chloroform ($CHCl_3$), dichloromethane (CH_2Cl_2), acetone (C_3H_6O), ethanol (C_2H_6O) and methanol (CH_3OH) were used for VOC sensing performance test. The sensors were placed into the stainless steel chamber and N_2 gas was introduced into the chamber at a flow rate of 3.0 liters per minute (lpm) for 180 s as a baseline. Then, N_2 was replaced with VOC vapor by bubbling liquid VOC with N_2 carrier gas at a flow rate of 1.5 lpm for 180 s. At that time, VOC liquid was boiled at temperature of 90% of its boiling point. The sensors were recovered by purging with 3.0 lpm of N_2 for 180 s. The schematic views of the setup of the sensor measurement system and the profile of gas flow are shown in Fig. 3.5 and 3.6, respectively. The conditions for gas sensor measurement are summarized in Table 3.3.

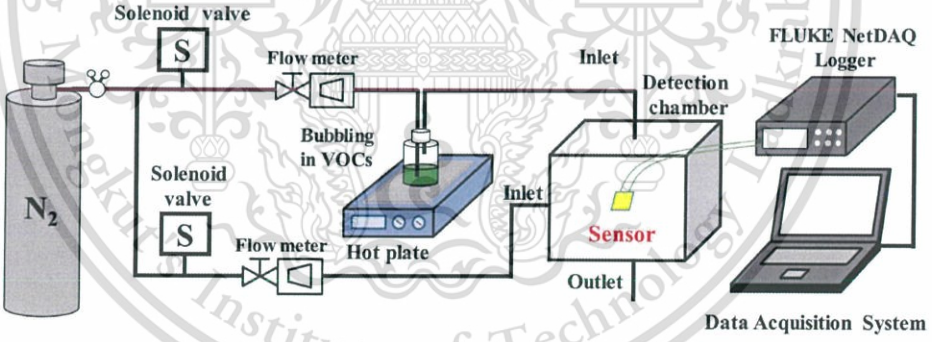

Figure 3.5 Schematic view of a gas sensor measurement.

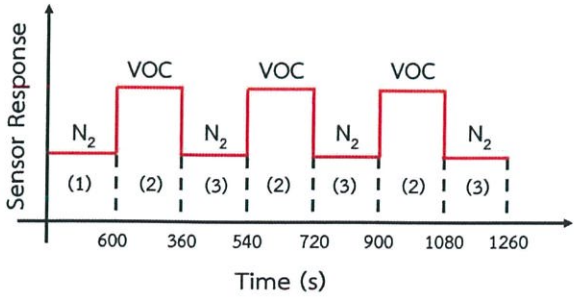

(1) Under N_2 atmosphere

(2) VOC adsorption

(3) Recovery under N_2 atmosphere

Figure 3.6 Schematic view of flow profile of gas sensor measurement.

Table 3.3 Conditions for gas sensing characterization.

Volatile organic compounds:	Benzene (113-127 ppt*), Chloroform (279-477 ppt)
	Dichloromethane (495-666 ppt)
	Acetone (2493-2796 ppt)
	Ethanol (112-134 ppt) , Methanol (236-276 ppt)
Temperature of the VOC liquid:	90% of boiling point
N_2 flow rate:	3.0 lpm (base line), 1.5 lpm (VOC bubbling)
Operation temperature:	Room temperature (25 °C)
Pressure:	Atmospheric pressure

*ppt: Parts per thousand

The sensor response (*SR*) was defined as shown in equation (3.2)

$$SR = \frac{(R_{VOC} - R_0)}{R_0} \tag{3.2}$$

where R_{VOC} and R_0 are the resistances of the sensor after and before VOC exposure, respectively.

To compare the responses of all sensors, the sensor responses were normalized by the VOC concentration. The normalized sensor response (*NSR*) was defined as the ratio between the sensor response at a time of 360 s (SR_{360}) and the VOC concentration (C_{VOC}). The *NSR* were defined as shown in equation (3.3).

$$NSR = \frac{SR_{360}}{C_{VOC}} \tag{3.3}$$

3.3.2 Sensor Response of Polymer-Functionalized Single-Walled Carbon Nanotube to Volatile Organic Compound System

The sensing performance to VOCs of the fabricated pristine SWNT, monomer/SWNT and polymer/SWNT sensors were investigated. The initial resistance of pristine SWNT, monomer/SWNT and polymer/SWNT are summarized in table 3.4.

Table 3.4 Initial resistance of SWNT, monomer/SWNT and polymer/SWNT.

Sensor	Initial resistance (kΩ)
Pristine SWNT	95.92 ± 8.20
Thiophene/SWNT	108.82 ± 25.26
EC/SWNT	146.13 ± 12.85
PMMA/SWNT	131.52 ± 23.53
PS/SWNT	111.62 ± 3.61
PVA/SWNT	124.36 ± 23.52

Fig. 3.7(a-f) shows sensor responses as a function of time of each sensor under an alternating supply VOC and N_2 gas for 3 cycles. VOCs were benzene, chloroform, dichloromethane, acetone, ethanol and methanol. The electrical resistance of almost the sensors increased upon VOC exposure and decreased after replacing VOC with N_2 gas. However, in the case of PVA/SWNT, the electrical resistance decreased upon chloroform and dichloromethane exposure (Fig. 3.7(b-c)). Almost all sensors were recovered to their initial resistance under N_2 gas purging due to physically adsorb onto the sensor materials via van der Waals forces, which is a weak interaction. Thus, VOC molecule was easily removed by N_2 gas purging. However, in a few cases, gas sensors were hardly recovered to their initial resistances. In this case, the response characteristics between sensor materials and VOC molecule may be attributed to chemisorption. VOC molecules seem to strongly interact with the sensor materials through chemisorption, which is relatively strong interaction, resulting in difficulty in removing VOC molecule from sensor material. The reversibility of the sensor can be improved by applying heat or ultraviolet (UV) exposure, similar to SWNT sensor system [6–8].

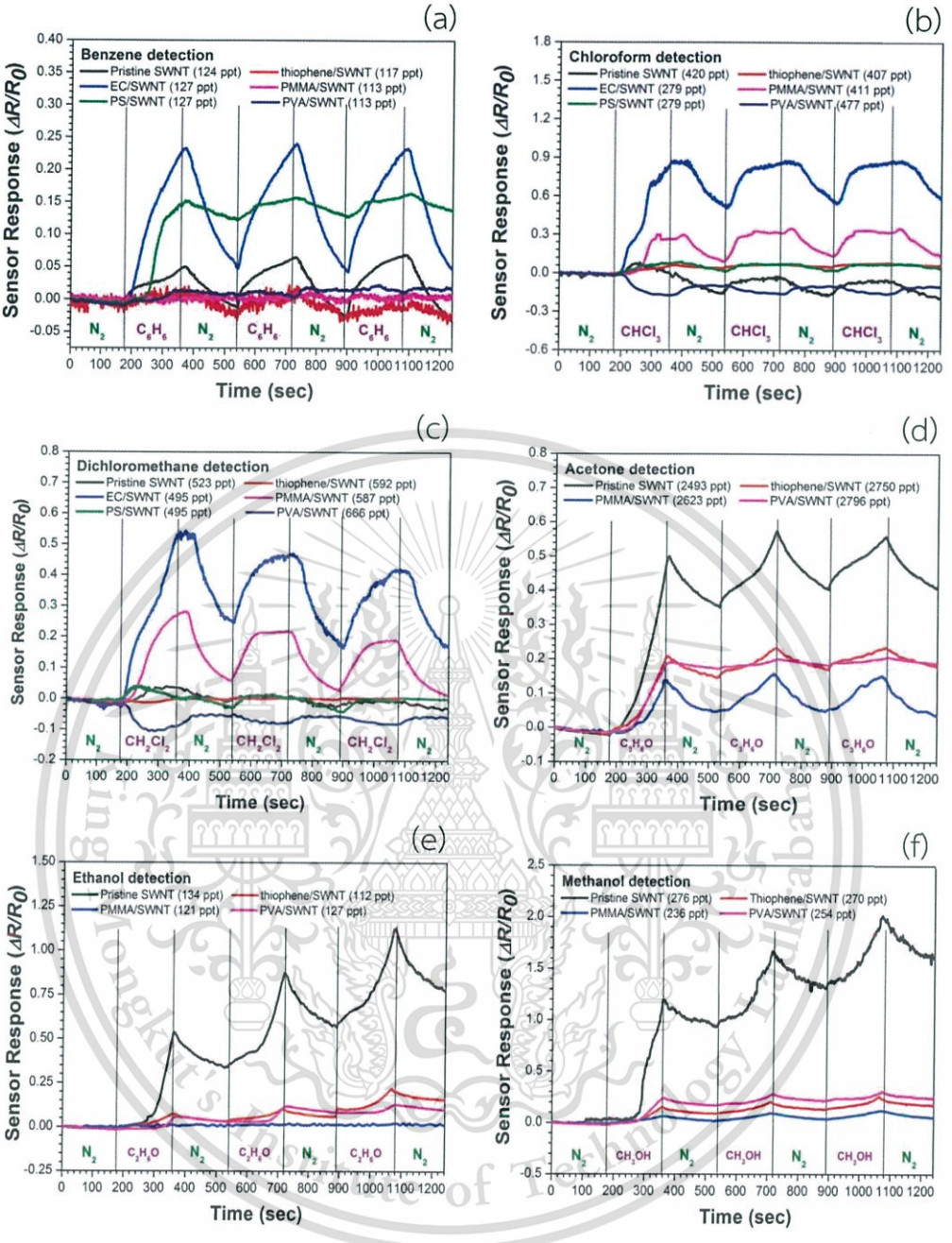

Figure 3.7 Sensor response as a function of time for pristine SWNT and polymer-coated SWNT toward (a) benzene (b) chloroform (c) dichloromethane (d) acetone (e) ethanol and (f) methanol.

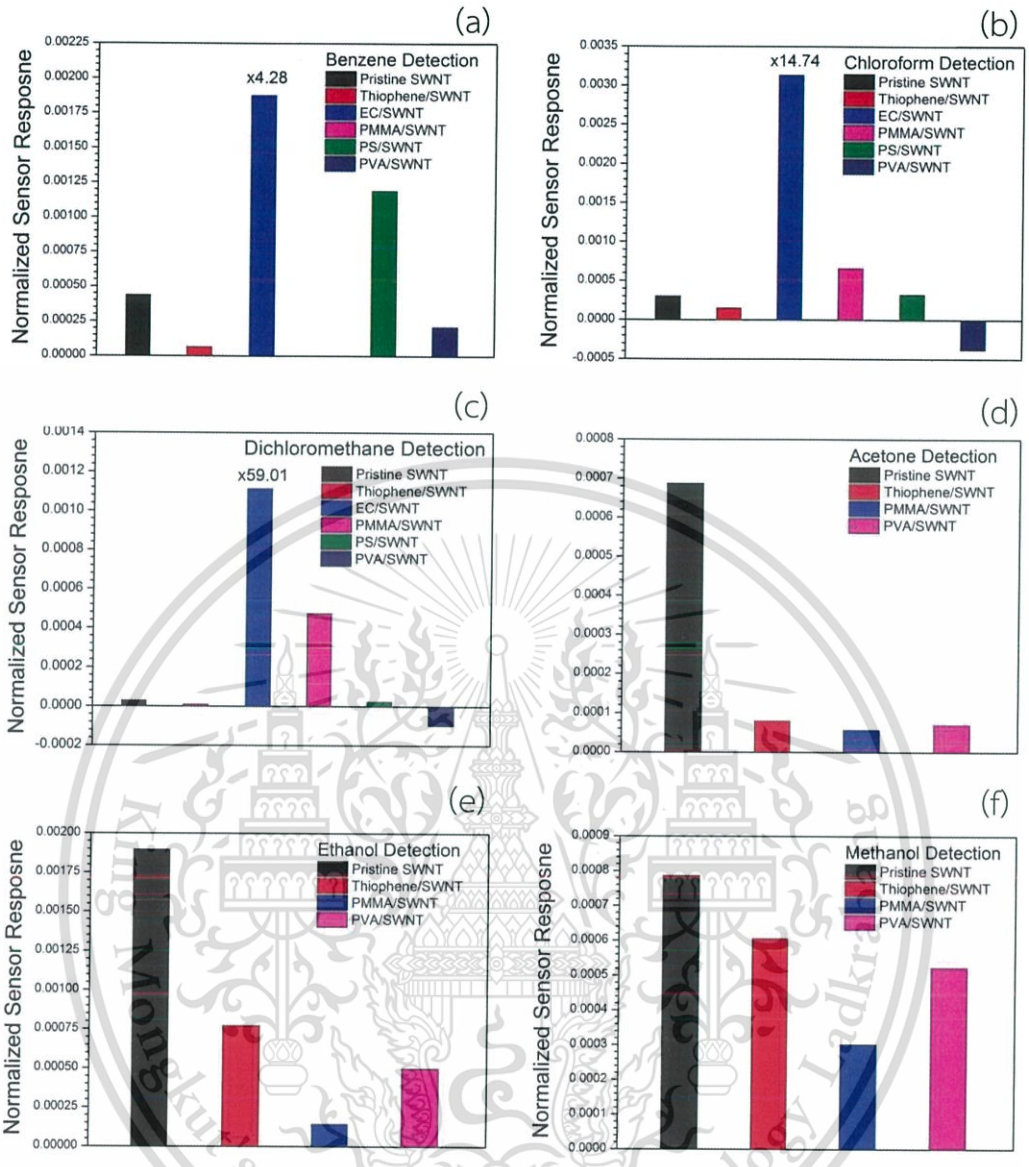

Figure 3.8 Normalized sensor response of pristine SWNT and metal NP/SWNT toward (a) benzene (b) chloroform (c) dichloromethane (d) acetone (e) ethanol and (f) methanol.

Fig. 3.8(a-f) shows the normalized sensor response of each sensor to VOC. The normalized sensor response of EC/SWNT greatly increased 4.28-, 14.74- and 59.01-fold to benzene, chloroform and dichloromethane, respectively, higher than that of pristine SWNT (Fig. 3.8(a-c)), For alcohol group detection, the polymer-coated SWNT reduced the responses to acetone, ethanol and methanol (Fig. 3.8(d-f)). The sensing mechanism of pristine SWNT can be described in terms of the dielectric constant, which involves the solvent polarity of VOCs. The solvent polarity is in the following order: benzene <

chloroform < dichloromethane < acetone < ethanol < methanol [80]. Molecules with higher polarity can hold moving holes and interrupt the movement of holes along the p-type SWNTs, resulting in a large increase in electrical resistance and thus an increase in sensor response [81]. Fig. 3.9 shows schematic diagram of sensing mechanism of pristine CNT for VOC detection. The trend of the normalized sensor response of pristine SWNT to acetone and methanol coincided with the VOC polarity. However, the dielectric constant cannot describe the sensor responses for methanol, benzene, chloroform and dichloromethane. For polymer-coated SWNT, the sensing mechanism would be ascribed to monomer or polymer swelling due to VOC adsorption and Hansen solubility parameter (HSP). A hypothesis based on monomer or polymer swelling can be described as follows. After VOC adsorption, monomer or polymer coatings on SWNTs are swollen, thus possibly increasing the monomer or polymer volume and lossening the SWNT network, resulting in an increase in the electrical resistnce [10,11]. The schematic diagram of sensing mechanism of monomer- or polymer-coated CNT for VOC detection is shown in Fig. 3.10. The sensing mechanism of monomer- or polymer-coated SWNT for VOC detection. For the hypothesis based on HSP, HSP is the value of relative energy difference (*RED*) used to predict the solubility between solvent with monomer or polymer. The *RED* value was calcultaed by the eqaution (2.10). Table 3.5 shows HSP and *RED* between monomer or polymer with variuos VOC. The smaller *RED* value means the higher miscibility. The EC/SWNT has the minimum *RED* for benzene, chloroform and dichloromethane. Hence, the EC/SWNT responds more sensitively to benzene, chloroform and dichloromethane vapors. The trend of the normalized sensor response of EC/SWNT to benzene, chloroform and dichloromethane coincided with the HSP calculation.

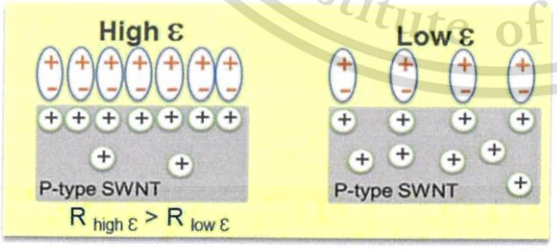

Solvent Polarity	High	Low
The movement of hole	Difficult	Easy
Resistance of sensor	High	Low
Sensor response	Good	Bad

Figure 3.9 Schematic diagram of gas sensing mechanism of pristine CNT for VOC detection.

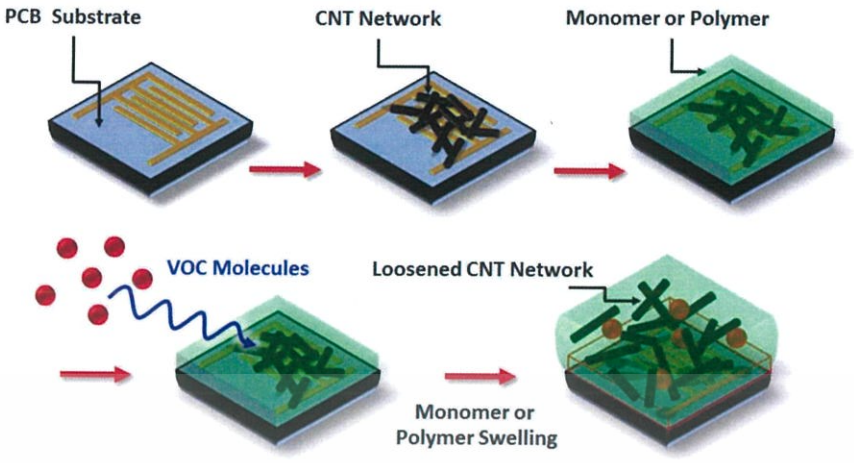

Figure 3.10 Schematic diagram of gas sensing mechanism of monomer- and polymer-coated CNT for VOC detection.

Table 3.5 Hansen solubility parameter and RED between polymer and VOCs.

Polymer and solvent	Hansen solubility parameter, HSP $(MPa)^{1/2}$			R_0	R_a	RED (R_a/R_0)
	δ_D	δ_p	δ_H			
Benzene	18.4	0.0	2.0	-	-	-
EC	19.0	5.6	4.9	7.9	6.42	0.81
PMMA	17.9	10.1	5.4	11.0	10.7	0.97
PS	22.8	6.3	6.1	12.7	10.8	0.85
PVA	20.9	11.3	9.6	13.7	14.5	1.06
Chloroform	17.8	3.1	5.7	-	-	-
EC	19.0	5.6	4.9	7.9	3.56	0.45
PMMA	17.9	10.1	5.4	11.0	7.01	0.64
PS	22.8	6.3	6.1	12.7	10.5	0.82
PVA	20.9	11.3	5.7	13.7	11.0	0.80

Table 3.5 (Continue)

Polymer and solvent	Hansen solubility parameter, HSP $(MPa)^{1/2}$			R_0	R_a	RED (R_a/R_0)
	δ_D	δ_P	δ_H			
Dichloromethane	18.2	6.3	6.1	-	-	-
EC	19.0	5.6	4.9	7.9	2.12	0.27
PMMA	17.9	10.1	5.4	11.0	3.91	0.36
PS	22.8	6.3	6.1	12.7	9.39	0.74
PVA	20.9	11.3	5.7	13.7	8.1	0.59

3.3.3 Volatile Organic Compound Discrimination by Principal Component Analysis

In this section, the potential use of polymer/SWNT sensors for VOC discrimination was explored. Pristine SWNT-based sensor was highly sensitive to ethanol, but exhibited similar response magnitudes for acetone and methanol, and was nearly insensitive to dichloromethane. The enhancement of sensitivity to dichloromethane was successfully obtained using PMMA/SWNT as shown in section 3.3.2. In addition, pristine SWNT, thiophene/SWNT and PMMA/SWNT upon exposure to dichloromethane, acetone and methanol show different patterns of sensor response. The normalized sensor response of thiophene/SWNT and PMMA/SWNT upon methanol exposure are different magnitude. Thus, pristine SWNT-, pristine SWNT-, PMMA/SWNT- and thiophene/SWNT-based sensors were focused for dichloromethane, acetone and methanol discrimination. The pattern recognition of dichloromethane, acetone and methanol were studied using principal component analysis (PCA) to statistical process the sensor response data of each sensor. Fig. 3.11 shows the PC1-PC2 map after PCA data processing of sensor array exposed to dichloromethane, acetone and methanol. PC1 and PC 2 are the most and the second-most variation, respectively. All the vapors have been successfully classified into distinct groups. These results demonstrate that using thiophene- and PMMA-coated on the pristine SWNT network is a promising approach for effective VOC discrimination.

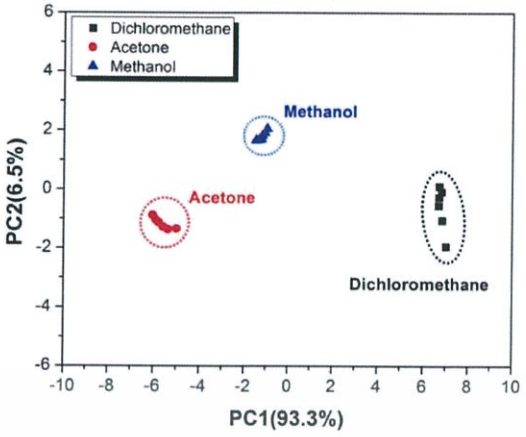

Figure 3.11 PCA plots of dichloromethane, acetone and methanol vapors.

The selectivity is an important feature of gas sensor for real-time monitoring. The air in atmosphere is composed of different gases, i.e., mixed gases. Even though the gas sensor responds to the target gas, it also possibly responds to some interference gases with a lower response. To overcome, these drawbacks of the interference gas sensing, it is necessary to study the cross-sensitivity characteristics of the sensors. The database of the patterns of the sensor responses to mixing gases should be collected. Finally, the PCA should be plotted based on the response data of the single gas and mixed gases. The pattern of the mixed gases will be shown between the data of single gas. The comparison of pattern recognition between single gas and mixed gases could predict the kind of mixed gases.

3.4 Summary

A simple sensor based on pristine SWNT for VOC detection with improved sensitivity and selectivity was fabricated by coating SWNTs with monomer and polymer. The monomer- or polymer-coated SWNT sensor was fabricated by spin-coating method. The results showed that EC/SWNT greatly improved the sensor response to benzene, chloroform and dichloromethane 4.28-, 14.74- and 59.01-fold, respectively compared to that of pristine SWNT. While the polymer-coated SWNT reduced the responses to acetone, ethanol and methanol vapors. The sensing mechanism could be attributed to polymer swelling and HSP. Moreover, the VOC discrimination was successfully performed by pristine SWNT, thiophene/SWNT and

PMMA/SWNT sensors using PCA technique. PCA clearly showed the discrimination between of dichloromethane, acetone and methanol vapors. The integration of pristine SWNTs with monomer or polymer is a promising approach for improving the sensitivity and selectivity for VOC detection at room temperature.

CHAPTER 4

METAL NANOPARTICLE-FUNCTIONALIZED SINGLE-WALLED CARBON NANOTUBE FOR VOLATILE ORGANIC COMPOUNDS DETECTION

This chapter describes the fabrication of gas sensor from pristine single-walled carbon nanotube (SWNT) and hybrid materials based on metal nanoparticle (NP)-functionalized SWNT. Metal NP-coated SWNTs were prepared by electron-beam (EB) deposition. Morphology and structure of sensing materials were characterized by transmission electron microscopy (TEM) and Raman spectroscopy. The sensing performances to volatile organic compound (VOC) were investigated in terms of sensitivity and selectivity.

4.1 Fabrication of Gas Sensor Based on Polymer-Functionalized Carbon Nanotubes

The preparation of sensor platform prepared by the process explained in section 3.1.1. To form metal NP with uniform diameter on the predropped SWNT network which prepared by the process explained in section 3.1.2, gold (Au), palladium (Pd) and platinum (Pt) pellets were used as targets for EB deposition. A quartz crystal oscillator was used to monitor the film thickness. The base pressure was less than 3×10^{-6} mbar. The temperature of PCB substrate during metal deposition was kept at 100 °C. The metal NPs were deposited onto the predropped SWNT network. The amount of the deposited metal NPs was monitored by a quartz crystal oscillator embedded in the electron-beam evaporation equipment. The amount of the deposition metal NPs was referred from the quartz crystal oscillator as the thickness of 5 nm. The metal elements used in this research are shown in Table 4.1. The schematic view of pristine SWNT and metal NP/SWNT sensors are shown in Fig. 4.1.

Table 4.1 List of metal elements and their purity.

Metal element	Purity (%)
Gold (Au)	99.999
Palladium (Pd)	99.999
Platinum (Pt)	99.999

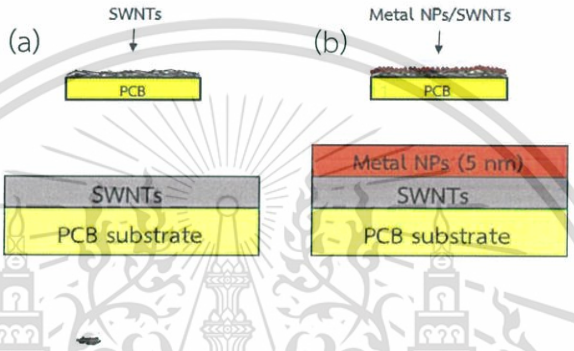

Figure 4.1 Schematic view of (a) SWNTs and (b) metal NPs/SWNTs sensors.

4.2 Morphology and Structural Characterization of Sensing Materials

4.2.1 Transmission Electron Microscopy Characterization

The morphologies of the pristine SWNT and metal NPs/SWNT were transmission electron microscopy (TEM; JEOL JE-2010) was employed to characterize the nanostructure of the metal NPs/SWNT. For sample preparation, SWNTs suspension from the process explained in section 3.1.2 was drop-casted onto copper (Cu) grid. Next, the metal NPs were directly decorated onto pre-dropped SWNT network on Cu grid by the process explained in section 4.1. The carbon structure, purity and crystallinity of pristine SWNT and metal NPs/SWNT were analyzed by Raman spectroscopy (Thermo SCIENTIFIC DXR) with an Ar ion laser wavelength of 532 nm (2.33 eV). Fig. 4.2(a-c) shows the TEM images of the Au, Pd and Pt-decorated SWNT, respectively.

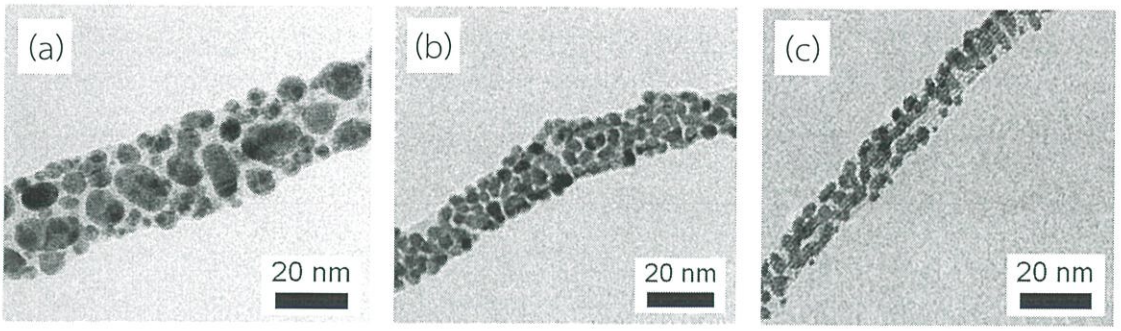

Figure 4.2 TEM images of (a) Au, (b) Pd and (c) Pt-decorated SWNT.

Fig. 4.2(a-c) shows the TEM images of the Au, Pd and Pt-decorated SWNT, respectively. The metal NPs were attached to the sidewalls of pristine SWNT bundles, whereas the SWNT bundles maintained their structure. The average diameters of the Au, Pd and Pt on SWNT were 7.11±2.76, 5.77±1.16 and 4.01±0.77 nm, respectively. The Pt NPs on SWNT exhibited a narrower size distribution compare to those of Au and Pd NPs.

4.2.2 Raman Spectroscopy Characterization

The carbon structure, purity and crystallinity of pristine SWNT and metal NPs/SWNT were analyzed by Raman spectroscopy (Thermo SCIENTIFIC DXR) with an Ar ion laser wavelength of 532 nm (2.33 eV). Figure 4.3 shows Raman spectra of pristine SWNT, Au-, Pd- and Pt-decorated SWNT. Raman spectroscopy was utilized to characterize the structure, purity and crystallinity of pristine SWNT and metal NPs-decorated SWNT. Fig. 4.3 shows the four significant Raman peaks: SWNT-derived Raman breathing mode (RBM) at 190 and 273 cm^{-1}, disorder carbon-derived D-band at 1332 cm^{-1} and graphitic-structure-derived G-band at 1588 cm^{-1}. The intensity ratio between the G- and D-bands (I_G/I_D) of pristine SWNT was approximately 14.03±1.20. After metal NPs-decoration, the I_G/I_D ratio of Au/SWNT, Pd/SWNT and Pt/SWNT were significantly decreased to 6.01±0.18, 9.52±1.01 and 10.97±1.45, respectively, implying that the crystallinity and purity of SWNT deteriorated. The decrease in the I_G/I_D value could be attributed to the damage during metal NPs adhesion on the SWNT with high energy.

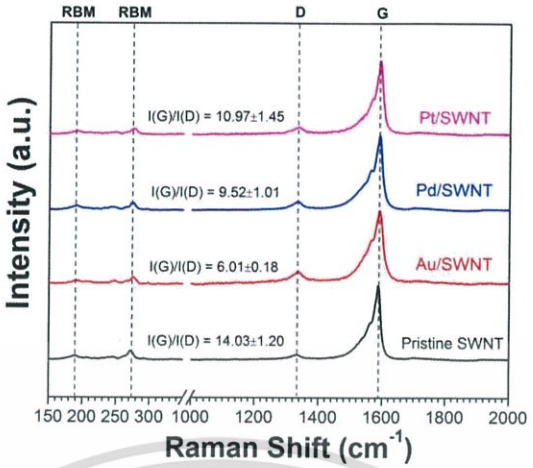

Figure 4.3 Raman spectra of pristine SWNT, Au-, Pd- and Pt-decorated SWNT.

4.3 Sensor performance of metal nanoparticles-functionalized carbon nanotubes

4.3.1 Gas Sensor Measurement System

The sensor response to VOC vapor was investigated at room temperature by recording the electrical resistance using a FLUKE NetDAQ during cycles of alternating supply of dry N_2 gas and VOC vapor. The sensor response to VOC vapor was investigated at by process explained in section 3.3.1. The sensor response (*SR*) and normalized sensor response (*NSR*) were calculated by equation (3.1) and (3.2), respectively. The schematic views of the setup of the sensor measurement system and the profile of gas flow are used by process explained in Fig. 3.4 and 3.5, respectively. The conditions for gas sensor measurement are summarized in Table 4.2.

Table 4.2 Conditions for gas sensing characterization.

Volatile organic compounds:	Acetone, ethanol, methanol, benzene, chloroform, dichloromethane
Concentration:	Benzene (124-161 ppt*)
	Chloroform (420-457 ppt)

Table 4.2 (Continued)

	Dichloromethane (523-638 ppt)
	Acetone (2415-2922 ppt)
	Ethanol (134-162 ppt)
	Methanol (268-276 ppt)
Temperature of the VOC liquid:	90% of boiling point
N_2 flow rate for baseline:	3.0 lpm
N_2 flow rate for VOC bubbling:	1.5 lpm
Operation temperature:	Room temperature (25 °C)
Pressure:	Atmospheric pressure

*Parts per thousand: ppt

4.3.2 Sensor Response of Metal Nanoparticles-Functionalized Single-Walled Carbon Nanotube to Volatile Organic Compound

The performance of the fabricated pristine SWNT, and metal NP/SWNT sensors were investigated. The initial resistance of pristine SWNT and metal NP/SWNT are summarized in table 4.3. Fig. 4.4 shows sensor response as a function of time for pristine SWNT and metal NP-decorated SWNT upon VOC exposure. Fig. 4.5 shows normalized sensor response of pristine SWNT and metal NP-decorated toward VOCs.

Table 4.3 Initial resistance of SWNT and metal NP/SWNT.

Sensor	Initial resistance (kΩ)
Pristine SWNT	95.92 ± 8.20
Au/SWNT	25.78 ± 5.01
Pd/SWNT	12.19 ± 4.03
Pt/SWNT	0.34 ± 0.02

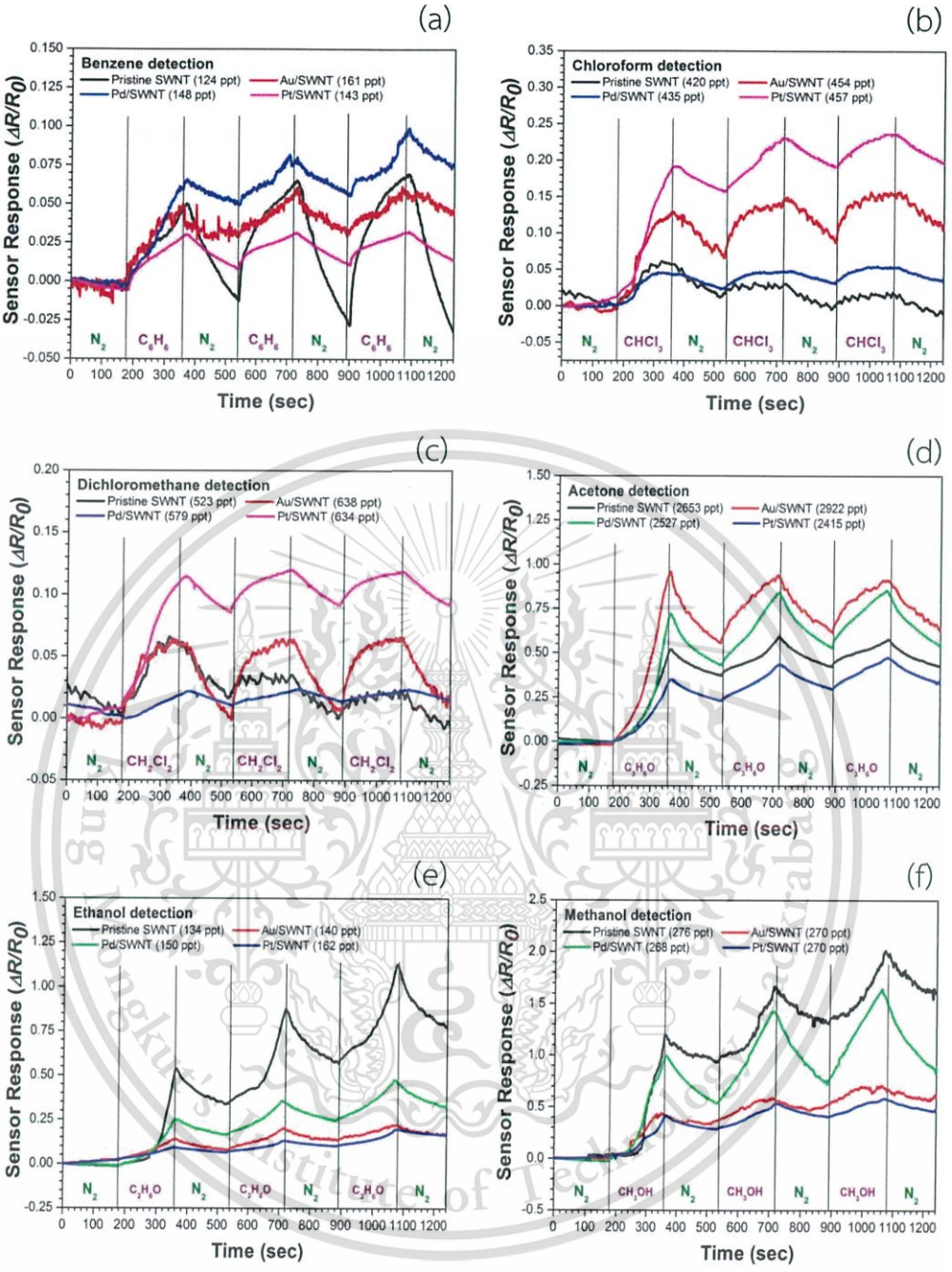

Figure 4.4 Sensor response as a function of time for pristine SWNT and metal NP-decorated SWNT toward (a) benzene (b) chloroform (c) dichloromethane (d) acetone (e) ethanol and (f) methanol.

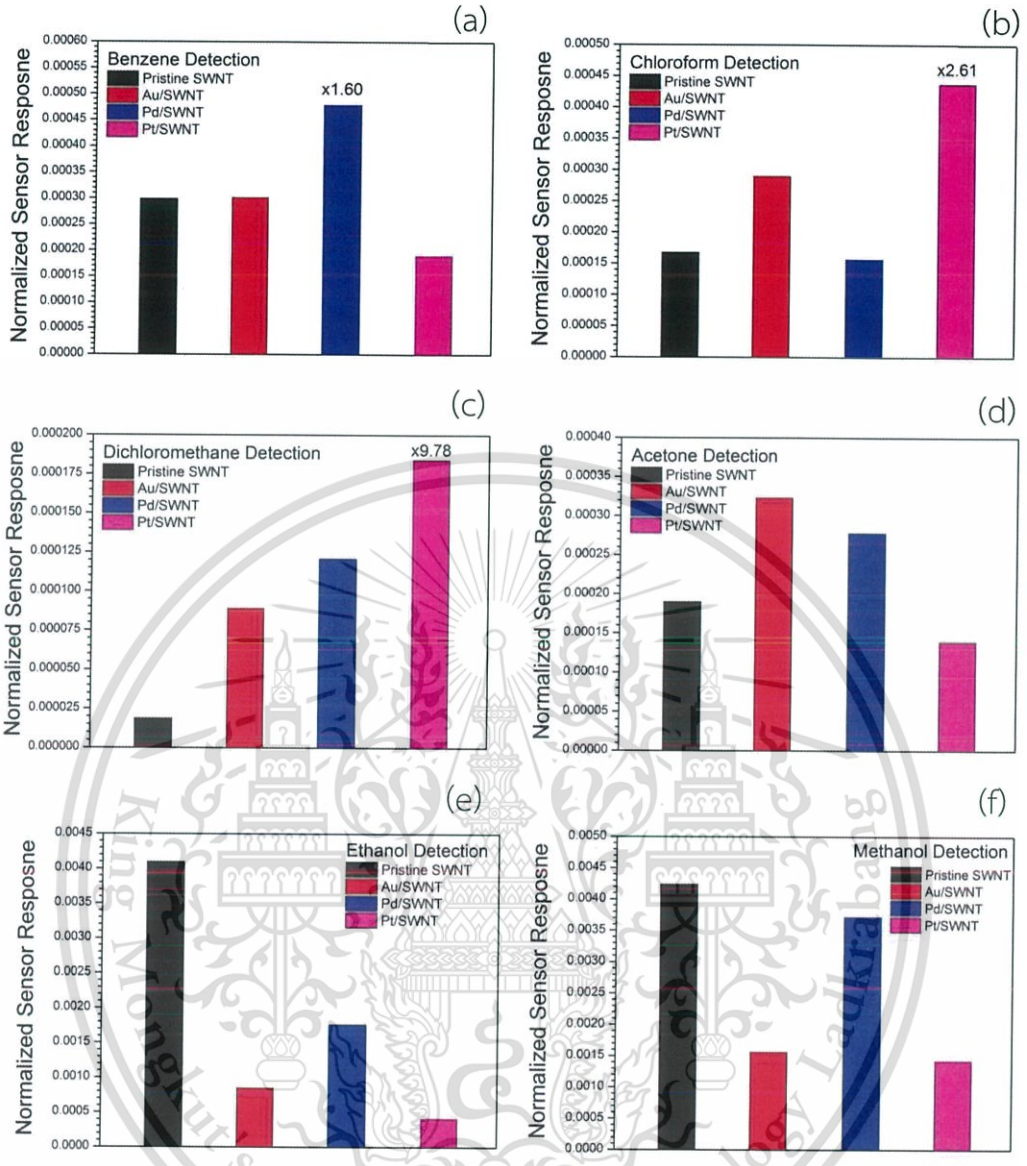

Figure 4.5 Normalized sensor response of pristine SWNT and metal NP/SWNT toward (a) benzene (b) chloroform (c) dichloromethane (d) acetone (e) ethanol and (f) methanol.

Fig. 4.4(a-f) shows the sensor responses as a function of time of pristine SWNT and metal NPs/SWNT sensors under alternating supply of benzene, chloroform, dichloromethane, acetone, ethanol and methanol and N_2 gas for 3 cycles. Fig. 4.5(a-f) shows the normalized sensor response of pristine SWNT and metal NPs/SWNT sensors to VOCs. The electrical resistance of all sensors increased upon VOC exposure and decreased after replacing VOC with N_2 gas (Fig. 4.4(a-f)). All sensors were hardly recovered to their initial resistances. The response characteristics between sensor

materials and VOC molecule may be attributed chemisorption. VOC molecules seem to strongly interact with the sensor materials through chemisorption, which is relatively strong interaction, resulting in difficultly in removing VOC molecule from sensor material. For benzene detection, the normalized sensor response of Pd/SWNT greatly increased 1.60-fold higher than that of pristine SWNT (Fig. 4.5(a)), while chloroform and dichloromethane detections, the normalized sensor response of Pt/SWNT greatly increased 2.61- and 9.78-fold higher than that of pristine SWNT, respectively (Fig. 4.5(b-c)),. In addition, the normalized sensor response of Au/SWNT greatly increased 1.70 higher than that of pristine SWNT upon acetone exposure (Fig. 4.5(d)). However, metal NPs-decorated SWNT reduced the responses to ethanol and methanol (Fig. 4.5(e-f)).

The sensing mechanism of metal NPs-decorated SWNT, we envision that the sensing mechanism of metal NPs/SWNT toward VOC is similar to that of Pt-deposited SWNTs toward CO systems [57]. The mechanism is based on the dissociation of VOC to CO and subsequently CO oxidation on the metal catalyst surface. The surface of the metal catalyst is saturated with chemisorbed O_2 molecules under atmospheric pressure [82], whereas some O_2 molecules are dissociated into O^- on the surface of metal catalyst. Upon exposure to VOC, VOC molecule reacts with the pre-adsorbed O_2 and dissociate on the metal catalyst surface according to the reaction [83] for benzene, chloroform, dichloromethane and acetone as shown in equation (4.1)-(4.4), respectively. Consequently, interacts with O^- by reaction via the Langmuir-Hinshelwood mechanism [57,58] as shown in equation (4.5). Finally, the electron captured by pre-adsorbed O^- is released and donated to the p-type semiconducting SWNT, resulting in an increase in electrical resistance. Fig. 4.6 shows a schematic view of sensing mechanism of metal NPs/polymer/SWNT upon VOC exposure.

$$2C_6H_6(g) + 9O_2(ad) \rightarrow 12CO(g) + 6H_2O \quad (4.1)$$

$$4CHCl_3(g) + 3O_2(ad) \rightarrow 4CO(g) + 2H_2O + 6Cl_2 \quad (4.2)$$

$$CH_2Cl_2(g) + (1/2)O(ad) \rightarrow CO(g) + 2HCl \quad (4.3)$$

$$2C_3H_6O(g) + 5O_2(ad) \rightarrow 6CO(g) + 6H_2O \quad (4.4)$$

$$CO(ad) + O^-(ad) \rightarrow CO_2(g) + e^- \quad (4.5)$$

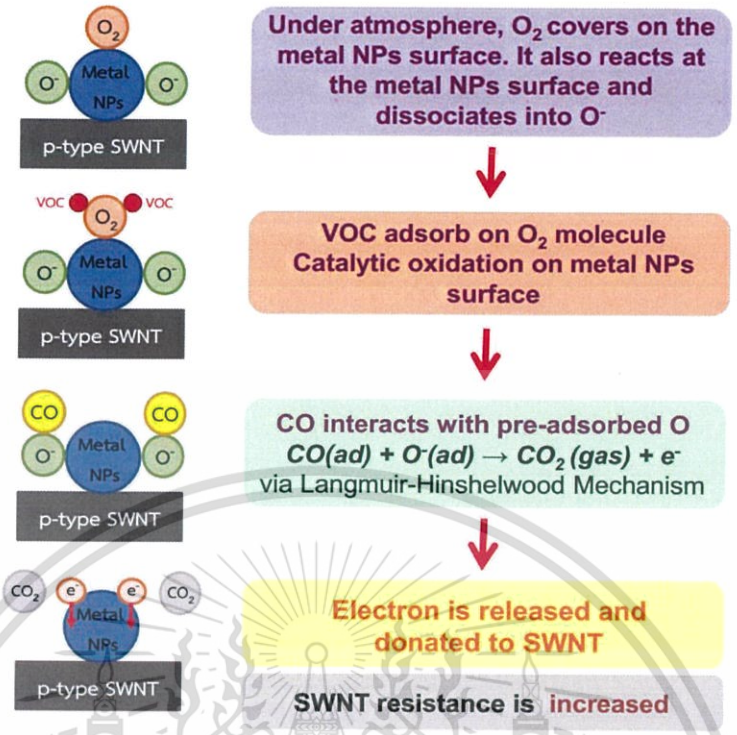

Figure 4.6 Sensing mechanism of metal NPs/polymer/SWNT upon VOC exposure.

4.4 Summary

Gas sensor using pristine SWNT and metal NPs-decorated SWNT was developed for VOC detection under room temperature. The metal NPs-coated SWNT sensor was fabricated by drop-casting and EB evaporation methods. The results showed that Pd/SWNT greatly improved the response to benzene 1.60-fold, while Pt/SWNT greatly improved responses to chloroform and dichloromethane 2.61- and 9.78-fold, respectively. In addition, Au/SWNT greatly improved response to acetone 1.70-fold. The sensing mechanism was elucidated by catalytic oxidation on the metal catalyst surface. The integration of pristine SWNT with metal NPs is a promising approach for improving the sensitivity and selectivity for VOC detection.

CHAPTER 5

POLYMER AND METAL NANOPARTICLE-FUNCTIONALIZED SINGLE-WALLED CARBON NANOTUBE FOR VOLATILE ORGANIC COMPOUNDS DETECTION

Gas sensor based on polymer-coated or metal nanoparticles (NPs)-decorated single-walled carbon nanotube (SWNT) greatly improved the response to volatile organic compound (VOC). In this chapter, we proposed the new type gas sensor based on dual-functionalized SWNTs through polymer coating and metal NP deposition. Morphology and structure of sensing materials were characterized by field emission scanning electron microscopy (FESEM), transmission electron microscopy (TEM), Fourier transform infrared spectroscopy (FTIR), Raman spectroscopy, and X-ray diffraction (XRD). The sensing performances to benzene, chloroform and dichloromethane were investigated in terms of sensitivity and selectivity. The sensing mechanism of polymer/SWNT were investigated by fluorescence spectrometer.

5.1 Fabrication of Gas Sensor Based on Metal Nanoparticles/Polymer-Functionalized Carbon Nanotubes

The hybrid sensor based on metal nanoparticle/polymer-functionalized carbon nanotubes were fabricated by considering the sensitivity of polymer/SWNT and metal NPs/SWNT sensors. The types of polymer and metal NPs for dual- functionalized SWNTs were selected by the highest sensitivity of polymer and metal NPs for each VOC. To fabricate hybrid sensor, ethyl cellulose (EC) was selected as polymer-coated SWNT due to the highest sensitivity for benzene, chloroform and dichloromethane. EC solution was spin coated on to the predropped SWNT network by the condition of spin coating is following in section 3.1. EC concentration was varied between 1 and 5 wt%. Next, palladium (Pd) and platinum (Pt) were selected as metal NPS due to the highest sensitivity for benzene, chloroform and dichloromethane. The metal NPs were decorated by electron-beam (EB) evaporation on to EC-coated CNT by the condition of EB evaporation is following in section 4.1. The amount of the deposited metal NPs was monitored by a quartz crystal oscillator embedded in the EB evaporation equipment. The thickness was varied at 2 and 5 nm. For comparison, SWNT with only EC coating or Pd and Pt NP decoration were also fabricated. The details of the

fabricated gas sensor is shown in Table 5.1. The schematic view of pristine SWNT, polymer/SWNT, metal NPs/SWNT and metal NPs/polymer/SWNT are shown in Fig. 5.1.

Table 5.1 Summary of sensors based on hybrid SWNTs.

Sensor configuration
SWNT
EC(1 wt%)/SWNT
EC(5 wt%)/SWNT
Pd(2 nm)/SWNT
Pd(5 nm)/SWNT
Pt(2 nm)/SWNT
Pt(5 nm)/SWNT
Pd(2 nm)/EC(1 wt%)/SWNT
Pd(2 nm)/EC(5 wt%)/SWNT
Pd(5 nm)/EC(1 wt%)/SWNT
Pd(5 nm)/EC(5 wt%)/SWNT
Pt(2 nm)/EC(1 wt%)/SWNT
Pt(2 nm)/EC(5 wt%)/SWNT
Pt(5 nm)/EC(1 wt%)/SWNT
Pt(5 nm)/EC(5 wt%)/SWNT

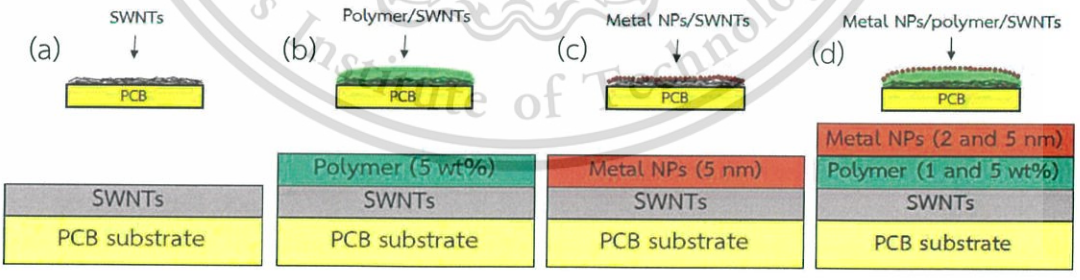

Figure 5.1 Schematic view of (a) SWNTs, (b) polymer/SWNTs, (c) metal NP/SWNTs and (d) metal NPs/polymer/SWNTs sensors.

5.2 Morphology and Structural Characterization of Sensing Materials

5.2.1 Scanning Electron Microscopy Characterization

The morphologies of the pristine SWNT and EC/SWNT were characterized by field emission scanning electron microscopy (FESEM; JEOL JSM-7800F). The FESEM observation was carried out in a high vacuum mode with a base pressure of approximately 9×10^{-5} Pa and an acceleration voltage of 1 kV without any surface treatment with metallic materials. The elemental composition of Pd/EC/SWNT and Pt/EC/SWNT were studied by FESEM equipped with an energy dispersive X-ray spectrometer (EDS; OXFORD). The samples for FESEM and EDS analysis were prepared by the process explained in sections 3.1, 4.1 and 5.1 using silicon (Si) as a substrate instead of the printed circuit board (PCB). Fig. 5.2(a-b) shows FESEM images of EC(1 wt%)/SWNT and EC(5 wt%)/SWNT.

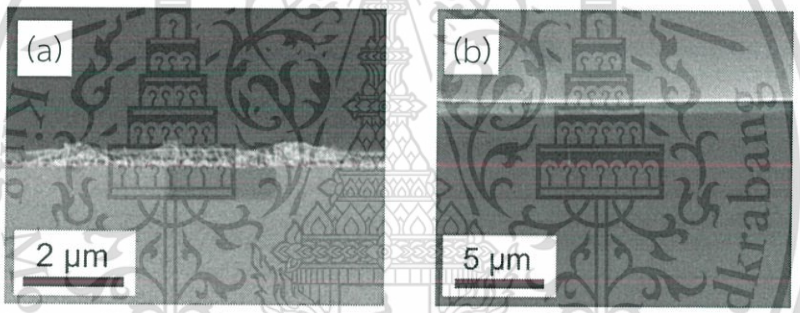

Figure 5.2 FESEM images of (a) EC(1 wt%)/SWNT and (b) EC(5 wt%)/SWNT.

Fig. 5.2(a-b) shows the cross-sectional FESEM images of EC(1 wt%)/SWNT and EC(5 wt%)/SWNT, respectively. The thickness of the EC(1 wt%)/SWNT and EC(5 wt%)/SWNT coatings on the SWNTs were 0.41±0.08 and 5.50±0.01 μm, respectively. For EC(1 wt%)/SWNT (Fig. 5.2(a)), the SWNT bundles were protruding from the EC surface. However, in the case of EC(5 wt%)/SWNT (Fig. 5.2(b)), EC completely covered the pristine SWNT network. The thickness of the EC film was controlled by the concentration and viscosity of the EC solution.

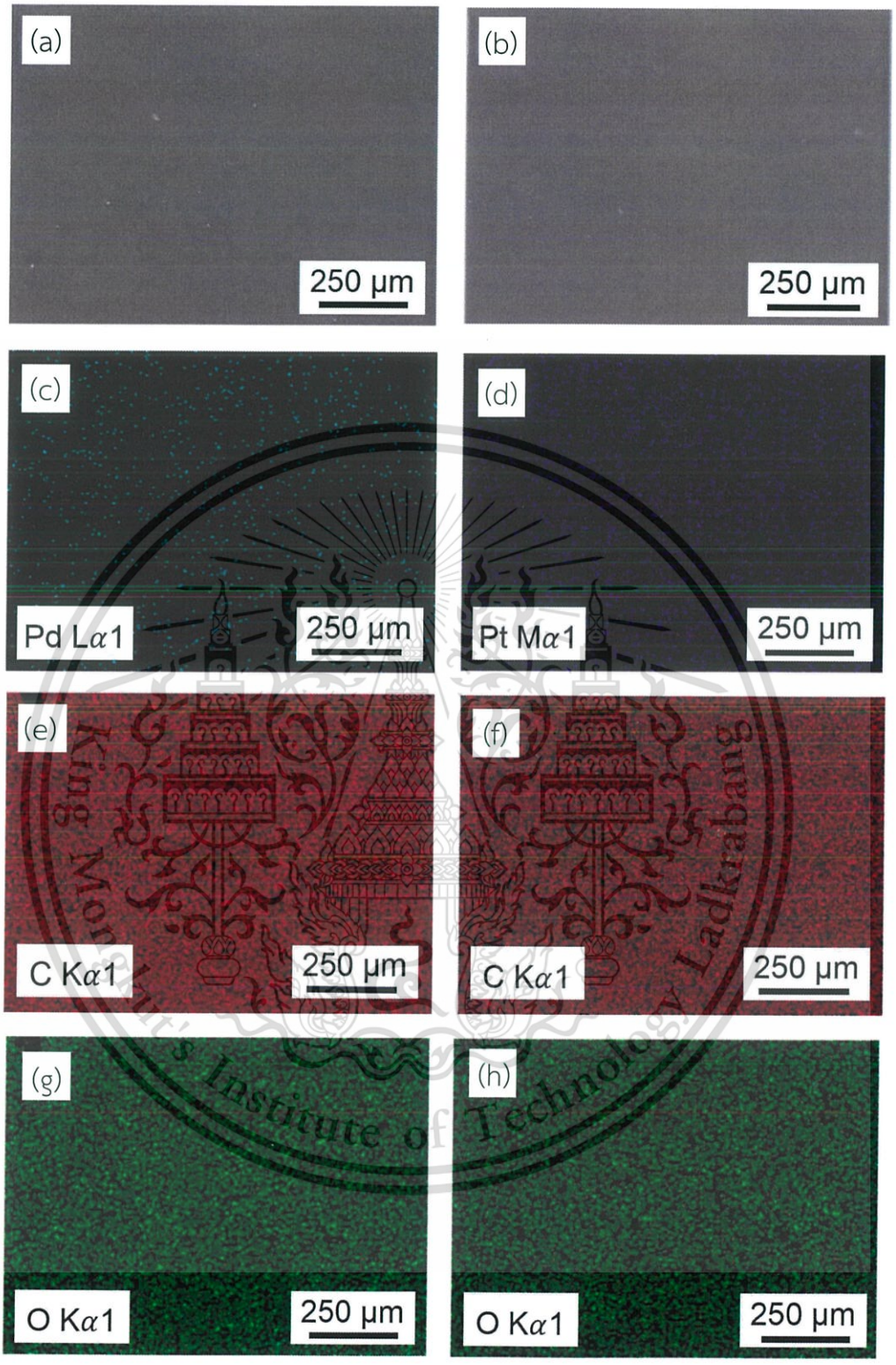

Figure 5.3 FESEM of (a) Pd(5 nm)/EC(5 wt%)/SWNT, EDS mapping of (c) palladium, (e) carbon, and (g) oxygen elements. FESEM of (b) Pt(5 nm)/EC(5 wt%)/SWNT, EDS mapping of (d) platinum, (f) carbon, and (h) oxygen elements.

The elemental composition of Pd(5 nm)/EC(5 wt%)/SWNT and Pt(5 nm)/EC(5 wt%)/SWNT were determined by EDS. The analyzed surface area for EDS mapping of Pd(5 nm)/EC(5 wt%)/SWNT and Pt(5 nm)/EC(5 wt%)/SWNT are show in Fig. 5.3(a) and 5.3(b), respectively. The EDS element mapping image revealed that Pd(5 nm)/EC(5 wt%)/SWNT consists of Pd (in blue), carbon (in red) and oxygen (in green) are show in Fig 5.3(c), (e) and (g), respectively, while the Pt(5 nm)/EC(5 wt%)/SWNT consists of Pt (in purple), carbon (in red) and oxygen (in green) are show in Fig 5.3(d), (f) and (h), respectively. The Pd or Pt mapping clearly indicates that the Pd and Pt NPs are homogenous distributed on the sensor Pd(5 nm)/EC(5 wt%)/SWNT and Pt(5 nm)/EC(5 wt%)/SWNT as shown in Fig. 5.3(c) and (d), respectively. Carbon and oxygen elements may be derived from SWNT and EC.

5.2.2 Transmission Electron Microscopy Characterization

The morphologies of the pristine SWNT, Pd/SWNT and Pt/SWNT were transmission electron microscopy (TEM; JEOL JE-2010) was employed to characterize the nanostructure of the metal NPs/SWNT. For sample preparation, SWNTs suspension from the process explained in section 3.1 was drop-casted onto copper (Cu) grid. Next, the metal NPs were directly decorated onto pre-dropped SWNT network on Cu grid by the process explained in section 4.1. The thickness was varied at 2 and 5 nm.

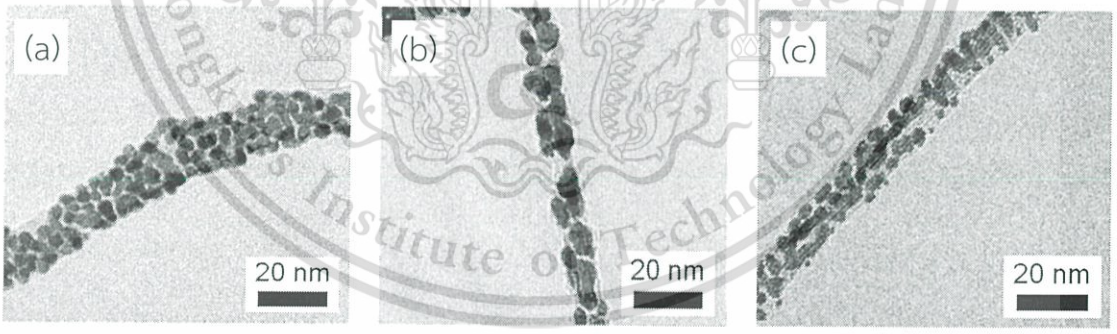

Figure 5.4 TEM images of (a) Pd(5 nm)/SWNT, (b) Pt(2 nm)/SWNT and (c) Pt(5 nm/ SWNT).

Fig. 5.4(a-c) shows the TEM images of Pd(5nm)/SWNT, Pt(2 nm)/SWNT and Pt(5 nm)/SWNT, respectively. The metal NPs were attached to the sidewalls of pristine SWNT bundles, whereas the SWNT bundles maintained their structure. The average diameters of Pd(5 nm)/SWNT, Pt(2 nm)/SWNT and Pt(5 nm)/SWNT were 5.77±1.16,

3.53±0.94 and 4.01±0.77 nm, respectively. Pt(5 nm)/SWNT show the higher distribution and greater coverage than that of sensor Pt(2 nm)/SWNT and greater.

5.2.3 Fourier Transform Infrared Spectroscopy Characterization

The functional group of EC was characterized by Fourier transform infrared spectroscopy (FTIR; Perkin Elmer, Spectrum One). The FTIR sample was prepared by mixing SWNTs powder with potassium bromide (KBr) and pressing in a pellet form. Then, the prepared pellet was coated and decorated with EC, Pd NPs and Pt NPs, respectively. Typical FTIR spectra in a transmittance mode were scanned in a wavenumber range of 500-4000 cm^{-1}.

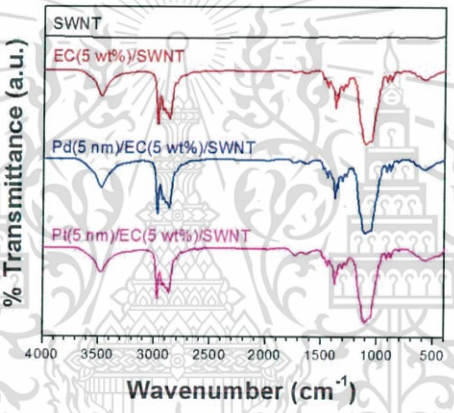

Figure 5.5 FTIR spectra of SWNT, EC(5 wt%)/SWNT, Pd(5 nm)/EC(5 wt%)/SWNT and Pt(5 nm)/EC(5 wt%)/SWNT.

To confirm the EC existence in the Pd(5 nm)/EC(5 wt%)/SWNT and Pt(5 nm)/EC(5 wt%)/SWNT, the samples were characterized by FTIR. Fig. 5.5 show FTIR spectra of SWNT, EC(5wt%)/SWNT, Pd(5 nm)/EC(5wt%)/SWNT and Pt(5 nm)/EC(5 wt%)/SWNT. FTIR spectra of EC(5 wt%), Pd(5 nm)/EC(5 wt%)/SWNT and Pt(5 nm)/EC(5 wt%)/SWNT show almost identical feature. The peak assigned to the –OH stretching vibration occurred at 3480 cm^{-1}. The peak at 2850-2960 cm^{-1} is assigned to –CH stretching vibration. The peak at 1450 cm^{-1} correspond to $-CH_3$ stretching vibration. The peak observed at 1375 cm^{-1} is $-CH_2$ stretching vibration and the peak at 1065 cm^{-1} is attributed to the C-O-C stretching vibration [84,85]. This results confirms the existence of EC and the same composition of the functional group of EC before and after Pd or Pt depositions.

5.2.3 X-ray Diffraction Characterization

The crystal structure of polymer/SWNT, metal NPs/SWNT and metal NPs/polymer/SWNT were characterized by X-ray diffraction (XRD; Rigaku TTRAX II) using Cu Kα with a wavelength of 1.54 Å at a scan rate of 1 °/min. The samples for XRD analysis were prepared by the process explained in sections 3.1, 4.1 and 5.1 using silicon (Si) as a substrate instead of the PCB.

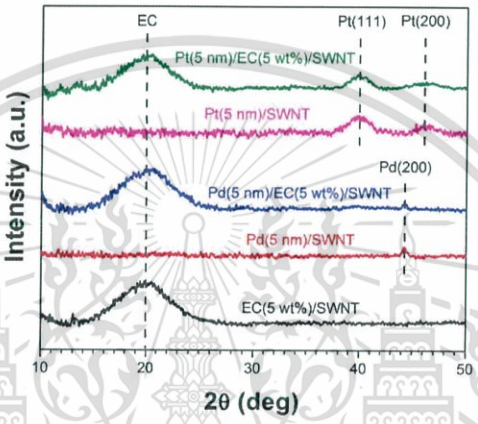

Figure 5.6 XRD spectra of EC(5 wt%)/SWNT, Pd(5 nm/SWNT), Pt(5 nm)/SWNT, Pd(5 nm)/EC(5 wt%)/SWNT and Pt(5 nm)/EC(5 wt%)/SWNT.

To confirm the crystallinity, the sample was characterized by XRD. The typical XRD diffraction patterns of EC(5 wt%)/SWNT, Pd(5 nm)/SWNT, Pt(5 nm)/SWNT, Pd(5 nm)/EC(5 wt%)/SWNT and Pt(5 nm)/EC(5 wt%)/SWNT are show in Fig. 5.6. EC(5 wt%)/SWNT exhibited a board peak at ~20°, which corresponds to the structure of EC [86,87]. The diffraction peaks of Pd(5 nm)/SWNT located at 44.3° can be assigned to the reflection from then (200) plane of the face-centered cubic Pd [88,89], whereas the diffraction peaks of Pt(5 nm)/SWNT located at 39.7° and 46.2° can be assigned to reflections from the (111) and (200) planes of the face-centered cubic Pt, respectively [90,91]. For Pd(5 nm)/EC(5 wt%)/SWNT and Pt(5 nm)/EC(5 wt%)/SWNT, the diffraction pattern shows diffraction peak from EC at ~20° and diffraction peak from Pd NPs at 44.3° and Pt NPs at 39.7° and 46.2° , respectively, confirming the existence of EC and metal NPs.

5.2.4 Raman Spectroscopy Characterization

The carbon structure, purity and crystallinity of pristine SWNT, polymer/SWNT, metal NPs/SWNT and metal NPs/polymer/SWNT were analyzed by Raman spectroscopy (Thermo SCIENTIFIC DXR) with an Ar ion laser wavelength of 532 nm (2.33 eV).

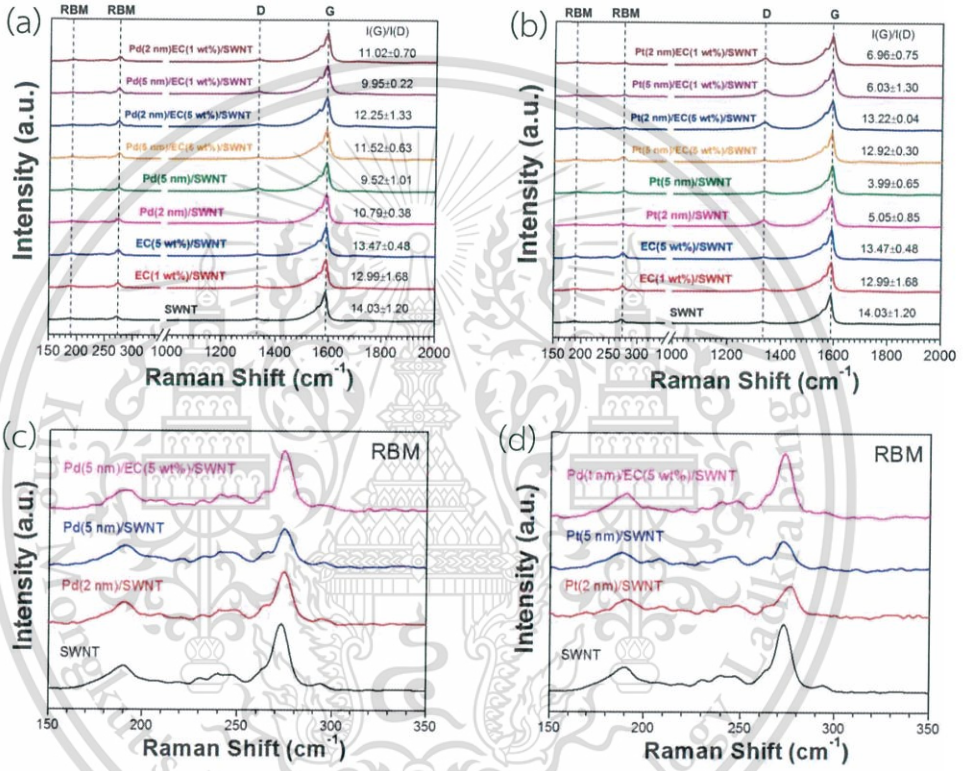

Figure 5.7 Raman spectra of (a) pristine SWNT, EC/SWNT, Pd/SWNT and Pd/EC/SWNT and (b) pristine SWNT, EC/SWNT, Pt/SWNT and Pt/EC/SWNT. RBM spectra of (c) SWNT, Pd(2 nm)/SWNT, Pd(5 nm)/SWNT and Pd(5 nm)/EC(5 wt%)/SWNT, and (d) SWNT, Pt(2 nm)/SWNT, Pt(5 nm)/SWNT, Pt(5 nm)/EC(5 wt%)/SWNT.

Raman spectroscopy was utilized to characterize the structure, purity and crystallinity of pristine SWNT. Fig. 5.7(a-b) shows the four significant Raman peaks: SWNT-derived Radial breathing mode (RBM) at 190 and 273 cm^{-1}, disorder carbon-derived D-band at 1332 cm^{-1} and graphitic-structure-derived G-band at 1588 cm^{-1}. After EC coating, the I_G/I_D ratio of sensor EC(1 wt%)/SWNT and EC(5 wt%)/SWNT were 12.99±1.68 and 13.47±0.48, respectively, with no obvious difference from the pristine

SWNTs. However, after Pd and Pt decoration, the I_G/I_D ratio of Pd(2 nm)/SWNT, Pd(5 nm)/SWNT, Pt(2 nm)/SWNT and Pt(5 nm)/SWNT were significantly decrease to 10.79±0.38, 9.52±1.01, 5.05±0.85, and 3.99±0.65, respectively, implying that the crystallinity and purity of the SWNTs deteriorated, especially for Pd(5 nm)/SWNT and Pt(5 nm)/SWNT in which highest amount of Pd or Pt NPs show the lowest I_G/I_D value. The decrease in the I_G/I_D value could be attributed to the damage during metal NPs adhesion on the SWNTs with high energy.

For hybrid sensor, the I_G/I_D value of Pd(2 nm)/EC(5 wt%)/SWNT, Pd(5 nm)/EC(5 wt%)/SWNT were greater than those of Pd(2 nm)/SWNT, Pd(5 nm)/SWNT, Pd(2 nm)/EC(1 wt%)/SWNT and Pd(5 nm)/EC(1 wt%)/SWNT, and the I_G/I_D value of Pt(2 nm)/EC(5 wt%)/SWNT, Pt(5 nm)/EC(5 wt%)/SWNT were greater than those of Pt(2 nm)/SWNT, Pt(5 nm)/SWNT, Pt(2 nm)/EC(1 wt%)/SWNT and Pt(5 nm)/EC(1 wt%)/SWNT, indicating higher crystallinity and purity of the SWNTs. These results show that thick film of EC effectively protects the SWNTs during metal NPs deposition. These results clearly confirm that EC can act as a protective layer on a SWNTs during metal NPs deposition. Fig. 5.7(c-d) show RBM spectra of pristine SWNT, Pd/SWNT, Pt/SWNT, Pd/EC/SWNT and Pt/EC/SWNT sensors. The intensity of the RBM peak at 273 cm^{-1} and the I_G/I_D ratios of Pd(2 nm)/SWNT, Pd(5 nm)/SWNT, Pt(2 nm)/SWNT and Pt(5 nm)/SWNT gradually decreased with increasing amount deposited Pd or Pt NPs on the pristine SWNT, whereas those of Pd(5 nm)/EC(5 wt%)/SWNT and Pt(5 nm)/EC(5 wt%)/SWNT were relatively comparable to those of the pristine SWNT. The decrease in the RBM peak and I_G/I_D ratios of Pd(2 nm)/SWNT, Pd(5 nm)/SWNT, Pt(2 nm)/SWNT and Pt(5 nm)/SWNT are attributed to the damage of small-diameter SWNTs during Pd or Pt NPs adhesion with high energy. These results also clearly confirm that EC can act as a protective layer on SWNTs during Pd or Pt NPs deposition.

5.3 Sensor Performance of Metal Nanoparticles/Polymer-Functionalized Single-Walled Carbon Nanotubes

5.3.1 Gas Sensor Measurement System

The sensor response to VOC vapor was investigated at room temperature by recording the electrical resistance using a FLUKE NetDAQ during cycles of alternating supply of dry N_2 gas and VOC vapor. Benzene (C_6H_6), chloroform ($CHCl_3$) and dichloromethane (CH_2Cl_2) were used as VOC. The sensors were placed into the stainless steel chamber and N_2 gas was introduced into the chamber at a flow rate of 3.0 liters per minute (lpm) for 600 s as a baseline. Then, N_2 was replaced with VOC

vapor by bubbling liquid VOC with N_2 carrier gas at a flow rate of 1.5 lpm for 300 s. The sensors were recovered by purging with 3.0 lpm of N_2 for 600 s. The sensor response (*SR*) was calculation by equation (3.1). To compare the responses of all sensors, the sensor responses were normalized by the VOC concentration. The normalized sensor response (*NSR*) was defined as the ratio between the sensor response at a time of 900 s (SR_{900}) and the VOC concentration (C_{VOC}). The *NSR* were defined as shown in equation (5.1).

$$NSR = \frac{SR_{900}}{C_{VOC}} \tag{5.1}$$

The schematic views of the setup of the sensor measurement system and the profile of gas flow are shown in Fig. 3.4 and Fig. 5.8. The conditions for gas sensor measurement at ppt level is summarized in Table 5.2.

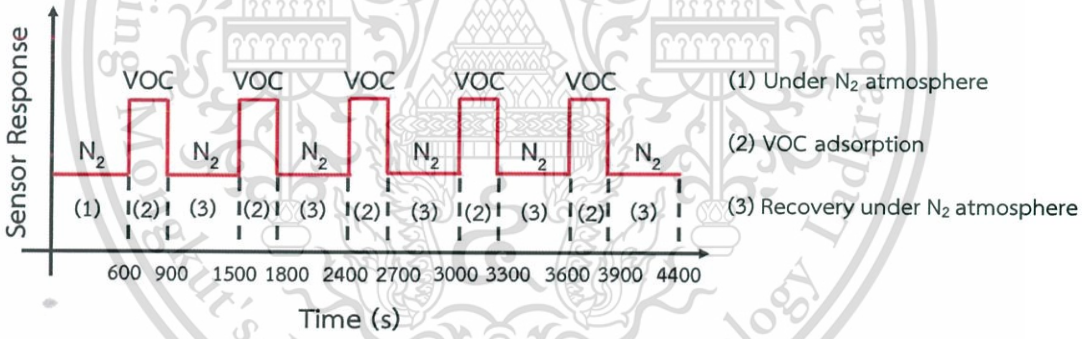

Figure 5.8 Schematic view of flow profile of gas sensor measurement.

Table 5.2 Conditions for gas sensing characterization.

Volatile organic compounds:	Benzene, chloroform, dichloromethane
Concentration:	Benzene (143-199 ppt)
	Chloroform (294-373 ppt)
	Dichloromethane (446-483 ppt)
N_2 flow rate for baseline:	3.0 lpm

Table 5.2 (Continued)

N_2 flow rate for VOC bubbling:	1.5 lpm
Operation temperature:	Room temperature (25 °C)
Pressure:	Atmospheric pressure

To control the detection of VOC at low concentration, the VOC liquid was injected by syringe into detection chamber by controlling the volume of VOC. Firstly, N_2 gas was introduced into the chamber at a flow rate of 3.0 lpm for 30 min as a baseline. Then, VOC liquid was injected into detection chamber and closed the detection system for 30 min. Finally, the sensors were recovered by purging with 3.0 lpm of N_2 for 30 min. The concentration of VOC was in range of 250 to 3000 parts per million (ppm). The schematic views of the setup of the sensor measurement system and profile of gas flow at ppm level are shown in Fig. 5.9 and 5.10, respectively. The conditions for gas sensor measurement at ppm level is summarized in Table 5.3.

Table 5.3 Conditions for gas sensing characterization for ppm level detection.

Volatile organic compounds:	Benzene, chloroform, dichloromethane
Concentration:	Benzene (250-3000 ppm)
	Chloroform (250-3000 ppm)
	Dichloromethane (250-3000 ppm)
N_2 flow rate for baseline:	3.0 lpm
Operation temperature:	Room temperature (25 °C)
Pressure:	Atmospheric pressure

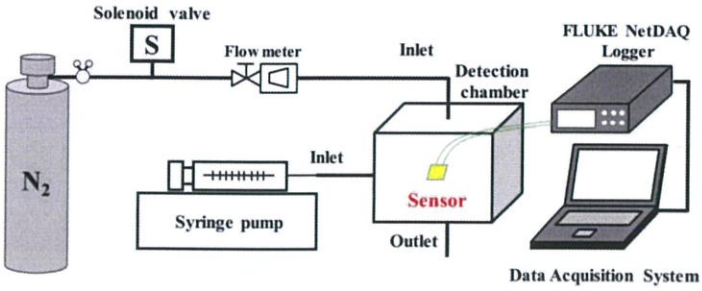

Figure 5.9 Schematic view of a gas sensor measurement for ppm level detection.

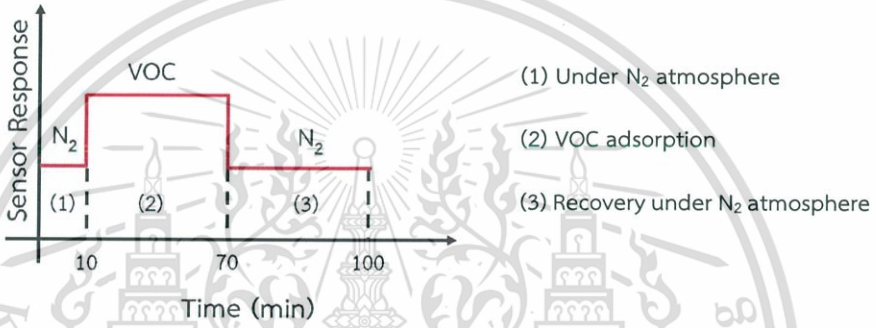

Figure 5.10 Schematic view of flow profile of gas sensor measurement for ppm level detection.

5.3.2 Sensor Response of Metal nanoparticles/Polymer-Functionalized Single-Walled Carbon Nanotube to Volatile Organic Compound

The performance of the fabricated pristine SWNT, EC/SWNT, Pd/SWNT, Pt/SWNT, Pd/EC/SWNT and Pt/EC/SWNT sensors were investigated. The initial resistance of pristine SWNT and hybrid sensors are summarized in table 5.4. Fig. 5.11 shows sensor response as a function of time of pristine SWNT, EC/SWNT, Pd/SWNT, Pt/SWNT, Pd/EC/SWNT and Pt/EC/SWNT upon benzene, chloroform and dichloromethane exposure. Fig. 5.12 shows normalized sensor response of pristine SWNT, EC/SWNT, Pd/SWNT, Pt/SWNT, Pd/EC/SWNT and Pt/EC/SWNT toward benzene, chloroform and dichloromethane.

Table 5.4 Initial resistance of SWNT, EC/SWNT, Pd/SWNT, Pt/SWNT, Pd/EC/SWNT and Pt/EC/SWNT.

Sensor	Initial resistance (kΩ)
SWNT	95.92 ± 8.20
EC(1 wt%)/SWNT	101.16 ± 5.11
EC(5 wt%)/SWNT	146.13 ± 12.85
Pd(2 nm)/SWNT	27.80 ± 4.52
Pd(5 nm)/SWNT	12.19 ± 4.03
Pt(2 nm)/SWNT	10.24 ± 2.26
Pt(5 nm)/SWNT	0.34 ± 0.02
Pd(2 nm)/EC(1 wt%)/SWNT	88.29 ± 4.31
Pd(2 nm)/EC(5 wt%)/SWNT	138.10 ± 12.03
Pd(5 nm)/EC(1 wt%)/SWNT	55.42 ± 2.20
Pd(5 nm)/EC(5 wt%)/SWNT	118.33 ± 8.01
Pt(2 nm)/EC(1 wt%)/SWNT	35.61 ± 0.23
Pt(2 nm)/EC(5 wt%)/SWNT	72.91 ± 2.40
Pt(5 nm)/EC(1 wt%)/SWNT	17.17 ± 3.22
Pt(5 nm)/EC(5 wt%)/SWNT	19.08 ± 2.03

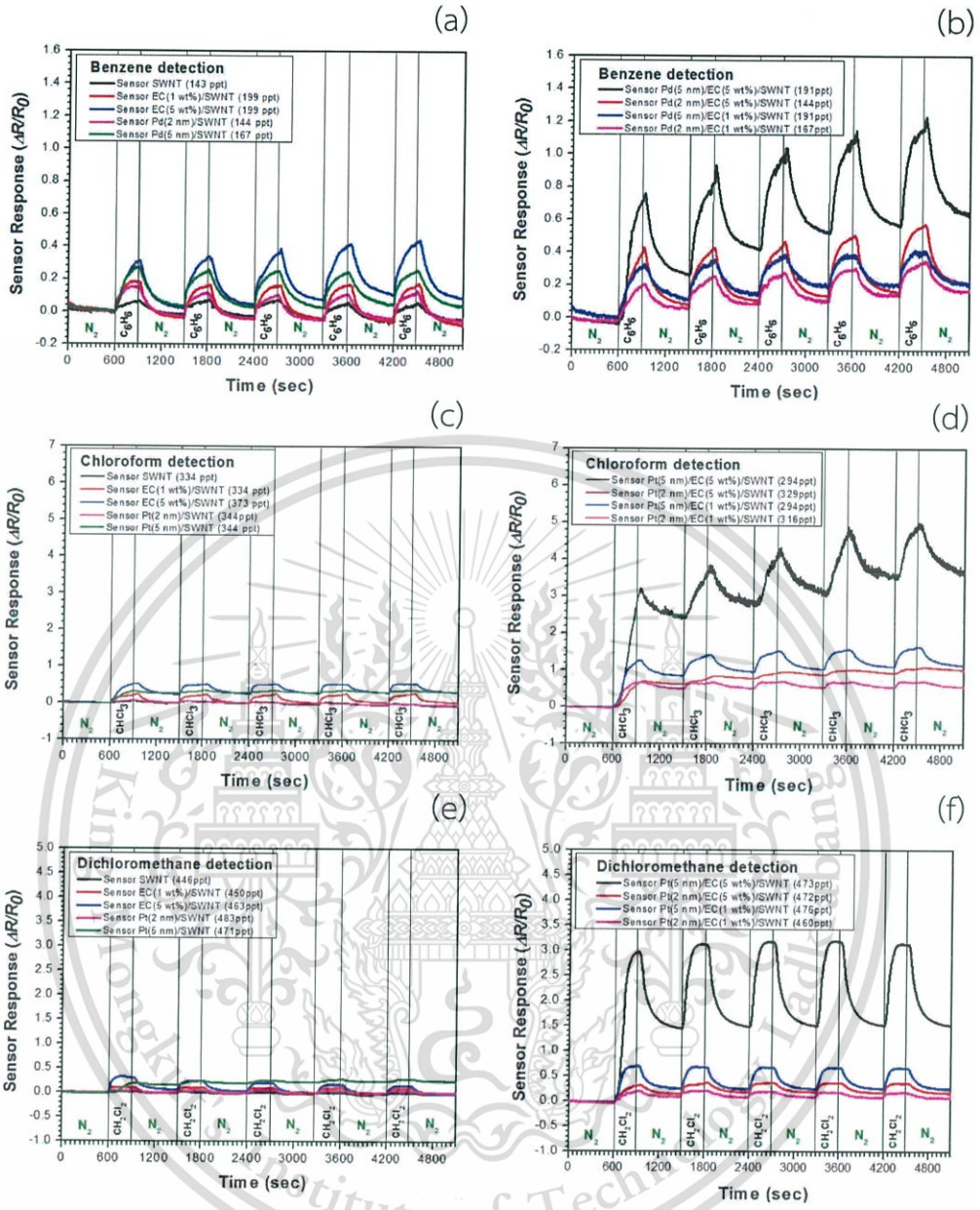

Figure 5.11 Sensor response as a function of time of pristine SWNT, EC/SWNT, Pd/SWNT and Pd/EC/SWNT toward (a-b) benzene and pristine SWNT, EC/SWNT, Pt/SWNT and Pt/EC/SWNT toward (c-d) chloroform and (e-f) dichloromethane.

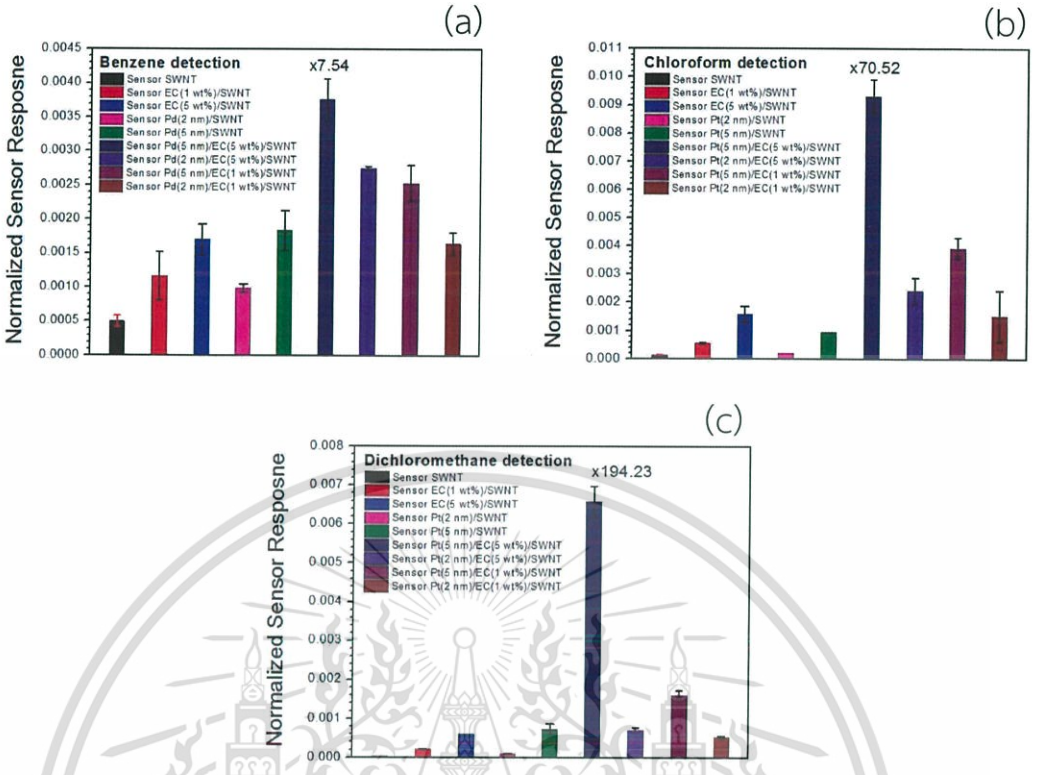

Figure 5.12 Normalized sensor response of pristine SWNT, EC/SWNT, Pd/SWNT and Pd/EC/SWNT toward (a) benzene and pristine SWNT, EC/SWNT, Pt/SWNT and Pt/EC/SWNT toward (b) chloroform and (c) dichloromethane.

Fig. 5.11(a-f) shows the sensor responses as a function of time of pristine SWNT, polymer/SWNT, metal NPs/SWNT and metal NPs/polymer/SWNT sensors under alternating supply of benzene, chloroform and dichloromethane and N_2 gas for 5 cycles. Fig. 5.12(a-c) shows the normalized sensor response of pristine SWNT, polymer/SWNT, metal NPs/SWNT and metal NPs/polymer/SWNT sensors to benzene, chloroform and dichloromethane. The electrical resistance of all sensors increased upon VOC exposure and decreased after replacing VOC with N_2 gas (Fig. 5.11(a-f)). Sensor SWNT, EC(1 wt%)/SWNT and EC(5 wt%)/SWNT were recovered to their initial resistances by N_2 gas purging. Conversely, sensor Pd(2 nm)/SWNT, Pd(5 nm)/SWNT, Pt(2 nm)/SWNT and Pt(5 nm)/SWNT were hardly recovered to their initial resistances. The different response characteristics between EC/SWNT and Pd/ or Pt/SWNT may be attributed to the difference in VOC molecule adsorption behavior. In the case of pristine SWNT and EC/SWNT, VOC molecule are likely to physically adsorb onto pristine SWNT and the EC/SWNT via van der Waals forces, which is a weak interaction. Thus, VOC molecule was easily removed by N_2 gas purging. In the case of Pd/SWNT and

Pt/SWNT, VOC molecules seem to strongly interact with the metal NPs through chemisorption, which is relatively stronger interaction than the physisorption, resulting in difficultly in removing VOC molecule from sensor material, especially in the case of sensor Pd(5 nm)/SWNT and Pt(5 nm)/SWNT. The Pd/EC/SWNT and Pt/EC/SWNT also show the similar recovery behavior to the Pd/SWNT and Pt/SWNT. The reversibility of the sensor can be improved by applying heat or UV exposure. The sensor responses of sensor EC(1 wt%)/SWNT and EC(5 wt%)/SWNT greatly increased to VOC exposure. The sensing mechanism could be explained by polymer swelling as a result of VOC adsorption, which explained in section 3.3.2. Furthermore, sensor EC(5 wt%)/SWNT shows a higher response to VOC compare to sensor EC(1 wt%)/SWNT. These results may be attributed to the effect of the EC film thickness coating on the SWNTs (Fig. 5.2). A thicker film enhances swelling, resulting in a higher sensor response. For metal NPs-decorated SWNT, Pd/SWNT greatly increased to benzene, while, Pt/SWNT greatly increased to chloroform and dichloromethane. The sensing mechanism of Pd/SWNT and Pt/SWNT were explained in section 4.3.2. In addition, sensor Pd(5 nm)/SWNT and Pt(5 nm)/SWNT shows higher response to VOC than that of sensor Pd(2 nm)/SWNT and Pt(2 nm)/SWNT, respectively. A uniform size distribution, full coverage and nanometer-sized Pt NPs on the SWNTs of sensor Pt(5 nm)/SWNT, as confirmed by the TEM images in Fig. 4.2(b-c), resulting in the high sensitivity of sensor Pd(5 nm)/SWNT and Pt(5 nm)/SWNT to VOCs.

For the integration sensors of SWNT, EC and Pd or Pt NPs, all of the sensors selectively responded to VOC vapor with high response magnitude. The sensor response of sensor Pd(5 nm)/EC(5 wt%)/SWNT toward benzene greatly increased by 7.54-fold compared to that of sensor A (Fig. 5.12(a)), while sensor Pt(5 nm)/EC(5 wt%)/SWNT toward chloroform and dichloromethane greatly increased by 70.52- and 194.23-fold compared to that of sensor SWNT, respectively (Fig. 5.12(b-c)). The high response magnitude of the metal NPs/polymer/SWNT was successfully achieved as a result of the incorporation of polymer and metal NPs functions. The sensing mechanism of the Pd/EC/SWNT and Pt/EC/SWNT could possibly explain by the combination of the following phenomena, which involve polymer swelling and catalytic oxidation on the metal NPs surface which explained by section 3.3.2 and 4.3.2, respectively. Regarding the response time of the sensor, the response time is defined as the time taken by the sensor to reach 90% of its maximum sensor response. The sensor A showed the fastest response to benzene and dichloromethane with a response time of approximately 225 and 17 s, but it exhibited the smallest response magnitude. On the other hand, the hybrid sensor Pd(5 nm)/EC(5 wt%)/SWNT enabled 7.54-fold improvement in benzene detection, while sensor Pt(5 nm)/EC(5 wt%)/SWNT enabled 194.23-fold improvement in dichloromethane detection compared to pristine

SWNT. However, the response time of sensor Pd(5 nm)/EC(5 wt%)/SWNT and Pt(5 nm)/EC(5 wt%)/SWNT upon benzene and dichloromethane exposure increased up to 268 and 65 s, respectively, which is approximately 1.19- and 3.82-time higher than that of then sensor A. In the case of chloroform detection, the response time of sensor SWNT and Pt(5 nm)/EC(5 wt%)/SWNT were 278 and 275 s which similar response time. The hybrid metal NPs/polymer/SWNT shows a merit for a significant enhancement of sensor response magnitude but there is room for improvement in its response time.

Next, the sensor performance at the concentration in ppm range was investigated. Fig. 5.13 shows sensor response as a function of time of sensor Pd(5 nm)/EC(5 wt%)/SWNT toward benzene vapor and sensor Pt(5 nm)/EC(5 wt%)/SWNT toward chloroform and dichloromethane vapors at 250-3000 ppm.

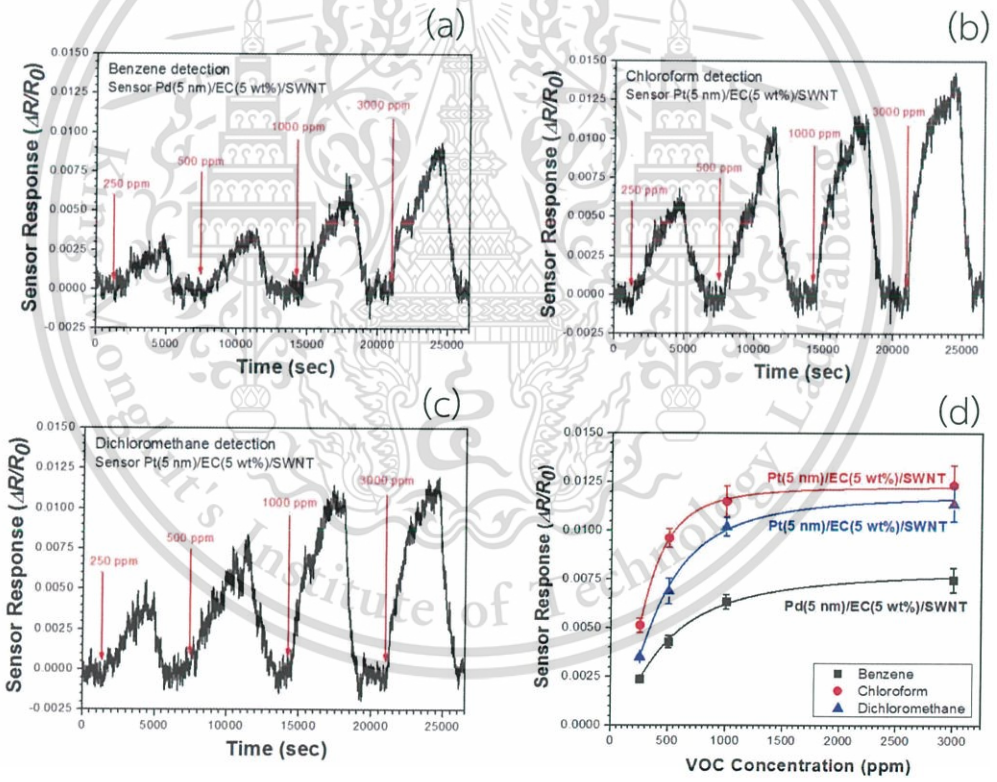

Figure 5.13 Sensor response as a function time of sensor Pd(5 nm)/EC(5 wt%)/SWNT toward (a) benzene vapor and sensor Pt(5 nm)/EC(5 wt%)/SWNT toward (b) chloroform and (c) dichloromethane vapors at 250-3000 ppm. (d) Sensor response of sensor Pd(5 nm)/EC(5 wt%)/SWNT and Pt(5 nm)/EC(5 wt%)/SWNT as a function of benzene, chloroform and dichloromethane concentration.

Fig. 5.13(a-c) shows the sensor response of Pd(5 nm)/EC(5 wt%)/SWNT and Pt(5 nm)/EC(5 wt%)/SWNT and VOC as a function time toward VOC. The electrical resistance of the sensor Pd(5 nm)/EC(5 wt%)/SWNT and Pt(5 nm)/EC(5 wt%)/SWNT increased under VOC exposure and recovered to their initial electrical resistance under N_2 exposure. Fig. 5.13(d) shows the sensor response of Pd(5 nm)/EC(5 wt%)/SWNT and Pt(5 nm)/EC(5 wt%)/SWNT as a function of benzene, chloroform and dichloromethane concentrations in the range of 250-3000 ppm. The sensor response of Pd(5nm)/EC(5 wt%)/SWNT and Pt(5 nm)/EC(5 wt%)/SWNT increased linearly with VOC concentration in the range of 250-1000 ppm. In the range of 1000-3000 ppm, the sensor response increased with VOC concentration but tended to saturate at a concentration higher than 1000 ppm. The feature of VOC adsorption on Pd(5 nm)/EC(5 wt%)/SWNT and Pt(5nm)/EC(5 wt%)/SWNT sensors can be described based on the Langmuir isotherm. The results showed that hybrid sensor based on metal NPs/polymer/SWNT could detect VOC vapor down to ppm level.

In addition, the calculations of limit of detection (*LOD*) for sensing VOC with Pd(5 nm)/EC(5 wt%)/SWNT and Pt(5 nm)/EC(5 wt%)/SWNT sensors were investigated. Each sensor exposure to VOC, we took 30 consecutive data points were collected prior to exposure to VOC. The data were plotted fit it to a fifth-order polynomial. Then, the V_{x^2} was calculated using equation (5.2). In this equation, y_i is the measured value of sensor response ($\Delta R/R_0$) and y is the corresponding the value calculated from the fifth-order polynomial fit. Equation (5.3) was used to calculate the rms_{noise} of the sensors, where *N* is the number of data points used for curve fitting (*N* = 30). Finally, the *LOD* of the sensors can be obtained from Equation (5.4) obtained the *LOD* of the sensors; in this equation, *slope* is the slope of the linear regression fit on the sensor response vs concentration plot. The calculation exhibited that the *LOD* of Pd(5 nm)/EC(5 wt%)/SWNT upon benzene exposure is 127 ppm, while Pt(5 nm)/EC(5 wt%)/SWNT upon chloroform and dichloromethane exposure are 99 and 101 ppm, respectively. These results imply that hybrid gas sensor based on metal NPs/polymer-functionalized SWNT can detect VOC at ppm level.

$$V_{x^2} = \sum(y_i - y)^2 \tag{5.2}$$

$$rms_{noise} = \sqrt{\frac{V_{x^2}}{N}} \tag{5.3}$$

$$LOD = 3\frac{(rms_{noise})}{slope} \tag{5.4}$$

The quantitative measurement of VOC concentration from the sensor response is an important issue for its practical application. This research demonstrated the quantitative VOC detection in the range of 250-3000 ppm was focused. The feature of gas adsorption in this sensing system can be explained based on the Langmuir adsorption isotherm [92] as shown in equation (2.9). θ is the monolayer coverage of VOC molecules on sensor surface, K [ppm^{-1}] is the equilibrium constant for VOC adsorption and C [ppm] is VOC concentration. θ is assumed to be proportional to the sensor response

$$\theta = \frac{number\ of\ sites\ occupied\ by\ gas\ moleclues}{total\ number\ of\ adsorption\ sites} = \frac{\frac{\Delta R}{R_0}}{\frac{\Delta R_{max}}{R_0}} = \frac{SR}{SR_{max}} \tag{5.5}$$

where ΔR and SR are the resistance change and sensor response of the hybrid sensor, ΔR_{max} and SR_{max} are the maximum ones at the saturation coverage. Thus, C is given by

$$C\ [ppm] = \frac{SR}{K \cdot (SR_{max} - SR)} \tag{5.6}$$

To confirm the adsorption behavior of VOC on hybrid sensor based on the Langmuir adsorption isotherm, equation (5.6) was transformed to

$$\frac{C}{SR} = \frac{1}{KSR_{max}} + \frac{1}{SR_{max}} C \tag{5.7}$$

Fig. 5.14 shows the relationship between sensor response and concentration (C/SR vs S) of (a) benzene, (c) chloroform and (e) dichloromethane. Solid circle are experimental results and a dashed line is a fitting curve. The results show the linear curve, showing that the adsorption of VOC molecules on hybrid sensor follows the Langmuir isotherm. From the best fitting curve and using equation (5.7), K values of benzene, chloroform and dichloromethane were estimated to be 0.0013, 0.0037 and 0.0014 [ppm^{-1}], while *SRmax* values of benzene, chloroform and dichloromethane were approximately 0.0103, 0.0136 and 0.0154, respectively. The obtained K and *SRmax* values were assigned to equation (5.6), and the relationship between sensor

response and VOC concentration was obtained as shown in Fig. 5.14 for (b) benzene, (d) chloroform and (e) dichloromethane. The results show that the sensor response from experimental data has a good fitting to the Langmuir isotherm fitting curve, implying that the sensor response of hybrid sensor is based on Langmuir adsorption isotherm.

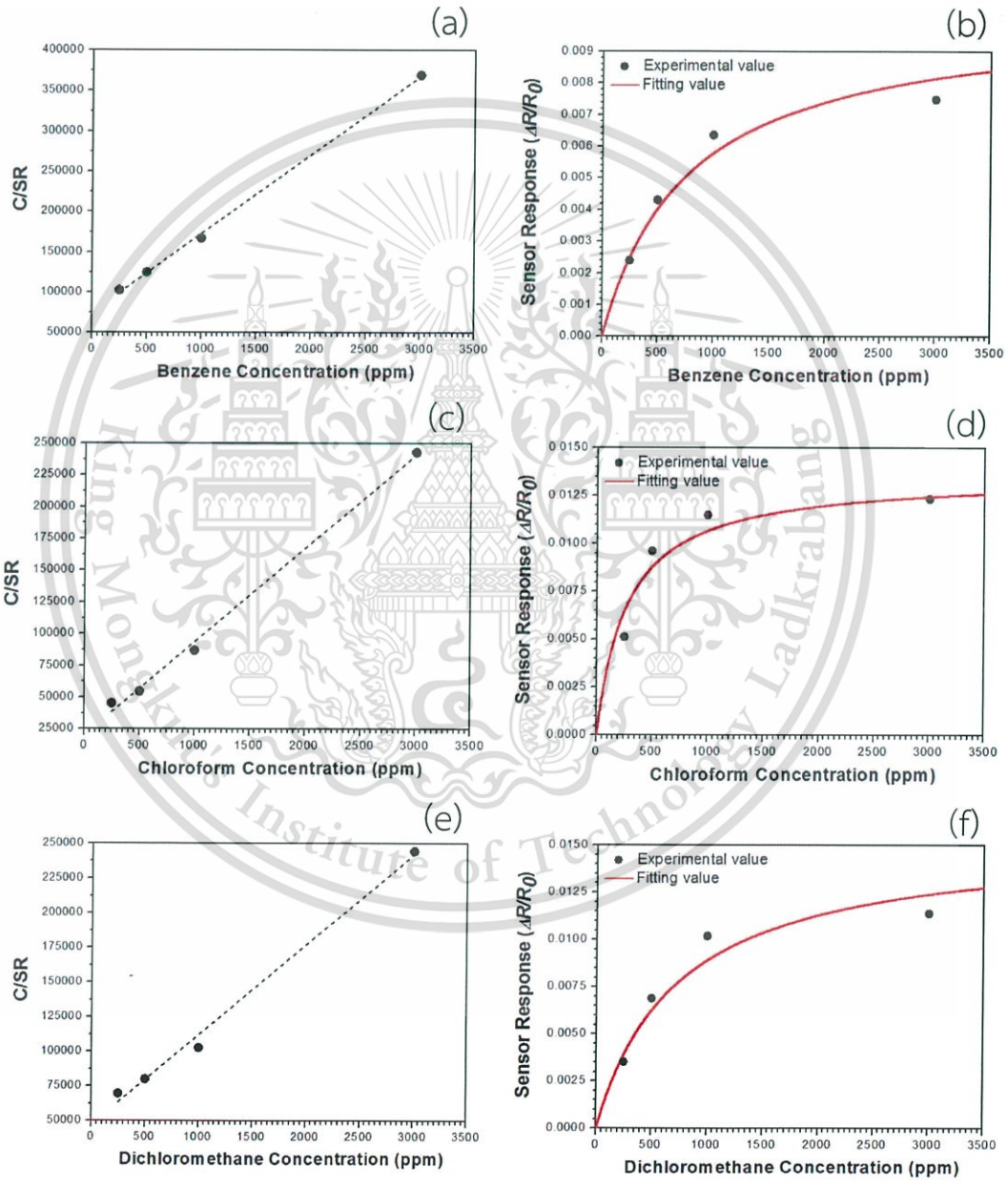

Figure 5.14 Relationship between sensor response and concentration; C/SR vs. C of (a) benzene, (c) chloroform and (e) dichloromethane. Relationship between sensor response and VOC concentration of (b) benzene, (d) chloroform and (f) dichloromethane.

5.4 Investigation of Sensing Mechanism

5.4.1 Fluorescence Spectroscopy Characterization

To prove the sensing mechanism, fluorescence spectroscopy technique was employed to prove the sensing mechanism of polymer-coated SWNT that is attributed to the swelling of polymer. The electrons in molecules of sample are excited from ground state to excite state by ultraviolet light. The light emitted from sample gives the information of the excited energy, which has a specific energy. EC/SWNT used in fluorescence spectroscopy were prepared by the process explained in subsections 3.1 using Si as a substrate instead of the PCB. A schematic view of the swelling process of VOC adsorption onto EC/SWNT is shown in Fig. 5.15(a). Polymer/SWNTs were analyzed before and after saturated VOC exposure for 10 min to obtain the spectra as shown in Fig. 5.15(b). After VOC adsorption, polymer layer was swollen and conformational changed of the backbone of polymer, resulting in an increased in emission spectra (Fig. 5.15(b)). The structural change in polymer gives the different information of emitted light.

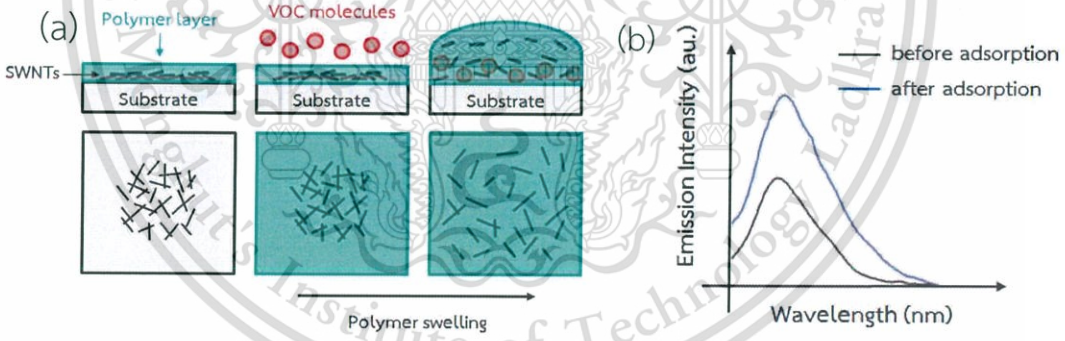

Figure 5.15 Schematic view of (a) the swelling process of VOC adsorption and (b) emission spectra before and after VOC adsorption.

5.4.2 The Proposed Sensing Mechanism of Polymer-Functionalized Carbon Nanotubes

To investigate the sensing mechanism of EC/SWNT, fluorescence spectrometer was utilized to analyze EC/SWNT before and after VOC exposure. Fig. 5.16 shows the change in fluorescence in terms of emission intensity of EC/SWNT in response to benzene, chloroform and dichloromethane at saturated vapor by process explained

in section 5.4. Upon exposure to saturated benzene, chloroform and dichloromethane increased the emission intensity of EC/SWNT at 615 nm by 8.22, 12.52 and 64.84 %. The increase in an emission intensity indicates that the VOC induced conformational change of the polymer backbone, resulting in an increased physical separation of SWNTs caused by the interaction between the EC and VOC [14]. These results prove that the increasing in the emission intensity coincided to polymer swelling which described in section 3.3.

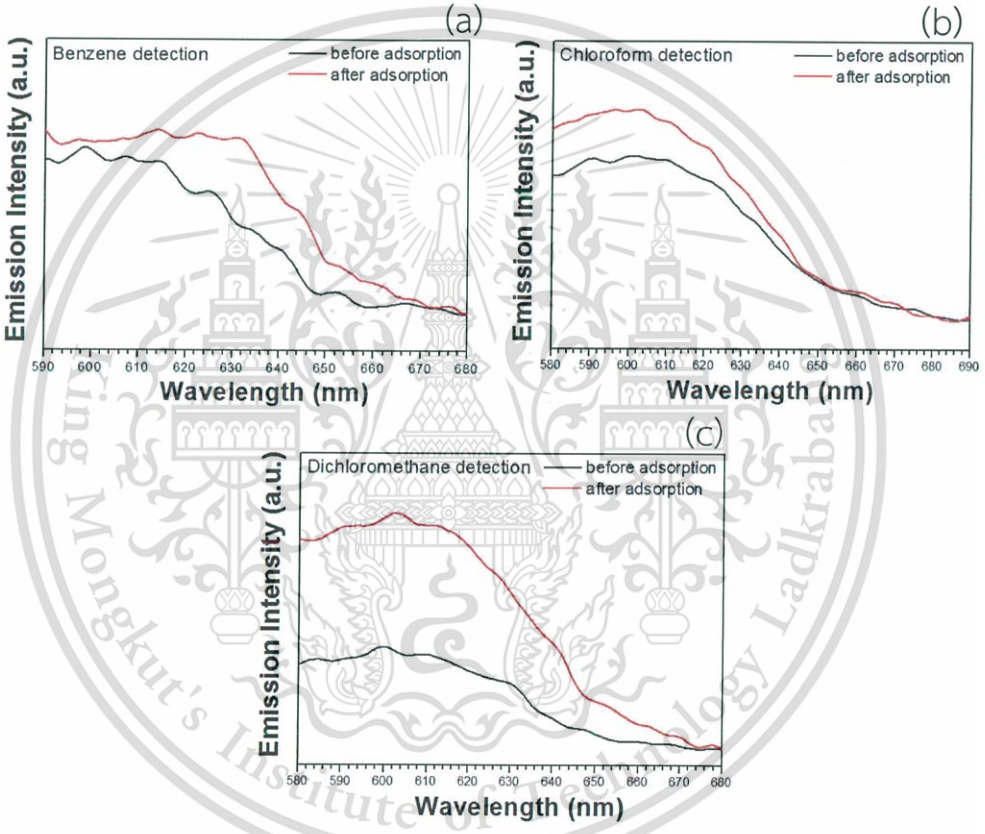

Figure 5.16 Emission of EC/SWNT in air (black) and after 10 min exposure to saturated (a) benzene (b) chloroform and (c) dichloromethane vapors (red).

5.5 Dichloromethane Sensor Based on Platinum Nanoparticle/Poly(methyl methacrylate)/Single-Walled Carbon Nanotube

A dichloromethane sensor with a high response magnitude was fabricated using the integration of SWNT, PMMA, Pt NP. Morphology and structure of Pt NP/PMMA/SWNT

were characterized by FESEM, TEM, FTIR, Raman spectroscopy, and XRD. The sensing performances to dichloromethane were investigated.

5.5.1 Fabrication of Gas Sensor Based on Platinum Nanoparticles/Poly (methyl methacrylate)-Functionalized Carbon Nanotubes

The hybrid sensor based on Pt NP/PMMA-functionalized SWNT was fabricated for dichloromethane detection. The preparation of PMMA coating and Pt NP deposition on the SWNT network is following in section 5.1. PMMA was varied between 1 and 5 wt% and the thickness of Pt NP was varied at 2 and 5 nm. For comparison, SWNT with only PMMA coating or Pt NP decoration were also fabricated. The details of the fabricated gas sensor is shown in Table 5.5.

Table 5.5 Summary of sensors based on hybrid SWNTs.

Sensor configuration
SWNT
PMMA(1 wt%)/SWNT
PMMA(5 wt%)/SWNT
Pt(2 nm)/SWNT
Pt(5 nm)/SWNT
Pt(2 nm)/PMMA(1 wt%)/SWNT
Pt(2 nm)/PMMA(5 wt%)/SWNT
Pt(5 nm)/PMMA(1 wt%)/SWNT
Pt(5 nm)/PMMA(5 wt%)/SWNT

5.5.2 Morphology and structural characterization of sensing materials

5.5.2.1 Scanning Electron Microscopy Characterization

The morphologies of the PMMA/SWNT was characterized by FESEM (JEOL JSM-7800F) is following in section 5.2.1. The element composition of Pt/PMMA/SWNT were studied by FESEM equipped with an EDS as explained in section 5.2.1.

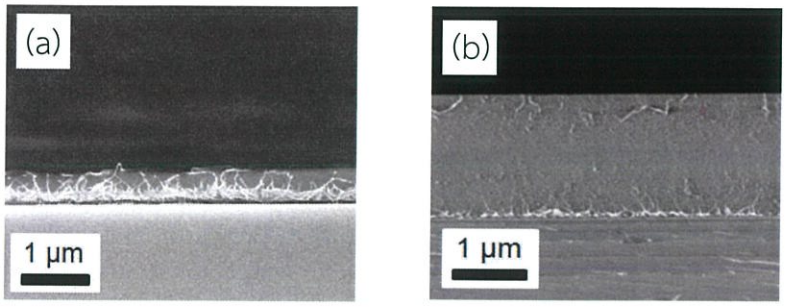

Figure 5.17 FESEM images of (a) PMMA(1 wt%)/SWNT and (b) PMMA(5 wt%)/SWNT.

Fig. 5.17(a-b) shows the cross-sectional FESEM images of PMMA(1 wt%)/SWNT and PMMA(5 wt%)/SWNT, respectively. The thickness of the PMMA(1 wt%)/SWNT and PMMA(5 wt%)/SWNT coatings on the SWNTs were 0.40 and 2.64 μm, respectively. For PMMA(1 wt%)/SWNT (Fig. 5.17(a)), the SWNT network was shown to be buried in the PMMA matrix and some of the SWNT bundles were protruding from the PMMA surface. However, in the case of PMMA(5 wt%)/SWNT (Fig. 5.17(b)), PMMA completely covered the pristine SWNT network. The thickness of the PMMA film was controlled by the concentration and viscosity of the PMMA solution.

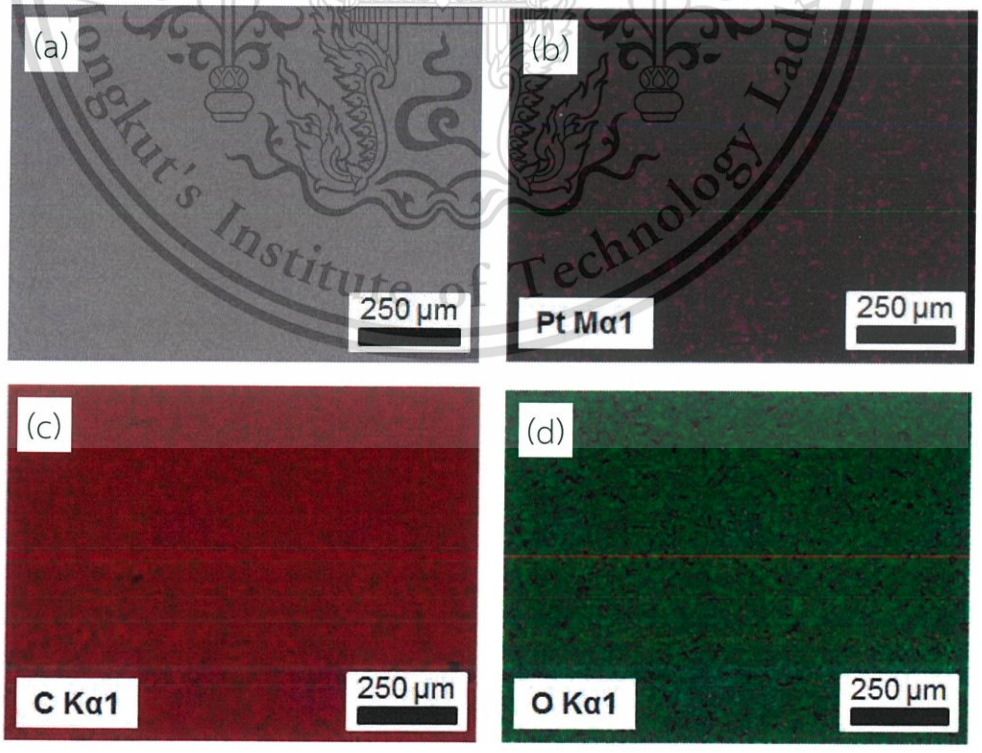

Figure 5.18 FESEM of (a) Pt(5 nm)/PMMA(5 wt%)/SWNT, EDS mapping of (b) platinum, (c) carbon, and (d) oxygen elements.

The elemental composition of Pt(5 nm)/PMMA(5 wt%)/SWNT was determined by EDS. The analyzed surface area for EDS mapping of Pt(5 nm)/PMMA(5 wt%)/SWNT is show in Fig. 5.18(a). The EDS element mapping image revealed that Pt(5 nm)/PMMA(5 wt%)/SWNT consists of Pt (in purple), carbon (in red) and oxygen (in green) as shown in Fig. 5.18(b-d), respectively. The Pt mapping clearly indicates that the Pt NPs are homogenous distributed on the sensor Pt(5 nm)/PMMA(5 wt%)/SWNT as shown in Fig. 5.18(b). Carbon and oxygen elements may be derived from SWNT and PMMA.

5.5.2.2 Transmission Electron Microscopy Characterization

The morphologies of the pristine SWNT and Pt/SWNT were characterized by TEM (JEOL JE-2010) to characterize the nanostructure of the metal NPs/SWNT as explained in section 5.2.2. The thickness was varied at 2 and 5 nm. The TEM images of Pt(2 nm)/SWNT and Pt(5 nm)/SWNT are shown in Fig. 5.4(b-c), respectively. The Pt NPs were attached to the sidewalls of pristine SWNT bundles, whereas the SWNT bundles maintained their structure. The average diameters of Pt(2 nm)/SWNT and Pt(5 nm)/SWNT were 3.53±0.94 and 4.01±0.77 nm, respectively. Pt(5 nm)/SWNT show the higher distribution and greater coverage than that of sensor Pt(2 nm)/SWNT and greater.

5.5.2.3 Fourier Transform Infrared Spectroscopy Characterization

The functional group of PMMA was characterized by FTIR (Perkin Elmer, Spectrum One) as explained in section 5.2.3. The FTIR sample was prepared by mixing SWNTs powder with potassium bromide (KBr) and pressing in a pellet form. Then, the prepared pellet was coated and decorated with PMMA and Pt NPs, respectively. Typical FTIR spectra in an absorbance mode were scanned in a wavenumber range of 500-4000 cm^{-1}. To confirm the PMMA existence in the Pt(5 nm)/PMMA(5 wt%)/SWNT, the samples were characterized by FTIR. Fig. 5.19 show FTIR spectra of SWNT, PMMA(5wt%), Pt(5 nm)/PMMA(5wt%)/SWNT. FTIR spectra of PMMA(5 wt%)/SWNT and Pt(5 nm)/PMMA(5 wt%)/SWNT show almost identical feature. The peak assigned to the C–H stretching vibration occurred at 2977 cm^{-1}. The strong peak at 1730 cm^{-1} is assigned to C=O stretching vibration. The peak at 1157, 1199 and 1265 cm^{-1} correspond to C–O–C stretching and deformation vibrations. The peaks observed at 999 cm^{-1} and 858 cm^{-1} are due to C–H bending vibrations and the peak at 746 cm^{-1} is attributed to the vibrations of the polymer chain [93,94]. This results confirm the existence of PMMA and the same composition of the functional group of PMMA before and after Pt depositions.

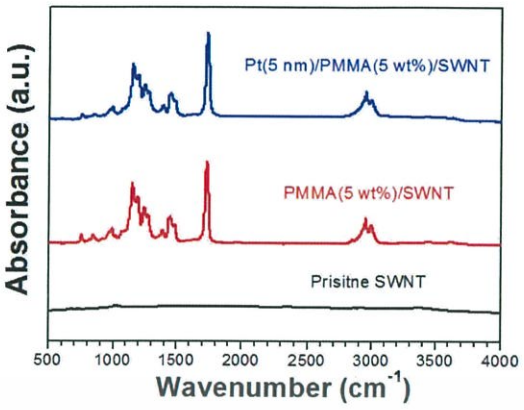

Figure 5.19 FTIR spectra of SWNT, PMMA(5 wt%)/SWNT, Pt(5 nm)/PMMA(5 wt%)/ SWNT.

5.5.2.4 X-ray Diffraction Characterization

The crystal structure of PMMA/SWNT, Pt NP/SWNT and Pt NP/PMMA/SWNT were characterized by XRD (Rigaku TTRAX II) using Cu Kα with a wavelength of 1.54 Å at a scan rate of 1 °/min. The samples for XRD analysis were prepared by the process explained in sections 3.1, 4.1 and 5.1 using silicon (Si) as a substrate instead of the PCB.

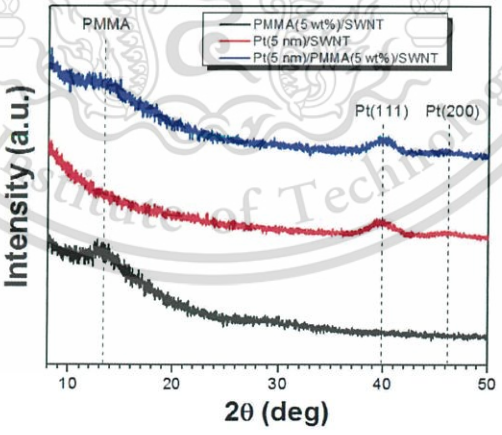

Figure 5.20 XRD spectra of PMMA(5 wt%)/SWNT, Pt(5 nm)/SWNT and Pt(5 nm)/PMMA (5 wt%)/SWNT.

To confirm the crystallinity, the sample was characterized by XRD. The typical XRD diffraction patterns of PMMA(5 wt%)/SWNT, Pt(5 nm)/SWNT and Pt(5 nm)/PMMA(5

wt%)/SWNT are show in Fig. 5.20. PMMA(5 wt%)/SWNT exhibited a board peak at ~13°, which corresponds to the structure of PMMA [95], whereas the diffraction peaks of Pt(5 nm)/SWNT located at 39.7° and 46.2° can be assigned to the reflection from the (111) and (200) planes of the face-centered cubic Pt, respectively [90,91]. For Pt(5 nm)/PMMA(5 wt%)/SWNT the diffraction pattern shows diffraction peak from PMMA at ~13° and diffraction peak from Pt NPs at 39.7° and 46.2° , respectively, confirming the existence of PMMA after Pt deposition. These results imply changes in the structural regularity of the main chains of the polymeric molecules.

5.5.2.5 Raman Spectroscopy Characterization

The carbon structure, purity and crystallinity of pristine SWNT, PMMA/SWNT, Pt NP/SWNT and Pt NP/PMMAr/SWNT were analyzed by Raman spectroscopy (Thermo SCIENTIFIC DXR) with an Ar ion laser wavelength of 532 nm (2.33 eV).

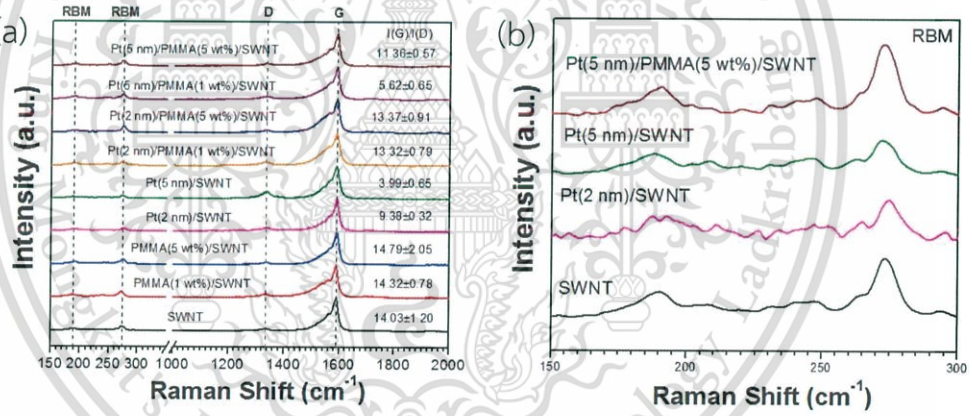

Figure 5.21 (a) Raman spectra of pristine SWNT, PMMA/SWNT, Pt/SWNT and Pt/PMMA/SWNT. (b) RBM spectra of pristine SWNT, Pt(2 nm)/SWNT, Pt(5 nm)/SWNT and Pt(5 nm)/PMMA(5 wt%)/SWNT.

Raman spectroscopy was utilized to characterize the structure, purity and crystallinity of pristine SWNT. Fig. 5.21(a) shows the four significant Raman peaks: SWNT-derived Radial breathing mode (RBM) at 190 and 273 cm^{-1}, disorder carbon-derived D-band at 1332 cm^{-1} and graphitic-structure-derived G-band at 1588 cm^{-1}. After PMMA coating, the I_G/I_D ratio of sensor PMMA(1 wt%)/SWNT and PMMA(5 wt%)/SWNT were 14.32±0.78 and 14.79±2.05, respectively, with no obvious difference from the pristine SWNTs. However, after Pt decoration, the I_G/I_D ratio of Pt(2 nm)/SWNT and Pt(5 nm)/SWNT were significantly decrease to 9.38±0.32, and 3.99±0.65, respectively,

implying that the crystallinity and purity of the SWNTs deteriorated, especially for Pt(5 nm)/SWNT in which highest amount of Pt NPs show the lowest I_G/I_D value. The decrease in the I_G/I_D value could be attributed to the damage during metal NPs adhesion on the SWNTs with high energy.

For hybrid sensor, the I_G/I_D value of Pt(2 nm)/PMMA(5 wt%)/SWNT, Pt(5 nm)/PMMA(5 wt%)/SWNT were greater than those of Pt(2 nm)/SWNT, Pt(5 nm)/SWNT, Pt(2 nm)/PMMA(1 wt%)/SWNT and Pt(5 nm)/PMMA(1 wt%)/SWNT, indicating higher crystallinity and purity of the SWNTs. These results show that thick film of PMMA effectively protects the SWNTs during metal NPs deposition. These results clearly confirm that PMMA can act as a protective layer on a SWNTs during Pt NPs deposition. Fig. 5.21(b) shows RBM spectra of pristine SWNT, Pt/SWNT and Pt/EC/SWNT sensors. The intensity of the RBM peak at 273 cm^{-1} and the I_G/I_D ratios of Pt(2 nm)/SWNT and Pt(5 nm)/SWNT gradually decreased with increasing amount deposited Pt NPs on the pristine SWNT, whereas those of Pt(5 nm)/PMMA(5 wt%)/SWNT were relatively comparable to those of the pristine SWNT. The decrease in the RBM peak and I_G/I_D ratios of Pt(2 nm)/SWNT and Pt(5 nm)/SWNT are attributed to the damage of small-diameter SWNTs during Pt NPs adhesion with high energy. These results also clearly confirm that PMMA can act as a protective layer on SWNTs during Pt NPs deposition.

5.5.3 Sensor Performance of Platinum Nanoparticles/Poly(methyl methacrylate)-Functionalized Single-Walled Carbon Nanotubes

5.5.3.1 Gas Sensing Measurement System

The condition for gas sensor measurement is summarized in table 5.6. Dichloromethane was used as VOC. The schematic views of the setup of the sensor measurement system and the profile of gas flow are shown in Fig. 3.4 and Fig. 5.8, respectively. The concentration of the dichloromethane vapor was adjusted by controlling the temperature of the dichloromethane liquid The sensor response and normalized sensor response are calculated by equation (3.1) and (5.1), respectively.

Table 5.6 Conditions for gas sensing characterization.

Volatile organic compounds:	Dichloromethane
Concentration:	Dichloromethane (495-615 ppt)
N_2 flow rate for baseline:	3.0 lpm

Table 5.6 (Continued)

N_2 flow rate for VOC bubbling:	1.5 lpm
Operation temperature:	Room temperature (25 °C)
Pressure:	Atmospheric pressure

5.5.3.2 Sensor Response of Platinum Nanoparticles/Poly(methyl methacrylate)-Functionalized Single-Walled Carbon Nanotube to Volatile Organic Compound

The performance of the fabricated pristine SWNT, PMMA/SWNT, Pt/SWNT and Pt/EC/SWNT sensors were investigated. Fig. 5.22(a-b) shows sensor response as a function of time of pristine SWNT, PMMA/SWNT, Pt/SWNT and Pt/PMMA/SWNT upon dichloromethane exposure. Fig. 5.22(c) shows normalized sensor response of pristine SWNT, PMMA/SWNT, Pt/SWNT and Pt/PMMA/SWNT toward dichloromethane. Figs. 5.22(a-b) show sensor responses as a function of time of each sensor under an alternating supply of dichloromethane (495 ppt) and N_2 gas for 4 cycles. Fig. 5.22(c) shows the normalized sensor response of each sensor to dichloromethane. The electrical resistance of all the sensors increased upon dichloromethane exposure and decreased after replacing dichloromethane with N_2 gas (Figs. 5.22(a-b)). For pristine SWNT, PMMA(1 wt%)/SWNT and PMMA(5 wt%)/SWNT, gas sensors can recover to their initial resistance by N_2 gas purging. We envision that the interaction between sensor material and dichloromethane molecule is physisorption that is a weak interaction. Thus, dichloromethane molecule was easily removed by N_2 gas purging. However, in the case of Pt(2 nm)/SWNT and Pt(5 nm)/SWNT, gas sensors were not completely recover to their initial resistance by N_2 gas purging. This is likely due to the chemisorption between dichloromethane molecule and sensor material (Pt/SWNT), which is relatively stronger interaction than the physisorption, resulting in difficulty in removing DCM molecule from sensor material, especially in the case of Pt(5 nm)/SWNT. The Pt/PMMA/SWNT also shows the similar recovery behavior to the Pt/SWNT. The reversibility of the sensor can be improved by applying heat or UV exposure, similar to SWNT sensor system. Regarding the response time of the sensor, the response time is defined as the time taken by the sensor to reach 90% of its

maximum sensor response. The pristine SWNT shows the fastest response time of response time of approximately 17±4 s, but nevertheless it shows the smallest sensor response magnitude. On the other hand, the hybrid Pt/PMMA/SWNT enables 69-fold improved dichloromethane detection compared with the pristine SWNT. However, the response time of the Pt/PMMA/SWNT increases up to 190±6 s, which is approximately 11-time higher than that of the pristine SWNT. Thus, the hybrid Pt/PMMA/SWNT shows a merit for a significant enhancement of sensor response magnitude but there is room for improvement in its response time.

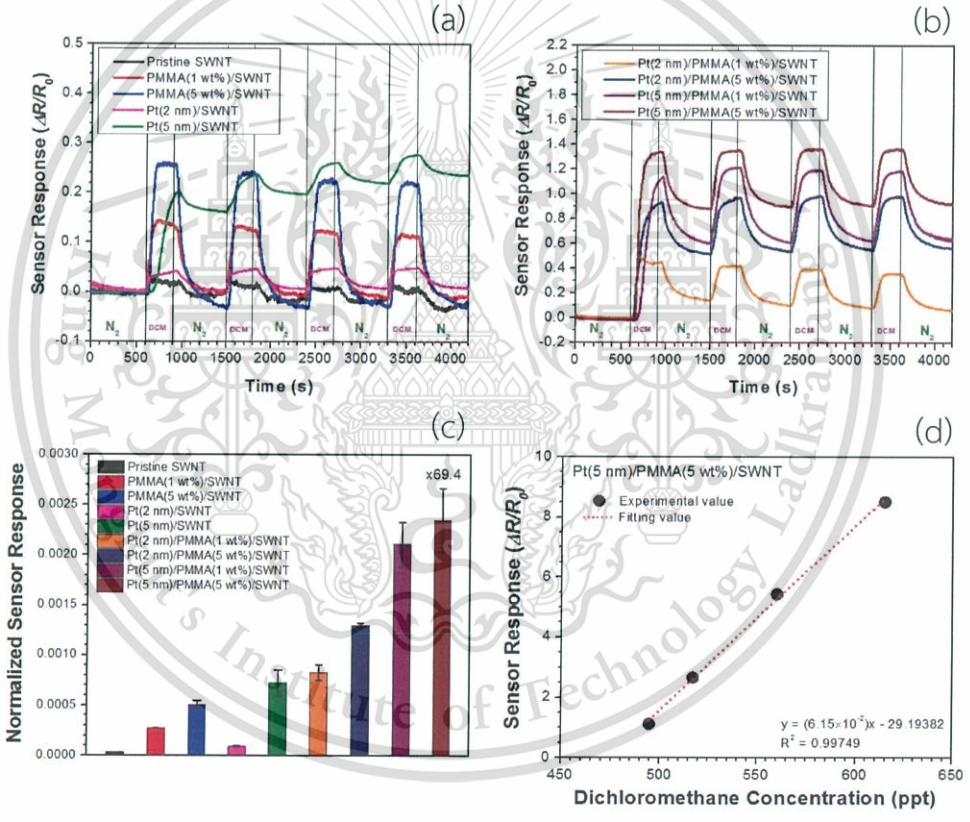

Figure 5.22 Sensor response as a function of time of (a) pristine SWNT, PMMA/SWNT, Pt/SWNT and (b) Pt/PMMA/SWNT toward dichloromethane. (c) Normalized sensor response of pristine SWNT, PMMA/SWNT, Pt/SWNT and Pt/PMMA/SWNT toward dichloromethane. (d) Sensor response of Pt(5 nm)/PMMA(5 wt%)/SWNT as a function of dichloromethane concentration.

The sensing mechanism of the pristine SWNTs can be described in terms of the dielectric constant, which involves the solvent polarity of dichloromethane. The sensing mechanism is explained in section 3.3.2. For PMMA/SWNT, the sensor responses of PMMA(1 wt%)/SWNT and PMMA(5 wt%)/SWNT to toward dichloromethane greatly increased 8.0- and 14.9-fold higher compared to than that of pristine SWNT, implying indicating sensor response enhancement by PMMA functionalization. The sensing mechanism could be explained by to the polymer swelling which describe in section 3.3.2. Furthermore, PMMA(5 wt%)/SWNT shows a higher response to dichloromethane than compare to that of PMMA(1 wt%)/SWNT. These results could be owing to may be attributed to the effect of the PMMA film thickness coating on the SWNTs (Fig. 5.17). The A thicker film enhances swelling, resulting in a higher sensor response. For Pt/SWNT, the sensor response of Pt(2 nm)/SWNT and Pt(5 nm)/SWNT to dichloromethane greatly increased 2.7- and 21.4-fold higher than that of pristine SWNT, indicating sensor response improvement by Pt NPs functionalization. The sensing mechanism would be explained by the catalytic oxidation which is described in section 4.3.2. In addition, Pt(5 nm)/SWNT shows higher response to dichloromethane than that of Pt(2 nm)/SWNT. A uniform size distribution, a full coverage and nanometer-sized Pt NPs on the SWNTs of Pt(5 nm)/SWNT as confirmed by the TEM images in Figs. 5.4(b-c), afford result in the high sensitivity of Pt(5 nm)/SWNT to dichloromethane.

In the case of the hybrid Pt/PMMA/SWNT sensors, all of the sensors extremely selectivity responded to dichloromethane vapor with high response magnitude. The sensor response of Pt(5 nm)/PMMA(5 wt%)/SWNT to toward dichloromethane greatly increased by 69.4-fold higher than compared to that of pristine SWNT. The high response magnitude of the Pt/PMMA/SWNTs was successfully achieved owing as a result of to the incorporation of PMMA and Pt functions. The mechanism of the Pt/PMMA/SWNTs could possibly explain by the combination of the following phenomena by catalytic reaction on Pt NPs and swelling of PMMA. Regarding the catalytic reaction on Pt NPs of the Pt/PMMA/SWNT based on PMMA 1% (Pt(2 nm)/PMMA(1 wt%)/SWNT and Pt(5 nm)/PMMA(1 wt%)/SWNT), the thickness of the PMMA layer is approximate 0.40 μm. SWNT network was partly buried in PMMA matrix and some of SWNT bundles were clearly seen to protrude to PMMA surface (Fig. 5.17(a)). Thus, the released electron from dissociation reaction of dichloromethane can directly donate to SWNT. In the case of PMMA 5% with a thick thickness of 2.64 μm (Pt(2 nm)/PMMA(5 wt%)/SWNT and Pt(5 nm)/PMMA(5 wt%)/SWNT), SWNT seems to be completely covered by PMMA. However, careful observation reveals that there are bundles of SWNT were drawn to the surface of PMMA layer, forming a conduction path in the SWNT-PMMA matrix, as a white line shown in an SEM image (Fig. 5.17(b)). Thus,

these SWNT bundles can act as a conductive path for the released electron through the PMMA to the beneath SWNT network. The donation of electron to the p-type semiconducting SWNT causes an increase in electrical resistance.

Fig. 5.22(d) shows the sensor response of the Pt(5 nm)/PMMA(5 wt%)/SWNT as a function of dichloromethane concentration in ranges of 495-615 ppt. A linear relationship was obtained between the sensor response of the Pt(5 nm)/PMMA(5 wt%)/SWNT and the concentration of dichloromethane, namely the sensor response increased proportionally with the dichloromethane concentration. The concentration in the experiment is in a high concentration range. Nevertheless, the advantage of the hybrid Pt/PMMA/SWNT is the enhancement of the sensor response magnitude. The hybrid sensor based Pt/PMMA/SWNT enables 69-fold improved dichloromethane detection compared with pristine SWNT. Moreover, our proposed sensor can operate at room temperature and consume low power. These advantages let our sensor become a potential candidate for a portable sensing device with real-time monitoring.

5.6 Summary

A new type gas sensor based on metal NPs/polymer-functionalized carbon nanotubes was successfully fabricated for VOC detection. The dual-functionalized SWNTs through polymer coating and metal NP deposition were prepared by spin-coating and EB evaporation methods. The results showed that Pd/EC/SWNT greatly improved the sensor response to benzene 7.54-fold, while the Pt/EC/SWNT greatly improved the sensor response to chloroform and dichloromethane 70.52- and 194.23-fold, respectively compared to that of pristine SWNT. The sensing mechanism of hybrid materials incorporate of polymer and metal NPs, i.e., polymer swelling and catalytic oxidation on metal NP surface. In addition, we successfully fabricated a dichloromethane sensor with a high response magnitude using the integration of SWNT, PMMA and Pt NPs. Pt/PMMA/SWNT exhibited a 69.4-fold improvement in the sensor response to dichloromethane. The sensor response of Pt/PMMA/SWNT linearly increased with increasing dichloromethane concentration. The integration of pristine SWNT with polymer and metal NPs is a promising approach for extremely improved sensitivity and selectivity for VOC detection

CHAPTER 6

CONCLUSIONS

We successfully demonstrated volatile organic compound (VOC) sensor for highly sensitive and selective using hybrid materials based on polymer and metal nanoparticles (NPs)-functionalized carbon nanotubes (CNTs). Thiophene, ethyl cellulose (EC), poly(methyl methacrylate) (PMMA), polystyrene (PS), and polyvinyl acetate (PVA) were used as monomer and polymer, while gold (Au), palladium (Pd), and platinum (Pt) were used as a metal NPs. The monomer or polymer-coated and metal NPs-coated CNT were fabricated by spin coating and electron-beam evaporation methods, respectively. Test VOCs were acetone, ethanol, methanol, benzene, chloroform and dichloromethane.

First part, the sensor response of the monomer or polymer-coated CNT sensors to various VOCs were investigated. EC-coated SWNT highly respond to benzene, chloroform and dichloromethane with an increase in electrical resistance. The sensor response of EC/CNT to benzene, chloroform and dichloromethane greatly increase 4.28-, 14.74- and 59.01-fold higher than that of pristine CNT, respectively. The sensing mechanism of polymer-coated SWNT would be ascribed to monomer or polymer swelling, swelling of the monomer or polymer as a result of VOC adsorption leads to monomer or polymer volume expansion. Furthermore, the sensing mechanism would be ascribed Hansen solubility parameter which related the suability between monomer or polymer with VOC.

Second part, the sensor response of the metal NPs-coated CNT sensors to various VOCs were investigated. The results show that Pd-coated SWNT highly respond to benzene, while and Pd NPs-coated CNT highly response to benzene with an increase in electrical resistance. The sensor response of Pd/CNT to benzene greatly increase 1.60-fold, while the sensor response of Pt/CNT to chloroform and dichloromethane greatly increase 2.61- and 9.78-fold than that of pristine CNT, respectively. The sensing mechanism of metal NPs-decorated CNT was attributed by catalytic oxidation. Metal NPs promote the dissociation of VOC to CO, and consequently the CO oxidation on the metal NPs catalyst surface and electron donation from metal NPs to CNT.

Third part, hybrid sensor with high response magnitude was successfully fabricated using the integration of SWNT, polymer and metal NPs. The high response magnitude of the metal NPs/polymer/SWNT was achieved because of the

incorporation of polymer and metal NP functions. The results showed that the hybrid Pt/EC/CNT enabled an approximately 70.52- and 194.23-fold improvement in chloroform and dichloromethane detection, respectively compared to the pristine CNT. While the hybrid Pd/EC/CNT enabled an approximately 7.54-fold improvement in benzene detection, respectively compared to the pristine CNT. Moreover, the sensor response increased linearly with VOC concentration in range of 250-1000 parts per million (ppm) but tended to saturate at a concentration higher than 1000 ppm. In addition, the gas sensing mechanism of EC-coated SWNT upon VOC exposure were investigated by fluorescence spectroscopy. The results showed that the intensity of emitted light of EC-coated SWNT increased upon VOC exposure, implying polymer are swollen and conformational changed of the backbone of polymer. These results confirm the sensing mechanism of EC-coated SWNT upon VOC exposure in the chapter 3.

A novel gas sensor device based on dual-functionalized SWNTs through polymer coating and metal NP deposition was successfully developed. Gas sensor based on polymer/metal NPs/SWNT extremely improved the sensitivity and selectivity to VOCs. The integration of pristine SWNT with polymer and metal NPs offers a promising material for practical and high-performance VOC sensing applications to real-time monitoring of VOC.

REFERENCES

[1] Amor, J.N. 1992. "Environmental catalysis." **Appl. Catal. B Environ.** 1 : 221–256.

[2] Huang, B., Lei, C., Wei, C., and Zeng, G. 2014. "Chlorinated volatile organic compounds (Cl-VOCs) in environment - sources, potential human health impacts, and current remediation technologies" **Environ. Int.** 71 : 118–138.

[3] Vu, V.H., Belkouch, J., Ould-Dris, A., and Taouk, B. 2009. "Removal of hazardous chlorinated VOCs over Mn-Cu mixed oxide based catalyst" **J. Hazard. Mater.** 169 : 758–765.

[4] Chen, Q.Y., Li, N., Luo, M.F., and Lu, J.Q. 2012. "Catalytic oxidation of dichloromethane over $Pt/CeO_2–Al_2O_3$ catalysts." **Appl. Catal. B Environ.** 127 : 159–166.

[5] กรมควบคุมมลพิษ. 2014. **รายงานสถานการณ์มลพิษของประเทศไทย ปี 2557**. [online]. Available: http://infofile.pcd.go.th/mgt/pcdreport_Pollution2557.pdf?CFID=1312011&CFTOKEN=97230177

[6] Qi, P., Vermesh, O., Grecu, M., Javey, A., Wang, Q., Dai, H., Peng, S., and Cho, K.J. 2003. "Toward large arrays of multiplex functionalized carbon nanotube sensors for highly sensitive and selective molecular detection." **Nano Lett.** 3 : 347–351.

[7] Wongwiriyapan, W., Honda, S.I., Konishi, H., Mizuta, T., Ikuno, T., Ito, T., Maekawa, T., Suzuki, K., Ishikawa, H., Oura, K., and Katayama, M. 2005. "Single-walled carbon nanotube thin-film sensor for ultrasensitive gas detection." **Jpn. J. Appl. Phys.**, 44 : L482-L484.

[8] Li, J., Lu, Y., Ye, Q.L., Han, J., and Meyyappan, M. 2003. "Carbon Nanotube Based Chemical Sensors for Gas and Vapor Detection." **Nano. Lett.** 3 : 929-933.

[9] Cantalini, C., Valentini, L., Armentano, I., Lozzi, L., Kenny, J.M., and Santucci, S. 2003. "Sensitivity to NO_2 and cross-sensitivity analysis to NH_3, ethanol and humidity of carbon nanotubes thin film prepared by PECVD." **Sens. Actuators B Chem.** 95 : 195–202.

[10] Abraham, J.K., Philip, B., Witchurch, A., Varadan, V.K., and Reddy, C.C. 2004. "A compact wireless gas sensor using a carbon nanotube/PMMA thin film chemiresistor." **Smart Mater. Struct.** 13 : 1045–1049.

[11] Yoon, H., Xie, J., Abraham, J.K., Varadan, V.K., and Ruffin, P.B. 2006. "Passive wireless sensors using electrical transition of carbon nanotube junctions in polymer matrix." **Smart Mater. Struct.** 15 : S14–S20.

[12] Santhanam, K.S.V., Sangoi, R., and Fuller, L. 2005. "A chemical sensor for chloromethanes using a nanocomposite of multiwalled carbon nanotubes with poly(3-methylthiophene)." **Sens. Actuators B Chem.** 106 : 766–771.

[13] Cho, S.M., Kim, Y.J., Kim, Y.S., Yang, Y., and Ha, S.C. 2004. "The application of carbon nanotube - polymer composite as gas sensing materials." **Proc. IEEE Sensors** 701–704.

[14] Wang, F., Gu, H., and Swager, T.M. 2008. "Carbon nanotube/polythiophene chemiresistive sensors for chemical warfare agents." **J. Am. Chem. Soc.** 130 : 5392–5393.

[15] Wei, C., Dai, L., Roy, A., and Tolle, T.B. 2006. "Multifunctional chemical vapor sensors of aligned carbon nanotube and polymer composites." **J. Am. Chem. Soc.** 128 : 1412–1413.

[16] Castro, M., Kumar, B., Feller, J.F., Haddi, Z., Amari, A., and Bouchikhi, B. 2011. "Novel e-nose for the discrimination of volatile organic biomarkers with an array of carbon nanotubes (CNT) conductive polymer nanocomposites (CPC) sensors." **Sens. Actuators B Chem.** 159 : 213–219.

[17] Kumar, B., Castro, M., and Feller, J.F. 2013. "Quantum resistive vapour sensors made of polymer coated carbon nanotubes random networks for biomarkers detection." **Chem. Sens.** 3 : 1–7.

[18] Lu, Y., Partridge, C., Meyyappan, M., and Li, J. 2006. "A carbon nanotube sensor array for sensitive gas discrimination using principal component analysis." **J. Electroanal. Chem.** 593 : 105–110.

[19] Leghrib, R. Felten, A., Demoisson, F., Reniers, F., Pireaux, J.J. and Llobet, E. 2010. "Room-temperature, selective detection of benzene at trace levels using plasma-treated metal-decorated multiwalled carbon nanotubes", **Carbon** 48 : 3477–3484.

[20] Baccar, H., Thamri, A., Clément, P., Llobet, E., and Abdelghani, A., 2015. "Pt- and Pd-decorated MWCNTs for vapour and gas detection at room temperature." **Beilstein J. Nanotechnol.** 6 : 919–927.

[21] Iijima, S. 1991. "Helical microtubules of graphitic carbon." **Nature** 354 : 56–58.

[22] Iijima, S. 2002. "Carbon nanotubes: past, present, and future." **Phys. B.** 323 : 1–5.

[23] Terrones, M. 2003. "Science and technology of the twenty-first century: Synthesis, properties, and applications of carbon nanotubes." **Annu. Rev. Mater. Res.** 33 : 419–501.

[24] Hong, S., and Myung, S. 2007. "Nanotube electronics: A flexible approach to mobility." **Nat. Nanotechnol.** 2 : 207–208.

[25] Pop, E., Mann, D., Wang, Q., Goodson, K., and Dai, H.J. 2006. "Thermal conductance of an individual single-wall carbon nanotube above room temperature." **Nano Lett.** 6 : 96–100.

[26] Kim, P., Shi, L., Majumdar, A., and McEuen, P.L. 2001. "Thermal transport measurements of individual multiwalled nanotubes." **Phys. Rev. Lett.** 87 : 215502(1-4).

[27] Parker, W.J., Jenkins, R.J., Butler, C.P., and Abbott,, G.L. 1961. "Flash method of determining thermal diffusivity, heat capacity, and thermal conductivity." **J. Appl. Phys.** 32 : 1679–1684.

[28] Anthony, T.R., Banholzer, W.F., Fleischer, J.F., Wei, L., Kuo, P.K., Thomas, R.L., and Pryor, R.W. 1990, "Thermal diffusivity of isotopically enriched C12 diamond." **Phys. Rev. B.** 42 : 1104–1111.

[29] Peng, B., Locascio, M., Zapol, P., Li, S., Mielke, S.L., Schatz, G.C., and Espinosa, H.D. 2008. "Measurements of near-ultimate strength for multiwalled carbon nanotubes and irradiation-induced crosslinking improvements." **Nat Nano.** 3 : 626–631.

[30] Demczyk, B.G., Wang, Y.M., Cumings, J., Hetman, M., Han, W., Zettl, A., and Ritchie, R.O. 2002. "Direct mechanical measurement of the tensile strength and elastic modulus of multiwalled carbon nanotubes." **Mater. Sci. Eng. A.** 334 : 173–178.

[31] Sinnott, S.B., and Andrews, R. 2010. "Carbon nanotubes : Synthesis, properties, and applications." **Crit. Rev. Solid State Mater. Sci.** 26 : 37–41.

[32] Meo, M. and Rossi, M. 2006. "Prediction of Young's modulus of single wall carbon nanotubes by molecular-mechanics based finite element modelling." **Compos. Sci. Technol.** 66 : 1597–1605.

[33] Chae, H.G., and Kumar, S. 2006. "Rigid-rod polymeric fibers." **J. Appl. Polym. Sci.** 100 : 791–802.

[34] Bellucci, S. 2005. "Carbon nanotubes: physics and applications." **Phys. Status Solidi.** 2 : 34–47.

[35] Szabó, A., Perri, C., Csató, A., Giordano, G., Vuono, D., and Nagy, J.B. 2010. "Synthesis methods of carbon nanotubes and related materials." **Materials (Basel).** 3 : 3092–3140.

[36] Guo, T., Nikolaev, P., Thess, A., Colbert, D.T., and Smalley, R.E. 1995. "Catalytic growth of single-walled manotubes by laser vaporization." **Chem. Phys. Lett.** 243 : 49–54.

[37] Muangrat, W., Gallnom, E., Issro, C., Pfeiler, W., and Bohnes, V.P. 2012. "Effect of structure and morphology of carbon nanotubes on NO_2 gas sensing." **Songklanakarin J. Sci. Technol.** 34 : 695–699.

[38] Lee, C.J., Park, J., and Yu, J.A. 2002. "Catalyst effect on carbon nanotubes synthesized by thermal chemical vapor deposition." **Chem. Phys. Lett.** 360 : 250–255.

[39] Kong, J., Cassell, A.M., and Dai, H. 1998. "Chemical vapor deposition of methane for single-walled carbon nanotubes." **Chem. Phys. Lett.** 292 : 567–574.

[40] Muangrat, W., Porntheeraphat, S., and Wongwiriyapan, W., 2013. "Effect of metal catalysts on synthesis of carbon nanomaterials by alcohol catalytic chemical vapor deposition." **Eng. J.** 17 : 35–39.

[41] Kumar, M., and Ando, Y. 2010. "Chemical vapor deposition of carbon nanotubes: A review on growth mechanism and mass production." **J. Nanosci. Nanotechnol.** 10 : 3739–3758.

[42] Banica, F.G. 2012. **Chemical Sensors and Biosensors: Fundamentals and Applications,** John Wiley & Sons.

[43] Alothman, Z.A. 2012. "A review: Fundamental aspects of silicate mesoporous materials." **Materials (Basel)** 5 : 2874–2902.

[44] The National Institute for Occupational Safety and Health (NIOSH). 2016. **Immediaely Dangerous to Life or Health Concentrations (IDLH).** [online]. Available: Available: http://www.cdc.gov/niosh/

[45] กรมควบคุมมลพิษ. 2012. **มาตรฐานค่าสารอินทรีย์ระเหยง่ายในบรรยากาศโดยทั่วไป.** [online]. Available: http://www.pcd.go.th/info_serv/reg_std_airsnd01.html

[46] Kanan, S.M., El-Kadri, O.M., Abu-Yousef, I.A., and Kanan, M.C. 2009. "Semiconducting metal oxide based sensors for selective gas pollutant detection." **Sensors** 9 : 8158–8196.

[47] Fine, G.F., Cavanagh, L.M., Afonja, A., and Binions, R. 2010. "Metal oxide semi-conductor gas sensors in environmental monitoring." **Sensors** 10 : 5469–5502.

[48] Peigney, A., Laurent, C., Flahaut, E., Bacsa, R.R., and Rousset, A. 2001. "Specific surface area of carbon nanotubes and bundles of carbon nanotubes." **Carbon** 39 : 507–514.

[49] Odom, T.W. 2001. "Electronic properties of single-walled carbon nanotubes." **Aust. J. Chem.** 54 : 601–604.

[50] Kong, J., Franklin, N.R., Zhou, C., Chapline, M.G., Peng, S., Cho, K. and Dai, H. 2000. "Nanotube molecular wires as chemical sensors." **Science** 287 : 622–625.

[51] Someya, T., Small, j., Kim, P., Nuckolls, C., and Yardley, J.T. 2003. "Alcohol vapor sensors based on single-walled carbon nanotube field effect transistors." **Nano. Lett.** 3 : 877-881.

[52] Lu, Y., Li, J., Han, J., Ng, H.T., Binder, C., Partridge, C., and Meyyappan, M. 2004. "Room temperature methane detection using palladium loaded single-walled carbon nanotube sensors." **Chem. Phys. Lett.** 391 : 344–348.

[53] Athawale, A.A., Bhagwat, S.V., and Katre, P.P. 2006. "Nanocomposite of Pd-polyaniline as a selective methanol sensor." **Sens. Actuators B Chem.** 114 : 263–267.

[54] Choudhury, A. 2009. "Polyaniline/silver nanocomposites: Dielectric properties and ethanol vapour sensitivity." **Sens. Actuators B Chem.** 138 : 318–325.

[55] Shirsat, M.D., Bangar, M.A., Deshusses, M.A., Myung, N.V., and Mulchandani, A. 2009. "Polyaniline nanowires-gold nanoparticles hybrid network based chemiresistive hydrogen sulfide sensor." **Appl. Phys. Lett.** 94 : 2–4.

[56] Bilić, A., Reimers, J.R., Hush, N.S., and Hafner, J. 2002. "Adsorption of ammonia on the gold (111) surface." **J. Chem. Phys.** 116 : 8981–8987.

[57] Wongwiriyapan, W., Inoue, S., Ito, T., Shimazaki, R., Maekawa, T., Suzuki, K., Ishikawa, H., Honda, S.I., Oura, K., and Katayama, M. 2008. "Highly sensitive detection of carbon monoxide at room temperature using platinum-decorated single-walled carbon nanotubes." **Appl. Phys. Express** 1 : 1–3.

[58] Yasumatsu, H., and Fukui, N. 2015. "Size Dependence of Low-Temperature Catalytic Activity of CO Oxidation Driven by Platinum Clusters Directly Bound to Silicon Substrate Surface." **J. Phys. Chem. C.** 119 : 11217–11223.

[59] Shiraishi, M. and Ata, M., 2001. "Work function of carbon nanotubes." **Carbon** 39 : 1913–1917.

[60] Halas, S., and Durakiewicz, T. 1998. "Work functions of elements expressed in terms of the Fermi energy and the density of free electrons." **J. Phys. Condens. Matter.** 10 : 10815–10826.

[61] Lohninger, H. 2012. **PCA - Loadings and Scores.** [online]. Available: http://www.statistics4u.info/fundstat_germ/cc_pca_loadscore.html

[62] Smith, L.I. 2002. **A tutorial on Principal Components Analysis**, John Wiley & Sons.

[63] Hyvarinen, A. 2009. **Principal component analysis**, Springer-Verlag

[64] Kandjani, S.A., Mirershadi, S. and Niknaiz, A. 2015. **Spin-coating technique.** [online]. Available: http://www.intechopen.com/books/solar-cells-new-approaches-and-reviews/inorganic-organic-perovskite-solar-cells

[65] JEOL. 2016. **Electron Beam Evaporation.** [online]. Available: http://www.jeol.co.jp/en/science/eb.html

[66] Wikipedia. 2016. **Scanning Electron Microscopy.** [online]. Available: https://en.wikipedia.org/wiki/Scanning_electron_microscope

[67] Wikipedia. 2016. **Energy-Dispersive X-ray Spectroscpy**. [online]. Available: https://en.wikipedia.org/wiki/Energy-dispersive_X-ray_spectroscopy

[68] Wikipedia. 2016. **Transmission Electron Microscopy**. [online]. Available: https://en.wikipedia.org/wiki/Transmission_electron_microscopy

[69] The Prashant Kamat Laboratory. 2012. **Raman Spectroscopy**. [online]. Available: https://www3.nd.edu/~kamatlab/facilities_spectroscopy.html

[70] Wikipedia. 2016. **Raman Spectroscopy**. [online]. Available: https://en.wikipedia.org/wiki/Raman_spectroscopy

[71] Wikipedia. 2016. **Fourier Transform Infrared Spectroscopy**. [online]. Available: https://en.wikipedia.org/wiki/Fourier_transform_infrared_ spectroscopy

[72] Wikipedia. 2016. **X-ray Crystallography**. [online]. Available: https://en.wikipedia.org/wiki/X-ray_crystallography

[73] Bourne, D.W.A. 2016. **Fluorescence Spectroscopy**. [online]. Available: https://www.boomer.org/c/p4/c24/c2403.html

[74] Wikipedia. 2016. **Thiophene**. [online]. Available: https://en.wikipedia.org/wiki/Thiophene

[75] Wikipedia. 2016. **Ethyl Cellulose**. [online]. Available: https://en.wikipedia.org/wiki/Ethyl_cellulose

[76] Wikipedia. 2016. **Poly(methyl methacrylate)**. [online]. Available: https://en.wikipedia.org/wiki/Poly(methyl_methacrylate)

[77] Wikipedia. 2016. **Polystyrene**. [online].Available: https://en.wikipedia.org/wiki/Polystyrene

[78] Wikipedia. 2016. **Polyvinyl Acetate**. [online].Available: https://en.wikipedia.org/wiki/Polyvinyl_acetate

[79] A. Jorio, R. Saito, J.H. Hafner, C.M. Lieber, M. Hunter, T. McClure, G. Dresselhaus, M.S. Dresselhaus, Structural (n, m) determination of isolated single-wall carbon nanotubes by resonant Raman scattering, Phys. Rev. Lett. 86 (2001) 1118–1121.

[80] Reichardt, C. 2003. **Solvents and solvent effects in organic chemistry**, 3 rd ed., Wiley-VCH.

[81] Kim, T. and Kwak, D. 2012. "Flexible VOC sensors using conductive polymers and porous membranes for application to textiles." **Fibers Polym.** 13 : 471–474.

[82] Gland, J.L., Sexton, B. A., and Fisher, G.B. 1980. "Oxygen interactions with the Pt(111) surface." **Surf. Sci.** 95 : 587–602.

[83] Papenmeier, D.M., and Rossin, J.A. 1994. "Catalytic oxidation of dichloromethane, chloroform, and their binary mixtures over a platinum alumina catalyst." **Ind. Eng. Chem. Res.** 33 : 3094–3103.

[84] Bai, Y., Jiang, C., Wang, Q., and Wang, T. 2013. "A novel high mechanical strength shape memory polymer based on ethyl cellulose and polycaprolactone." **Carbohydr. Polym.** 96 : 522–527.

[85] Li, X., Jiang, F., Ni, X., Yan, W., Fang, Y., Corke, H., and Xiao, M. 2015. "Preparation and characterization of konjac glucomannan and ethyl cellulose blend films." **Food Hydrocoll.** 44 : 229–236.

[86] Trivedi, M.K., Branton, A., Trivedi, D., Nayak, G., Mishra, R.K., and Jana, S. 2015. "Characterization of physicochemical and thermal properties of biofield treated ethyl cellulose and methyl cellulose." **J. Biomed. Mater. Res.** 3 : 83–91.

[87] Parida, P., Mishra, S.C., Sahoo, S., Behera, A., and Nayak, B.P. 2014. "Development and characterization of ethylcellulose based microsphere for sustained release of nifedipine." **J. Pharm. Anal.** 6 : 1–5.

[88] Yuan, J. Zhu, Y., and Li, L. 2014. "Highly efficient bimetal synergetic catalysis by a multi-wall carbon nanotube supported palladium and nickel catalyst for the hydrogen storage of magnesium hydride." **Chem. Commun.** 50 : 6641–4.

[89] Guo, Q., Liu, D., Huang, J., Hou, and You, T. 2014. "A composite made from palladium nanoparticles and carbon nanofibers for superior electrocatalytic oxidation of formic acid." **Microchim. Acta.** 181 : 797–803.

[90] Li, W., Waje, M., Chen, Z., Larsen, P., and Yan, Y. 2010. "Platinum nanopaticles supported on stacked-cup carbon nanofibers as electrocatalysts for proton exchange membrane fuel cell." **Carbon** 48 : 995–1003.

[91] Li, W., Liang, C., Zhou, W., Qiu, J., Zhou, Z., Sun, G., and Xin, Q. 2003. "Preparation and characterization of multiwalled carbon nanotube-supported platinum for cathode catalysts of direct methanol fuel cells." **J. Phys. Chem. B.** 107 : 6292–6299.

[92] Oura, K., Lifshits, V.G., Saranin, A.A., Zotov, A.V., and Katayama, M. 2003. **Surface Science**, New York, Springer-Verlag Berlin Heidelberg GmbH

[93] Jang, J., Kim, S., and Lee, K.J. 2007. "Fabrication of CdS/PMMA core/shell nanoparticles by dispersion mediated interfacial polymerization." **Chem. Commun.** : 2689–2691.

[94] Zhang, L. Li, F., Chen, Y., and Wang, X. 2011. "Synthesis of transparent ZnO/PMMA nanocomposite films through free-radical copolymerization of asymmetric zinc methacrylate acetate and in-situ thermal decomposition.", **J. Lumin.** 131 : 1701–1706.

[95] Zanotto, A., Luyt, A.S., Spinella, A., and Caponetti, E. 2013. "Improvement of interaction in and properties of PMMA-MWNT nanocomposites through microwave assisted acid treatment of MWNT." **Eur. Polym. J.** 49 : 61–69.

APPENDIX

Effect of Metal Catalysts on Synthesis of Carbon Nanomaterials by Alcohol Catalytic Chemical Vapor Deposition

A.1 Synthesis carbon nanomaterials by alcohol catalytic chemical vapor deposition

An electron-beam evaporator was used to sequentially deposit an under layer (Al (5 nm)/Cr (2 nm)) and a metal catalyst layer (Ni, Co or Fe (5 nm)) on Si substrate. The deposited substrates were then annealed in a quartz tube at 700°C for 60 min under a flow of Ar gas at a flow rate of 500 standard cubic centimeters per minute (sccm). Then, ethanol vapor was introduced by bubbling Ar gas through ethanol at a flow rate of 800 sccm. The chemical vapor deposition (CVD) growth was carried out for 20 min at atmospheric pressure. After that, the synthesized material was cooled down to room temperature under Ar gas at a flow rate of 500 sccm.

A.2 Morphology and structural characterization of carbon nanomaterials

A.2.1 Scanning electron microscopy characterization

The morphology of synthesized CNMs were characterized by field emission scanning electron microscopy (FESEM; JEOL JSM-7800F). The FESEM observation was carried out in a high vacuum mode without any surface treatment with metallic materials.

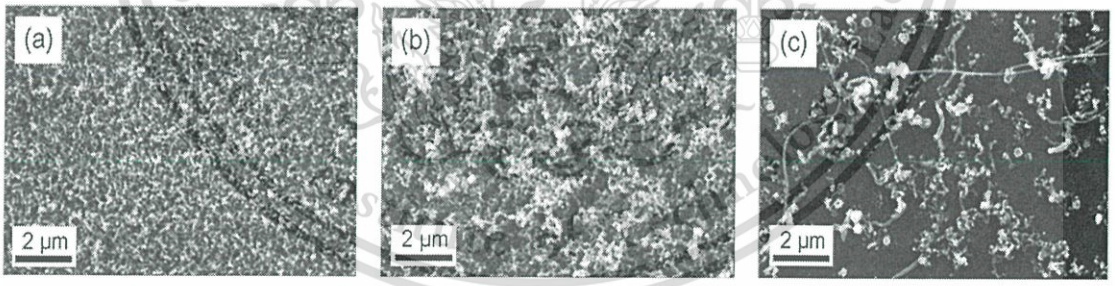

Figure A.1 SEM images of synthesized CNMs from different metal catalyst; (a) Ni, (b) Co and (c) Fe.

Figures A.1(a-c) show FESEM images of CNMs synthesized from Ni, Co and Fe catalysts, respectively. Tubular structures were synthesized in all cases, but their morphologies and structures were different. The SEM images shows that the CNMs grown from Ni and Co catalysts had a relatively high density of tubular structures covered wholly on the surface of substrates (Figs. A.1(a) and 1(b)), while the CNMs

grown from Fe had a low density with a mixture of long-straight and shortly random CNMs (Fig. A.1(c)).

A.2.2 Transmission electron microscopy characterization

The nanostructure of synthesized CNMs were characterized by transmission electron microscopy (TEM; JEOL JE-2010). For sample preparation, synthesized CNMs from the process in section A.2 was diluted with ethanol, followed by drop-casted onto copper (Cu) grid.

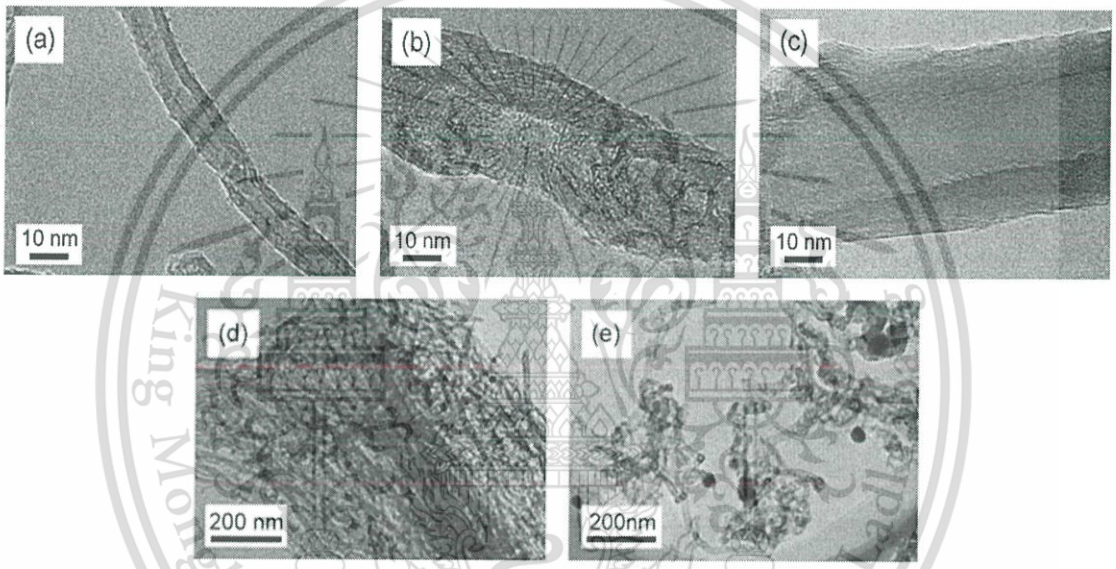

Figure A.2 TEM images of synthesized CNMs from different metal catalyst; (a) Ni, (b) Co and (c) Fe. TEM images at low magnification of CNMs synthesized from (g) Ni and (h) Co.

Figures A.2(a-c) show TEM images of CNMs synthesized from Ni, Co and Fe catalysts, respectively. The TEM images, clearly show that the structures of CNMs grown from different metal catalysts were completely different. The CNMs grown from Ni catalyst shows graphene planes aligning paralleling to each other and to the axis of the tubular structure, indicating multi-walled carbon nanotube (MWNT) structure (Fig. A.2(a)). For the CNMs grown from Co catalysts, their graphene planes are parallel to each other but made an angle with the axis of the tube with bamboo compartments along the tube, indicating bamboo like-MWNT structure (Fig. A.2(b)). CNFs were also mixed in the CNMs grown from Co catalyst. For the CNM grown from Fe catalyst, their

graphene planes are parallel to each other, indicating MWNT structure. The average diameters of the synthesized CNMs from Ni, Co and Fe catalysts were approximately 9.35±4.29, 30.20±12.18 and 43.67±18.70 nm, respectively. From the TEM images at low magnification (Fig. A.2(d-e)), two types of CNMs were observed. One was CNMs without metal catalyst at the tube end. The other was CNMs with clusters of metal catalyst (dark contrast in TEM image) encapsulated at the tube end. This implies that the growth of the synthesized CNMs was based on both the base growth and the tip growth mechanisms, respectively. Moreover, as can be seen in the TEM images at low magnification, the CNMs grown from Ni catalyst showed a higher density of a relatively uniform diameter of MWNTs with a small amount of by-products, when compared to those grown from Co catalyst.

A.2.3 Raman spectroscopy characterization

The carbon structure, purity and crystallinity of synthesized CNMs were analyzed by Raman spectroscopy (Thermo SCIENTIFIC DXR) with an Ar ion laser wavelength of 532 nm (2.33 eV). Figure A.3 shows Raman spectra of synthesized CNMs from different metal catalysts.

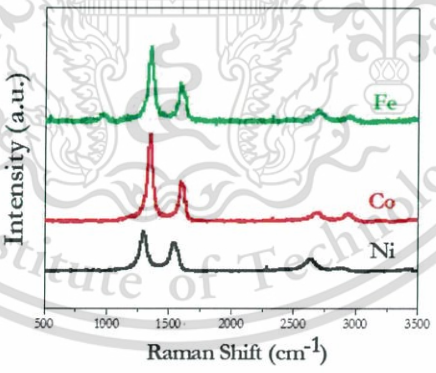

Figure A.3 Raman Spectroscopy of synthesized CNMs from different metal catalysts.

All spectra showed mainly two bands at ~1340 cm^{-1} (D-band disorder carbon) and ~1590 cm^{-1} (G-band graphitic structure), corresponding to MWNT structure. Furthermore, the small peaks at ~2700 cm^{-1} (G´band) were also observed in every sample. This spectrum indicates the overtone or second order of D band, which originates from the two phonon double resonance Raman process. The intensity ratio between G (I_G) band and D (I_D) band, (I_G/I_D) is an indication of the crystallinity of CNMs.

The I_G/I_D ratio of the CNMs synthesized from Ni, Co and Fe were 0.73, 0.44 and 0.49, respectively. Hence, it can be concluded that the CNMs synthesized from Ni catalyst had the highest crystallinity.

A.3 Discussion of effect of metal catalyst on morphology of carbon nanomaterials

In order to understand the effect of Ni catalyst on high yield growth of CNMs, the growth mechanism of CNMs is explained based on the thermodynamics of carbon-metal reaction. The possible growth model of CNMs is as follows: carbon source decomposes and dissolves forming metal carbides on the surface of metal catalyst nanoparticles: additional carbon atoms precipitate and get extracted easily from the metal carbides, leading to formation of CNMs [14]. The direction of the reaction can be considered thermodynamically by the change in Gibbs free energy (ΔG). The reaction proceeds forward when ΔG value is less than zero or negative value ($\Delta G<0$). A previous study has reported that the ΔG of ethanol decomposition at a reaction temperature of 700°C, as shown in Eq. (1), is less than zero [15].

$$C_2H_5OH \rightarrow 2C(s) + 2H_2 + H_2O \quad (1)$$

For the carburization of decomposed carbon source by metal catalyst, the reaction can be expressed as Eq. (2) bellow.

$$C_2H_5OH + M \rightarrow MC_2 + 2H_2 + H_2O \quad (2)$$

where M denotes a metal catalyst and MC_2 denotes metal carbide.

ΔG of carburization reaction of different metal catalysts under acetylene (C_2H_2) system has been reported in several studies. The magnitude of ΔG of Ni, Co and Fe catalysts were in the following order: Fe<Co<Ni [14]. For the C_2H_2OH system, we assumed that ΔG behaves like the C_2H_2 system. That is why the Ni catalyst with the highest magnitude of ΔG gave the highest yield of CNMs, while the Fe catalyst with the lowest magnitude of ΔG gave the lowest yield of CNMs. However, a more accurate

determination of the ΔG for the ethanol system is needed and will be addressed in future work.

A.4 Conclusion

CNMs were successfully synthesized by alcohol catalytic CVD at 700°C using from three different metal catalysts using ethanol as a carbon source. Ni and Fe were shown to be active catalysts for MWNTs growth, while Co acted as an active catalyst for bamboo-like MWNTs and CNFs. Ni catalyst afforded the highest yield and crystallinity, while Fe catalyst afforded the lowest. The average diameter of CNMs synthesized from each catalyst was in the following order: Ni<Co<Fe. The relationship between CNMs yield and metal catalyst type can be explained by the change in Gibbs free energy. We conclude that the desired yield, diameter, structure, morphology and crystallinity of CNMs can be controlled by judicious selection of appropriate metal catalyst.

AUTHOR BIOGRAPHY

Name-Surname	Mr. Worawut Muangrat
Date of Birth	August 5, 1982
Present Address	96/145 moo1, Mheung Sub-district, Muangchonburi District, Chonburi, Thailand 20130

Education

2001-2004	Bachelor of Education (B.Ed.) in Physics, Faculty of Education, Nakhon Pathom Rajabhat University
2009-2011	Master of Science (MSc.) in Physics, Faculty of Science, Burapha University
2012-2016	Doctor of Philosophy (Ph.D.) in Nanoscience and Nanotechnology, College of Nanotechnology, King Mongkut's Institute of Technology Ladkrabang

Scholarships

2009-2010	Scholarship for study in Master of Science in Physics by the Thailand Research Funds (TRF)-Master Research Grant under project "Synthesis of Carbon Nanotubes for Nitrogen Dioxide Detection"
2012-2014	Scholarship for study in Doctor of Philosophy in Nanoscience and Nanotechnology by Thailand Graduate Institute of Science and Technology (TGIST), the National Science and Technology Development Agency (NSTDA) under project "Synthesis of Hybrid Nanocarbon Materials and their Air Pollution Monitoring Application"
2013	Research Scholarship, New Energy and Industrial Technology Development Organization (NEDO) under project "Study on Structure and its Electric Properties of Nanocarbon Materials by Transmission Electron Microscopy", Institute of Carbon Science And Technology, Shinshu University, Nagano, Japan (January 7 to February 2, 2013)
2013	Electronic and Sensor study Visit Scholarship by National Science and Technology Development Agency (NSTDA) and Ministry of Foreign Affairs of the Kingdom of Thailand, Republic of China (ROC) (August 19-23, 2013)

2015-2016 Ph.D. Research Scholarship, Technology Grants (Sanwich Programme) by Austria Government under project "The Doping Carbon Nanotubes with Nitrogen, Boron and Nitrogen-boron and their Gas Sensor Applications", Electronic Properties of Materials Group, Faculty of Physics, University of Vienna, Vienna, Austria (February 1, 2015 – January 31, 2016)

2015 Research Scholarship, The King Prajadhipok and Queen Rambhai Barni Memorial Foundation for Graduate Student under project "Hybrid Nanocarbon Material for Volatile Organic Compounds Detection"

Awards

2013 The Best Presentation Award 1st Place of the 8th Annual Conference of Siam Physics Congress (SPC), March, 21-23, 2013, **"Volatile Organic Compounds Sensors Based on Poly(methyl methacrylate)/single Walled Carbon Nanotubes"**
Worawut Muangrat, Supanit Porntheeraphat and Winadda Wongwiriyapan

2014 The Best Presentation Award 1st Place of the Annual Conference of Siam Physics Congress (SPC), March, 26-29, 2014 **"Benzene Sensor Based on Ethyl Cellulose-coated Single-walled Carbon Nanotubes"**
Worawut Muangrat, Thanattha Chobsilp, Rungroj Maolanon, Supanit Porntheeraphat and Winadda Wongwiriyapan

Achievements

International Journal

(1) Worawut Muangrat, Rungroj Maolanon, Sirapat Pratontep, Supanit Porntheeraphat and Winadda Wongwiriyapan
"Polymer-coated Single-walled Carbon Nanotubes for Ethanol and Dichloromethane Discrimination"
Advanced Materials Research **802**, 267-272 (2013).

(2) Worawut Muangrat, Supanit Porntheeraphat and Winadda Wongwiriyapan
"Effect of Metal Catalysts on Carbon Nanotubes by Alcohol Catalytic Chemical Vapor Deposition"
Engineering Journal **17**, 35-40 (2013).

(3) Thanattha Chobsilp, Winadda Wongwiriyapan, Chaisak Issro, Worawut Muangrat, Weerawut Chaiwat, Apiluck Eiad-ua, Tawatchai Charinpanitkul and Komkrit Suttiponpanit

"Study on Effect of Acid and Heat Treatments of Multi-walled Carbon Nanotubes on Benzene Detection"

Advanced Materials Research, **1103**, 105-111 (2015).

(4) Worawut Muangrat, Thanawee Chodjarusaward, Sirapat Pratontep, Rungroj Maolanon, Supanit Porntheeraphat and Winadda Wongwiriyapan

"Poly(methyl methacrylate) and Thiophene Coated Single-walled Carbon Nanotubes for Volatile Organic Compounds Discrimination"

The Japanese Journal of Applied Physics 55(2), 02BD04 (1-6) (2016).

(5) Worawut Muangrat, Visittapong Yordsri, Rungroj Maolanon, Supanit Porntheeraphat and Winadda Wongwiriyapan

"Hybrid Sensor based on Platinum Nanoparticles/Poly(methyl methacrylate)-coated Single-walled Carbon Nanotubes for Dichloromethane Detection with High Response Magnitude"

Diamond and Related Materials, **65**, 183-190 (2016).

International Proceeding

(1) Worawut Muangrat, Supanit Porntheeraphat and Winadda Wongwiriyapan

"Effect of Metal Catalysts on Synthesis of Carbon Nanotubes by Alcohol Catalytic Chemical Vapor Deposition"

The 1st Joint Conference in Renewable Energy and Nanotechnology (JCREN2012), Bangkok, Thailand, December 19-20, 2012, 216-219.

(2) Worawut Muangrat, Rungroj Maolanon, Sirapat Pratontep, Supanit Porntheeraphat and Winadda Wongwiriyapan

"Polymer-coated Single-walled Carbon Nanotubes for Ethanol and Dichloromethane Discrimination"

International Conference of Engineering, Applied Sciences, and Technology (ICEAST2013), Bangkok, Thailand, August 21-24, 2013, 267-272.

(3) Thanattha Chobsilp, Winadda Wongwiriyapan, Chaisak Issro, Worawut Muangrat, Weerawut Chaiwat, Apiluck Eiad-ua, Tawatchai Charinpanitkul and Komkrit Suttiponpanit

"Study on Effect of Acid and Heat Treatments of Multi-walled Carbon Nanotubes on Benzene Detection"

The German-Thai Symposium on Nanoscience and Nanotechnology (GTSNN2014), Phitsanulok, Thailand, October 14-17, 2014.

(4) Thanattha Chobsilp, Winadda Wongwiriyapan, Chaisak Issro, Worawut Muangrat, Weerawut Chaiwat, Apiluck Eiad-ua, Tawatchai Charinpanitkul and Komkrit Suttiponpanit

"Surface Functionalization of Multi-walled Carbon Nanotubes by Oxygen Plasma Treatment for Benzene Detection"

The 3rd Joint Conference in Renewable Energy and Nanotechnology (JCREN2014), Kanchanaburi, Thailand, December 22-23, 2014.

National Proceeding

(1) Chidchanok Markjun, Siriwat Potivejkul, Winadda Wongwiriyapan and Worawut Muangrat

"Techniques to determination of the ozone generators rated and operation time based on the spreading and the half-life of ozone"

The 37th Electrical Engineering Conference (EECON37), Khonkaen, Thailand, November 19-21, 2014.

International Conference Presentation

(1) Worawut Muangrat, Supanit Porntheeraphat and Winadda Wongwiriyapan

"Effect of Metal Catalysts on Synthesis of Carbon Nanotubes by Alcohol Catalytic Chemical Vapor Deposition"

The 1st Joint Conference in Renewable Energy and Nanotechnology (JCREN2012), Bangkok, Thailand, December 19-20, 2012, 216-219.

(2) Worawut Muangrat, Thanawee Chodjarusaward, Sirapat Pratontep, Rungroj Maolanon Supanit Porntheeraphat and Winadda Wongwiriyapan

"Poly(methyl methacrylate) and Thiophene-coated Single-Walled Carbon Nanotubes for Volatiles Organic Compounds Discrimination"

The 5th International Symposium on Organic and Inorganic Electronic Materials and Related Nanotechnologies (EM-NANO 2015), Niigata, Japan, June 16-19, 2015.

(3) Worawut Muangrat, Visittapong Yordsri, Rungroj Maolanon, Sirapat Pratontep, Supanit Porntheeraphat and Winadda Wongwiriyapan

"Hybrid Sensor based on Platinum Nanoparticles/Poly(methyl methacrylate)-coated Single-walled Carbon Nanotubes for Dichloromethane Detection with High Response Magnitude"

International Conference on Diamond and Carbon Materials, Bad Homburg, Germany, September 6-10, 2015.

National Conference Presentation

(1) Worawut Muangrat, Supanit Porntheeraphat and Winadda Wongwiriyapan **"Growth of Carbon Spheres and Carbon Onions by Alcohol Catalytical Chemical Vapor Deposition"**
The Microscopy Society of Thailand 30th, Chanthaburi, Thailand, January 23-25, 2013, 169.

(2) Worawut Muangrat, Supanit Porntheeraphat and Winadda Wongwiriyapan **"Volatile Organic Compounds Sensors Based on Poly(methyl methacrylate)/single-walled Carbon Nanotubes"**
The 8th Annual Conference of Thai Physics Society, Chaingmai, Thailand, March 21-23, 2013, 304.

(3) Worawut Muangrat, Thanawee Chodjarusaward, Sirapat Pratontep, Rungroj Maolanon Supanit Porntheeraphat and Winadda Wongwiriyapan **"Thiophene and Poly(methyl methacrylate)-coated Single-walled Carbon Nanotubes for Volatile Organic Compounds Discrimination"**
Conference of the 9th Annual Conference of Thai Physics Society, Nakhon Ratchasima, Thailand, March 26-29, 2014, 107.

(4) Worawut Muangrat, Thanattha Chobsilp, Rungroj Maolanon, Supanit Porntheeraphat and Winadda Wongwiriyapan **"Benzene Sensor Based on Ethyl Cellulose-coated Single-walled Carbon Nanotubes"**
The 9th Annual Conference of Thai Physics Society, Nakhon Ratchasima, Thailand, March 26-29, 2014, 199.

(5) Nuttaya Sukgorn, Chinathun Pinming, Chaiyanut. Jirayupat, Rattanachai Inyeaw, Visittapong Yordsri, Worawut Muangrat, Paweena Dulyaseree and Winadda Wongwiriyapan **"Synthesis of Carbon Nanotubes Using Cooking Oils as Carbon Precursors"**
The 9th Annual Conference of Thai Physics Society, Nakhon Ratchasima, Thailand, March 26-29, 2014, 229.

Work Experience

2005-2007	Mathematics Teacher, Assumption College Rayong
2007-2008	Head of Mathematics Learning Group, Assumption College Rayong
2010-2011	Special Lecturer, Department of Physics, Faculty of Science, Burapha University
2011-2012	Lecturer, Department of Physics, Faculty of Science and Technology, Rambhai Barni Rajabhat University

2016-Present	Lecturer, Department of Basic Science and Mathematics, Navamindradhiraj University

Diamond & Related Materials 65 (2016) 183–190

Contents lists available at ScienceDirect

Diamond & Related Materials

journal homepage: www.elsevier.com/locate/diamond

Hybrid gas sensor based on platinum nanoparticles/poly(methyl methacrylate)-coated single-walled carbon nanotubes for dichloromethane detection with a high response magnitude

Worawut Muangrat [a], Visittapong Yordsri [b], Rungroj Maolanon [c], Sirapat Pratontep [a,d,e], Supanit Porntheeraphat [f], Winadda Wongwiriyapan [a,d,e,*]

[a] College of Nanotechnology, King Mongkut's Institute of Technology Ladkrabang, Chalongkrung Rd., Ladkrabang, Bangkok 10520, Thailand
[b] National Metal and Materials Technology Center, Phahonyothin Rd., Khlong Luang, Pathumthani 12120, Thailand
[c] National Nanotechnology Center, Phahonyothin Rd., Khlong Luang, Pathumthani 12120, Thailand
[d] Nanotec-KMITL Center of Excellence on Nanoelectronic Devices, Chalongkrung Rd., Ladkrabang, Bangkok 10520, Thailand
[e] Thailand Center of Excellence in Physics, CHE, 328 Si Ayutthaya Rd., Bangkok 10400, Thailand
[f] National Electronics and Computer Technology Center, Phahonyothin Rd., Khlong Luang, Pathumthani 12120, Thailand

ARTICLE INFO

Article history:
Received 1 December 2015
Received in revised form 15 March 2016
Accepted 17 March 2016
Available online 24 March 2016

Keywords:
Single-walled carbon nanotube
Dichloromethane
Poly(methyl methacrylate)
Platinum nanoparticles
Gas sensor

ABSTRACT

A dichloromethane (DCM) sensor with a high response magnitude was successfully fabricated using the integration of single-walled carbon nanotubes (SWNTs), poly(methyl methacrylate) (PMMA) and platinum nanoparticles (Pt NPs). A pristine SWNT network was first formed by drop-casting onto printed circuit board (PCB) substrates. Next, PMMA was coated onto the pre-dropped SWNT network by spin coating using a PMMA-toluene solution, followed by the deposition of Pt NPs by electron-beam evaporation (hereafter referred to as Pt/PMMA/SWNT). The Pt/PMMA/SWNT enabled an approximately 69-fold improvement in DCM detection compared to pristine SWNT. The high response magnitude of the Pt/PMMA/SWNT was successfully achieved because of the incorporation of PMMA and Pt functions. Swelling of the PMMA matrix as a result of DCM adsorption leads to PMMA volume expansion, thereby increasing the SWNT-SWNT distance, which results in an increase in the resistance. Pt NPs promote the dissociation of DCM to CO, and consequently the CO oxidation on the Pt NPs catalyst and electron donation from Pt NPs to SWNTs, resulting in an increase in the resistance. Moreover, a linear relationship was obtained between the sensor response of the Pt/PMMA/SWNT and the concentration of DCM. These results suggest that the integration of SWNTs with PMMA and Pt NPs is a promising approach for improving DCM detection at room temperature.

1. Introduction

Volatile organic compounds (VOCs) [1] have been widely used in various industrial processes and commercial products, such as transport, household chemicals, paints and adhesives. Several VOCs are directly harmful to environmental and human health even at trace levels in ambient air. For example, dichloromethane (DCM, CH_2Cl_2), which is mainly used in the metal surface degreasing and electronics industry, is known as the cause of respiratory and central nervous system, chronic toxicity and carcinogenicity [2–4]. Hence, environmental monitoring and industrial safety are absolutely crucial for the protection of environmental and human health. Since the last decade, the most widely used analytical methods for VOC detection have been gas chromatography/mass spectrometry (GC/MS), high-performance liquid chromatography (HPLC) and photoionization detection (PID) because of their high sensitivity and reliability. Nevertheless, their practical application is highly limited as a result of their complexity, relatively high cost, unportability and calibration requirements to maintain accuracy. Recently, a gas sensor based on the simple change in its resistance in response to analytes has become a promising candidate for practical sensing devices. The advantages of a gas sensor include its compact size, real-time monitoring and low power consumption. Gas sensors based on metal oxide materials have been widely developed for VOC detection with a detection limit down to the parts per million (ppm) level [5,6]. Despite their high sensitivity, these sensors exhibit drawbacks, including nonselectivity and high power consumption (operating temperature > 200 °C). Several nanostructured materials, such as single-walled carbon nanotubes (SWNTs) [7], have attracted considerable attention as alternative sensing materials because of their distinctive characteristics in structural, electrical, optical, mechanical and thermal properties. SWNTs have shown outstanding potential for gas sensing

* Corresponding author at: College of Nanotechnology, King Mongkut's Institute of Technology Ladkrabang, Chalongkrung Rd., Ladkrabang, Bangkok 10520, Thailand.
E-mail address: winadda.wo@kmitl.ac.th (W. Wongwiriyapan).

http://dx.doi.org/10.1016/j.diamond.2016.03.016
0925-9635/

applications because of their well-organized nanostructure, large specific surface area [8] and electrical properties [9,10]. SWNT-based sensors have demonstrated high response to oxidizing gases down to the parts per billion (ppb) level under room-temperature operation [11–14]; however, they are weakly sensitive to VOCs. In recent years, to overcome these obstacles, many efforts have been made aiming to improve the VOC sensing performance of such sensors by means of SWNTs functionalized with polymers [15–18] and metal nanoparticles (NPs) [19–21]. For instance, a gas sensor based on functionalized-multi-walled carbon nanotubes and poly(methyl methacrylate) composites (f-MWNT-PMMA) by dip-coating technique has been demonstrated for VOC detection [15,16]. This f-MWNT-PMMA-based sensor shows a high response to a saturated vapor of DCM [15] but a low sensor response to DCM vapor in a partial pressure range of 27–273 Torr [16]. In addition, MWNTs were functionalized using potassium permanganate with the help of a phase transfer catalyst. Although the major advantage of this process is a high yield of functionalized MWNTs, but it is time-consuming and involves the use of hazardous chemicals. Another type of gas sensor was fabricated using conductive polymer-MWNT composites by spray layer by layer (sLbL) without further treatment of MWNTs for VOC detection at a saturated vapor [17]. Recently, W. Muangrat et al. [18] demonstrated a simple preparation of gas sensor by spin-coating PMMA on the drop-casted SWNTs (PMMA/SWNT). The sensor response of PMMA/SWNT to DCM greatly increases 5.4-fold higher than that of pristine SWNTs. The sensing mechanism of the polymer-functionalized carbon nanotubes (CNTs) is attributed to the swelling of the polymer matrix upon exposure to the organic vapor molecules, leading to volume expansion, and thereby giving rise to an increase in the CNT–CNT distance, resulting in an increase in the resistance. Additionally, the deposition of palladium (Pd) and platinum (Pt) nanoparticles (NPs) on MWNTs enhances the sensor response toward aromatic VOCs (benzene and toluene) and non-aromatic VOCs (acetone, ethanol and methanol) [21]. The sensing mechanism of metal NP-decorated CNTs can be explained by the electron transport from the metal NPs to the CNTs, resulting in an increase in the resistance. As mentioned above, polymer and metal NPs are effective in improving VOC sensitivity by different mechanisms. Thus, utilizing the functions of both the polymer and the metal NPs in a single device is a promising route to improving its VOC sensitivity and response magnitude.

In this work, we successfully demonstrated highly sensitive detection of DCM vapor under room temperature conditions by means of SWNTs functionalized with PMMA and Pt NPs without further SWNT treatment. The response magnitude of the hybrid sensor to DCM was 69-fold higher than that of pristine SWNTs and linearly increased with increasing DCM concentration. The sensing mechanism was elucidated by catalytic oxidation on the Pt NPs catalyst surface and polymer swelling. The proposed hybrid sensor shows figures of merit over the previous reports in terms of the simplicity in sensor fabrication and the enhancement of the sensor response magnitude to VOCs at the concentration lower than a saturated vapor.

2. Experimental methods

2.1. Fabrication of gas sensor device

A printed circuit board (PCB) consisting of an interdigitated Cu/Au electrode with a gap of 250 μm was used as the sensor platform. An SWNT suspension was prepared by dispersing SWNTs, (diameter and length in the ranges of 1.2–1.5 nm and 2–5 μm, respectively) in 1,2-dichloroethane by ultrasonication for 3 h and subsequently dropping onto the PCB. The electrical resistance of the SWNT on the PCB was adjusted to approximately 100 kΩ. A solution of PMMA (M_w = 94,600 g/mol) was prepared in toluene and stirred for 24 h. Then, the PMMA solution was spin-coated onto the predropped SWNT network at a spinning speed of 3000 rounds per minute for 5 min, followed by heating at 100 °C for 24 h to eliminate the solvent in the sensor samples. The PMMA concentration was varied between 1 and 5 wt.%. Next, the prepared PMMA-coated SWNTs were deposited with Pt NPs by electron-beam evaporation. The amount of the deposited Pt NPs was monitored by a quartz crystal oscillator embedded in the electron-beam evaporation equipment as a thickness of 2 and 5 nm (hereafter referred to as Pt/PMMA/SWNT). For comparison, SWNTs with only a PMMA coating or Pt NP decoration were also fabricated (hereafter referred to as PMMA/SWNT and Pt/SWNT, respectively). A schematic view of the hybrid sensor and details of the fabricated gas sensor are shown in Fig. 1 and Table 1, respectively.

2.2. Characterization techniques

The morphologies of the pristine SWNTs and PMMA/SWNTs were characterized by field emission scanning electron microscopy (FESEM; JEOL JSM-7800F). The FESEM observation was carried out in a high vacuum mode with a base pressure of approximately 9×10^{-5} Pa and an acceleration voltage of 1 kV without any surface treatment with metallic materials. The elemental composition of Pt/PMMA/SWNT was studied by FESEM equipped with an energy dispersive X-ray spectrometer (EDS; OXFORD). Transmission electron microscopy (TEM; JEOL JE-2010) was employed to characterize the nanostructure of the Pt/SWNTs. The carbon structure, purity and crystallinity were analyzed by Raman spectroscopy (Thermo SCIENTIFIC DXR) with an Ar ion laser wavelength of 532 nm (2.33 eV). The crystal structure was characterized by X-ray diffraction (XRD; Rigaku TTRAX II) using Cu Kα with a wavelength of 1.54 Å at a scan rate of 1 °/min. The functional group of PMMA was characterized by Fourier transform infrared spectroscopy (FTIR; Perkin Elmer, Spectrum One). The FTIR sample was prepared by mixing SWNTs powder with potassium bromide (KBr) and pressing in a pellet form. Then, the prepared pellet was coated and decorated with PMMA and Pt NPs, respectively. Typical FTIR spectra in an absorbance mode were scanned in a wavenumber range of 500–4000 cm^{-1}.

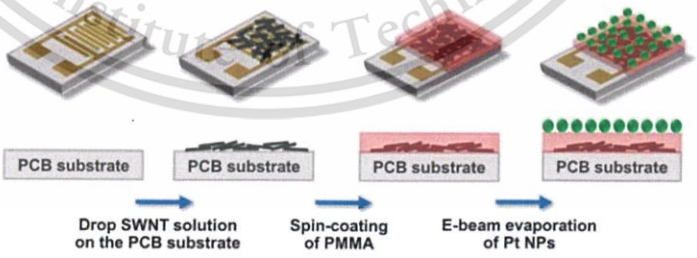

Fig. 1. Schematic view of hybrid sensor.

Table 1
Summary of sensors based on hybrid SWNTs.

Sensor configuration	Designation of sensor
Pristine SWNT	$S_{0.0}$
PMMA(1 wt.%)/SWNT	$S_{0.1}$
PMMA(5 wt.%)/SWNT	$S_{0.5}$
Pt(2 nm)/SWNT	$S_{2.0}$
Pt(5 nm)/SWNT	$S_{5.0}$
Pt(2 nm)/PMMA(1 wt.%)SWNT	$S_{2.1}$
Pt(2 nm)/PMMA(5 wt.%)SWNT	$S_{2.5}$
Pt(5 nm)/PMMA(1 wt.%)SWNT	$S_{5.1}$
Pt(5 nm)/PMMA(5 wt.%)SWNT	$S_{5.5}$

2.3. Gas sensor measurement

The sensor response to DCM vapor was investigated at room temperature by recording the electrical resistance using a FLUKE NetDAQ during cycles of alternating supply of dry N_2 gas and DCM vapor. The sensors were placed in a stainless steel chamber and N_2 gas was introduced into the chamber at a flow rate of 3.0 lpm for 600 s as a baseline. Then, N_2 was replaced with DCM vapor by bubbling liquid DCM with N_2 carrier gas at a flow rate of 1.5 lpm for 300 s. The concentration of the DCM vapor was adjusted by controlling the temperature of the DCM liquid. The sensors were recovered by purging with 3.0 lpm of N_2 for 600 s. The sensor response (SR) was defined as $SR = (R_{DCM} - R_0) / R_0$, where R_{DCM} and R_0 are the resistances of the sensor after and before DCM exposure, respectively. To compare the responses of all the sensors, the sensor responses were normalized by the DCM concentration. The normalized sensor response (NSR) was defined as the ratio between the sensor response at a time of 900 s (SR_{900}) and the DCM concentration (C_{DCM}): $NSR = SR_{900} / C_{DCM}$.

3. Results and discussion

3.1. Characterization of sensor materials: morphology, structure, composition, and crystallinity

First, pristine SWNTs and PMMA/SWNTs were morphologically characterized by FESEM. The pristine SWNTs assembled into a network of overlying SWNTs, forming a conductive network structure on the substrate, as shown in Fig. 2(a). Fig. 2(b and c)shows the cross-sectional FESEM images of PMMA(1 wt.%)/SWNT ($S_{0.1}$) and PMMA(5 wt.%)/SWNT ($S_{0.5}$), respectively. The thicknesses of the PMMA(1 wt.%) and PMMA(5 wt.%) coatings on the SWNTs were 0.40 and 2.64 μm, respectively. From the FESEM image of $S_{0.1}$ (Fig. 2(b)), the SWNT network was shown to be buried in the PMMA matrix and some of the SWNT bundles were protruding from the PMMA surface. However, in the case of $S_{0.5}$, PMMA(5 wt.%)/SWNT, PMMA completely covered the pristine SWNT network. The thickness of the PMMA film was controlled by the concentration and viscosity of the PMMA solution. Fig. 1(d and e)shows the TEM images of the Pt-decorated SWNT with different Pt loading amounts ($S_{2.0}$ and $S_{5.0}$, respectively). The Pt NPs were attached to the sidewalls of the pristine SWNT bundles, whereas the SWNT bundles maintained their structure. The average diameters of the Pt NPs of $S_{2.0}$ and $S_{5.0}$ were 3.53 ± 0.94 and 4.04 ± 0.77 nm, respectively. The Pt NPs on $S_{5.0}$ exhibited greater coverage and a narrower size distribution compared to those of $S_{2.0}$. For Pt/PMMA/SWNT, it is hard to directly observe its structure by TEM because of the damage of the electron beam on PMMA. Thus, FESEM-EDS, XRD and FTIR techniques were utilized to confirm the existence of the Pt NPs and PMMA in the Pt/PMMA/SWNT.

The elemental composition of $S_{5.5}$ was determined by EDS. The analyzed surface area for EDS mapping is shown in Fig. 3(a). The EDS elemental mapping image revealed that $S_{5.5}$ consists of Pt (in purple), carbon (in red) and oxygen (in green), as shown in Fig. 3(b–d), respectively. The Pt mapping clearly indicates that the Pt NPs are homogeneously distributed on the $S_{5.5}$ as shown in Fig. 3(b). Carbon and

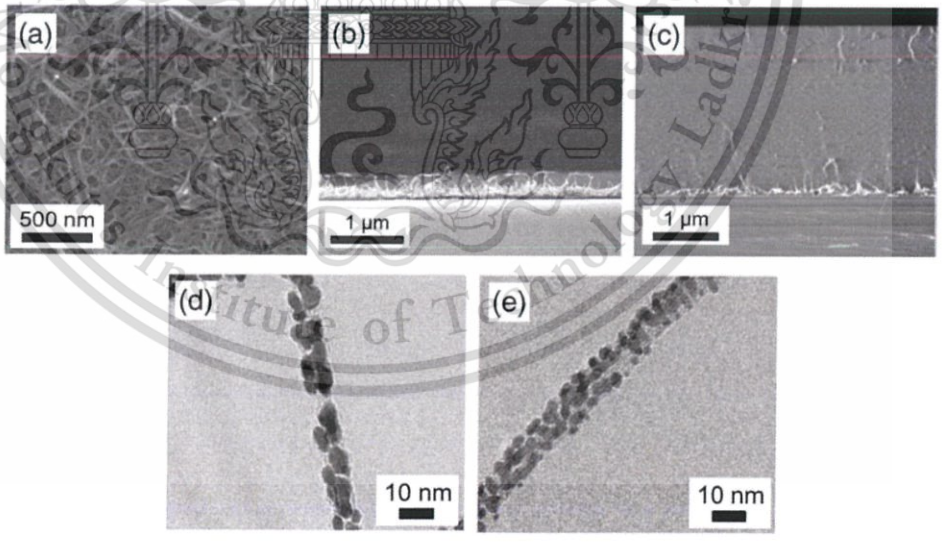

Fig. 2. FESEM images of (a) $S_{0.0}$, (b) $S_{0.1}$, and (c) $S_{0.5}$. TEM images of (d) $S_{2.0}$ and (e) $S_{5.0}$.

oxygen elements may be derived from SWNT and PMMA. To confirm the PMMA existence in the $S_{5.5}$, the sample was characterized by FTIR. Fig. 3(e) shows FTIR spectra of $S_{0.0}$, $S_{0.5}$ and $S_{5.5}$. FTIR spectra of $S_{0.5}$ and $S_{5.5}$ show almost identical feature. The peak assigned to the C–H stretching vibration occurred at 2977 cm^{-1}. The strong peak at 1730 cm^{-1} is assigned to C=O stretching vibration. The peaks at 1157, 1199, and 1265 cm^{-1} correspond to C–O–C stretching and deformation vibrations. The peaks observed at 999 cm^{-1} and 858 cm^{-1} are due to C–H bending vibrations and the peak at 746 cm^{-1} is attributed to the vibrations of the polymer chains [22,23]. This result confirms the existence of PMMA and the same composition of the functional group of PMMA before and after Pt deposition.

To confirm the crystallinity, the sample was characterized by XRD. The typical XRD diffraction patterns of $S_{0.5}$, $S_{5.0}$ and $S_{5.5}$ are shown in Fig. 3(f). $S_{0.5}$ exhibited a broad peak at ~13°, which corresponds to the structure of PMMA [24], whereas the diffraction peaks of $S_{5.0}$ located at 39.7° and 46.2° can be assigned to reflections from the (111) and (200) planes of the face-centered cubic Pt, respectively [25,26]. The (111) and (200) diffraction peaks of the Pt NPs at $2\theta = 39.7°$ and 46.2° correspond to d-spacings of 0.227 and 0.196 nm, respectively. For $S_{5.5}$, the XRD diffraction pattern shows a diffraction peak from PMMA at ~13° and diffraction peaks from Pt NPs at 39.7° and 46.2°, respectively, confirming the existence of PMMA and Pt NPs. However, $S_{5.5}$ has a slightly broader peak from PMMA at ~13°, indicating the higher weight fraction of amorphous PMMA after Pt deposition. These results imply changes in the structural regularity of the main chains of the polymeric molecules. The average size of the Pt NPs was calculated from the Pt(111) peak using the Scherrer equation: $L = (0.9\lambda_{K\alpha}) / \beta_{(2\theta)}\cos\theta$, where L is the mean size of the Pt NPs, λ is the X-ray wavelength (Cu $K\alpha = 1.54$ Å), θ is half of the scattering angle, and β is the full-width half-maximum (FWHM) of the X-ray diffraction [25]. The calculated Pt NPs average sizes of $S_{5.0}$ and $S_{5.5}$ were approximately 3.99 and 3.29 nm, respectively, which are consistent with the TEM results.

Raman spectroscopy was utilized to characterize the structure, purity and crystallinity of SWNT. Fig. 4(a) shows the four significant Raman peaks: SWNT-derived Raman breathing mode (RBM) at 190

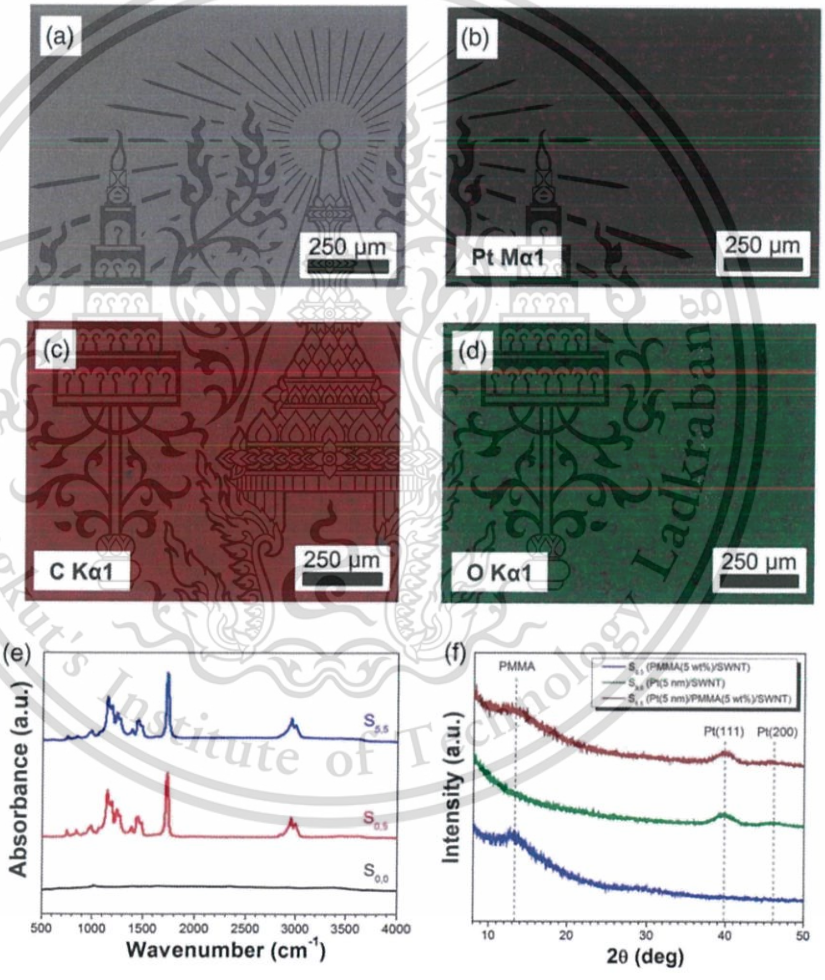

Fig. 3. (a) FESEM images of $S_{5.5}$ and EDS-mapping of (b) platinum, (c) carbon, and (d) oxygen elements. (e) FTIR spectra of $S_{0.0}$, $S_{0.5}$, and $S_{5.5}$. (f) XRD spectra of $S_{0.5}$, $S_{5.0}$, and $S_{5.5}$.

and 273 cm^{-1}, disorder carbon-derived D-band at 1332 cm^{-1} and graphitic-structure-derived G-band at 1588 cm^{-1}. The intensity ratio between the G- and D-bands (I_G/I_D) of pristine SWNTs was approximately 14.03 ± 1.2. After PMMA coating, the I_G/I_D ratios of $S_{0,1}$ and $S_{0.5}$ were 14.32 ± 0.8 and 14.79 ± 2.1, respectively, with no obvious difference from the pristine SWNTs. However, after Pt decoration, the I_G/I_D ratio of $S_{2,0}$ and $S_{5,0}$ were significantly decreased to 9.38 ± 0.3 and 3.99 ± 0.7, respectively, implying that the crystallinity and purity of the SWNTs deteriorated, especially for $S_{5,0}$ in which the highest amount of Pt NPs showed the lowest I_G/I_D value. The decrease in the I_G/I_D value could be attributed to the damage during Pt NPs adhesion on the SWNTs with high energy. For Pt/PMMA/SWNT, the I_G/I_D values of $S_{2,1}$, $S_{5,1}$, $S_{2,5}$, and $S_{5,5}$ were 13.32 ± 0.8, 5.62 ± 0.7, 13.37 ± 0.9 and 11.36 ± 0.6, respectively. The I_G/I_D values of $S_{2,5}$ and $S_{5,5}$ were greater than those of $S_{2,0}$, $S_{5,0}$ $S_{2,1}$ and $S_{5,1}$, indicating higher crystallinity and purity of the SWNTs. These results show that a thick film of PMMA effectively protects the SWNTs during Pt NPs deposition. Fig. 4(b) shows RBM spectra derived from $S_{0,0}$, $S_{2,0}$, $S_{5,0}$ and $S_{5,5}$. The diameter of the pristine SWNTs (d) can be estimated from the RBM peak using the formula $d = 248/\Omega_{RBM}$ [27], where Ω_{RBM} is the Raman shift of RBM peak. Although SWNTs with d ≥ 2 nm are generally difficult to detect by Raman spectroscopy, this laser excitation shows the existence of SWNTs with diameters of 0.91 and 1.31 nm. The intensity of the RBM peak at 273 cm^{-1} and the I_G/I_D ratios of $S_{2,0}$ and $S_{5,0}$ gradually decreased with increasing amount of deposited Pt NPs on the pristine SWNT, whereas those of $S_{5,5}$ were relatively comparable to those of the pristine SWNTs. The decrease in the RBM peak and I_G/I_D ratios of $S_{2,0}$ and $S_{5,0}$ is attributed to the damage of small-diameter SWNTs during Pt NPs adhesion with high energy. These results also clearly confirm that PMMA can act as a protective layer on SWNTs during Pt NP deposition.

3.2. Gas sensing characteristics

Fig. 5(a and b)shows sensor responses as a function of time of each sensor under an alternating supply of DCM (1700 mg/L) and N_2 gas for 5 cycles. Fig. 5(c) shows the normalized sensor response of each sensor to DCM. The electrical resistance of all the sensors increased upon DCM exposure and decreased after replacing DCM with N_2 gas (Fig. 5(a and b)). $S_{0,0}$, $S_{0,1}$, and $S_{0.5}$, were recovered to their initial resistances by N_2 gas purging. Conversely, $S_{2,0}$ and $S_{5,0}$ were hardly recovered to their initial resistances. The different response characteristics between PMMA/SWNT and Pt/SWNT may be attributed to the difference in DCM molecule adsorption behaviors. In the case of $S_{0,0}$, $S_{0,1}$, and $S_{0,5}$, DCM molecules are likely to physically adsorb onto the pristine SWNTs and the PMMA/SWNTs via van der Waals forces, which is a weak interaction. Thus, DCM molecule was easily removed by N_2 gas purging. In the case of $S_{2,0}$ and $S_{5,0}$, DCM molecules seem to strongly interact with the Pt NPs through chemisorption, which is relatively stronger interaction than the physisorption, resulting in difficulty in removing DCM molecule from sensor material, especially in the case of $S_{5,0}$. The Pt/PMMA/SWNT also shows the similar recovery behavior to the Pt/SWNT. The reversibility of the sensor can be improved by applying heat or UV exposure, similar to SWNT sensor system [12–14]. Regarding the response time of the sensor, the response time is defined as the time taken by the sensor to reach 90% of its maximum sensor response. The pristine SWNT showed the fastest response with a response time of approximately 17 ± 4 s, but it exhibited the smallest response magnitude. On the other hand, the hybrid Pt/PMMA/SWNT enabled 69-fold improvement in DCM detection compared to the pristine SWNT. However, the response time of the Pt/PMMA/SWNT increased up to 190 ± 6 s, which is approximately 11-time higher than that of the pristine SWNT. The hybrid Pt/PMMA/SWNT shows a merit for a significant enhancement of sensor response magnitude but there is room for improvement in its response time.

The sensing mechanism of the pristine SWNTs can be described in terms of the dielectric constant, which involves the solvent polarity of DCM. Molecules with polarity can hold moving holes and interrupt movement of holes along the p-type SWNTs, resulting in an increase in electrical resistance and thus an increase in sensor response [28]. The sensor responses of $S_{0,1}$, and $S_{0.5}$ toward DCM greatly increased 8.0- and 14.9-fold compared to that of $S_{0,0}$ (Fig. 5(c)), indicating sensor response enhancement by PMMA functionalization. The sensing mechanism could be explained by polymer swelling as a result of DCM adsorption. A hypothesis based on polymer swelling can be described as follows: after DCM adsorption, the PMMA coating on the SWNTs swell, possibly increasing the PMMA volume and loosening the SWNT network in the polymer [15,16,18], which would result in an increase in the electrical resistance. Furthermore, $S_{0.5}$ shows a higher response to DCM compare to $S_{0,1}$. These results may be attributed to the effect of the PMMA film thickness coating on the SWNTs (Fig. 2(b and c)). A thicker film enhances swelling, resulting in a higher sensor response.

For Pt/SWNTs, the sensor response of $S_{2,0}$ and $S_{5,0}$ to DCM greatly increased 2.7- and 21.4-fold higher than that of $S_{0,0}$ (Fig. 5(c)), indicating sensor response improvement by Pt NP functionalization. We envision that the sensing mechanism of Pt/SWNT toward DCM is similar to that of Pt-deposited SWNTs toward CO systems [29]. The mechanism is based on the dissociation of DCM to CO and subsequently CO oxidation on the Pt catalyst surface. The surface of the Pt NPs is saturated with chemisorbed O_2 molecules under atmospheric pressure [30], whereas some O_2 molecules are dissociated into O^- on the surface of Pt NPs. Upon exposure to DCM, DCM molecule reacts with the pre-adsorbed O_2 and dissociate on the Pt NP surface according to the reaction

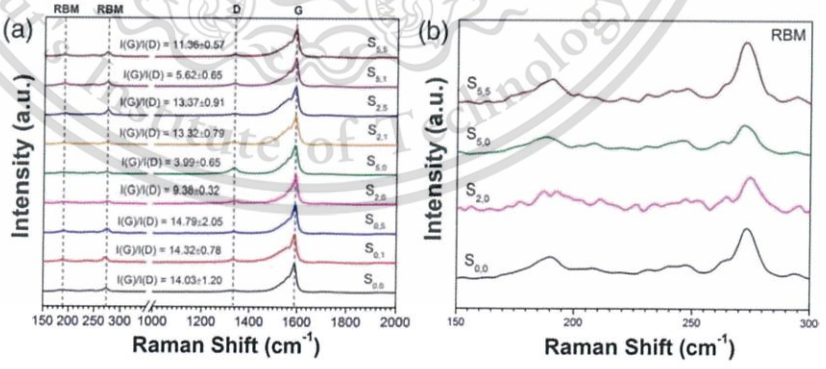

Fig. 4. (a) Raman spectra of all sensors and (b) RBM spectra of $S_{0,0}$, $S_{2,0}$, $S_{5,0}$, and $S_{5,5}$.

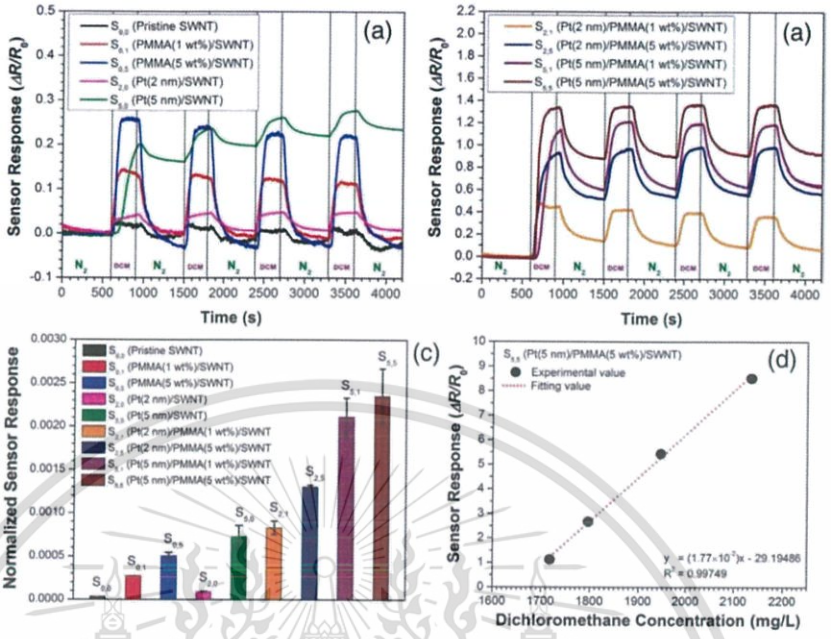

Fig. 5. Sensor response as a function of time for (a) $S_{0,0}$, $S_{0,1}$, $S_{0,5}$, $S_{2,0}$, and $S_{5,0}$ and (b) $S_{2,1}$, $S_{2,5}$, $S_{5,1}$, and $S_{5,5}$ toward DCM vapor; (c) normalized sensor response of all sensors toward DCM; and (d) sensor response of $S_{5,5}$ as a function of DCM concentration.

$CH_2Cl_2(g) + (1/2)O_2(ad) \rightarrow CO(g) + 2HCl(g)$ [31]. Consequently, CO interacts with O^- by the reaction, $CO(ad) + O^-(ad) \rightarrow CO_2(g) + e^-$, via the Langmuir–Hinshelwood mechanism [29,32]. Finally, the electron captured by pre-adsorbed O^- is released and donated to the p-type semiconducting SWNT, resulting in an increase in electrical resistance. $S_{5,0}$ shows higher response to DCM than does sensor $S_{2,0}$. A uniform size distribution, full coverage and nanometer-sized Pt NPs on the SWNTs of $S_{5,0}$, as confirmed by the TEM images in Fig. 2(d and e), result in the high sensitivity of $S_{5,0}$ to DCM.

For the integration sensors of SWNTs, PMMA and Pt NPs ($S_{2,1}$, $S_{2,5}$, $S_{5,1}$ and $S_{5,5}$), all of the sensors selectively responded to DCM vapor with high response magnitude. In particular, the sensor response of $S_{5,5}$ toward DCM greatly increased by 69.4-fold compared to that of $S_{0,0}$. The high response magnitude of the Pt/PMMA/SWNTs was successfully achieved as a result of the incorporation of PMMA and Pt functions. The sensing mechanism of the Pt/PMMA/SWNTs could possibly explain by the combination of the following phenomena, which involve catalytic oxidation on the Pt surface and polymer swelling. Regarding the catalytic reaction on the Pt surface of the Pt/PMMA/SWNT based on PMMA 1 wt.% ($S_{2,1}$ and $S_{5,1}$), the thickness of the PMMA layer was approximately 0.40 μm. SWNT network was partly buried in the PMMA matrix and some of the SWNT bundles were clearly seen to protrude from the PMMA surface (Fig. 2(b)). Thus, the released electron from dissociation reaction of DCM can directly donate to the SWNTs. In the case of the Pt/PMMA/SWNT based on PMMA 5 wt.%, the thickness of the PMMA layer was approximately 2.64 μm ($S_{2,5}$ and $S_{5,5}$). PMMA completely covered the pristine SWNT network. However, a careful observation of Fig. 2(c) reveals that there are bundles of SWNTs were drawn to the surface of the PMMA layer, forming a conduction path in the SWNT-PMMA matrix, as shown in Fig. 2(c) as a white line. Thus, these SWNT bundles can act as a conductive path for the released electron through the PMMA to the beneath SWNT network. The donation of electron to the p-type semiconducting SWNTs increases the electrical resistance.

Regarding the swelling of PMMA of the Pt/PMMA/SWNTs, it could be explained by three possible mechanisms; (I) the swelling of PMMA matrix upon DCM exposure [15,18]. (II) The swelling upon CO_2 produced by dissociation of DCM [33]. The simulation results show that CO_2 could diffuse in PMMA obeying a common hopping mechanism. The origin of solubility of CO_2 in PPMA is due to a stronger gas-polymer interaction, mainly between carbonyl group of polymer and CO_2, resulting in a higher swelling of polymer upon CO_2 uptake. (III) The swelling of PMMA at the interface between Pt NPs and PMMA layer. The swelling of PMMA is enhanced by the presence of inorganic clusters in the polymer with metal content below the percolation threshold [34–39]. After Pt NP decoration, the PMMA retained the same functional groups but its crystallinity degree and thickness decreased. The decrease in the crystallinity degree may enhance the swelling volume of the PMMA upon DCM exposure, resulting in the increase in the response magnitude [40]. Additionally, the morphology of the polymer such as roughness could also effect on the sensor response as reported in the ethanol detection by polypyrrole in which the high surface roughness enhances the sensitivity [41]. Further systematical research into the area of morphology effect of polymer on gas response is necessary.

Fig. 5(d) shows the sensor response of $S_{5,5}$ as a function of DCM concentration in the range of 1700 to 2150 mg/L. A linear relationship was obtained between the sensor response of the Pt/PMMA/SWNT and the concentration of DCM, i.e., the sensor response increased proportionally with DCM concentration. The DCM concentration studied in this research was in a high concentration range. Future work will study the limit of detection of the hybrid Pt/PMMA/SWNT sensor by modifying the sensor measurement system to the ppb-ppm level detection and optimizing the electrode configuration such as the electrode gap. Nevertheless, the advantage of the hybrid Pt/PMMA/SWNT is the significant improvement in response magnitude. The Pt/PMMA/SWNT enabled 69-fold improvement in DCM detection compared to pristine SWNT. Moreover, our proposed sensor can operate under room-temperature

condition and consume low power. These advantages let our proposed sensor become a potential candidate for a portable sensing device with real-time monitoring.

4. Conclusion

We successfully demonstrated a DCM sensor with a high response magnitude using the integration of SWNTs, PMMA and Pt NPs. Pt/PMMA/SWNTs exhibited a 69.4-fold improvement in the response to DCM. The sensor response of Pt/PMMA/SWNT linearly increased with increasing DCM concentration. The sensing mechanism of the hybrid sensor was attributed to the incorporation of polymer swelling and catalytic oxidation functions. These results clearly demonstrate that the integration of pristine SWNTs with PMMA and Pt NPs offers a promising material for practical and high-performance DCM sensing applications.

Prime novelty statement

- The novel of our work is the integration of single-walled carbon nanotubes (SWNTs), poly(methyl methacrylate) (PMMA) and platinum nanoparticles (Pt NPs) (hereafter referred to as Pt/PMMA/SWNT) as hybrid materials for dichloromethane (DCM) detection with a high response magnitude.
- The Pt/PMMA/SWNT enabled approximately 69-fold improvement in DCM detection compared to pristine SWNT under room-temperature condition.

Acknowledgments

This work has partially been supported by the National Nanotechnology Center (NANOTEC), NSTDA, Ministry of Science and Technology, Thailand, through its program of Center of Excellence Network. We acknowledge facility support from the Thai Microelectronics Center (TMEC) and the National Metal and Materials Technology Center (MTEC). We also acknowledge the financial support from the Toray Science Foundation (TSF), Japan, the King Prajadhipok and Queen Rambhai Barni Memorial Foundation, and the Thailand Graduate Institute of Science and Technology (TGIST) under contact number 01-55-13.

References

[1] J.N. Armor, Environmental catalysis, Appl. Catal. B Environ. 1 (1992) 221–256, http://dx.doi.org/10.1016/0926-3373(92)80051-Z.
[2] V.H. Vu, J. Belkouch, A. Ould-Dris, B. Taouk, Removal of hazardous chlorinated VOCs over Mn–Cu mixed oxide based catalyst, J. Hazard. Mater. 169 (2009) 758–765, http://dx.doi.org/10.1016/j.jhazmat.2009.04.010.
[3] M.V. Evans, J.C. Caldwell, Evaluation of two different metabolic hypotheses for dichlorotomethane toxicity using physiologically based pharmacokinetic modeling for in vivo inhalation gas uptake data exposure in female B6C3F1 mice, Toxicol. Appl. Pharmacol. 244 (2010) 280–290, http://dx.doi.org/10.1016/j.taap.2010.01.018.
[4] Q.-Y. Chen, N. Li, M.-F. Luo, J.-Q. Lu, Catalytic oxidation of dichloromethane over Pt/CeO_2–Al_2O_3 catalysts, Appl. Catal. B Environ. 127 (2012) 159–166, http://dx.doi.org/10.1016/j.apcatb.2012.08.020.
[5] S.M. Kanan, O.M. El-Kadri, I.A. Abu-Yousef, M.C. Kanan, Semiconducting metal oxide based sensors for selective gas pollutant detection, Sensors 9 (2009) 8158–8196, http://dx.doi.org/10.3390/s91008158.
[6] G.F. Fine, L.M. Cavanagh, A. Afonja, R. Binions, Metal oxide semi-conductor gas sensors in environmental monitoring, Sensors 10 (2010) 5469–5502, http://dx.doi.org/10.3390/s100605469.
[7] S. Iijima, T. Ichihashi, Single-shell carbon nanotubes of 1-nm diameter, Nature 363 (1993) 603–605, http://dx.doi.org/10.1038/363603a0.
[8] A. Peigney, C. Laurent, E. Flahaut, R.R. Bacsa, A. Rousset, Specific surface area of carbon nanotubes and bundles of carbon nanotubes, Carbon 39 (2001) 507–514, http://dx.doi.org/10.1016/S0008-6223(00)00155-X.
[9] T.W. Odom, Electronic Properties of Single-walled Carbon Nanotubes, 54 (2001) 601–604.
[10] S. Hong, S. Myung, Nanotube electronics: a flexible approach to mobility, Nat. Nanotechnol. 2 (2007) 207–208, http://dx.doi.org/10.1038/nnano.2007.89.
[11] C. Cantalini, L. Valentini, I. Armentano, L. Lozzi, J.M. Kenny, S. Santucci, Sensitivity to NO_2 and cross-sensitivity analysis to NH_3, ethanol and humidity of carbon nanotubes thin film prepared by PECVD, Sensors Actuators B Chem. 95 (2003) 195–202, http://dx.doi.org/10.1016/S0925-4005(03)00418-0.
[12] P. Qi, O. Vermesh, M. Grecu, A. Javey, Q. Wang, H. Dai, S. Peng, K.J. Cho, Toward large arrays of multiplex functionalized carbon nanotube sensors for highly sensitive and selective molecular detection, Nano Lett. 3 (2003) 347–351, http://dx.doi.org/10.1021/n1034010k.
[13] J. Li, Y. Lu, Q.L. Ye, J. Han, M. Meyyappan, Carbon nanotube based chemical sensors for gas and vapor detection, Nano Lett. 3 (2003) 929–933, http://dx.doi.org/10.1021/nl034220x.
[14] W. Wongwiriyapan, S.I. Honda, H. Konishi, T. Mizuta, T. Ikuno, T. Ito, T. Maekawa, K. Suzuki, H. Ishikawa, K. Oura, M. Katayama, Single-walled carbon nanotube thin-film sensor for ultrasensitive gas detection, Jpn. J. Appl. Phys 2 Lett. 44 (2005) http://dx.doi.org/10.1143/JJAP.44.L482.
[15] J.K. Abraham, B. Philip, A. Witchurch, V.K. Varadan, C.C. Reddy, A compact wireless gas sensor using a carbon nanotube/PMMA thin film chemiresistor, Smart Mater. Struct. 13 (2004) 1045–1049, http://dx.doi.org/10.1088/0964-1726/13/5/010.
[16] H. Yoon, J. Xie, J.K. Abraham, V.K. Varadan, P.B. Ruffin, Passive wireless sensors using electrical transition of carbon nanotube junctions in polymer matrix, Smart Materials and Structures. 15 (2006) S14–S20, http://dx.doi.org/10.1088/0964-1726/15/1/004.
[17] M. Castro, B. Kumar, J.F. Feller, Z. Haddi, A. Amari, B. Bouchikhi, Novel e-nose for the discrimination of volatile organic biomarkers with an array of carbon nanotubes (CNT) conductive polymer nanocomposites (CPC) sensors, Sensors Actuators B Chem. 159 (2011) 213–219, http://dx.doi.org/10.1016/j.snb.2011.06.073.
[18] W. Muangrat, T. Chodjarusawad, R. Maolanon, S. Pratontep, S. Porntheeraphat, W. Wongwiriyapan, Poly (methyl methacrylate) and thiophene-coated single-walled carbon nanotubes for volatile organic compound discrimination, Jpn. J. Appl. Phys. 55 (2016) http://dx.doi.org/10.7567/JJAP.55.02BD04 (02BD04 (1–6)).
[19] A. Star, V. Joshi, S. Skarupo, D. Thomas, J.-C.P. Gabriel, Gas sensor array based on metal-decorated carbon nanotubes, J. Phys. Chem. B 110 (2006) 21014–21020, http://dx.doi.org/10.1021/jp064371z.
[20] R. Leghrib, E. Llobet, Quantitative trace analysis of benzene using an array of plasma-treated metal-decorated carbon nanotubes and fuzzy adaptive resonant theory techniques, Anal. Chim. Acta 708 (2011) 19–27, http://dx.doi.org/10.1016/j.aca.2011.09.038.
[21] H. Baccar, A. Thamri, P. Clément, E. Llobet, A. Abdelghani, Pt- and Pd-decorated MWCNTs for vapour and gas detection at room temperature, Beilstein J. Nanotechnol. 6 (2015) 919–927, http://dx.doi.org/10.3762/bjnano.6.95.
[22] J. Jang, S. Kim, K.J. Lee, Fabrication of CdS/PMMA core/shell nanoparticles by dispersion mediated interfacial polymerization, Chem. Commun. 2689–2691 (2007) http://dx.doi.org/10.1039/b703717a.
[23] L. Zhang, F. Li, Y. Chen, X. Wang, Synthesis of transparent ZnO/PMMA nanocomposite films through free-radical copolymerization of asymmetric zinc methacrylate acetate and in-situ thermal decomposition, J. Lumin. 131 (2011) 1701–1706, http://dx.doi.org/10.1016/j.jlumin.2011.03.065.
[24] A. Zanotto, A.S. Luyt, A. Spinella, E. Caponetti, Improvement of interaction in and properties of PMMA-MWNT nanocomposites through microwave assisted acid treatment of MWNT, Eur. Polym. J. 49 (2013) 61–69, http://dx.doi.org/10.1016/j.eurpolymj.2012.10.030.
[25] W. Li, C. Liang, W. Zhou, J. Qiu, Z. Zhou, G. Sun, Q. Xin, Preparation and characterization of multiwalled carbon nanotube-supported platinum for cathode catalysts of direct methanol fuel cells, J. Phys. Chem. B 107 (2003) 6292–6299, http://dx.doi.org/10.1021/jp022505c.
[26] W. Li, M. Waje, Z. Chen, P. Larsen, Y. Yan, Platinum nanoparticles supported on stacked-cup carbon nanofibers as electrocatalysts for proton exchange membrane fuel cell, Carbon 48 (2010) 995–1003, http://dx.doi.org/10.1016/j.carbon.2009.11.017.
[27] A. Jorio, R. Saito, J.H. Hafner, C.M. Lieber, M. Hunter, T. McClure, G. Dresselhaus, M.S. Dresselhaus, Structural (n,m) determination of isolated single-wall carbon nanotubes by resonant Raman scattering, Phys. Rev. Lett. 86 (2001) 1118–1121, http://dx.doi.org/10.1103/PhysRevLett.86.1118.
[28] T. Kim, D. Kwak, Flexible VOC sensors using conductive polymers and porous membranes for application to textiles, Fibers Polym. 13 (2012) 471–474, http://dx.doi.org/10.1007/s12221-012-0471-7.
[29] W. Wongwiriyapan, S. Inoue, T. Ito, R. Shimazaki, T. Maekawa, K. Suzuki, H. Ishikawa, S. Honda, K. Oura, M. Katayama, Highly sensitive detection of carbon monoxide at room temperature using platinum-decorated single-walled carbon nanotubes, Appl. Phys. Express 1 (2008) 1–3, http://dx.doi.org/10.1143/APEX.1.014004.
[30] J.L. Gland, B.A. Sexton, G.B. Fisher, Oxygen interactions with the Pt(111) surface, Surf. Sci. 95 (1980) 587–602, http://dx.doi.org/10.1016/0039-6028(80)90197-1.
[31] D.M. Papenmeier, J.A. Rossin, Catalytic oxidation of dichloromethane, chloroform, and their binary mixtures over a platinum alumina catalyst, Ind. Eng. Chem. Res. 33 (1994) 3094–3103, http://dx.doi.org/10.1021/ie00036a026.
[32] H. Yasumatsu, N. Fukui, Size dependence of low-temperature catalytic activity of CO oxidation driven by platinum clusters directly bound to silicon substrate surface, J. Phys. Chem. C 119 (2015) 11217–11223, http://dx.doi.org/10.1021/jp512172v.
[33] H. Eslami, M. Kesik, H.A. Karimi-Varzaneh, F. Müller-Plathe, Sorption and diffusion of carbon dioxide and nitrogen in poly(methyl methacrylate), J. Chem. Phys. 139 (2013) 124902, http://dx.doi.org/10.1063/1.4821585.
[34] T. Vossmeyer, B. Guse, I. Besnard, R.E. Bauer, K. Müllen, A. Yasuda, Gold nanoparticle/polyphenylene dendrimer composite films : preparation and vapor-sensing properties, Adv. Mater. 14 (2002) 238–242.
[35] A. Convertino, A. Valentini, A. Bassi, N. Cioffi, L. Torsi, E.N.M. Cirillo, Effect of metal clusters on the swelling of gold-fluorocarbon-polymer composite films, Appl. Phys. Lett. 80 (2002) 1565–1567, http://dx.doi.org/10.1063/1.1448858.

[36] S.D. Evans, S.R. Johnson, Y.L. Cheng, T. Shen, Vapour sensing using hybrid organic–inorganic nanostructured materials, J. Mater. Chem. 10 (2000) 183–188, http://dx.doi.org/10.1039/A903951A.
[37] A. Convertino, G. Leo, M. Tamborra, C. Sciancalepore, M. Striccoli, M.L. Curri, A. Agostiano, TiO_2 colloidal nanocrystals functionalization of PMMA: a tailoring of optical properties and chemical adsorption, Sensors Actuators B Chem. 126 (2007) 138–143, http://dx.doi.org/10.1016/j.snb.2006.11.043.
[38] A. Convertino, M. Tamborra, M. Striccoli, G. Leo, A. Agostiano, M.L. Curri, Poly(methyl methacrylate) nanocomposites based on TiO_2 nanocrystals: tailoring material properties towards sensing, Thin Solid Films 519 (2011) 3931–3938, http://dx.doi.org/10.1016/j.tsf.2011.01.359.
[39] N. Cioffi, L. Torsi, I. Farella, D. Altamura, A. Valentini, M. Quinto, L. Sabbatini, P.G. Zambonin, The swelling of vapor-sensitive fluoropolymers modified with metal nanoparticles: interpretation of the material–vapor interaction mechanism, Sensors Actuators B Chem. 100 (2004) 9–16, http://dx.doi.org/10.1016/j.snb.2003.12.058.
[40] S. Lampman (Ed.), Characterization and Failure Analysis of Plastics, ASM International 2003, p. 149.
[41] Q. Fang, D.G. Chetwynd, J.A. Covington, C.-S. Toh, J.W. Gardner, Micro-gas-sensor with conducting polymers, Sensors Actuators B Chem. 84 (2002) 66–71, http://dx.doi.org/10.1016/S0925-4005(01)01076-0.

Japanese Journal of Applied Physics **55**, 02BD04 (2016)
http://doi.org/10.7567/JJAP.55.02BD04

REGULAR PAPER

Poly(methyl methacrylate) and thiophene-coated single-walled carbon nanotubes for volatile organic compound discrimination

Worawut Muangrat[1], Thanawee Chodjarusawad[2], Rungroj Maolanon[3], Sirapat Pratontep[1,4,5], Supanit Porntheeraphat[6], and Winadda Wongwiriyapan[1,4,5*]

[1]*College of Nanotechnology, King Mongkut's Institute of Technology Ladkrabang, Bangkok 10520, Thailand*
[2]*Department of Physics, Faculty of Science, Burapha University, Chonburi 20131, Thailand*
[3]*National Nanotechnology Center, Pathumthani 12120, Thailand*
[4]*Nanotec-KMITL Center of Excellence on Nanoelectronic Devices, Bangkok 10520, Thailand*
[5]*Thailand Center of Excellence in Physics, Bangkok 10400, Thailand*
[6]*National Electronics and Computer Technology Center, Pathumthani 12120, Thailand*

*E-mail: kwwinadd@kmitl.ac.th

Received June 30, 2015; revised September 17, 2015; accepted September 18, 2015; published online January 26, 2016

Poly(methyl methacrylate) (PMMA) and thiophene-coated single-walled carbon nanotubes (SWNTs) were fabricated for use in volatile organic compound (VOC) detection. Pristine SWNTs were separately coated with PMMA (PMMA/SWNTs) and thiophene (thiophene/SWNTs) by spin-coating. Pristine SWNTs showed the highest response to methanol, while PMMA/SWNTs enabled 5.4-fold improved dichloromethane detection and thiophene/SWNTs enabled 1.4-fold improved acetone detection compared with pristine SWNTs. The sensor response of PMMA/SWNTs to dichloromethane and that of thiophene/SWNTs to acetone can be attributed to the Hildebrand solubility parameter (HSP). The more similar the HSP, the higher the sensor response. The sensor response of pristine SWNTs to methanol is related to the diffusion coefficient and molecular size. The relationships between the vapor concentration and sensor response of PMMA/SWNTs to dichloromethane and thiophene/SWNTs to acetone are based on Henry's adsorption isotherm, while that of pristine SWNTs to methanol is based on the Henry–clustering model. Principal component analysis (PCA) results show that dichloromethane, acetone, and methanol were successfully discriminated.

1. Introduction

Nowadays, air pollution is an important problem in human health and the environment. The main causes of this problem are the toxic chemicals and waste released from chemical industries, especially volatile organic compounds (VOCs).[1] VOCs are of extreme danger to human health, cause eye, nose and throat irritation, can also damage the liver and central nervous system, and present a risk of cancer. Currently, gas chromatography/mass spectrometry (GC/MS), high-performance liquid chromatography (HPLC), photoionization detection (PID), and cyclic voltammetry are the most widely used for VOC analysis. These techniques have the advantages of high sensitivity and reliability; however, their applications are limited owing to their complexity, relatively high cost, disposable parts, unportability, and calibration requirement to maintain accuracy. In order to overcome the disadvantages of conventional VOC analysis techniques, gas sensor technology is proposed for VOC monitoring and detection with a compact and portable device. The ideal gas sensor requires high sensitivity, high selectivity, fast response, real-time monitoring, low power consumption, and long-term stability. To date, commercial gas sensors such as metal oxide materials have been developed to detect VOCs with a detection limit down to the parts per million (ppm) level.[2,3] However, the main demerits of metal oxide material-based gas sensors are nonselectivity, slow response, and high operating temperature (>200 °C), which requires high power consumption. Recently, single-walled carbon nanotubes (SWNTs)[4] have been focused on as the most promising materials for next-generation innovative chemical sensor applications, owing to their nanostructure, large specific area,[5] high electron mobility,[6,7] and superior electrical properties.[8,9] Gas sensors based on SWNTs have been demonstrated to be ultrasensitive for the detection of oxidizing gases down to the parts per billion (ppb) level at room-temperature operation.[10–13] Nevertheless, SWNT-based sensors are still insensitive to many kinds of gas molecules, such as reducing gases and VOCs, owing to the weak or nonspecific interactions between the SWNT and these molecules. Furthermore, another drawback of SWNT-based sensors is their lack of selectivity for different kinds of gases. These issues limit the practical applications of SWNT-based sensors to on-site monitoring. To overcome these drawbacks, combining polymer functionalization or metal nanoparticle decoration with carbon nanotubes (CNTs) is the most promising route.[14–19] For example, in their pioneering work, Abraham et al. demonstrated a compact wireless gas sensor using composites of multi-walled carbon nanotubes and poly(methyl methacrylate) (MWNT/PMMA). The MWNT/PMMA sensors could detect dichloromethane, acetone, and chloroform with a fast response. The sensing mechanism of the polymer-functionalized CNTs is attributed to the swelling of the polymer matrix because of the organic vapor molecule, leading to volume expansion, and thereby an increase in the CNT–CNT distance, resulting in an increase in the resistance.[14] However, the CNT/polymer composites are prepared mostly in the form of CNTs dispersed in a polymer matrix on the basis of percolation theory by a complicated polymerization process.[14–16] In addition, the selectivity of the gas sensor based on CNTs and their functionalization has been developed by data analysis. Several statistical techniques are utilized to identify and discriminate different gases and VOCs. The most popular technique is principal component analysis (PCA), because it is a powerful tool for pattern recognition. For instance, a clear discrimination between gases or VOCs was attained with a gas sensor based on CNTs and polymer functionalization, by using the PCA technique.[20–22]

In this work, we proposed a simple fabrication method for a VOC sensor using a polymer-coated SWNT network. Three types of sensors were prepared; pristine SWNT, PMMA-coated SWNT, and thiophene-coated SWNT sensors. The improvements of their sensor response and selectivity to dichloromethane, acetone, and methanol vapors were investigated. Moreover, the PCA of sensor responses was used to discriminate between the tested VOC vapors.

2. Experimental methods

A printed circuit board (PCB) consisting of an interdigitated Cu/Au electrode with gaps of 250 μm was used as the sensor platform. A SWNT suspension was prepared by dispersing SWNTs (diameter and length in the ranges of 1.2–1.5 nm and 2–5 μm, respectively) in 1,2-dichloroethane by ultrasonication for 3 h and subsequently dropping it onto the PCB. The electrical resistance of the SWNT on the PCB was adjusted to be approximately 100 kΩ. Solutions of PMMA (M_w = 94600 g/mol) and thiophene (M_w = 84.14 g/mol) were prepared in toluene at a concentration of 5 wt % and stirred for 24 h. Then, PMMA and thiophene solution were separately spin-coated onto the predropped SWNT network at a spinning speed of 3000 rounds per minute for 5 min, followed by heating at 100 °C for 24 h to eliminate solvent in sensor samples (hereafter referred to as PMMA/SWNTs and thiophene/SWNTs). The morphology and carbon structure of SWNTs, PMMA/SWNTs, and thiophene/SWNTs were characterized by field-emission scanning electron microscopy (FESEM; Hitachi S4700) and Raman spectroscopy (Thermo SCIENTIFIC DXR) with an Ar ion laser wavelength of 532 nm (2.33 eV), respectively.

Next, sensor responses to dichloromethane, chloroform, acetone, ethanol, and methanol vapors were investigated at room temperature by recording their electrical resistance using a FLUKE NetDAQ during cycles of alternating supply of dry N_2 gas and test vapor. Sensors were placed in a stainless-steel chamber and N_2 gas as a baseline was introduced into the chamber at a flow rate of 3.0 lpm for 600 s. Then, N_2 gas was replaced with test vapor by bubbling the liquid of test vapor with N_2 carrier gas at a flow rate of 1.5 lpm for 180 s. The concentration of the test vapor was adjusted by controlling the temperature of the test vapor liquid. Sensors were recovered by purging with 3.0 lpm of N_2 for 600 s. The sensor response (SR) was defined as $SR = (R_{VOC} - R_0)/R_0$, where R_{VOC} and R_0 are the resistances of the sensor after and before vapor exposure, respectively. In order to compare the responses of all sensors, the sensor responses were normalized by the VOC concentration. Normalized sensor response (NSR) was defined as the ratio between sensor response at the time of 780 s (SR_{780}) and the VOC concentration (C_{VOC}): $NSR = SR_{780}/C_{VOC}$.

3. Results and discussion

Firstly, responses of the pristine SWNT sensor to various VOCs were preliminarily investigated. Test vapors were dichloromethane (2126 mg/L), chloroform (1566 mg/L), acetone (1094 mg/L), ethanol (181 mg/L), and methanol (329 mg/L). The sensitivity of pristine SWNTs to VOCs determined from the normalized sensor response was in the following order: dichloromethane < chloroform < acetone ≈ methanol < ethanol (see Fig. 1). Pristine SWNTs were highly sensitive to ethanol, but exhibited similar response magnitudes for acetone and methanol, and were nearly insensitive to dichloromethane. Thus, in this study, the enhancement of the sensitivity to dichloromethane and the improvement of selectivity between acetone and methanol were focused on using PMMA/SWNTs and thiophene/SWNTs.

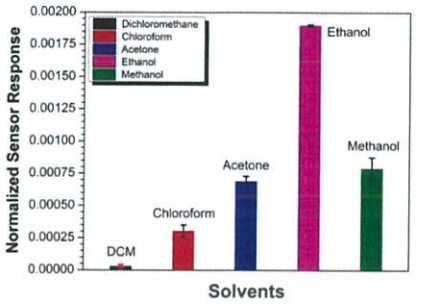

Fig. 1. (Color online) Normalized sensor response of pristine SWNT to VOCs.

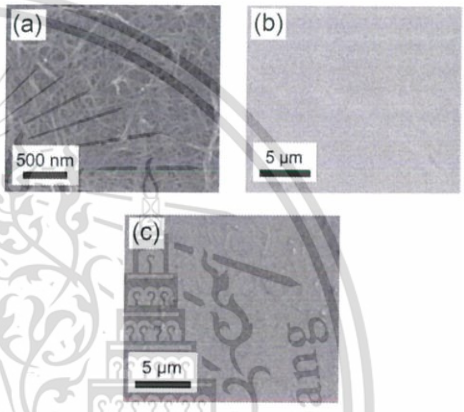

Fig. 2. FESEM images of (a) pristine SWNTs, (b) PMMA/SWNTs, and (c) thiophene/SWNTs.

Next, sensors based on pristine SWNTs, PMMA/SWNTs, and thiophene/SWNTs for acetone, methanol, and dichloromethane detection, respectively, were investigated. Figures 2(a)–2(c) show FESEM images of pristine SWNTs, PMMA/SWNTs, and thiophene/SWNTs, respectively. Pristine SWNTs assembled into a network of overlying SWNTs and formed a conductive network structure [Fig. 2(a)]. After PMMA or thiophene was spin-coated onto the pristine SWNT network, PMMA completely covered the pristine SWNT network [Fig. 2(b)], whereas thiophene solution, which has a low viscosity, could penetrate into spaces between the entangled SWNTs, resulting in the appearance of the SWNT network on the surface of thiophene/SWNTs [Fig. 2(c)]. Raman spectroscopy was utilized to characterize the structure, purity, and crystallinity of all samples. Four significant Raman peaks were observed: SWNT-derived

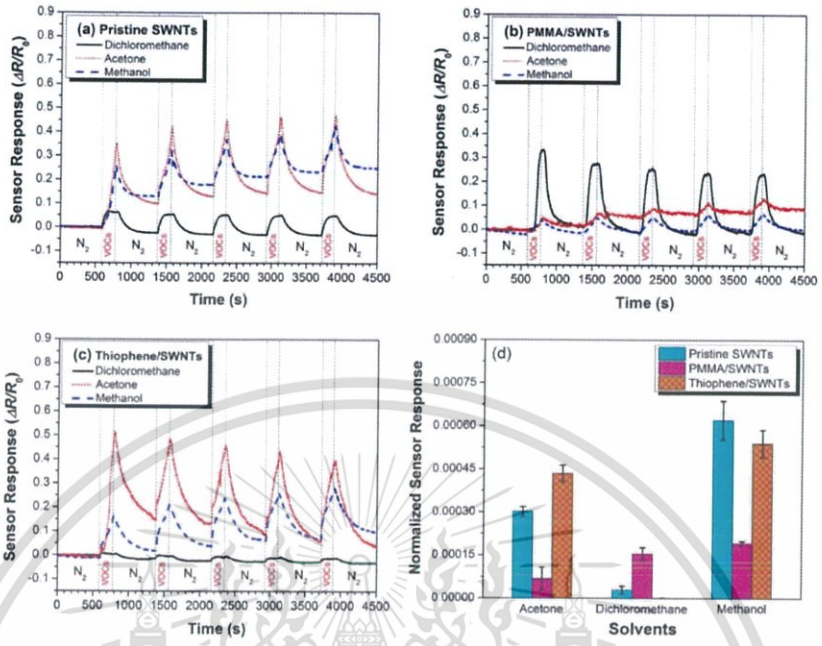

Fig. 3. (Color online) Sensor responses to dichloromethane (2126 mg/L), acetone (1094 mg/L) and methanol (329 mg/L) as functions of time: (a) pristine SWNTs, (b) PMMA/SWNTs, and (c) thiophene/SWNTs. (d) Normalized sensor response of each sensor to VOCs.

Raman breathing mode (RBM) at 188 and 272 cm^{-1}, disordered carbon-derived D-band at 1332 cm^{-1}, graphitic-structure-derived G-band at 1588 cm^{-1}, and two-phonon double-resonance Raman-process-derived 2D-band at 2663 cm^{-1} (data not shown).[23] After coating PMMA or thiophene on pristine SWNTs, there were slight Raman shifts of the Raman peaks, but the four significant Raman peaks were still observed. The intensity ratio between the G- and D-bands (I_G/I_D) is an indication of the crystallinity of SWNTs. The I_G/I_D ratios of pristine SWNTs, PMMA/SWNTs, and thiophene/SWNTs were 14.03 ± 1.20, 14.79 ± 2.05, and 15.87 ± 1.40, respectively, implying that the structure of SWNTs was maintained even when coated with PMMA or thiophene.

Figures 3(a)–3(c) show sensor responses as a function of time of each sensor under alternating supply of VOC and N_2 gas for five cycles. The electrical resistance of all sensors increased upon VOC exposure and decreased after replacing VOCs with N_2 gas [Figs. 3(a)–3(c)]. Figure 3(d) shows the normalized sensor response of each sensor to VOCs. The normalized sensor response of pristine SWNTs showed the highest response to methanol but the lowest response to dichloromethane. The sensing mechanism can be described in terms of the dielectric constant, which involves the solvent polarity of VOCs. The solvent polarity is in the following order: dichloromethane < acetone < methanol.[24] Molecules with higher polarity can hold moving holes and interrupt the movement of holes along SWNTs, resulting in a large increase in resistance and thus sensor response.[25,26] The trend of the normalized sensor response of pristine SWNTs to acetone, methanol, and dichloromethane coincided with the VOC polarity.

The sensor response of PMMA/SWNTs to dichloromethane greatly increased 5.4-fold higher than that of pristine SWNTs, and conversely, the sensor response to acetone and methanol dramatically decreased [see Fig. 3(d)]. Thiophene/SWNTs improved the response to acetone 1.4-fold higher than that of pristine SWNTs, whereas the responses to dichloromethane and methanol decreased [see Fig. 3(d)]. These results imply that the sensor responses to dichloromethane and acetone were enhanced by PMMA and thiophene functionalization, respectively. The sensing mechanism would be ascribed to monomer or polymer swelling due to VOC adsorption and the Hildebrand solubility parameter (HSP). A hypothesis based on monomer or polymer swelling can be described as follows. After VOC adsorption, monomer or polymer coatings on SWNTs are swollen, thus possibly increasing the monomer or polymer volume and loosening the SWNT network, resulting in an increase in the electrical resistance.[14,16] The sensing mechanism of PMMA/SWNTs and thiophene/SWNTs for VOC detection is illustrated in Fig. 4. For the hypothesis based on HSP, HSP is the numerical value used to predict the solubility (δ) of solvent with monomer or polymer, where δ is defined as the square root of the cohesive energy density. The smaller the solubility parameter difference between solvent and monomer or polymer ($\delta_{\text{monomer or polymer}} - \delta_{\text{solvent}}$), the higher the miscibility (see Table I).[27,28] PMMA/SWNTs and

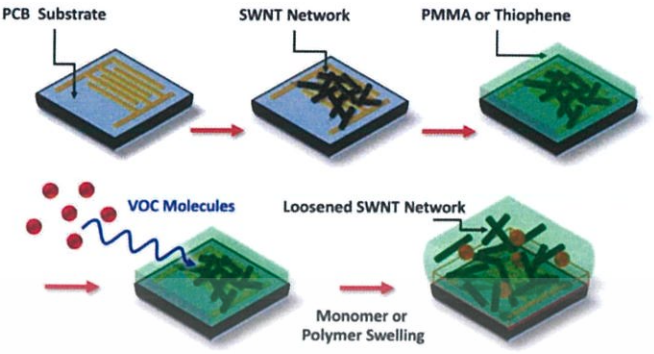

Fig. 4. (Color online) Schematic diagram of gas sensing mechanism of PMMA/SWNTs and thiophene/SWNTs for VOC detection.

Table I. Hildebrand solubility parameter and the solubility parameter difference between PMMA and thiophene with various VOCs.[27,28]

Monomer or polymer and VOCs	Hildebrand solubility parameter, δ $(MPa)^{1/2}$	$\lvert\delta_{PMMA} - \delta_{VOC}\rvert$ $(MPa)^{1/2}$	$\lvert\delta_{Thiophene} - \delta_{VOC}\rvert$ $(MPa)^{1/2}$
PMMA	19.0	—	—
Thiophene	20.1	—	—
Dichloromethane	19.8	0.8	0.3
Acetone	20.3	1.3	0.2
Methanol	29.7	10.7	9.6

thiophene/SWNTs have the minimum solubility parameter difference for dichloromethane and acetone, respectively. Hence, PMMA/SWNTs respond more sensitively to dichloromethane than to acetone and thiophene/SWNTs respond more sensitively to acetone than to dichloromethane. Our results for PMMA/SWNTs and thiophene/SWNTs conform to the HSP for dichloromethane and acetone detection.

However, the HSP hypothesis cannot describe the sensor responses of PMMA/SWNTs and thiophene/SWNTs to methanol. The molecular sizes of dichloromethane, acetone, and methanol are 63.86, 73.52, and 40.56 cm^3/mol, respectively,[29] while the diffusion coefficients under the same conditions (temperature 25 °C and pressure 1 atm) for dichloromethane, acetone, and methanol are 10.37×10^{-2}, 10.49×10^{-2}, and 15.20×10^{-2} cm^2/s, respectively.[30] It can be clearly seen that methanol has the smallest molecular size and highest diffusion coefficient. Thus, not only the polarity and HSP, but the molecular size and diffusion coefficient may also affect the methanol sensing mechanism. Compared with dichloromethane and acetone molecules, a large number of methanol molecules can penetrate and diffuse into monomer or polymer thin films, resulting in a higher sensor response despite the high solubility parameter difference between methanol and PMMA or thiophene.

Figures 5(a)–5(c) show the sensor responses of pristine SWNTs, PMMA/SWNTs, and thiophene/SWNTs to dichloromethane, acetone, and methanol as a function of VOC concentration, respectively. The sensor response characteristics of the sensors were different. Normally, the amplitude of sensor response is expected to be proportional to the concentration of VOCs. The Langmuir–Henry–clustering (LHC) model is used to describe the evolution of the response of the conductive polymer-based sensor with VOC concentration.[31,32] As the LHC model is derived from a classical dual-mode sorption model, it can determine whether VOC molecules on the sensing material surfaces slightly adsorb on specific sites (Langmuir), forming several layers of molecules (Henry) or plasticizing and swelling the polymer matrix as a results of clustering (clustering). For dichloromethane detection, the responses of all sensors increased linearly with dichloromethane concentration in the range of 639–2981 mg/L. For acetone detection, a nonlinear correlation was observed in pristine SWNTs and thiophene/SWNTs in the range of 714–1383 mg/L. Their responses to acetone were linear at low concentrations and tended to saturate at high concentrations. The sensor surface may be completely covered by acetone molecules, resulting in sensor response saturation, implying a Langmuir (L) model in this VOC concentration range. PMMA/SWNTs, which have a smaller magnitude of response to acetone, show a linear correlation between sensor response and concentration. For methanol detection, thiophene/SWNTs follow the LHC model, while pristine SWNTs and PMMA/SWNTs follow the Henry–clustering (HC) model. The sensor response of thiophene/SWNTs rapidly increased at low concentrations, tended to slowly increase when the concentration reached approximately 252 mg/L, and finally dramatically increased at a concentration higher than 363 mg/L, implying the LHC model. Moreover, pristine SWNTs and PMMA/SWNTs followed the HC model. For the clustering model of methanol molecules, sorption can be explained as follows. Firstly, methanol molecules adsorb onto the sensing material surface and act as nuclei for the next methanol molecules. Then,

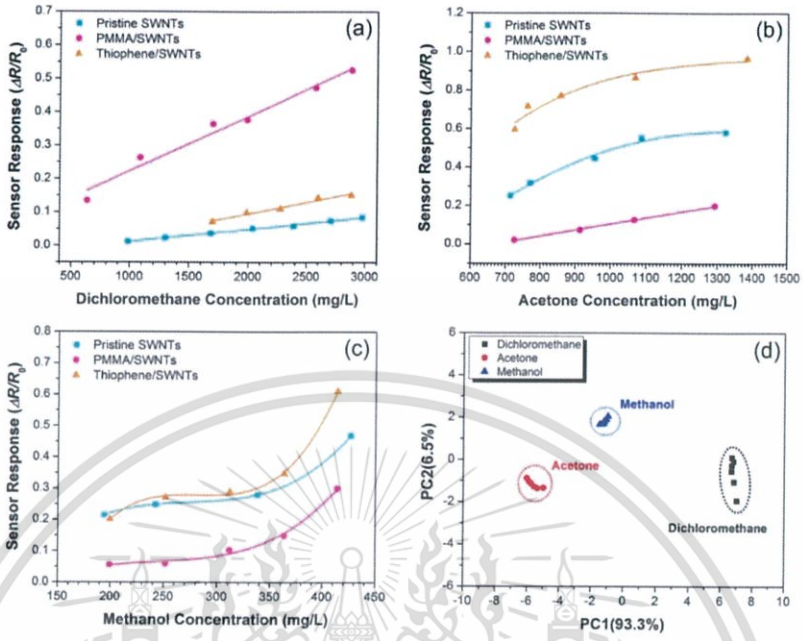

Fig. 5. (Color online) Sensor responses as a function of concentration of each sensor to (a) dichloromethane (b) acetone, and (c) methanol. (d) PCA plots of dichloromethane, acetone, and methanol.

successive methanol molecules adsorb onto the surface by forming two or more H-bonds with the previously adsorbed methanol molecules with strong interaction,[33] resulting in methanol clustering. This is the reason why the sensor response to methanol extremely increases when the concentration of methanol vapor is higher than 363 mg/L.

Next, the potential of pristine SWNTs-, PMMA/SWNTs-, and thiophene/SWNTs-based sensors for VOC discrimination was explored. The pattern recognition of dichloromethane, acetone, and methanol was studied by the PCA technique. Figure 5(d) shows the PC1–PC2 map after PCA data processing for an array of three sensors exposed to dichloromethane, acetone, and methanol. All the vapors have been successfully classified into distinct groups. These results demonstrate that coating PMMA and thiophene on the pristine SWNT network is a promising approach for effective VOC discrimination.

4. Conclusions

A simple sensor based on pristine SWNTs for VOC detection with improved sensitivity and selectivity was fabricated by coating SWNTs with PMMA and thiophene. PMMA/SWNTs greatly improved the response to dichloromethane 5.4-fold, while it greatly reduced the responses to acetone and methanol. Thiophene/SWNTs increased the response to acetone 1.4-fold and decreased the responses to dichloromethane and methanol. The features of the sensor response at different concentrations can be described by the Langmuir–Henry–clustering sorption model. PCA results clearly showed the discrimination of dichloromethane, acetone, and methanol vapors. The integration of pristine SWNTs with PMMA and thiophene is a promising approach for improving the sensitivity and selectivity for VOC detection.

Acknowledgments

This work has partially been supported by the National Nanotechnology Center (NANOTEC), NSTDA, Ministry of Science and Technology, Thailand, through its program of Center of Excellence Network. We also acknowledge the financial support and facilities from the Office of the National Research Council of Thailand, the Toray Science Foundation, Japan (TSF), The King Prajadhipok and Queen Rambhai Barni Memorial Foundation, and the Thailand Graduate Institute of Science and Technology (TGIST) under contact TGIST 01-55-013. We thank Mr. Chaiyanut Jirayupat, of College of Nanotechnology, King Mongkut's Institute of Technology Ladkrabang, for his assistance in sensor measurement.

1) B. Huang, C. Lei, C. Wei, and G. Zeng, Environ. Int. **71**, 118 (2014).
2) S. M. Kanan, O. M. El-Kadri, I. A. Abu-Yousef, and M. C. Kanan, Sensors **9**, 8158 (2009).
3) G. F. Fine, L. M. Cavanagh, A. Afonja, and R. Binions, Sensors **10**, 5469 (2010).
4) S. Iijima and T. Ichihashi, Nature **363**, 603 (1993).
5) A. Peigney, Ch. Laurent, E. Flahaut, R. R. Bacsa, and A. Rousset, Carbon **39**, 507 (2001).
6) X. Zhou, J.-Y. Park, S. Huang, J. Liu, and P. L. McEuen, Phys. Rev. Lett. **95**, 146805 (2005).

7) J. Zaumseil, Semicond. Sci. Technol. **30**, 074001 (2015).
8) T. W. Odom, Aust. J. Chem. **54**, 601 (2001).
9) S. Hong and S. Myung, Nat. Nanotechnol. **2**, 207 (2007).
10) C. Cantalini, L. Valentini, I. Armentano, L. Lozzi, J. M. Kenny, and S. Santucci, Sens. Actuators B **95**, 195 (2003).
11) P. Qi, O. Vermesh, M. Grecu, A. Javey, Q. Wang, H. Dai, S. Peng, and K. J. Cho, Nano Lett. **3**, 347 (2003).
12) J. Li, Y. Lu, Q. Ye, M. Cinke, J. Han, and M. Meyyapan, Nano Lett. **3**, 929 (2003).
13) W. Wongwiriyapan, S. Honda, H. Konishi, T. Mizuta, T. Ikuno, T. Ito, T. Maekawa, K. Suzuki, H. Ishikawa, K. Oura, and M. Katayama, Jpn. J. Appl. Phys. **44**, L482 (2005).
14) J. K. Abraham, B. Philip, A. Witchurch, V. K. Varadan, and C. C. Reddy, Smart Mater. Struct. **13**, 1045 (2004).
15) K. S. V. Santhanam, R. Sangoi, and L. Fuller, Sens. Actuators B **106**, 766 (2005).
16) F. Wang, H. Gu, and T. M. Swager, J. Am. Chem. Soc. **130**, 5392 (2008).
17) A. Star, V. Joshi, S. Skarupo, D. Thomas, and J.-C. P. Gabriel, J. Phys. Chem. B **110**, 21014 (2006).
18) W. Wongwiriyapan, S. Inoue, T. Ito, R. Shimazaki, T. Maekawa, K. Suzuki, H. Ishikawa, S. Honda, K. Oura, and M. Katayama, Appl. Phys. Express **1**, 014004 (2008).
19) H. Baccar, A. Thamri, P. Clément, E. Llobet, and A. Abdelghani, Beilstein J. Nanotechnol. **6**, 919 (2015).
20) Y. Lu, C. Partridge, M. Meyyappan, and J. Li, J. Electroanal. Chem. **593**, 105 (2006).
21) M. Castro, B. Kumar, J. F. Feller, Z. Haddi, A. Amari, and B. Bouchikhi, Sens. Actuators B **159**, 213 (2011).
22) J. F. Feller, N. Gatt, B. Kumar, and M. Castro, Chemosensors **2**, 26 (2014).
23) C. Thomsen and S. Reich, Phys. Rev. Lett. **85**, 5214 (2000).
24) C. Reichardt, *Solvents and Solvent Effects in Organic Chemistry* (Wiley-VCH, Weinheim, 2003) 3rd ed., pp. 418, 419, and 421.
25) K. Parikh, K. Cattanach, R. Rao, D.-S. Suh, A. Wu, and S. K. Manohar, Sens. Actuators B **113**, 55 (2006).
26) T. Kim and D. Kwak, Fiber Polym. **13**, 471 (2012).
27) H. J. Vandenburg, A. A. Clifford, K. D. Bartle, R. E. Carlson, J. C. Carroll, and I. D. Newton, Analyst **124**, 1707 (1999).
28) J. E. Mark, *Physical Properties of Polymers Handbook* (Springer, New York, 2007) 2nd ed., p. 296.
29) T. Villmow, A. John, P. Pötschke, and G. Heinrich, Polymer **53**, 2908 (2012).
30) G. A. Lugg, Anal. Chem. **40**, 1072 (1968).
31) A. Bouvree, J. F. Feller, M. Castro, Y. Grohens, and M. Rinaudo, Sens. Actuators B **138**, 138 (2009).
32) J. F. Feller, J. Lu, K. Zhang, B. Kumar, M. Castro, N. Gatt, and H. J. Choi, J. Mater. Chem. **21**, 4142 (2011).
33) C. L. McCallum, T. J. Bandosz, S. C. McGrother, E. A. Müller, and K. E. Gubbins, Langmuir **15**, 533 (1999).

Advanced Materials Research Vol. 802 (2013) pp 267-272
© (2013) Trans Tech Publications, Switzerland
doi:10.4028/www.scientific.net/AMR.802.267

Polymer-coated single-walled carbon nanotubes for ethanol and dichloromethane discrimination

Worawut Muangrat[1,a], Rungroj Maolanon[2,b] Sirapat Pratontep[1,3,c], Supanit Porntheeraphat[3,4,d], Winadda Wongwiriyapan[1,3,e]

[1]College of Nanotechnology, King Mongkut's Institute of Technology Ladkrabang, Bangkok, Thailand

[2]National Nanotechnology Center, Pathumthani, Thailand

[3]NANOTEC-KMITL Center of Excellence on Nanoelectronic Device, Bangkok, Thailand

[4]National Electronics and Computer Technology Center, Pathumthani, Thailand

[a]m.worawut@hotmail.com, [b]rungroj@nanotec.or.th, [c]kpsirapa@kmitl.ac.th, [d]tonnam@nectec.or.th, [e]kwwinadd@kmitl.ac.th

Keywords: single-walled carbon nanotubes, poly(methyl methacrylate), thiophene, ethanol, dichloromethane, discrimination, pattern recognition, principal component analysis

Abstract. Sensor response and pattern recognition of polymer-coated single-walled carbon nanotubes (SWNTs) were investigated. Printed circuit board (PCB) with Cu/Au interdigitated electrode was used as sensor platform. SWNTs network was firstly formed on PCB by drop-casting. For polymer-coated SWNTs preparation, poly(methyl methacrylate) (PMMA) and thiophene were employed as polymers to coat on SWNTs by spin coating: PMMA/SWNTs and thiophene/SWNTs. Raman spectra showed no obvious structure changes of SWNTs after polymer coating. Next, gas sensing test was conducted. Pristine SWNTs, PMMA/SWNTs and thiophene/SWNTs were exposed to vapors of ethanol and dichloromethane at room temperature. From normalized sensor response results, it was found that pristine SWNTs and PMMA/SWNTs showed the highest response to ethanol and dichloromethane vapors, respectively. In order to discriminate vapors between ethanol and dichloromethane, pattern recognition technique was utilized. Principal component analysis (PCA) results showed that pattern recognition of ethanol and dichloromethane vapors can be discriminated by using pristine SWNTs and polymer-coated SWNTs sensors.

Introduction

Single-walled carbon nanotubes (SWNTs) is the most promising materials for the next-generation of the innovative chemical sensor applications owing to their well-organized nanostructure, large specific surface area, high electron mobility and interesting electrical properties [1]. Recently, SWNT-based sensors have been demonstrated to be an ultrasensitive sensor for the detection of oxidizing gases down to parts per billion levels at room-temperature operation [2-4]. However, the SWNTs are still insensitive to many kinds of gas molecules, including reducing gases and volatile organic compounds (VOCs) due to their weak or nonspecific interactions between the SWNT and these molecules. To overcome this drawback, the functionalization of SWNTs with polymers and catalyst metal nanoparticles is one of the most promising routes [5-8]. For instance, the pioneering work by J. K. Abraham *et al.* showed that the composite of multi-walled carbon nanotubes and poly(methyl methacrylate) (MWNT/PMMA) enables VOCs detection [6]. However, so far, carbon nanotube/polymer composites mostly are prepared in the form of carbon nanotubes dispersing in an insulating polymer matrix based on percolation theory [7-8].

In this study, the polymer functionalization of SWNTs by coating a thin film of polymer onto SWNTs by spin coating method was proposed. By taking ethanol and dichloromethane as an example, the author demonstrated sensitive and selective detection of VOCs by means of functionalization of SWNT with PMMA and thiophene coating. Moreover, the combination of polymer-functionalized SWNTs transducer with classical pattern recognition methods provides interesting perspective for ethanol and dichloromethane discrimination.

Experimental Detail

Preparation of SWNTs and Polymer-coated SWNTs Sensor.

SWNTs (purchased from ALDRICH, diameter and length in range of 1.2-1.5 nm and 2-5 μm, respectively) were dispersed in 1,2-dichloroethane by ultrasonication for 3 h. SWNTs suspension was dropped onto printed circuit board (PCB) which was adjusted the resistance to be approximately 100 kΩ. PCB consists of interdigitated Cu/Au electrodes with a gap of 250 μm. For polymer preparation, PMMA (M_w = 97000 g/mol) and thiophene (M_w = 84.14 g/mol) were diluted in toluene at concentration of 5wt% and was stirred for 24 h. Prepared polymer solution were subsequently spin-coated on the pre-dropped SWNTs network with a spinning speed of 3000 rounds per minute for 5 min, followed by heating at 100°C for 24 h to eliminate solvent in sensor samples. Schematic view of pristine SWNTs and polymer-coated SWNTs on PCB were illustrated in Fig. 1.

Fig. 1 Schematic view of (a) pristine SWNTs and (b) PMMA/SWNTs on PCB.

Sensor Measurement.

Sensor response of SWNTs, PMMA/SWNTs and thiophene/SWNTs to ethanol and dichloromethane vapors were investigated at room temperature by recording their electrical resistance during alternate cycles of dry N_2 gas and test vapor. Sensors were placed in stainless chamber and N_2 gas with a flow rate of 3.0 *l*/min was introduced into chamber for 180 s. Then, N_2 gas was replaced with test vapor by bubbling liquid of test vapor with N_2 gas at a flow rate of 1.5 *l*/min for 180 s. At that time, test liquid was boiled at temperature of 90% of its boiling point. The resistance of the sensor was measured using a multimeter (UNI-T; UT71D). The sensor response (S) was defined as in equation (1), where R and R_0 are the resistance of sensor when exposed to test vapor and N_2 gas, respectively.

$$S = (R - R_0) / R_0 \quad (1)$$

Results and Discussion

Characterization of SWNTs and Polymer-coated SWNTs.

Raman spectroscopy (Thermo SCIENTIFIC DXR) was utilized to characterize the structure, purity and crystallinty of the SWNTs and polymer-coated SWNTs. Ar ion laser with a wavelength of 532 nm (2.33 eV) was used as excitation light. Raman spectra were shown in Fig. 2., Outstanding peak at ~1590 cm^{-1} (G-band graphitic structure), small peak at ~ 190-273 cm^{-1} (SWNTs structure) and 1334 cm^{-1} (D-band disorder carbon) were observed. In addition, the peaks at ~2664 cm^{-1} (G' band) were also observed from all samples. From Raman results, the obvious change in Raman peaks of all samples was not observed after polymer coating. The intensity ratio between G and D band (I_G/I_D) is an indication of the crystallinity of samples. The I_G/I_D ratio of SWNTs, PMMA/SWNTs and thiophene/SWNTs were 14.03±1.20, 14.79±2.05 and 15.87±1.40 respectively.

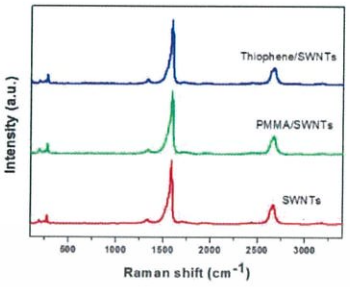

Fig. 2 Raman spectra of SWNTs and polymer-coated SWNTs.

Sensor Response of SWNTs and Polymer-coated SWNTs Sensors.

Fig. 3 shows the sensor responses as a function of time of all samples when it was exposed to ethanol and dichloromethane vapors. The sensor resistance increased when the sensor responded to vapors and decreased after replacing test vapor with N_2 gas. For ethanol sensing, pristine SWNTs showed higher response than that of thiophene/SWNTs, while PMMA/SWNTs was insensitive (Fig. 3(a)). For dichloromethane sensing, PMMA/SWNTs exhibited higher response than that of pristine SWNTs, while thiophene/SWNTs was insensitive (Fig. 3(b)). These results show that coating SWNTs with PMMA and thiophene affords sensing selectivity between ethanol and dichloromethane.

The sensing mechanism of pristine SWNTs can be explained by its p-type semiconducting property. Direct charge transfer on individual p-type SWNT with additional electron hopping effects on intertubes, resulting in decreasing the hole carrier density and increasing its resistance [3,6]. In case of polymer-coated SWNTs, the sensing mechanism can be explained by polymer volume expansion due to vapor exposure. After absorption of ethanol or dichloromethane vapors, polymer is swollen, thus possibly increases the volume and the distance between the SWNTs in polymer, resulting in resistance increase [6,8].

Next, the higher sensor response to ethanol than that of dichloromethane for pristine SWNTs and thiophene/SWNTs can be explained by the dielectric constant which mentioned about the polarity of vapor. Ethanol with higher dielectric constant interrupts moving electron and holes, resulting in a large decrease in resistance compare to that of dichloromethane [9]. While a higher response of PMMA/SWNTs to dichloromethane than ethanol can be explained by Flory-Huggins interaction which indicated the strength of interaction. Dichloromethane has a good solubility and high strength interaction in PMMA, thus PMMA/SWNTs exhibited higher response to dichloromethane than ethanol [10].

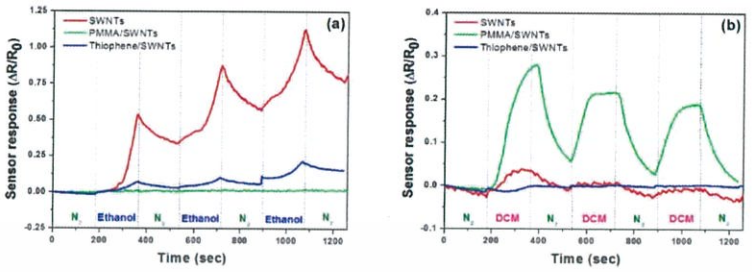

Fig. 3 Sensor response of SWNTs and polymer-coated SWNTs to (a) ethanol and (b) dichloromethane vapors.

To compare the sensor response of each sensor, the sensor response was normalized by its concentration. The sensor response was assumed to be proportional to vapor concentration [11]. The normalized sensor response was defined as a ratio between sensor response at time of 630 s and vapor concentration as shown in table 1 (S_{630s}/C_{vapor}). The normalized sensor responses of the SWNTs and polymer-coated SWNTs to ethanol and dichloromethane vapors are shown in Fig. 4. The normalized sensor responses corresponded with the sensor responses of all sensors shown in Fig. 3. Next, we explored the potential of SWNTs and polymer-coated SWNTs based sensors vapor discrimination. The pattern recognition of ethanol and dichloromethane vapors was utilized by principal component analysis (PCA) technique. PCA plots of ethanol was separated from that of dichloromethane, showing a distinguished pattern recognition between ethanol and dichloromethane vapor by using pristine SWNT and polymer-coated SWNTs as sensors (Fig. 5).

Table 1 Concentrations of ethanol and dichloromethane for each sensor test

Sensor	Ethanol concentration (ppm)	Dichloromethnae concentration (ppm)
SWNTs	271.11	1995.56
PMMA/SWNTs	203.89	2037.78
Thiophene/SWNTs	210.56	2056.57

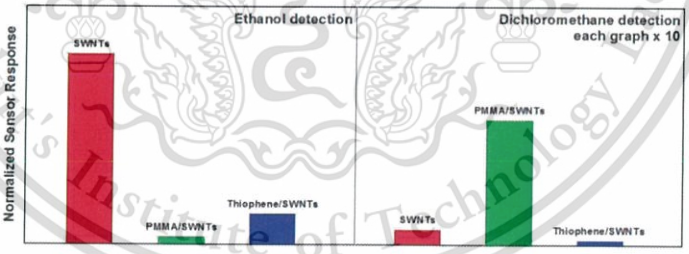

Fig. 4. Normalized sensor response of various sensors to ethanol and dichloromethane vapors.

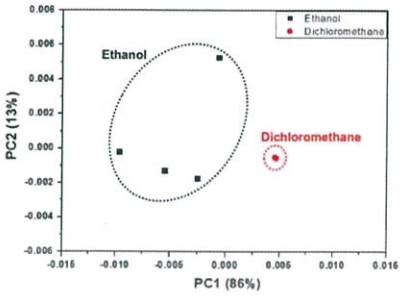

Fig. 5 PCA plots of ethanol and dichloromethane vapors.

Summary

Sensors based on pristine SWNTs and polymer-coated SWNTs were developed and applied for VOCs detection. Pristine SWNTs exhibited fast and high response to ethanol while PMMA/SWNTs improved the sensor response to dichloromethane, respectively. From PCA results, pattern recognition clearly showed the discrimination between ethanol and dichloromethane vapors. Integration of pristine SWNTs and polymer-coated SWNTs is a promising approach for selectivity of VOCs detection.

Acknowledgment

This work has partially supported by the National Nanotechnology Center (NANOTEC), NSTDA, Ministry of Science and Technology, Thailand, through its program of Center of Excellence Network. We also acknowledge the financial support and facilities from the Office of the National Research Council of Thailand, the Toray Science Foundation, Japan (TSF), the Thailand Graduate Institute of Science and Technology (TGIST) under contact TGIST 01-55-013. We thank to Mr. Thanawee Chodjarusawad, Burapha University for PCA technique suggestion.

References

[1] T. W. Odom, Electronic properties of single-walled carbon nanotubes, Aust. J. Chem. 54 (2001) 601-604.

[2] P. Qi, O. Vermesh, M. Grecu, A. Javey, Q. Wang, H. Dai, Toward large arrays of multiplex functionalized carbon nanotube sensors for highly sensitive and selective molecular detection, Nano Lett. 3 (2003) 347-351.

[3] J. Li, Y. Lu, Q. Ye, M. Cinke, J. Han, M. Meyyappan, Carbon nanotube sensors for gas and organic vapor detection, Nano Lett. 3 (2003) 929-933.

[4] W. Wongwiriyapan, S. Honda, H. Konishi, T. Mizuta, T. Ikuno, T. Ito, T. Maekawa, K. Suzuki, H. Ishikawa, K. Oura, M. Katayama, Single-walled carbon nanotube thin film sensor for ultrasensitive gas detection, Jpn. J. Appl. Phys. 44 (2005) 482-484.

[5] A. Star, V. Joshi, S. Skarupo, D. Thomas, J.-C.P. Gabriel, Gas sensor array based on metal-decorate carbon nanotubes, 110 (2006) 21014-21020.

[6] J. K. Abraham, B. Phillip, A. Witchurch, V. K. Varadan, C. C. Reddy, A compact wireless gas sensor using a carbon nanotube/PMMA thin film chemiresistor, Smart Mater. Struct. 13 (2004) 1045-1049.

[7] K.S.V. Santhanam, R. Sangoi, L. Fuller, A chemical sensor for chloromethane using a nanocomposite of multiwalled carbon nanotubes with poly(3-methylthiophene), Sens. Actuators B 106 (2005) 766-771.

[8] F. Wang, H. Gu, T. M. Swager, Carbon nanotube/polythiophene chemiresistive sensors for chemical warfare agents, J. AM. Chem. Soc. 130 (2008) 5392-5393.

[9] T. Kim, D. Kwak, Flexible VOC sensors using conductive polymers and porous membranes for application to textiles, Fibers and Polymer 13 (2012) 471-474.

[10]H. Eser, F. Tihminlioglu, Solubility and diffusivity of solvents and nonsolvents in poly(methyl methacrylate co butyl methacrylate), Fluid Phase Equilibrum, 237 (2005) 68-76.

[11]J. W. Gardner, P. N. Barlett, Electronic noses: Principles and applications, New York, NY: Oxford University Press (1999).

ENGINEERING JOURNAL

Article

Effect of Metal Catalysts on Synthesis of Carbon Nanomaterials by Alcohol Catalytic Chemical Vapor Deposition

Worawut Muangrat[1], Supanit Porntheeraphat[2], and Winadda Wongwiriyapan[1,3,4,*]

1 College of Nanotechnology, King Mongkut's Institute of Technology Ladkrabang, Ladkrabang, Bangkok 10520, Thailand
2 National Electronics and Computer Technology Center (NECTEC), Khlong Luang, Phathumthani 12120, Thailand
3 NANOTEC-KMITL Center of Excellence on Nanoelectronic Device, Ladkrabang, Bangkok 10520, Thailand
4 Thailand Center of Excellence in Physics, CHE, Si Ayutthaya Road, Bangkok 10400, Thailand
*E-mail: kwwinadd@kmitl.ac.th

Abstract. Carbon nanomaterials (CNMs) were synthesized by alcohol catalytic chemical vapor deposition (CVD) at atmospheric pressure using different metal catalysts (Ni, Co and Fe) at a growth temperature of 700°C. Ni and Fe acted as active catalysts for multi-walled carbon nanotubes (MWNTs) growth, while Co acted as an active catalyst for bamboo-like MWNTs and carbon nanofibers (CNFs) growth. The CNMs synthesized from Ni catalyst showed the highest crystallinity with a small amount of by-products. These results imply that metal catalyst is a key parameter to the structure, morphology and crystallinity of CNMs. The different effects of metal catalysts on the growth of CNMs can be explained in terms of the difference in the change in Gibbs free energy of metal carbide formation.

Keywords: Carbon nanomaterials, multi-walled carbon nanotubes, carbon nanofibers, alcohol catalytic chemical vapor deposition.

ENGINEERING JOURNAL Volume 17 Issue 5
Received 9 April 2013
Accepted 19 September 2013
Published 25 December 2013
Online at http://www.engj.org/
DOI:10.4186/ej.2013.17.5.35

This paper is based on the oral presentation at the 1st Joint Conference on "Renewable Energy and Nanotechnology" (JCREN 2012) in Bangkok, Thailand, 19-20 November 2012.

DOI:10.4186/ej.2013.17.5.35

1. Introduction

Carbon nanomaterials (CNMs) such as fullerenes [1], carbon nanotubes (CNTs) [2-3], carbon nanofibers (CNFs) [4] and graphene [5] have attracted great attention due to their excellent structural, electronic, thermal and mechanical properties. Especially, CNTs have been extensively studied for their potential applications of nanotechnology. To produce such CNMs, chemical vapor deposition (CVD) has been considered as a promising method for mass production with controlled diameter, purity, quantity and orientation [6].

One of the key parameters for CVD method is metal catalyst. There have been several reports on the effects of the metal catalysts on the synthesis of CNMs using methane [7], ethylene [8] and acetylene [9] as carbon sources. It was found that the structure, morphology and crystallinity of CNMs depend crucially on the selection of metal catalyst. Recently, a simple and safe technique for producing high quality CNTs has been proposed. It entails a low-temperature alcohol catalytic CVD method using ethanol (C_2H_5OH) as a carbon source [10]. However, the relationship between the obtained structure of CNMs and the metal catalyst type has not been fully explored.

In this work, the effects of metal catalysts on the synthesis of CNMs by alcohol catalytic CVD were investigated. Ni, Co and Fe were employed as metal catalyst. The morphology, structure and crystallinity of CNMs synthesized from these metal catalysts were characterized.

2. Experimental

An electron-beam evaporator was used to sequentially deposit an under layer (Al (5 nm)/Cr (2 nm)) and a metal catalyst layer (Ni, Co or Fe (5 nm)) on Si substrate. The deposited substrates were then annealed in a quartz tube at 700°C for 60 min under a flow of Ar gas at a flow rate of 500 sccm. Then, ethanol vapor was introduced by bubbling Ar gas through ethanol at a flow rate of 800 sccm. The CVD growth was carried out for 20 min at atmospheric pressure. After that, the synthesized material was cooled down to room temperature under Ar gas at a flow rate of 500 sccm. The morphology, structure and crystallinity of the obtained CNMs were characterized by scanning electron microscopy (SEM), transmission electron microscopy (TEM) and Raman spectroscopy.

3. Results and Discussion

3.1. CNMs Characterization

Figures 1(a)-1(c) and Figs. 1(d)-1(f) show SEM and TEM images of CNMs synthesized from Ni, Co and Fe catalysts, respectively. Tubular structures were synthesized in all cases, but their morphologies and structures were different. The SEM images shows that the CNMs grown from Ni and Co catalysts had a relatively high density of tubular structures covered wholly on the surface of substrates (Figs. 1(a) and 1(b)), while the CNMs grown from Fe had a low density with a mixture of long-straight and shortly random CNMs (Fig. 1(c)). The TEM images, clearly show that the structures of CNMs grown from different metal catalysts were completely different. The CNMs grown from Ni catalyst shows graphene planes aligning paralleling to each other and to the axis of the tubular structure, indicating multi-walled carbon nanotube (MWNT) structure (Fig. 1(d)). For the CNMs grown from Co catalysts, their graphene planes are parallel to each other but made an angle with the axis of the tube with bamboo compartments along the tube, indicating bamboo like-MWNT structure (Fig. 1(e)). CNFs were also mixed in the CNMs grown from Co catalyst. For the CNM grown from Fe catalyst, their graphene planes are parallel to each other, indicating MWNT structure. The average diameters of the synthesized CNMs from Ni, Co and Fe catalysts were approximately 9.35±4.29, 30.20±12.18 and 43.67±18.70 nm, respectively. From the TEM images at low magnification (Fig. 1(g) and 1(h)), two types of CNMs were observed. One was CNMs without metal catalyst at the tube end. The other was CNMs with clusters of metal catalyst (dark contrast in TEM image) encapsulated at the tube end. This implies that the growth of the synthesized CNMs was based on both the base growth [11] and the tip growth [12] mechanisms, respectively. Moreover, as can be seen in the TEM images at low magnification, the CNMs grown from Ni catalyst showed a higher density of a relatively uniform diameter of MWNTs with a small amount of by-products, when compared to those grown from Co catalyst.

DOI:10.4186/ej.2013.17.5.35

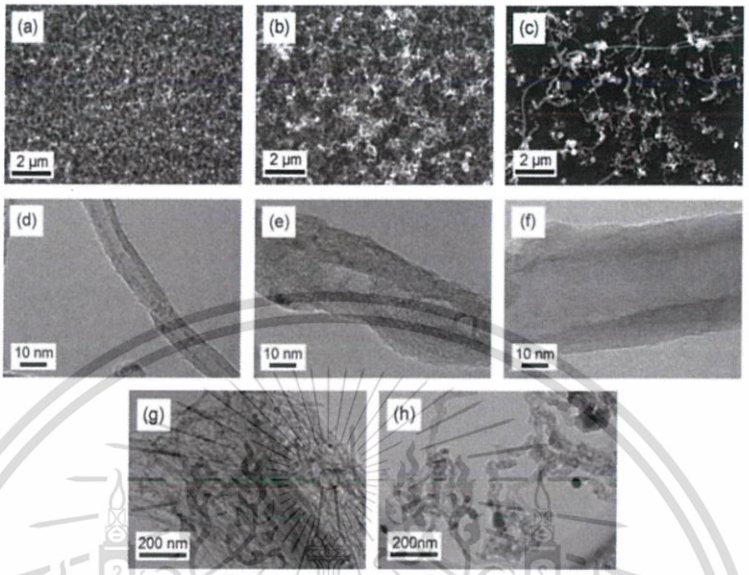

Fig. 1. SEM and TEM images of CNMs synthesized from different metal catalysts; (a), (d) Ni (b), (e) Co and (c), (f) Fe. TEM images at low magnification of CNMs synthesized from (g) Ni and (h) Co.

Next, Raman spectroscopy was utilized to characterize the structure, purity and crystallinity of the synthesized CNMs. Ar ion laser with a wavelength of 532 nm (2.33eV) was used as the excitation light. All spectra showed mainly two bands at ~1340 cm^{-1} (D-band disorder carbon) and ~1590 cm^{-1} (G-band graphitic structure), corresponding to MWNT structure. Furthermore, the small peaks at ~2700 cm^{-1} (G´ band) were also observed in every sample. This spectrum indicates the overtone or second order of D band, which originates from the two phonon double resonance Raman process [13]. The intensity ratio between G (I_G) band and D (I_D) band, (I_G/I_D) is an indication of the crystallinity of CNMs. The I_G/I_D ratio of the CNMs synthesized from Ni, Co and Fe were 0.73, 0.44 and 0.49, respectively. Hence, it can be concluded that the CNMs synthesized from Ni catalyst had the highest crystallinity.

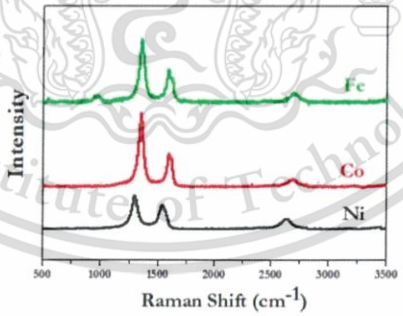

Fig. 2. Raman Spectra of synthesized CNMs from different metal catalysts.

DOI:10.4186/ej.2013.17.5.35

The obtained results, indicate that the morphology of CNMs strongly depended on the selection of metal catalyst. At the growth temperature of 700°C, Ni catalyst afforded a high density growth of a uniform diameter of MWNTs with a small amount of by-products, while Co catalyst afforded a high density growth of a mixture of bamboo-like MWNTs and CNFs. Fe catalyst afforded a growth of MWNTs at low density.

3.2. Discussion of Effect of Metal Catalyst on Morphology of CNMs

In order to understand the effect of Ni catalyst on high yield growth of CNMs, the growth mechanism of CNMs is explained based on the thermodynamics of carbon-metal reaction. The possible growth model of CNMs is as follows: carbon source decomposes and dissolves forming metal carbides on the surface of metal catalyst nanoparticles: additional carbon atoms precipitate and get extracted easily from the metal carbides, leading to formation of CNMs [14]. The direction of the reaction can be considered thermodynamically by the change in Gibbs free energy (ΔG). The reaction proceeds forward when ΔG value is less than zero or negative value ($\Delta G<0$). A previous study has reported that the ΔG of ethanol decomposition at a reaction temperature of 700°C, as shown in Eq. (1), is less than zero [15].

$$C_2H_5OH \rightarrow 2C(s) + 2H_2 + H_2O \quad (1)$$

For the carburization of decomposed carbon source by metal catalyst, the reaction can be expressed as Eq. (2) bellow [14-15].

$$C_2H_5OH + M \rightarrow MC_2 + 2H_2 + H_2O \quad (2)$$

where M denotes a metal catalyst and MC_2 denotes metal carbide.

ΔG of carburization reaction of different metal catalysts under acetylene (C_2H_2) system has been reported in several studies. The magnitude of ΔG of Ni, Co and Fe catalysts were in the following order: Fe<Co<Ni [14]. For the C_2H_5OH system, we assumed that ΔG behaves like the C_2H_2 system. That is why the Ni catalyst with the highest magnitude of ΔG gave the highest yield of CNMs, while the Fe catalyst with the lowest magnitude of ΔG gave the lowest yield of CNMs. However, a more accurate determination of the ΔG for the ethanol system is needed and will be addressed in future work.

4. Conclusion

CNMs were successfully synthesized by alcohol catalytic CVD at 700°C using from three different metal catalysts using ethanol as a carbon source. Ni and Fe were shown to be active catalysts for MWNTs growth, while Co acted as an active catalyst for bamboo-like MWNTs and CNFs. Ni catalyst afforded the highest yield and crystallinity, while Fe catalyst afforded the lowest. The average diameter of CNMs synthesized from each catalyst was in the following order: Ni<Co<Fe. The relationship between CNMs yield and metal catalyst type can be explained by the change in Gibbs free energy. We conclude that the desired yield, diameter, structure, morphology and crystallinity of CNMs can be controlled by judicious selection of appropriate metal catalyst.

Acknowledgement

This work was partially supported by the National Nanotechnology Center (NANOTEC), NSTDA, Ministry of Science and Technology, Thailand, through its program of Center of Excellence Network. We would also like to acknowledge the financial support and facilities from King Mongkut's Institute of Technology Ladkrabang (KMITL) research fund and the Thailand Graduate Institute of Science and Technology (TGIST) under the contract TGIST 01-55-013.

References

[1] H. W. Kroto, "C_{60}: Buckminsterfullerene," *Natur*, vol. 318, pp. 162-163, 1985.
[2] A. Oberlin, M. Endo, and T. Koyama, "Filamentous growth of carbon through benzene decomposition," *J. Crystal Growth*, vol. 32, pp. 335-349, 1976.
[3] S. Iijima, "Helical microtubules of graphitic carbon," *Nature*, vol. 354, pp. 56-58, 1991.
[4] K. P. Jong and J. W. Geus, "Carbon nanofibers: catalytic synthesis and applications," *Catal. Rev. Sci. Eng.*, vol. 42, pp. 481-510, 2000.

DOI:10.4186/ej.2013.17.5.35

[5] K. S. Novoselov, A. K. Geim, S. V. Morozov, D. Jiang, Y. Zhang, S. V. Dubonos, I. V. Grigorieva, and A. A. Firsov, "Electric filed effect in atomically thin carbon film," *Science*, vol. 306, pp. 666-669, 2004.

[6] K. Hata, D. N. Futaba, K. Mizuno, T. Namai, M. Yumura, and S. Iijima, "Water-assisted highly efficient synthesis of impurity-free single-walled carbon nanotubes," *Science*, vol. 306, pp. 1362-1364, 2004.

[7] K. Kong, A. M. Cassell, and H. Dai, "Chemical vapor deposition of methane for single-walled carbon nanotubes," *Chem. Phys. Lett.*, vol. 292, pp. 567-574, 1998.

[8] L. Delzeit, C. V. Nguyen, B. Chen, R. Stevens, A. Cassell, J. Han, and M. Meyyappan, "Multiwalled carbon nanotubes by chemical vapor deposition using multilayered metal catalysts," *J. Phys. Chem. B*, vol. 106, pp. 5629-5635, 2002.

[9] C. J. Lee, J. Park, and J. A. Yu, "Catalyst effect on carbon nanotubes synthesized by thermal chemical vapor deposition," *Chem. Phys. Lett.*, vol. 360, pp. 250-255, 2002.

[10] S. Maruyama, R. Kojima, Y. Miyauchi, S. Chiashi, and M. Kohno, "Low-temperature synthesis of high-purity single-walled carbon nanotubes from alcohol," *Chem. Phys. Lett.*, vol. 360, pp. 229-234, 2002.

[11] R. T. K. Baker and R. J. Waite, "Formation of carbonaceous deposits from the platinum-iron catalyzed decomposition of acetylene," *J. Catalysis*, vol. 37, pp. 101-105, 1975.

[12] R. T. K. Baker, M. A. Barber, P. S. Harris, F. S. Feates, and R. J. Waite, "Nucleation and growth of carbon deposits from the nickel catalyzed decomposition of acetylene," *J. Catalysis*, vol. 26, pp. 51-56, 1972.

[13] C. Thomsen and S. Reich, "Double resonant scattering in graphite," *Phys. Rev. Lett.*, vol. 85, pp. 5214-5217, 2000.

[14] S. Esconjauregui, C. M. Whelan, and K. Maex, "The reasons why metals catalyze the nucleation and growth of carbon nanotubes and other carbon nanomorphologies," *Carbon*, vol. 47, pp. 659-669, 2009.

[15] J. P. Tessonnier and D. S. Su, "Recent progress on the growth mechanism of carbon nanotubes: A review," *ChemSusChem*, vol. 4, pp. 824-847, 2011.